



**HAL**  
open science

# Aerodynamic study of a 3D backward facing double step applied to safer launch and recovery of helicopters on ships

Benjamin Herry

► **To cite this version:**

Benjamin Herry. Aerodynamic study of a 3D backward facing double step applied to safer launch and recovery of helicopters on ships. Fluid mechanics [physics.class-ph]. Université de Valenciennes et du Hainaut-Cambresis, 2010. English. NNT : 10/47 . tel-00650410

**HAL Id: tel-00650410**

**<https://theses.hal.science/tel-00650410>**

Submitted on 10 Dec 2011

**HAL** is a multi-disciplinary open access archive for the deposit and dissemination of scientific research documents, whether they are published or not. The documents may come from teaching and research institutions in France or abroad, or from public or private research centers.

L'archive ouverte pluridisciplinaire **HAL**, est destinée au dépôt et à la diffusion de documents scientifiques de niveau recherche, publiés ou non, émanant des établissements d'enseignement et de recherche français ou étrangers, des laboratoires publics ou privés.

N° d'ordre : 10/47

**Université de Valenciennes et du Hainaut Cambrésis**  
*École Doctorale Sciences Pour l'Ingénieur Université Lille Nord-de-France*

**THÈSE DE DOCTORAT**

*présentée pour obtenir le titre de DOCTEUR*

Spécialité : **Mécanique**

*Par*

**Benjamin HERRY**

**ÉTUDE AÉRODYNAMIQUE D'UNE DOUBLE MARCHE DESCENDANTE  
3D APPLIQUÉE A LA SÉCURISATION DE L'APPONTAGE DES  
HÉLICOPTÈRES SUR LES FRÉGATES**

**Soutenue publiquement le 20 décembre 2010 devant le jury composé de:**

PRÉSIDENT

**Gérard BOIS**                      Professeur, Université de Lille

RAPPORTEURS

**Jean-Yves BILLARD**            Professeur, Université de Brest

**Azeddine KOURTA**            Professeur, Université d'Orléans

EXAMINATEURS

**Grégory COUSSEMENT**      Professeur, Université de Mons

**Éric GARNIER**                    HDR, ONÉRA Meudon

**Larbi LABRAGA**                Professeur, Université de Valenciennes, *Directeur de thèse*

**Laurent KEIRSBULCK**        Maître de conférences, Université de Valenciennes, *Co-encadrant*

**Bruno MIALON**                 Ingénieur, ONÉRA Lille

INVITÉS

**Jean-Bernard PAQUET**        Docteur Ingénieur, ONÉRA Lille, *Co-encadrant*

**Joop GOODEN**                 Ingénieur, National Aerospace Laboratory, Pays-Bas



*“Was mich nicht umbringt, macht mich stärker.”*

Friedrich Nietzsche, *Sprüche und Pfeile*, 8.



## Acknowledgements

Cette page est probablement la plus difficile de toutes à écrire. Il n’y a pourtant pas de calculs à faire. Au contraire, il s’agit d’exprimer avec sincérité la gratitude et la reconnaissance envers ceux qui ont marqué de près et/ou de loin ces trois dernières années passées à l’Onera de Lille.

Sans remonter à la genèse pour remercier toutes les raisons qui ont conduit à mon existence et mes conditions de vie, une pensée légitime devrait cependant au moins être attribuée à mes proches. Contrairement à beaucoup d’autres auteurs, ce ne sera pas fait ici: une page (aux bas mots) leur est en effet déjà dédiée ...

En revanche, un hommage doit être rendu à l’Onera qui a permis de remplir sans privation un grand réfrigérateur, notamment d’une petite collection à déguster de bières du *Noooooord*. Mais plus que l’institution, ce sont les hommes qui ont laissé leurs empreintes. Tout d’abord, Bruno Mialon, chef d’unité, qui a toujours fait son maximum pour qu’avancent les choses et en particulier pour que soient réglées au mieux les difficultés basement matérielles. Dans son rôle de manager de personnel, ce fut lui qui apporta aussi (peut-être à son insu d’ailleurs!) la reconnaissance tant attendue dans l’inévitable moment de solitude et de perte de confiance que vivent certains doctorants... Mon “plus que collègue maintenant”, François Touron sait de quoi il s’agit, lui qui prenait les relais au mégaphone pour le ‘Rame!’ (ter repetitam). Le relai passe désormais dans les mains de mes amis, Thomas et Stéphane de MMHD, qui auront rempli cette dernière année de mémorables cartons jaunes et rouges. Bon courage et réussite à eux. Bonne continuation aussi à ceux qui ont apporté leur aide ... toute l’équipe MMHD en fait! Certains gardent une place particulière dans ma mémoire; ils se reconstruiront.

Enfin, ces trois années ont été très riches en enseignement et pas uniquement sur le plan scientifique, loin s’en faut. Je remercierai à cet égard les encadrants de cette thèse, Larbi Labraga, Laurent Keirsbulck et Jean-Bernard Paquet, qui ont partagé bien plus que leurs connaissances, puisqu’ils m’ont accordé leur confiance en me laissant par là même une grande autonomie.

Enfin, le ruban entourant ce mémoire ne pourrait jamais être noué sans les membres du jury. A cet égard, le rôle des rapporteurs est irremplaçable et bien entendu, j’exprime toute ma reconnaissance aux professeurs Jean-Yves Billard et Azeddine Kourta qui ont accepté cette tâche de relecture, parfois ingrate. Je remercie aussi Eric Garnier ainsi que les professeurs Gérard Bois et Grégory Coussement dans leur rôle d’examineurs. Enfin, c’est un plaisir de revoir Joop Gooden au delà de la coopération Onera/NLR, et de pouvoir discuter à nouveau avec lui en toute modestie.

Cette liste de remerciements n’est bien sûr pas exhaustive, mais les absents savent qu’ils n’ont pas été oubliés.



## *Résumé détaillé*

Cette étude s'inscrit dans le domaine de la sécurisation de l'appontage des hélicoptères sur les frégates. En effet, cette phase d'une mission d'un pilote d'hélicoptère est l'une des plus difficile et dangereuse qui soit, principalement du fait de la forte charge de travail qu'il subit. Les principales causes résident dans les mouvements de plateformes et l'aérodynamique défavorable au dessus des ponts d'envol. Le problème étant complexe, il doit être simplifié. En particulier, l'impact du sillage aérodynamique de la frégate sur le vol de l'hélicoptère doit être isolé. Sachant que les taux de turbulence les plus élevés induisant une charge de travail maximum sur les pilotes sont rencontrés lorsque le vent relatif est fort et qu'il est dans l'axe du bateau, il s'agit d'analyser ce type d'écoulement à dérapage nul du navire, sans mouvement et sans hélicoptère. Une étude bibliographique a permis de montrer qu'il existait déjà des travaux sur la modélisation de sillages aérodynamiques de frégates. En particulier, des géométries génériques ont été définies sur lesquelles des essais expérimentaux ainsi que des calculs numériques ont été réalisés. Ces premiers travaux ont permis de donner une première description de la topologie de l'écoulement moyen au dessus de la plateforme d'appontage. Sur une configuration géométrique particulière (mais symétrique), deux auteurs observent à la fois expérimentalement et numériquement un phénomène inattendu d'asymétrie de l'écoulement moyen à angle de dérapage nul. Toutefois, il n'est ni décrit, ni expliqué. D'autre part, les travaux s'attardant sur la phénoménologie instantanée de l'écoulement sont très peu nombreuses alors que cet aspect est fondamental pour la problématique de l'appontage. Ainsi, afin de mieux comprendre ces caractéristiques qui ne sont pas abondamment décrites dans la littérature, une démarche a été entreprise afin d'isoler l'écoulement au dessus de la plateforme, de le sonder et d'en étudier en particulier l'asymétrie de l'écoulement moyen ainsi que ses conséquences éventuelles sur la problématique de l'appontage.

Cette démarche a d'abord consisté à définir une version améliorée de géométrie générique de frégate décrite dans la littérature afin d'obtenir en amont du hangar des conditions les plus uniformes possibles. Ceci conduit à modéliser le bateau par une double marche descendante 3D avec un nez en forme d'ogive. La forme est choisie afin que des couches limites de type plaque plane se développent sur les quatre faces de la maquette et donc d'obtenir en amont de la première marche (modélisant le hangar, de hauteur  $h$ ) des couche limites canoniques. Ceci est aussi permis en plaçant la maquette au bord d'attaque d'une table de  $49h$  de long, ce qui a pour effet d'extraire le maquette de la couche limite se développant sur le sol de la soufflerie, mais aussi créant un



espace libre permettant à l'air de librement circuler entre la maquette et le sol soufflerie. L'ensemble table/maquette est alors monté dans la soufflerie subsonique du laboratoire TEMPO de Valenciennes, disposant d'une veine d'essai de  $2 \times 2 \times 10 \text{ m}^3$ . Cette soufflerie est choisie pour son faible taux de turbulence et ses grandes dimensions permettant d'atteindre des nombres de Reynolds élevés, supérieurs à  $8.75 \times 10^4$  (basés sur la hauteur de marche et la vitesse amont de l'écoulement libre). Ces hauts nombres de Reynolds sont nécessaires afin que les couches limites qui se développent en amont de la première marche soient turbulentes établies, permettant d'obtenir un régime représentatif de l'écoulement à l'échelle 1. Cette caractéristique d'écoulement turbulent est vérifiée en sondant le profil d'une des couches limites latérales en amont de la première marche. L'uniformité de l'écoulement amont est qualitativement vérifiée par des visualisations par enduit gras et tomoscopie laser.

L'écoulement en amont de la première marche étant caractérisé, l'attention est alors portée sur l'écoulement en son aval. Pour cela, de l'enduit gras est utilisé pour tracer les lignes de frottement pariétales moyennes : les empreintes d'un tourbillon en U inversé apparaissent avec une très légère asymétrie. De plus, la longueur de rattachement est estimée à  $2,8h$ . Cette valeur est alors confirmée par PIV dans le plan de symétrie en localisant la position du point de vitesse longitudinale nulle en moyenne. Ce cliché met en évidence une zone de recirculation primaire et secondaire, tout comme en aval d'une marche 2D. Le tourbillon en U inversé est cependant mieux visualisé dans le plan PIV horizontal, réalisé à mi-hauteur de marche : les lignes de courant montrent alors une forte asymétrie de l'écoulement moyen dans ce plan. Une explication de ce phénomène est alors recherchée dans l'analyse de l'écoulement instationnaire.

Les fluctuations d'écoulement sont décrites et une analyse POD est entreprise à partir des données des 2 plans PIV. Le premier mode du plan de symétrie de la maquette semble traduire un phénomène de battement de la couche de cisaillement, ce que les mesures de corrélations croisées corroborent. Les modes suivants, quant à eux, semblent plus rapportés à un phénomène de lâchers tourbillonnaires dans la couche de cisaillement. En revanche, dans le plan à mi-hauteur de marche, les premiers modes ne traduisent a priori pas de phénomène instationnaire académique. Les modes dans ce plan sont asymétriques, traduisant l'asymétrie de l'écoulement fluctuant à dérapage nul malgré une géométrie symétrique. Pour mieux comprendre la phénoménologie instationnaire de cet écoulement, un spectre est obtenu de part et d'autre du plan de symétrie, en aval de la première marche. Un pic net apparaît pour un Strouhal de 0,08 (basé sur la hauteur de marche et la vitesse infinie amont). Une forte contribution des plus basses fréquences est aussi bien visible, sans cependant noter de pic étroit. De la tomoscopie laser haute cadence est alors réalisée afin de tenter d'associer une fréquence à un phénomène aérodynamique particulier. L'approche n'est pas parfaitement concluante. Elle permet cependant d'estimer et de confronter les mesures par fil chaud

de la vitesse d'advection des structures cohérentes, montrant une accélération de ces dernières lors de leur éloignement de la marche. Leur trajectoire est enfin déterminée par une analyse statistique utilisant le critère de détection. Cette approche requiert cependant un approfondissement afin de mieux comprendre la phénoménologie 3D instationnaire de cet écoulement.

Une des originalités principales de cette étude réside toutefois dans l'élaboration d'un protocole expérimental visant à mettre en évidence des cas d'apparition de cette asymétrie de l'écoulement moyen. Le premier paramètre étudié est l'angle de dérapage. La très grande sensibilité de l'écoulement moyen avec ce paramètre est observée par PIV dans le plan à mi-hauteur de marche. L'écoulement moyen symétrique n'est d'ailleurs pas obtenu. Les conditions amont à la marche sont alors modifiées pour voir si elles ont une quelconque influence sur le résultat. Tout d'abord, la maquette est posée au sol d'une autre soufflerie (Onera L2) ayant la propriété de simuler une couche limite atmosphérique marine et donc de présenter des taux de turbulence élevés (jusqu'à 7% en proche paroi). Dans cette soufflerie, des visualisations par tomoscopie laser dans le plan à mi-hauteur de marche ainsi que des mesures de pression pariétales sont réalisées. Aucune influence de ce changement des conditions amont sur l'écoulement moyen n'est observée. Le résultat est le même lorsque le nez des maquettes est modifié, contrôlant ainsi l'état attaché ou détaché des couches limites supérieure et latérales en amont de la première marche. L'ajout d'un parallélépipède (modélisant une cheminée) sur la face supérieure de la maquette n'a pas non plus d'influence sur le résultat. La propriété d'asymétrie de l'écoulement moyen semble donc peu influencée par les conditions amont à la maquette. Pour vérifier cette hypothèse, une simulation numérique est conduite sur un domaine fluide débutant en aval du nez, annulant ainsi l'influence de ce dernier. L'angle de dérapage géométrique est nul et les conditions amont sont mathématiquement uniformes. Malgré cela, le modèle RANS stationnaire de Spalart-Almaras prédit un écoulement asymétrique en moyenne. Les coefficients de pression correspondent d'ailleurs bien avec les valeurs expérimentales. En plus de donner une idée de la topologie 3D de l'écoulement, ce calcul semble mettre en évidence l'absence d'influence des conditions amont sur l'écoulement moyen autour de telles géométries dans le domaine de conditions testées. Mais est-ce valable pour toutes conditions? Sachant que le nombre de Reynolds peut-être un paramètre critique conditionnant ou non de tels phénomènes, un troisième montage est réalisé utilisant une maquette de petite taille conduisant à un nombre de Reynolds de  $5.9 \times 10^3$  (basé sur la hauteur de marche). L'écoulement en amont de la marche est donc attendu laminaire et pourtant, l'asymétrie en aval est toujours visualisée par tomoscopie laser. Pour l'ensemble de valeurs étudiées, le nombre de Reynolds n'est donc pas un paramètre influençant cette asymétrie de l'écoulement moyen. Il reste cependant à expliquer ce phénomène d'asymétrie. Pour cela, les clichés instantanés PIV et tomoscopie laser sont analysés

individuellement. Ils peuvent être rangés en deux familles distinctes, l'une présentant un gros tourbillon d'un côté de la maquette, et l'autre étant son symétrique. Il est montré que les clichés d'une même famille se succèdent, laissant place à un ensemble de clichés de l'autre famille. Ceci suggère donc l'existence de deux solutions stables de l'écoulement et laissent penser que la solution moyenne symétrique est instable. La bascule d'une solution à l'autre est aléatoire à angle de dérapage nul avec, a priori, équiprobabilité d'apparition des deux solutions. En revanche, lorsque l'angle de dérapage devient non nul, une solution apparaît plus souvent que l'autre : l'asymétrie de l'écoulement moyen est donc un effet de moyenne dû à cette caractéristique de la bi-stabilité de l'écoulement. Ce phénomène est-il toutefois important pour la problématique de l'appontage ?

Une première approche considérant quelques critères de la littérature laisse penser que le phénomène de bascule d'une solution à l'autre risque d'avoir des conséquences néfastes sur l'appontage des hélicoptères. De ce fait, une modélisation fidèle de ce phénomène peut s'avérer nécessaire. Pour cela, des travaux complémentaires sur la compréhension de l'écoulement 3D instationnaire ne semblent pas inutiles. Comprendre les origines du phénomène de bi-stabilité serait aussi d'une grande aide pour son éventuel contrôle. Cependant, avant cela, une hypothèse forte qui avait été faite pour cette étude doit être vérifiée : l'approche considérant négligeable l'influence du sillage rotor sur l'écoulement est-elle valable ? Si cela justifie l'étude du sillage aérodynamique seul en absence de rotor, est-ce la bonne approche ? Le phénomène de bi-stabilité est-il toujours présent lorsqu'un rotor d'hélicoptère se trouve au dessus de la plateforme ? Une étude paramétrique devrait être réalisée afin de déterminer pour quelles caractéristiques de triplet hélicoptères/frégates/conditions de vent l'hypothèse précédente est valable. Le sujet est donc encore loin d'être clos.

# Contents

<b>Acknowledgements</b>	<b>v</b>
<b>Résumé détaillé</b>	<b>vii</b>
<b>List of Figures</b>	<b>xvii</b>
<b>List of Tables</b>	<b>xxi</b>
<b>Abbreviations</b>	<b>xxiii</b>
<b>Symbols</b>	<b>xxv</b>
<b>Introduction</b>	<b>1</b>
<b>1 Literature overview</b>	<b>5</b>
1.1 2D simple backward facing step . . . . .	5
1.1.1 Flow topology . . . . .	6
1.1.1.1 In the plane of symmetry . . . . .	6
1.1.1.2 Three-dimensional behavior . . . . .	7
1.1.1.3 Comparison criteria . . . . .	7
1.1.2 The effect of system parameters on reattachment . . . . .	8
1.1.2.1 Initial boundary layer state . . . . .	8
1.1.2.2 Boundary layer thickness . . . . .	8
1.1.2.3 Free stream turbulence . . . . .	9
1.1.2.4 Blockage coefficients . . . . .	9
Expansion ratio . . . . .	9
Aspect ratio . . . . .	10
1.1.3 Unsteady flow . . . . .	10
1.1.3.1 Reynolds stresses . . . . .	10
Turbulence intensity . . . . .	10
Turbulence production . . . . .	10
1.1.3.2 Spectral analysis . . . . .	11
1.1.3.3 Coherent structures . . . . .	11
1.2 2D cylinders at zero degree sideslip . . . . .	12
1.2.1 Flow topology and phenomenology . . . . .	12
1.2.2 Influence of some parameters . . . . .	14

1.2.2.1	Aspect ratio . . . . .	14
1.2.2.2	Blockage effect . . . . .	14
1.2.2.3	Free-stream turbulence intensity and turbulence length scales . . . . .	15
1.2.2.4	Reynolds number . . . . .	15
1.2.3	Unsteady flow . . . . .	16
1.2.3.1	Turbulence levels . . . . .	16
1.3	3D parallelepiped at zero degree sideslip . . . . .	16
1.3.1	Flow topology . . . . .	17
1.3.2	The effects of some parameters . . . . .	19
1.3.2.1	An illustration through the reattachment length . . . . .	19
1.3.2.2	Bluff body aspect ratio . . . . .	20
1.3.2.3	Upstream conditions: the atmospheric boundary layer . Mean velocity gradient . . . . .	20
1.3.2.4	Free-stream turbulence . . . . .	20
1.3.2.5	Reynolds number . . . . .	21
1.3.2.6	Blockage effect . . . . .	22
1.3.3	Unsteady flow . . . . .	22
1.3.3.1	Turbulent kinetic energy . . . . .	22
1.3.3.2	Spectral analysis . . . . .	22
1.3.3.3	Coherent structures . . . . .	23
1.4	3D double backward facing step at zero degree sideslip . . . . .	24
1.4.1	Definition of the Geometry . . . . .	24
1.4.2	Configuration SFS1 . . . . .	25
1.4.2.1	Mean flow description . . . . .	25
1.4.2.2	Some characteristics of the unsteady flow . . . . .	26
1.4.3	SFS2 geometry . . . . .	26
1.4.3.1	Mean flow description . . . . .	26
1.4.3.2	Reynolds effect . . . . .	27
1.4.3.3	Some features of the unsteady flow . . . . .	27
1.4.3.4	Frequencies involved . . . . .	27
1.4.3.5	Coherent structures detected . . . . .	28
1.4.4	Configuration SFSC . . . . .	28
1.4.5	Configuration SFST . . . . .	28
1.4.5.1	Mean flow description . . . . .	28
1.4.5.2	Flow statistics . . . . .	29
1.4.5.3	Coherent structures and frequencies involved . . . . .	29
1.5	Summary . . . . .	30
<b>2</b>	<b>Experimental and numerical setups</b> . . . . .	<b>31</b>
2.1	Defining a common coordinate system . . . . .	31
2.2	Campaign at the TEMPO wind-tunnel . . . . .	32
2.2.1	The model . . . . .	32
2.2.1.1	Controlling the model drift angle . . . . .	33
2.2.2	The wind-tunnel . . . . .	33
2.2.2.1	Determining the reference velocity $U_0$ . . . . .	34
2.2.3	Oil flow visualizations . . . . .	35

2.2.4	Laser tomoscopy . . . . .	36
2.2.4.1	Data acquisition . . . . .	36
2.2.4.2	Data post-processing . . . . .	36
2.2.4.3	Test program . . . . .	37
2.2.5	Hot-wire measurements . . . . .	37
2.2.5.1	Instrumentation and data acquisition . . . . .	37
2.2.5.2	Data processing . . . . .	40
2.2.6	PIV measurements . . . . .	40
2.2.6.1	Data acquisition . . . . .	40
2.2.6.2	Data processing . . . . .	43
2.2.6.3	Data post-processing . . . . .	43
	Ensemble averaging and field reconstruction . . . . .	44
	Turbulence integral length scale computation . . . . .	44
	Coherent structure detection . . . . .	44
2.3	Campaign at the L2 wind-tunnel . . . . .	44
2.3.1	Geometries tested . . . . .	44
2.3.2	Wind-tunnel . . . . .	45
2.3.2.1	Overview . . . . .	45
2.3.3	Laser tomoscopy visualizations . . . . .	46
2.3.3.1	Data acquisition . . . . .	46
2.3.3.2	Data processing . . . . .	48
2.3.4	Pressure measurements . . . . .	48
2.3.4.1	Data acquisition . . . . .	48
2.3.4.2	Data pre-processing . . . . .	49
2.3.5	Atmospheric boundary layer probing . . . . .	50
2.4	Campaign at the mini wind-tunnel . . . . .	51
2.4.1	Model . . . . .	51
2.4.2	Wind-tunnel . . . . .	51
2.4.3	Laser tomoscopy visualizations . . . . .	52
2.4.3.1	Data acquisition . . . . .	52
2.4.3.2	Data processing . . . . .	53
2.5	Numerical approach . . . . .	53
2.5.1	Geometry and mesh . . . . .	53
2.5.2	Computation parameter . . . . .	53
2.5.3	Computation convergence . . . . .	55
<b>3</b>	<b>Flow description downstream of a 3D double backward facing step at zero degree sideslip</b> . . . . .	<b>57</b>
3.1	Geometry design . . . . .	57
3.1.0.1	Aims . . . . .	57
3.1.0.2	Approach . . . . .	58
3.1.0.3	Experimental validation . . . . .	59
	Oil flow visualizations . . . . .	59
	Quantitative characterization of the upstream boundary layer . . . . .	60
3.2	Time-averaged flow . . . . .	60
3.2.1	Oil flow visualizations . . . . .	61

3.2.2	PIV measurements . . . . .	62
3.2.2.1	Plane of symmetry of the model $y = 0$ . . . . .	62
3.2.2.2	Constant $z$ planes . . . . .	64
3.3	Some features of the unsteady flow . . . . .	67
3.3.1	Time independent analysis . . . . .	67
3.3.1.1	Plane $y = 0$ . . . . .	67
	Statistic moments . . . . .	67
	POD analysis . . . . .	70
	Distance to Gaussian turbulence . . . . .	71
3.3.1.2	Plane $z/h = 0.5$ . . . . .	75
	Statistic moments . . . . .	75
	POD analysis . . . . .	77
	Distance to Gaussian turbulence . . . . .	78
3.3.2	Frequencies involved . . . . .	79
3.3.3	Interpreting the unsteady phenomena . . . . .	81
3.3.3.1	Comparing with laser tomoscopy results . . . . .	81
	Plane $x/h = 1.6$ . . . . .	82
	Vortex Shedding in the plane $y = 0$ . . . . .	82
	Plane $z/h = 0.47$ : vortex Shedding . . . . .	85
3.3.4	Coherent structures in the flow . . . . .	86
3.3.4.1	Spatial cross-correlations . . . . .	86
3.3.4.2	Turbulence spatial integral length scale . . . . .	87
3.3.4.3	Statistic study of the coherent structures . . . . .	88
	Detection criteria . . . . .	88
	Using spatially filtered snapshots . . . . .	90
	Trajectory of the vortices . . . . .	90
	Advection velocity . . . . .	93
3.3.4.4	Reynolds effect . . . . .	94
3.4	Summary . . . . .	95
<b>4</b>	<b>Analyzing the mean flow asymmetry downstream of 3D double backward facing steps around the zero degree sideslip angle</b> . . . . .	<b>97</b>
4.1	Mean flow sensitivity to variations of the drift angle . . . . .	98
4.1.0.5	Oil flow visualization . . . . .	98
4.1.0.6	PIV . . . . .	99
4.2	Influence of the upstream conditions on the mean flow asymmetry . . . . .	101
4.2.1	Approach . . . . .	101
4.2.2	Experimental results . . . . .	103
4.2.2.1	Verifying the test cases . . . . .	103
	Probing the boundary layers on the model walls . . . . .	103
	Determining $\Delta U$ . . . . .	104
4.2.2.2	Laser tomoscopy visualizations . . . . .	105
4.2.2.3	Pressure coefficient measurements . . . . .	107
4.2.3	Numerical approach . . . . .	110
	Results . . . . .	110
4.2.3.1	Reynolds effect . . . . .	115
4.3	The asymmetry is the consequence of a bi-stable flow . . . . .	116

4.3.1	Discrimination of the snapshots into 2 categories . . . . .	116
4.3.2	Occurrence of the two solutions in an intermittent manner . . . . .	119
4.3.3	Some clues towards an explanation of the bi-stability . . . . .	119
4.3.3.1	The effect of the second step on the bi-stability . . . . .	120
4.3.3.2	The effect of the streamwise vortices on the bi-stability . . . . .	120
4.4	Summary . . . . .	121
<b>5</b>	<b>Some issues of the flow bi-stability on the launch and recovery of helicopters on ships. Recommendations for future work</b>	<b>125</b>
5.1	The impact of the bi-stability on the flight of helicopters. Comparison with the impact of the other flow features . . . . .	125
5.1.1	Impact of the mean flow . . . . .	126
5.1.2	Impact of the unsteady flow . . . . .	127
5.1.3	Application to the impact of the bi-stability . . . . .	128
5.2	Simulating frigate airwakes in case of bi-stability . . . . .	130
5.2.1	Accurately interpreting the experimental validation database : the issue of data averaging in case of bi-stable flows . . . . .	130
5.2.2	Using the bi-stability property for data reduction . . . . .	132
5.2.3	Bi-stability and the limits of the one-way coupling approach . . . . .	134
5.3	Bi-stability and flow control . . . . .	136
5.4	Summary . . . . .	137
	<b>Conclusion</b>	<b>139</b>
<b>A</b>	<b>Basic theoretical background</b>	<b>143</b>
A.1	Simplified Navier-Stokes equations (NSE) . . . . .	143
A.2	Normalized NSE and similarity laws . . . . .	144
A.3	RANS equations and budget equations . . . . .	145
<b>B</b>	<b>Sampling parameters of a stationary ergodic random process</b>	<b>147</b>
B.1	Theory of uncertainty estimates . . . . .	147
B.2	Unbiased estimates of the statistic moments for the normal law . . . . .	150
B.3	Choosing the acquisition parameters . . . . .	150
B.4	Application to the experimental database . . . . .	151
B.4.1	TEMPO free-stream velocity and turbulence . . . . .	151
B.4.2	PIV measurements . . . . .	152
B.4.3	Hot-wire anemometry data . . . . .	153
B.4.3.1	Boundary layer probing at the L2 wind tunnel . . . . .	153
B.4.3.2	Boundary layer probing on the SFSSO' . . . . .	154
B.4.3.3	Spectrum . . . . .	154
B.4.4	Pressure measurements . . . . .	154
B.5	Remarks on uncertainty determination . . . . .	154
<b>C</b>	<b>POD</b>	<b>155</b>
	Mathematical definition of the problem . . . . .	155
	POD theorem . . . . .	156
	Determining the POD modes . . . . .	157



---

Decomposition and approximation . . . . .	157
<b>Bibliography</b>	<b>159</b>
<b>Abstract</b>	<b>176</b>

# List of Figures

1.1	Flow topology downstream of a 2D backward facing step flow . . . . .	6
1.2	Apparition of several secondary vortices for low aspect ratio steps . . . .	7
1.3	Dependence of the reattachment length with the upstream boundary layer state . . . . .	8
1.4	Dependence of the reattachment length on the upstream boundary layer thickness . . . . .	9
1.5	Dependence of the reattachment length on the expansion ratio . . . . .	9
1.6	Some vortex detection using the Q criterion . . . . .	12
1.7	Vortex shedding characteristics downstream of a cylinder . . . . .	13
1.8	Streamlines of the time-averaged flow around rectangular cylinders with different aspect ratios . . . . .	14
1.9	Flow topology around a wall-mounted cube . . . . .	18
1.10	Interpreting the 3D shape of a vortex through 2D measurements . . . . .	19
1.11	Von Karman street materialized by clouds downstream of Alexander Selkirk island in the southern Pacific ocean . . . . .	22
1.12	The effect of building geometry on vortex-shedding frequency in turbulent flow . . . . .	23
1.13	Several Simplified Frigate Shapes found in the literature . . . . .	25
1.14	Surface streaklines of the 1 <sup>st</sup> step of the SFS1: (a) experimental, (b) computation . . . . .	26
1.15	Mean and RMS streamwise velocities across the backward cuboid of the SFS2, in the vertical plane located at 1.1h downstream of the first step and at step height . . . . .	27
1.16	Perspective view of the flow downstream of the SFST . . . . .	29
1.17	Some features of the flow in x planes of the SFST . . . . .	30
2.1	Coordinate system and definition of the geometric drift angle . . . . .	32
2.2	SFSO': alone and on its table . . . . .	33
2.3	The TEMPO wind tunnel of Valenciennes . . . . .	34
2.4	Positioning of the hot wire probes for mean advection velocity measurements . . . . .	38
2.5	Positions of the hot-wire probes for spectra measurements and advection velocity determination . . . . .	39
2.6	PIV camera positioning in plane $y' = 0$ . . . . .	42
2.7	PIV camera positioning in the z planes . . . . .	43
2.8	The two positions of the perturbators on the SFSs . . . . .	45
2.9	Definition of the short SFS1' . . . . .	45
2.10	The L2 wind tunnel . . . . .	46

2.11	Smoke injection for the laser tomography visualizations . . . . .	47
2.12	Position of the camera for laser tomography visualizations . . . . .	47
2.13	Position of the pressure taps . . . . .	49
2.14	The L2 wind tunnel simulated atmospheric boundary layer . . . . .	50
2.15	The mini wind tunnel . . . . .	51
2.16	Probing the mini wind tunnel . . . . .	52
2.17	The computing domain and the structured mesh . . . . .	54
2.18	Evolution of the residuals against the number of iterations performed . .	55
3.1	Oil visualizations over the central cuboid of the SFSO' . . . . .	59
3.2	Flow visualization in the plane $x/h = -0.13$ . . . . .	60
3.3	Surface oil flow visualization on the top surface of the backward cuboid	62
3.4	Streamlines and streamwise and spanwise velocity contour levels in the high resolution $y' = 0$ plane at $Re_h = 8 \times 10^4$ . . . . .	63
3.5	Determining the reattachment length behind the first step $Re_h = 8 \times 10^4$	64
3.6	Streamlines and velocity contour levels in the plane $z/h = 0.784$ , $Re_h =$ $9.75 \times 10^4$ . . . . .	65
3.7	Streamlines and velocity contour levels in the plane $z/h = 0.5$ , $Re_h =$ $9.75 \times 10^4$ . . . . .	66
3.8	Estimated Position of the z planes relative to the estimated arch vortex shape . . . . .	66
3.9	3D view of the arch vortex . . . . .	67
3.10	Turbulence intensity and turbulence production in the plane $Y = 0$ , $Re_h = 9.75 \times 10^4$ . . . . .	68
3.11	Forward and upward flow intermittency factors in the plane $y = 0$ at $Re_h = 8 \times 10^4$ . . . . .	69
3.12	Evolution of the mean streamwise velocity and the forward flow inter- mittency factor . . . . .	70
3.13	POD energy of the modes and sum of the mode energy . . . . .	70
3.14	Streamlines and longitudinal velocity contour levels of the first 4 POD modes in the plane $y = 0$ at $Re_h = 9.75 \times 10^4$ . . . . .	71
3.15	Estimated values of Skewness and kurtosis in the plane $y = 0$ at $Re_h =$ $9.75 \times 10^4$ . . . . .	72
3.16	Illustration of the positions where the skewness, kurtosis and PDF are extracted in the plane $y = 0$ . . . . .	73
3.17	Estimated probability density functions compared to the normal distri- bution at different locations in the plane $y = 0$ at $Re_h = 9.75 \times 10^4$ . . . .	74
3.18	Turbulence intensities and turbulence production in the plane $z/h = 0.5$ , $Re_h = 9.75 \times 10^4$ . . . . .	76
3.19	Mean (solid) and RMS (dashed) streamwise velocities along the line $(x/h, z/h) =$ $(1.12, 0.814)$ . . . . .	76
3.20	Forward and sideways flow intermittency factors in the plane $z/h = 0.5$ at $Re_h = 9.75 \times 10^4$ . . . . .	77
3.21	Streamlines and longitudinal velocity contour levels of the first 4 POD modes in the plane $z/h = 0.5$ at $Re_h = 9.75 \times 10^4$ . . . . .	77
3.22	Estimated values of Skewness and kurtosis in the plane $z = 0.5$ at $Re_h =$ $9.75 \times 10^4$ . . . . .	78

3.23	Illustration of the positions where the skewness, kurtosis and PDF are extracted in the plane $z/h = 0.5$ . . . . .	79
3.24	Estimated probability density functions compared to the normal distribution at different locations in the plane $z/h = 0.5$ at $Re_h = 9.75 \times 10^4$ . . . . .	80
3.25	Illustration of the positions where the spectra were computed, in the vicinity of the plane $z/h = 0.5$ . . . . .	81
3.26	Normalized spectra at positions 2 : $(x/h, y/h, z/h) = (2.37, -0.61, 0.53)$ and 1 : $(x/h, y/h, z/h) = (2.34, 0.58, 0.45)$ for $Re_h = 1.675 \times 10^5$ . . . . .	81
3.27	Time evolution of streamwise vortices in the plane $x/h = 1.6$ at $Re_h = 9.75 \times 10^4$ . . . . .	83
3.28	Time evolution of shear layer smoke puffs in the plane $y/h = 0$ at $Re_h = 9.75 \times 10^4$ . . . . .	84
3.29	Time evolution of shear layer smoke puffs in the plane $z/h = 0.47$ at $Re_h = 9.75 \times 10^4$ . . . . .	85
3.30	Time evolution of shear layer smoke puffs in the plane $z/h = 0.47$ at $Re_h = 1.65 \times 10^5$ . . . . .	86
3.31	Spatial turbulence integral length scales in the plane $y = 0.5$ at $Re_h = 9.75 \times 10^4$ . . . . .	88
3.32	Spatial turbulence integral length scales in the plane $z/h = 0.5$ at $Re_h = 9.75 \times 10^4$ . . . . .	88
3.33	Streamwise autocorrelation coefficient along the x and the z axis in the plane $y = 0.5$ at $Re_h = 9.75 \times 10^4$ . . . . .	89
3.34	Coherent structures detection in the planes $y = 0$ and $z/h = 0.5$ at $Re_h = 9.75 \times 10^4$ using the $\Gamma_1$ criterion . . . . .	91
3.35	. . . . .	92
3.36	. . . . .	93
3.37	Mean advection velocity of the coherent structures in different positions behind the first step at Reynolds number $Re_h = 9.75 \times 10^4$ and $Re_h = 1.65 \times 10^5$ and illustration of the positions probed . . . . .	94
4.1	Surface oil flow visualization on the top surface of the backward cuboid at $\beta_g = 0.21^\circ$ . . . . .	98
4.2	PIV on the SFSO' in the $z/h = 0.5$ plane: evolution against the drift angle of streamlines and iso-contour of $U/U_0$ without and with the hysteresis test. $Re_h = 9.75 \times 10^4$ . . . . .	100
4.3	SFSC': flow is detached on the upper wall and attached on the lateral walls	104
4.4	Attached flow on the upper and sidewalls of the SFSO' . . . . .	104
4.5	Effect on the upper boundary layer of the cylinder placed upstream of the first step at (a) $x/D = -10$ and (b) $x/D = -2$ . . . . .	104
4.6	$\Delta Cp = Cp_{y>0} - Cp_{y<0}$ against $\beta_a$ at position $(x/h, z/h) = (-5.88, 0.5)$ at $Re_h = 1.8 \times 10^5$ for the SFSO', SFSC' and SFS1' . . . . .	106
4.7	Representative snapshot of the flow in the $z/h = 0.5$ plane when the mean flow asymmetry is observed . . . . .	107
4.8	Maps of pressure coefficients over the top surface of the SFSO' backward cuboid at several drift angles . . . . .	108
4.9	Maps of pressure coefficients over the top surface of the SFSC' backward cuboid at several drift angles . . . . .	109
4.10	Maps of pressure coefficients over the top surface of the SFS1' backward cuboid at several drift angles . . . . .	109

4.11	Observing the mean flow asymmetry using CFD at $Re_h = 4.9 \times 10^5$ . . .	111
4.12	Observing the mean flow asymmetry using CFD. 3D streamlines and friction velocity contours at the surface . . . . .	112
4.13	Comparison of the $\Delta C_p = C_{p_{y>0}} - C_{p_{y<0}}$ obtained through CFD and experiments on the SFSC' and SFSO' at positive drift angle . . . . .	113
4.14	Visualization of the $y < 0$ streamwise vortex through 3D streamlines. In color: normalized friction velocity contours levels . . . . .	114
4.15	$C_p$ coefficients in the $z/h = 0.02$ plane . . . . .	115
4.16	A representative snapshot from laser tomography in the $z/h = 0.5$ plane of the SFSC' at $Re_h = 5.9 \times 10^3$ . . . . .	116
4.17	Velocity streamlines and contour levels on a representative PIV snapshot	117
4.18	The 2 control contours $C_1$ and $C_2$ for the computation of the circulation .	117
4.19	An average field $A$ decomposed as the weighted sum of solutions $A_1$ and $A_2$ . Here, $\alpha = 33\%$ and $\beta_a = 0.04^\circ$ . . . . .	118
4.20	Proportion of type I snapshots against $\beta_a$ for the PIV measurements on the SFSO' at $Re_h = 9.75 \times 10^4$ and the tomography snapshots on the SFSC' at $Re_h = 5.9 \times 10^3$ . . . . .	118
4.21	Inclined splitter plate behind the second step of the SFSC' at $Re_h = 5.9 \times 10^3$	121
4.22	Some control devices put on the SFSC' to test the influence of the streamwise vortices on the bi-stability at $Re_h = 5.9 \times 10^3$ . . . . .	122
4.23	Control device on the lateral wall, upstream of the first step of the SFSC' at $Re_h = 5.9 \times 10^3$ . . . . .	122
5.1	FREMM: the next generation frigate of the French Navy with its helicopter	128
5.2	Change in mean velocity in the plane $z/h = 0.5$ at $Re_h = 9.75 \times 10^4$ resulting from the flow flip-flopping . . . . .	129
5.3	2D streamlines and contour levels of the normalized streamwise velocity in the plane $z/h = 0.5$ at $\beta_g = 8.7^\circ$ . . . . .	133
5.4	A proposition of active flow control device for ship airwake . . . . .	136

# List of Tables

2.1	Oil visualization test program . . . . .	36
2.2	Laser tomography visualization test program . . . . .	37
2.3	Hot-wire test program . . . . .	40
2.4	PIV test program . . . . .	41
2.5	Upstream conditions imposed at the entry of the computational domain	54
3.1	Some features at the surface of the flow behind the first step . . . . .	61
3.2	Characteristics of the recirculation bubbles behind both steps . . . . .	64
3.3	Characteristics of the vortices in the plane $z/h = 0.5$ . . . . .	66
3.4	Skewness and kurtosis at some locations in the plane $y = 0$ at $Re_h = 9.75 \times 10^4$ . . . . .	72
3.5	Skewness and kurtosis at some locations in the plane $y = 0$ at $Re_h = 9.75 \times 10^4$ . . . . .	78
4.1	Configuration tested . . . . .	102
4.2	Configurations of apparition of the mean flow asymmetry . . . . .	107
B.1	A Gaussian probability density distribution . . . . .	149
B.2	Expression of the error estimates for various quantities . . . . .	149
B.3	Uncertainty in the estimate of the true mean and mean square values in the TEMPO wind tunnel. Empty test-section . . . . .	152
B.4	Uncertainty in the estimate of the mean value for the PIV measurements	152
B.5	Uncertainty in the estimate of higher order moments for the PIV measurements at $Re_h = 9.75 \times 10^4$ . . . . .	153
B.6	Uncertainty in the estimate of the true mean and mean square values in the L2 wind tunnel. Empty test-section . . . . .	153



# Abbreviations

<b>2D,3D</b>	Two, three Dimensional
<b>CFD</b>	Computational Fluid Dynamics
<b>CIFER ®</b>	Comprehensive Identification from FrEquency Response
<b>DNS</b>	Direct Numerical Simulation
<b>FREMM</b>	FRégate Multi-Missions
<b>LES</b>	Large Eddy Simulation
<b>LSE</b>	Linear Stochastic Estimation
<b>NSE</b>	Navier-Stokes Equations
<b>NLR</b>	Nationaal Lucht- en Ruimtevaartlaboratorium
<b>PDF</b>	Probability Density Function
<b>PIV</b>	Particle Image Velocimetry
<b>POD</b>	Proper Orthogonal Decomposition
<b>RANS</b>	Reynolds Averaged Navier-Stokes equations
<b>SHOL</b>	Ship Helicopter Operating Limits
<b>SFS</b>	Simple Frigate Shape
<b>TEMPO</b>	Thermique Ecoulement Mécanique Matériaux Mise en forme PrOduction
<b>TTCP</b>	The Technical Cooperation Program
<b>UAV</b>	Unmanned Air Vehicle





# Symbols

$A_1$	Stable solution of the flow for $\beta_a > 0$	
$A_2$	Stable solution of the flow for $\beta_a < 0$	
$B$	SFS width	m
$b$	Parallelepiped width	m
$C_p = \frac{p}{1/2\rho U_0^2}$	Pressure coefficient	
$d$	Parallelepiped length	m
$d_1$	Distance to the wall of the first cell mesh	[-]
$D_1$	Diameter of vortex $D_1$	m
$d_1^+ = \frac{d_1 u_\tau}{\nu}$	Normalized distance to the wall of the first cell mesh	[-]
$E_1$	Energy of the fluctuating x velocity	J
$f$	Frequency	Hz
$f_s$	Sampling frequency of a time signal	Hz
$h$	First step height	m
$h_2$	Second step height	m
$L$	Length of the SFSs backward cuboid	m
$L_u^x$	Turbulence integral length scale of longitudinal velocity in streamwise direction	m
$L_u^y$	Turbulence integral length scale of longitudinal velocity in spanwise direction	m
$L_u^z$	Turbulence integral length scale of longitudinal velocity in vertical direction	m
$N_s$	Number of samples of a time signal	[-]
$p_i$	Pressure measured on the tap i	Pa
$p_{ref}$	Reference static pressure	Pa
$p(x)$	Probability density function	[-]

$Re_h = \frac{U_0 h}{\nu}$	Reynolds number based on the step height	[-]
$Re_\theta = \frac{U_0 \theta}{\nu}$	Reynolds number based on momentum thickness	[-]
$S_{ij}$	Deformation tensor	$s^{-1}$
$St_h = \frac{f h}{U_0}$	Strouhal number based on the step height	[-]
$t$	Time	s
$T$	Sampling period	s
$T_I$	Turbulence integral time scale	s
$t^+ = \frac{t U_0}{h}$	Normalized time variable	[-]
$U$	Mean longitudinal velocity (along the x axis)	m/s
$u$	Fluctuating longitudinal velocity (along the x axis)	m/s
$U^+ = \frac{U}{u_\tau}$	Normalized streamwise velocity	[-]
$U_0, U_{REF}$	Longitudinal upstream velocity	m/s
$V$	Mean velocity along the y axis	m/s
$v$	fluctuating velocity along the y axis	m/s
$V_1$	Right leg of the arch vortex	[-]
$V_2$	Left leg of the arch vortex	[-]
$W$	Mean velocity along the z axis	m/s
$w$	fluctuating velocity along the z axis	m/s
$x_{wt}$	Wind tunnel axis	[-]
$x_{model}$	Model axis	[-]
$X_R$	Reattachment length	m
$y^+ = \frac{y u_\tau}{\nu}$	Normalized wall distance in a boundary layer	[-]
$\beta_a$	Aerodynamic drift angle	deg
$\beta_g$	Geometric drift angle	deg
$\beta_x = \frac{\langle u^4 \rangle}{\sigma_x^4}$	Kurtosis (flatness factor) of the u velocity component	[-]
$\beta_y = \frac{\langle v^4 \rangle}{\sigma_y^4}$	Kurtosis (flatness factor) of the v velocity component	[-]
$\beta_z = \frac{\langle w^4 \rangle}{\sigma_z^4}$	Kurtosis (flatness factor) of the w velocity component	[-]
$\gamma_x = \frac{\langle u^3 \rangle}{\sigma_x^3}$	Skewness factor for velocity u	[-]
$\gamma_y = \frac{\langle v^3 \rangle}{\sigma_y^3}$	Skewness factor for velocity v	[-]
$\gamma_z = \frac{\langle w^3 \rangle}{\sigma_z^3}$	Skewness factor for velocity w	[-]
$\delta$	Boundary layer thickness	m
$\kappa$	Von Karman constant	0.41 [-]

---

$\theta_0, \delta_2$	Momentum thickness	m
$\Pi_x$	Forward flow probability, ie fraction of samples with $U>0$	[-]
$\Pi_y$	Fraction of samples with $V>0$	[-]
$\Pi_z$	Fraction of samples with $W>0$	[-]
$\rho$	Air density	$kg/m^3$
$\sigma_x$	Standard deviation along the x axis	m/s
$\sigma_y$	Standard deviation along the y axis	m/s
$\sigma_z$	Standard deviation along the z axis	m/s
$\langle . \rangle$	Ensemble average	



*To my loved ones*



# Introduction

Shipboard operations are among the most challenging tasks for rotary wing aircrafts. Indeed, helicopters face a hostile environment with strong unsteady winds and ship motions. This already affects the helicopter when it is manipulated on the platform: high amplitudes of roll and pitch can make the aircraft tip over [46, 61, 62]. Another danger during flight deck manipulations concerns the rotor engagement and disengagement phase. This is because during that stage, high levels of turbulence can induce an aeroelastic excitation of the rotor blades leading to resonance. This phenomenon, better known as blade sailing [23, 87, 93, 162, 191], can have dramatic consequences on the staff operating on the platform and also on the equipment. The influence of ship motion and ship airwake is also clear when the helicopter is in flight: the pilot strives to recover on (or launch from) a strongly moving target, which, furthermore, is relatively small. Risks of collision with the surrounding obstacles (hangar, masts, etc.) are thus high. This contributes to the pilot workload, increased by recurrent poor visibility conditions due to rain, sprays, night flights, etc. Risks of collision are also increased due to strong down- and side winds associated to high levels of turbulence. This consequently tires both the pilots and their gears but most of all can dangerously modify the helicopter flight path. The ship airwake will also be considered unfriendly when it blows the ship exhaust gases over the helicopter flight path possibly leading to engine failure and most probably accidents. Eventually, among all the causes that make shipboard operations so difficult, ship motion and ship airwake are certainly the two most important ones. Then, the problem consists in finding some ways of making such operations safer. This is why operational flight envelopes are defined for every couple of helicopter/ship. Those Helicopter Ship Operating Limits (SHOL) are determined during sea trials and draw envelopes of acceptable relative wind velocities and directions as well as the allowed ship roll and pitch angles. Those values are not the same if the helicopter operates at night or during daylight. Defining such SHOL's seems to be effective while looking at the statistics: helicopter accidents in maritime operations do not particularly occur during launch and recovery [27, 69, 168, 172]. However, as a drawback, the operational conditions are limited. This can reach the extreme case



where a helicopter can be grounded 90% of the time, as stated in Healey [74]: *a helicopter can operate from a 125 m. (400 ft.) frigate in the North Sea a mere ten percent of the time in winter*. Eventually, if the aim towards safer launch and recovery does not necessarily consist in extending the SHOLs, the issue is to find some ways of decreasing pilot workload. There are three main approaches to do so: stabilizing the helicopter [161], limiting the ship motions, or decreasing turbulence levels and side- and down winds over the flight deck. The present work focuses on the last approach. However, before improving the airflow, it is necessary to understand it in order to know what features can be changed. This airflow characterization will also be useful for a future high fidelity simulator implementation and/or validation as this could be required for SHOL pre-determination and pilot training.

In this respect, experimental and numerical studies have been performed. However, considering the complexity of the ship airwake on real ships [12, 85, 142], efforts were made to simplify the geometry, removing the small devices such as masts and only keeping the massive superstructures. This led to the definition of the Simple Frigate Shape (SFS1) within The Technical Cooperation Program [38]: the SFS1 is a basic 3D double backward facing step with a parallelepiped upstream on the first step, representing a funnel. The experimental work performed by Cheney and Zan [38] on this geometry is a reference in the understanding of the time-averaged flow close to the walls. It has enabled to roughly understand the mean flow features for several drift angles. At zero degree sideslip, the authors commented that, as expected, the mean flow is symmetric at the wall, over the platform. However, they did not present a model for the 3D topology of the flow. The latter is given by others who used this database to validate their RANS computations on the SFS1 [9, 112, 141, 182] and on a modified SFS1 [171]. Their conclusion was comparable to the wall visualizations of [38], namely that the mean flow is symmetric at zero degree sideslip. It is through a computation using the Lattice-Boltzmann method that Syms [170] observed a mean flow asymmetry at this drift angle. However, he did not study the flow around this angle nor did he bring any explanation on this unexpected result. An asymmetry also seems to appear on a modified SFS1, although not explicitly mentioned by its authors [175]. A description of some features of the unsteady flow is given in this work. However, the study was conducted at a much lower Reynolds number than the others.

Despite the simplification of the ship geometry, questions concerning the mean flow remain unanswered. In particular, at zero degree sideslip, a mean flow asymmetry is observed under some conditions by some studies. However, none of them explained the appearance of this phenomenon. The zero degree drift angle seems to be critical. However, it is a reference test case in the ship airwake community since, when looking

at the SHOLs, on a fore-aft procedure [32], the highest levels of turbulence can be encountered at and around this angle, and therefore leading to high pilot workload. Also, few studies focus on the unsteady flow.

Hence the present study. This work consists in characterizing the mean and unsteady airwake of generic frigates. One particular aim is to observe and explore some conditions under which the mean flow asymmetry appears. The eventual aim is to have a good understanding of the flow over the flight deck (or more precisely downstream of a 3D double backward facing step) that will be useful for flow control and ship airwake simulation towards safer shipboard operations of helicopters.

After a presentation of some characteristics of detached flows over academic bluff bodies (Chapter 1) and a review of the experimental and numerical methods employed in this work (Chapter 2), results are presented. The approach has first required designing a modified SFS so that a controlled and uniform flow could be obtained upstream of the first step. A special attention was paid to the shape of the nose. After an experimental validation of the geometry, the main mean and unsteady features of the flow downstream of the first step were studied (Chapter 3). Some parameters were then varied to study their influence on the apparition of the mean flow asymmetry at zero-degree sideslip (Chapter 4). The impact of the flow features on the issues related to the helicopter/ship dynamic interface is then discussed in the last chapter (Chapter 5). At the same time, orientations for future work are proposed.



# Chapter 1

## Literature overview

The flow downstream of 3D double backward facing steps is detached and complex. Therefore, to ease its understanding, simplifying the problem into sub problems could be helpful. For example, the geometry in the plane of symmetry of the body is similar to that of 2 successive 2D simple backward facing steps. On the planes normal to this one and slicing the mid-step heights, the geometry is similar to that of 2D rectangular cylinders. Therefore, this chapter overviews the property of those 2 basic geometries and gives a general description of detached flows. It is then followed by a synthesis of those two types of flows through the study of the aerodynamics of 3D parallelepiped. The main parameters that influence bluff body flows will also be discussed. Eventually, the bases set will give an overview of the flow around 3D double backward facing steps. The weaknesses of the studies found in the literature will be stressed to justify the present work.

### 1.1 2D simple backward facing step

The 2D backward facing step is probably the simplest existing geometry to study separated flows. It has therefore been extensively studied as shown by the review articles of Bradshaw and Wong [24], Durst and Tropea [54] and Eaton and Johnston [56]. This configuration has the advantage of fixing the separation line at the step edge while preserving the general phenomena related to detached-reattached flows. The interest expressed in this geometry is thus justified. Although the geometry is simple, the mean and unsteady flow features remain quite complex.

## 1.1.1 Flow topology

### 1.1.1.1 In the plane of symmetry

Figure 1.1 shows a typical flow topology downstream of a 2D backward facing step: as explained by Eaton and Johnston [56], the upstream boundary layer, characterized by a normalized thickness  $\delta/h$  and a free stream velocity  $U_{REF}$ , separates at the sharp step edge. A free-shear layer is then formed. Since its curvature is not very pronounced at first, it looks like an ordinary plane-mixing layer through the first half of the separated flow region, unaffected by the presence of the wall. However, the shear layer strongly differs from a plane-mixing layer on the second half of the separated region since its curvature becomes sharp towards the wall and the turbulence levels in the low-speed side are very high. It eventually impinges the wall at the reattachment zone, with part of the shear-layer fluid being deflected upstream, into the recirculation zone due to a strong adverse pressure gradient (the pressure is lower in the recirculation zone than around the reattachment area). The flow can then be decomposed in three main zones:

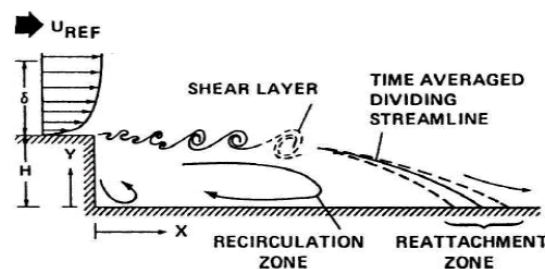


FIGURE 1.1: Flow topology downstream of a 2D backward facing step flow ([53])

the recirculation, reattachment and redeveloping regions. The first region where recirculation occurs, cannot be characterized as a dead air zone since the backflow velocities reach values up to 20% of the free stream velocity. It can first be described as a primary vortex, or bubble, (where the flow rotates on average in a clockwise manner on figure 1.1). It is bounded in the upstream direction by the step face, on top by the upper original shear layer and in the downstream direction by the reattachment zone. Under some conditions (see next paragraph 1.1.1.2), a secondary vortex (or bubble) can also be observed at the corner of the step, between the horizontal and the vertical walls [166]. The flow in the secondary bubble rotates opposite that in the primary bubble (that is in an anti-clockwise manner on figure 1.1). The reattachment region is highly unsteady as discussed in section 1.1.3.3. It separates the recirculation zone from the redeveloping one that is downstream. In this last region, a new sub-boundary layer develops at the wall. Over this boundary layer, a new shear layer spreads into the old shear layer with the characteristics of a free-shear layer. This property remains up to 50 step heights downstream of the reattachment [24].

### 1.1.1.2 Three-dimensional behavior

The early publication of Abbott and Kline [6] already reveals three dimensional behavior of the flow downstream of a backward facing step despite the two-dimensional geometry: within a region extending between the step face, the shear layer and about one step height, three secondary vortices can be seen in that study. Their axis is along the step height. This three-dimensional behavior can be explained as a direct consequence of the side walls whose influence is visible down to the heart of the flow. Such observations, de Brederode and Bradshaw [25] defined a critical value of the aspect ratio that ensures the bi-dimensionality of the flow (see paragraph 1.1.2.4). Papadopoulos and Ötügen [131] methodically studied this effect for aspect ratios varying from 1 to 28 with a Reynolds number  $Re_h = 2.62 \times 10^4$  and a turbulent upstream boundary layer. This study extends the results of Abbott and Kline [6] showing that the number of those secondary vortices depends on the aspect ratio. In what follows, considerations

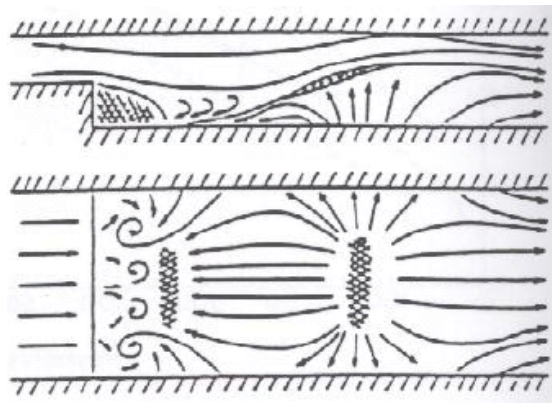


FIGURE 1.2: Apparition of several secondary vortices for low aspect ratio steps ([45])

are made in the plane of symmetry of high aspect ratio steps.

### 1.1.1.3 Comparison criteria

The mean reattachment length, noted  $X_R$ , is actually one of the most used parameter that characterizes detached flows. It is the point where a zero skin friction coefficient (or a zero longitudinal friction velocity at the wall) and/or a local maximum pressure coefficient is measured. It should be noted that the instantaneous reattachment length is highly unsteady due to high-scale structures passing by. Furthermore,  $X_R/h$  can be dramatically influenced by some parameters, varying from 4.9 to 8.2 as seen in the next section [56].

## 1.1.2 The effect of system parameters on reattachment

### 1.1.2.1 Initial boundary layer state

Studied by Eaton and Johnston [55], it is shown (see figure 1.3) that  $X_R/h$  strongly increases from 6.5 (when the initial boundary layer is laminar) to more than 8 (when it becomes transitional). However, when the initial boundary layer is fully turbulent,  $X_R$  seems to be quite independent of the Reynolds number.

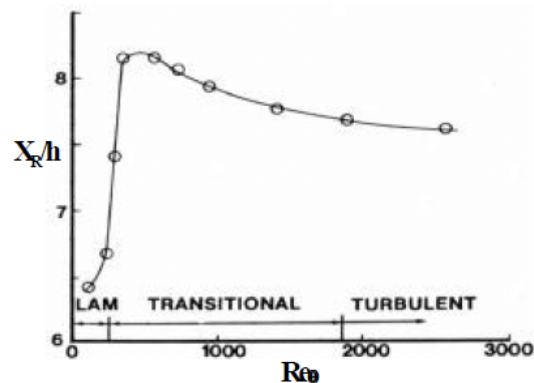


FIGURE 1.3: Dependence of the reattachment length with the upstream boundary layer state ([56])

### 1.1.2.2 Boundary layer thickness

Bradshaw and Wong [24] already used  $\delta/h$  (the ratio of the boundary layer thickness to the step height) to characterize the influence of the step on the downstream boundary layer. If  $\delta/h \gg 1$ , then the step does not significantly alter the velocity and length scales of the flow: the perturbation is said to be weak. Similarly,  $\delta/h = \mathcal{O}(1)$  is associated to a strong perturbation whereas  $\delta/h \ll 1$  corresponds to an overwhelming perturbation. In cases of overwhelming perturbations, experiments from Narayanan et al. [127] show a weak dependence of the reattachment length on the boundary layer thickness. However, as can be seen on figure 1.4, other authors have found a greater influence with the mean reattachment length decreasing with increasing boundary layer thickness. However, it must be noted that the turbulence level in those last experiments were higher than that in Narayanan et al. [127]. The influence of this last parameter will be discussed.

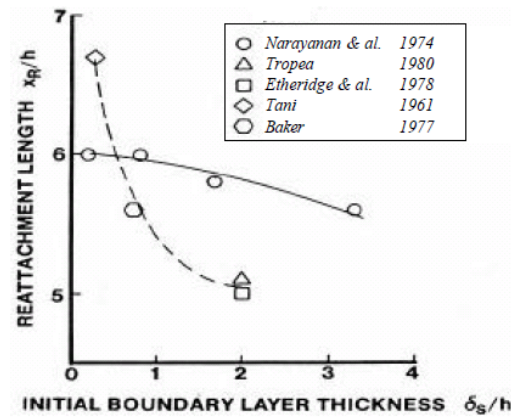


FIGURE 1.4: Dependence of the reattachment length on the upstream boundary layer thickness ([56])

### 1.1.2.3 Free stream turbulence

Even though this parameter has not been extensively studied, Eaton and Johnston [56] suggest that  $X_R$  is inversely proportional to free-stream turbulence. However, consideration should be given to the spectrum of the free stream turbulence since the influence of the low frequencies is unlikely to be the same as that of the higher frequencies.

### 1.1.2.4 Blockage coefficients

**Expansion ratio** The expansion ratio, defined as the ratio of the height of the test section downstream of the step to that upstream of the step, controls the streamwise pressure gradient. Eaton and Johnston [56] have summed up results of several authors to show that  $X_R$  increases with increasing expansion ratio (see figure 1.5)

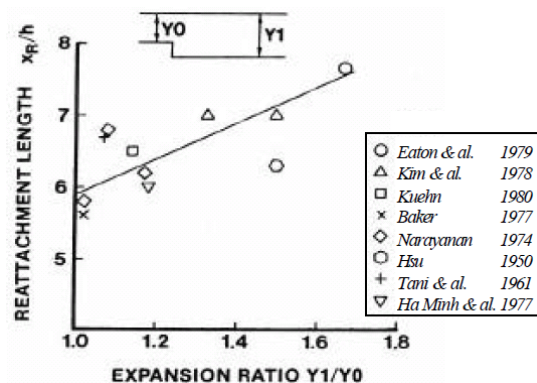


FIGURE 1.5: Dependence of the reattachment length on the expansion ratio ([56])



**Aspect ratio** The aspect ratio of the flow apparatus, defined as the ratio of the test section width to the step height has been shown by de Brederode and Bradshaw [25] to have negligible effects on  $X_R$  when the aspect ratio is greater than ten.

### 1.1.3 Unsteady flow

The Reynolds number based on the step height  $Re_h$  and the ratio  $\delta/h$  of the boundary layer thickness normalized by the step height appear to be the main governing parameters for turbulence characteristics [88]. Some of them are presented below.

#### 1.1.3.1 Reynolds stresses

**Turbulence intensity** In almost all cases reviewed by Eaton and Johnston [56], the maximum turbulence intensity appears to be one step height upstream of the reattachment. It then decays rapidly. The locations of the points where the maximum turbulence intensity occurs are relatively high upstream of the reattachment area. They get closer to the wall around  $X_R$  and increase again downstream of  $X_R$ . Values of the streamwise turbulence intensity up to 30% are measured near the center of the reattaching shear layer [56]. However, those values might be underestimated since the x-hot wires that have been used for those measures are not designed to evaluate such high turbulence levels [28]. This could also be a reason for the substantial differences that exist between the results presented by several authors. Another explanation could also lie in the existence of possible real differences in the flow. Indeed, turbulence intensities can be strongly affected by low-frequency motions, certainly present in some experiments but not necessarily in all of them. Despite those remarks, Eaton and Johnston [56] propose a typical peak value for the streamwise turbulence intensity of about 20%. Because of all the discrepancies among the works overviewed, this value should be taken with caution.

**Turbulence production** Despite discrepancies in the results of the different authors' works, the peak value of the normalized shear stress in the reattaching shear layer is given by Eaton and Johnston [56] to be  $\frac{\overline{u'v'}}{U_0^2} = 1.25 \times 10^{-3}$ . However, a rapid decay of Reynolds normal and shear stresses appear within the reattachment zone, which could be the result of one or several of the following effects: stabilizing shear layer curvature, adverse pressure gradient and strong interaction with the wall in the reattachment zone.

### 1.1.3.2 Spectral analysis

Abbott and Kline [6] show that the reattachment zone is highly unsteady. For the dominant frequency, Driver et al. [53] propose a Strouhal number of 0.2 based on the shear layer thickness and half the upstream velocity. This is a frequency characteristic of spanwise vortical structures as seen in free shear layers [70]. This Strouhal number does not contradict the value of 0.07 measured by Eaton and Johnston [57] when the step height and the upstream velocity are considered for normalization. The value is near 1 when the Strouhal number is normalized by the reattachment length. Eaton and Johnston [55] paid particular attention to the low frequency motion of the shear layer where the impingement point moves up- and downstream over a distance of about two step heights. This low frequency instability is associated with a flapping motion of the shear layer whose origin has had different explanations. Eaton and Johnston [56] assume that irregular local imbalances occur between reinjection of fluid near the reattachment region and shear layer entrainment by the recirculating region. Therefore the volume of the bubble varies, modifying the instantaneous reattachment length. This imbalance could result from short-term breakdown of the spanwise vortices in the shear layer. Driver et al. [53] do not suggest such vortex breakdown but rather occurrences of vortices with higher forward momentum than the others. When impacting the wall at reattachment, compared to the other vortices, less mass would be engulfed into the recirculation bubble, diminishing its volume. Also, since the curvature of the shear layer would increase, so would the adverse pressure gradient thus resulting in greater backflow later on. Spazzini et al. [166] worked on explaining the phenomenon using skin friction probes and time-resolved visualizations on a backward facing step flow at  $Re_h = 1.6 \times 10^4$ . Using various experimental techniques and processing tools, they suggested that the flapping motion may be linked to a growing in size and strength of the secondary bubble that, when it has reached the step height, breaks down. Eventually, the Strouhal number related to the flapping motion ranges in  $0.1 \leq St_{X_R} \leq 0.18$  depending on the authors and the location where the measurement was performed.

### 1.1.3.3 Coherent structures

Eaton and Johnston [56] suggest that very large turbulence structures with length scales equal to or larger than the step height pass through the reattachment region. Such high scale structures are also observed by Spazzini et al. [166]. Vortex pairing in the separated shear layer leads to fairly large scale eddies. This pairing is characterized by a decreasing Strouhal number along the shear layer [10]. Those eddies persist far downstream of the step.

Correlation measurements reveal that the large-scale eddies in the reattaching shear layer are significantly larger in the spanwise direction than in the other two directions [55]. However, their shape is complex and depends on the location. LES simulation have for example shown that spanwise vortices formed into  $\Lambda$  vortices [48].

The several reviews in the literature confirm that, despite a simple geometry, both the

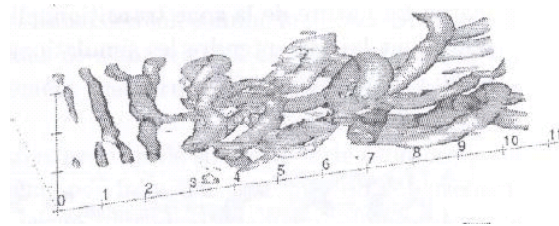


FIGURE 1.6: Some vortex detection using the Q criterion ([48])

mean and unsteady flow features downstream of a 2D backward facing step are not trivial. They are influenced by many parameters and therefore the '*one scheme fits all*' catchphrase cannot be directly applied to describe flows around steps. Nonetheless, some common characteristics can be found on all steps, despite operating differences. This kind of flow is not the least understood of all. Complexity is increased however when another shear layer is added. This is the case of cylinder flows.

## 1.2 2D cylinders at zero degree sideslip

On a 3D step, the step face has three edges, two of which face each other. In particular, separation occurs at both of those edges. This paragraph aims at isolating the interaction of two facing shear layers. The simplest geometries where this phenomenon is seen are probably the cylinders, which justifies this paragraph.

### 1.2.1 Flow topology and phenomenology

On sharp-edged cylinders ( $90^\circ$  angle), as for the backward facing step (see 1.1), separation occurs at the edges. Actually, for circular cylinder, as long as the Reynolds number is greater than 3-4 (non creeping flow), flow separation also occurs [156]. This leads to the formation of a recirculation bubble that, when time-averaged, has the shape of two counter rotating vortices as shown in figure 1.8. The difference between sharp-edged cylinders and circular cylinder lies in the separation point: since it is not fixed at the edge in the case of a circular cylinder, it can move. However, for most 2D bluff bodies placed normal to a stream of fluid, this separation will lead to vortex shedding. The big difference with the shedding observed in the shear layer of a 2D step is that the

shed vortices of the two shear layers interact. The interaction is such that the shedding occurs alternately from one side to the other resulting in staggered distribution of vortices in the cylinder wake. Kochin et al. [95] showed from a singularity approach that this was the least unstable configuration (called the von Karman street) compared to the symmetric distribution or the single vortex street that are fully unstable. Indeed, if the stability condition is satisfied, namely the ratio of the distance between the rows of the vortices to the distance between the vortices of a same row is worth 0.2806, this nonetheless preserves its value to a certain extent, since it characterizes the least unstable of all other vortex distributions. This value  $h/l = 0.2806$  was confirmed experimentally.

It is shown by Blevins [20] that the Strouhal number (based on a characteristic body dimension -usually the width- and the free stream velocity) depends on the cylinder shape and the Reynolds number, generally between 0.1 and 0.3. A typical wake behind such bluff bodies is illustrated in figure 1.7. Figure 1.7 also shows that the Strouhal

Reynolds number  $Re = V d / \nu$   
Strouhal number  $Sr = f d / V$

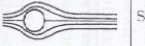




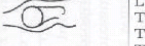

Reynolds number regime	Flow regime	Flow form	Flow characteristic	Strouhal number $Sr$	Drag coefficient $c_D$	Separation angle $\theta_S$
$Re \rightarrow 0$	Creeping flow		Steady, no wake	-	see Fig. 1.12	-
$3 - 4 < Re < 30 - 40$	Vortex pairs in wake		Steady, symmetric separation	-	$1.59 < c_D < 4.52$ ( $Re = 30$ ) ( $Re = 40$ )	$130^\circ < \theta_S < 180^\circ$ ( $Re = 35$ ) ( $Re = 5$ )
$30 < Re < 80$ $40 < Re < 90$	Onset of Karman vortex street		Laminar, unstable wake	-	$1.17 < c_D < 1.59$ ( $Re = 100$ ) ( $Re = 30$ )	$115^\circ < \theta_S < 130^\circ$ ( $Re = 90$ ) ( $Re = 35$ )
$80 < Re < 150$ $90 < Re < 300$	Pure Karman vortex street		Karman vortex street	$0.14 < Sr < 0.21$		
$150 < Re < 10^5$ $300 < Re < 1.3 \cdot 10^5$	Subcritical regime		Laminar, with vortex street instabilities	$Sr = 0.21$	$c_D \approx 1.2$	$\theta_S \approx 80^\circ$
$10^5 < Re < 3.5 \cdot 10^6$ $1.3 \cdot 10^5 < Re < 3.5 \cdot 10^6$	Critical regime		Laminar separation Turbulent reattachment Turbulent separation Turbulent wake	No preferred frequency	$0.2 < c_D < 1.2$	$80^\circ < \theta_S < 140^\circ$
$3.5 \cdot 10^6 < Re$	Supercritical regime (transcritical)		Turbulent separation	$0.25 < Sr < 0.30$	$c_D \approx 0.6$	$\theta_S \approx 115^\circ$

FIGURE 1.7: Vortex shedding characteristics downstream of a cylinder (Schlichting and Gersten [156])

number strongly varies with the Reynolds number, being even undefined in the critical range, where the shedding is aperiodic. Despite this, several authors have tried to define universal Strouhal numbers. Adachi [7] compared four of them on cylinders and concluded that in the Reynolds range of  $5 \times 10^4 < Re < 10^7$ , the best results were obtained by considering the Strouhal number based on the lateral vortex spacing and the upstream velocity, equal to 0.181.

If this Strouhal number seems to be reasonably universal, great variations can be observed when some parameters are changed.

## 1.2.2 Influence of some parameters

### 1.2.2.1 Aspect ratio

Contrary to the 2D step case (see 1.1.2.4), a third geometrical ratio can be defined as the length to the width of the cylinder. The influence of this aspect ratio on the flow downstream of rectangular cylinders has been studied by Yu and Kareem [196]. They used LES. The Reynolds number was kept constant at  $10^5$ . The aspect ratio was the only varying parameter, taking values from 1:1 to 1:4. For aspect ratios greater than 1:3, the mean flow reattaches to the lateral sides of the cylinder. As a consequence, the recirculation bubble behind the cylinder is smaller than that for cylinders with a smaller aspect ratio.  $X_R/b$  respectively reaches 1.5 and 0.5 (see figure 1.8, where  $b$  is the cylinder width). This affects the size of the eddies as well as on the non-universal Strouhal

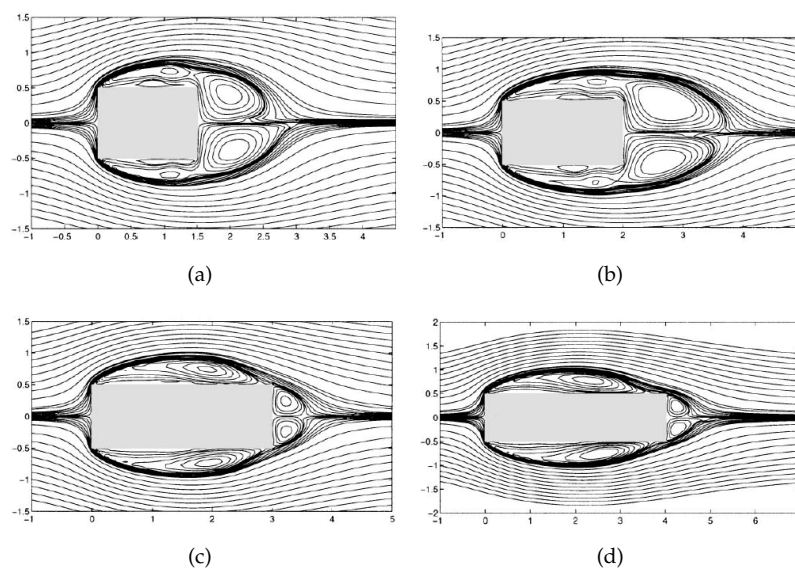


FIGURE 1.8: Streamlines of the time-averaged flow around rectangular cylinders with different aspect ratios: (a) 1:1.5; (b) 1:2; (c) 1:3; and (d) 1:4 (from Yu and Kareem [196])

number: the latter has a minimum value for the aspect ratio of 1:2 and a maximum value for the aspect ratio of 1:3. This corresponds with the experimental results of Okajima [128].

In all the cases of figure 1.8, as suggested by Yu and Kareem [196], the mean flow is symmetric.

### 1.2.2.2 Blockage effect

If the obstruction of the test section due to the presence of the cylinder is too high, the pressure distribution, the drag coefficient and the Strouhal numbers are affected. West

and Apelt [186] performed tests on circular cylinders of various aspect ratios and at Reynolds numbers ranging from  $10^4$  to  $10^6$ . They concluded that in these conditions, the blockage effect is negligible for values under 6%.

### 1.2.2.3 Free-stream turbulence intensity and turbulence length scales

As suggested by Buresti [29], for rounded bodies with free separation points, when the free-stream turbulence increases, it can trigger the transition of the boundary layer from laminar to turbulent. There is thus an equivalent effect between increasing the free-stream turbulence and increasing the Reynolds number. On the other hand, when the separation points are determined by the sharp edges of the geometry, an increase of turbulence can favor a steady or intermittent reattachment of the shear layers to the sides of the body, which, for rectangular cylinders, corresponds more to an increase in aspect ratio (see paragraph 1.2.2.1). This effect strongly depends on the shape of the cross-section. However, the turbulence length scale should be defined as suggested by Lee [103]. In Mair and Maull [114], it is precised that turbulence with length scales (the most important being that of the longitudinal velocity in streamwise direction  $L_u^x$ ) of the order of (or greater than) the diameter of the cylinder, affects vortex shedding. In the most extreme case, it can even suppress it. Smaller turbulence scales only act on the separation points. The effect of turbulence on flows around sharp edge cylinders has been studied by Vickery [181], Bearman and Morel [15], Nakamura and Ozono [124], Gartshore [68], Nakamura et al. [125], Namiranian and Gartshore [126], Lu and Laneville [113] and Nakamura [123].

Without giving a detailed analysis of those papers, we will only stress the observations of Wolochuk et al. [192] about the influence of turbulence on the Strouhal number: the increase of turbulence intensity from 2.5 to 10 % with turbulence integral length scales of 0.5 body diameter only increases the Strouhal number by 2.4%. The greatest effect occurs for length scales near 3 times the bluff body diameter, leading to a 26% increase in Strouhal number for the tests performed.

### 1.2.2.4 Reynolds number

The effects of the Reynolds number (especially on the Strouhal number) have already been mentioned (see 1.2.1). They will be dealt with in the general 3D case in section 1.3. However, it should be noted that a critical Reynolds number range exists both for circular and rectangular cylinders. Those ranges are respectively between  $10^5$  and  $3.5 \times 10^6$  [156] for the circular cylinder (see figure 1.7) and spread around Reynolds number 1220

for the rectangular cylinder [128]. For the rectangular case, two modes of the flow appear intermittently. For higher Reynolds number, Schewe [154] shows from tests in a pressurized wind tunnel on a square section cylinder that the mean force coefficients as well as the Strouhal number are Reynolds number independent for  $10^5 < Re < 4 \times 10^6$ . The influence of turbulence, Reynolds number and also Mach number on the flow around rectangular cylinders of various aspect ratios is discussed by Larose and D'Auteuil [101].

### 1.2.3 Unsteady flow

#### 1.2.3.1 Turbulence levels

Some turbulence profiles are given by Okajima [128] in the wake of rectangular cylinders of different width-to-height ratios (2 to 3) and for Reynolds number ranging from 70 to  $2 \times 10^4$ . The turbulence levels reach a maximum of about 20% at the highest Reynolds numbers for the position probed. The same value is found by Shi et al. [159]. The value is located in the cylinder axis for the profile drawn at 11.5 cylinder heights downstream of the cylinder. It is however observed at 1.5 cylinder height on the sides of the cylinder for the profile drawn at 6 cylinder heights downstream of the cylinder. This value and the measurement issues are similar to those mentioned in the 2D simple backward facing step case (see paragraph 1.1.3.1).

The present literature survey is intentionally not an exhaustive review of all the works that can be found in the literature. The papers chosen here present some features of the vortex shedding and interaction of two shear layers, as well as the influence of some parameters on the flow. The object is to point out some features characterizing the flow around such geometries, in particular, the universal Strouhal number with a value of about 0.18 which is verified for a wide range of flow conditions and cylinder geometries. The longitudinal turbulence level of 20% in the wake is also a significant value. Other relevant features are the influence of turbulence and aspect ratio on Strouhal numbers and eventually the existence of a critical Reynolds number range where the flow behavior is strongly different than for the other Reynolds numbers.

## 1.3 3D parallelepiped at zero degree sideslip

Another degree of complexity is added to this type of geometry: to compare with the previous sections (see 1.2.2.1 and 1.1.2.4), the geometry is now defined by two independent parameters being the width to height and the length to height ratios. Also, the

influence of the boundary conditions (wind-tunnel walls or computational domain) will depend on a blockage coefficient defined as the ratios of the geometry main cross-section (projected on the normal of the free-stream velocity) to that of the wind-tunnel. It should also be noted that the flow around such bodies has been studied for building issues to describe wind loads on them, pollution dispersion [4] or even winds in street canyons for pedestrian comfort [21]. The effect of the atmospheric boundary layer is another parameter that is studied, defined by mean velocity profiles, turbulence levels and length scales. Those characteristics also depend on the location on land/sea over which they are measured [139].

It can then easily be understood that with so many parameters involved, it is hardly trivial to build a universal theory that could describe such flows. Since this section is only aimed at introducing the 3D effect of the geometry on the flow and set some basis for understanding the 3D double backward facing step (see section 1.4), only a few chosen studies will be presented.

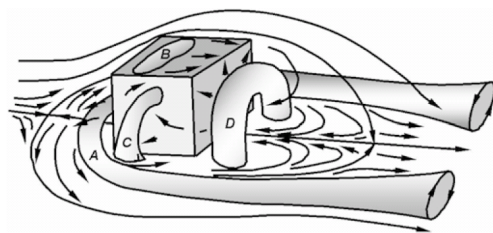
### 1.3.1 Flow topology

In its streamwise geometrical plane of symmetry, the geometry of a 3D parallelepiped mounted on a wall is similar to that of a 2D backward facing step: there is an upstream boundary layer, a step edge and a wall downstream. On the other hand, the geometry in the plane parallel to the wall and slicing the step mid-height is similar to that of a rectangular cylinder. However, is the flow around a 3D rectangular parallelepiped the combination of a backward facing step flow and a 2D cylinder flow ?

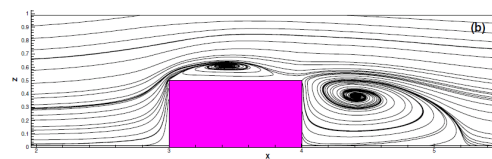
The cube is a widely studied particular parallelepiped. Several experimental works (see for example Castro and Robins [35] and Martinuzzi and Tropea [115]) have given some information about the main flow pattern around such geometries. In particular, they were used to discuss the accuracy of some computations that describe the mean and unsteady 3D flow. The reader should refer in particular to Iaccarino et al. [83] for the comparison of several computational works, especially RANS, URANS and LES, Krajnovic and Davidson [96] for LES and Yakhov et al. [194] for DNS. All those studies show that the flow is even more complex than that of the 2D geometries previously described (in sections 1.2.2.1 and 1.1). Indeed, the flow separates in the front of the cube at the top and side walls (see figure 1.9). At the front face, a horseshoe-type vortex is formed (marked A in figure 1.9(a)). It interacts with the downstream separation region behind the cube. There, the time-averaged flow pattern in the plane of symmetry (see figure 1.9(d)) is quite similar to that obtained on a backward-facing step (see figure 1.1): a primary bubble and a contra-rotating secondary one can be observed. The difference lies in the reattachment length that is much smaller for the cube than on the 2D step. At



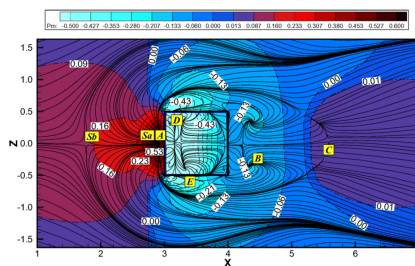
mid-cube height (see figure 1.9(b)), the time-averaged flow pattern behind the cube is similar to that behind rectangular cylinders (see figure 1.8(a)). Furthermore, it is symmetric. This symmetry of the time-averaged flow is also observed on parallelepiped of different aspect ratios. Castro and Dianat [34] used skin friction measurements whereas Kim et al. [94] used PIV fields. The latter could actually observe this mean flow symmetry all the way down to the wall where the parallelepiped is mounted. There, two symmetric counter-rotating flows are observed (marked B in figure 1.9(c) for the cube). They are actually the footprints of an arch vortex (marked D on figure 1.9(a)) which, in the streamwise plane of symmetry of the cube, is observed as the primary bubble and the two counter rotating vortices in the plane at mid-cube height.



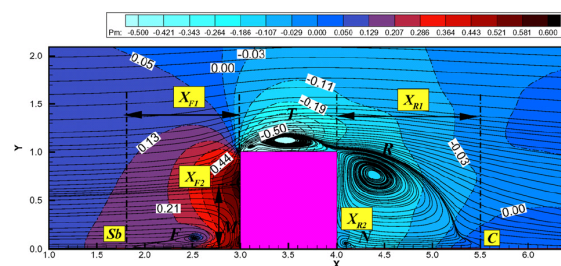
(a) Schematic representation of the vortical structures around a surface-mounted obstacle (Sousa [163])



(b) Time-averaged streamlines and pressure distribution at mid-cube height (Yakhot et al. [195])



(c) The near-wall and near-top-surface distribution of the time-averaged streamlines and pressure (Yakhot et al. [195])



(d) Time-averaged streamlines and pressure distribution in the symmetry plane (Yakhot et al. [195])

FIGURE 1.9: Flow topology around a wall-mounted cube

An alternative to CFD to obtain a picture of the time-averaged 3D flow or even sometimes the phase-averaged 3D flow is the use of several PIV planes (Kawai et al. [92], De Kat et al. [47], Wang and Zhou [184]). Thanks to the 3D recombination of the flow, Wang and Zhou [184] can overcome the difficulty of interpreting 2D slices of the flow as shown in figure 1.10.

When only surface flow patterns are available, a critical point approach <sup>1</sup> has also been used to interpret the flow visualizations (Hunt et al. [82], Woo et al. [193], Depardon et al. [50]).

When the height is smaller than the two other dimensions, the flow in the plane of symmetry of the parallelepiped reattaches on the upper face. Results from Kim et al. [94]

<sup>1</sup>Jean Délerly, cours de Master modélisation et simulation, INSTN, édition 2007

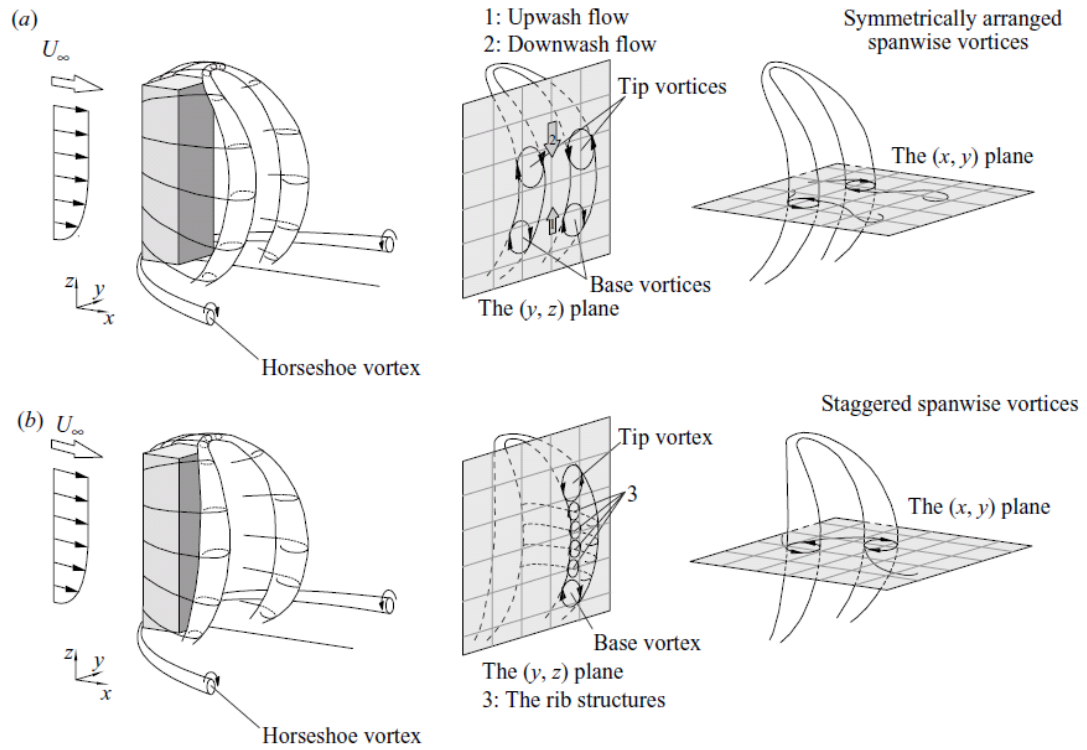


FIGURE 1.10: Interpreting the 3D shape of a vortex through 2D measurements: model of the flow structure around a wall-mounted finite-length square cylinder: (a) symmetrically arranged two spanwise vortex roll, (b) staggered arranged spanwise vortex roll. (Wang and Zhou [184])

show that the topology of the downstream separation bubble is, in this plane, similar to that of the cube.

## 1.3.2 The effects of some parameters

### 1.3.2.1 An illustration through the reattachment length

As mentioned previously in section 1.1.1.3, the mean reattachment length, noted  $X_R$ , is a good parameter to observe the effect of other parameters on the flow. For cubes at least, the reattachment length varies upon various parameters: at  $Re_h = 4 \times 10^4$  with a wind-tunnel section of  $5h$ , Depardon et al. [49] estimates  $X_R/h \approx 2$ . Krajnovic and Davidson [96] finds 1.44 for the same Reynolds number in a  $2h$  high channel. In similar conditions, Martinuzzi and Tropea [115] experimentally find  $X_R/h = 1.68$ . This reattachment length goes down to 1.5 cube height in the DNS computation of Yakhot et al. [195], performed at  $Re_h = 1.8 \times 10^3$  and with the cube put in a  $3h$  high channel. For non-cubic geometries, the size of the recirculation bubble also depends a priori on the aspect ratio of the model. This is illustrated by reattaching length of 1.93 body

height for a parallelepiped with a width to height ratio of 2.4 and a length to height ratio of 3.5 (the Reynolds number is  $Re_h = 7.9 \times 10^3$ ) [94]. All the previous values must be compared to the low aspect ratio rectangular cylinders with similar values (see paragraph 1.2.2.1). It must also be compared to the more than 2 times greater values of the backward-facing step (see paragraph 1.1.1.3). From this example, the influence of some parameters are discussed for the general case of 3D bluff bodies.

### 1.3.2.2 Bluff body aspect ratio

Woo et al. [193] discussed the influence of the different aspect ratios on the decay rate of the wake, which will not be detailed here. It should just be noted that different aspect ratios can greatly modify the flow topology, statistics and unsteady features, etc.

### 1.3.2.3 Upstream conditions: the atmospheric boundary layer

Kareem [91] observed that the peak associated to the shedding in the spectrum was not so pronounced when the parallelepiped was immersed in a simulated atmospheric boundary layer. For example, in their experiment performed in such conditions, Becker et al. [16] could not observe a clear periodicity of the vortex shedding in the plane of symmetry of a parallelepiped. This is probably the consequence of the influence of the mean velocity gradient and/or the extra turbulence added to the flow as discussed here.

**Mean velocity gradient** For tall buildings, if a mean velocity gradient exists (typically within an atmospheric boundary layer where the mean velocity increases with altitude), unexpected high winds are often observed near the ground [21]. It also results in a variation of the shedding frequency with height [116]. On tall buildings, the effect of vertical mean velocity gradient is significant.

**Free-stream turbulence** Healey [74] writes that one effect of turbulence on bluff body is to change the location of reattachment points. He adds that turbulence produces increased mixing near the separated shear layers, altering thus the flow field. However, the turbulence length scale must be mentioned as, for example, the effect of turbulence is not seen on the drag coefficients when the integral length scale is in the range  $0.6 < L_u^x < 5.0$  [99]. Also, attention should be paid to the roughness ratios: Wang et al. [185] mention the fact that the roughness ratio between model and full scale boundary layers should be the same as the ratio of the model and full-scale boundary layers thicknesses.

If done so, the Reynolds effect on pressure coefficients can be limited, if not suppressed. The general Reynolds effect is discussed in more detail in the following section.

#### 1.3.2.4 Reynolds number

This issue is of great importance to know how to extrapolate the data obtained in wind tunnels to full scale geometries of the size of buildings. Larose and D'Auteuil [100] discuss the general belief that bluff bodies with sharp edges can have aerodynamic characteristics almost insensitive to Reynolds number greater than  $Re_c = 10^4$ . The idea that the separation of the shear layer is fixed by the body edges and therefore all essential flow features must be rather independent of the Reynolds number. Healey [73] proposes  $Re_c = 1.1 \times 10^4$  while Castro and Dianat [34] observe in their experiments  $Re_c = 2 \times 10^4$ . Data from Laneville [99] suggest that the mean force coefficients for sharp-cornered rectangular parallelepiped are Reynolds number independent for Reynolds number  $Re_b > 3 \times 10^4$  (where  $b$  is the width of the parallelepiped). Those results were obtained for rectangular cross sections with  $b/d = 0.5, 1$  and  $2$  (where  $d$  is the parallelepiped length). Armitt [13] adds that if the surface roughnesses are controlled (typically characterized by a roughness Reynolds number  $Re_{K_s} = 10^3$ ), full-scale behaviors can be reproduced satisfactorily. However Larose and D'Auteuil [100] conclude that the critical Reynolds number depends on the geometry. Hoxey et al. [80] try to quantify the Reynolds number effect on pressure measurements on a bluff body. An extensive study was also conducted to compare full scale wind load measurements on a 6 m high cube and models to discuss the existence of Reynolds effect on this geometry (Richards and Hoxey [143, 144, 145], Richards et al. [146, 147]). In particular on this geometry, for  $2 \times 10^4 < Re_h < 10^6$ , Lim et al. [110] eventually conclude that for flow around bluff bodies where there appears to be no concentrated vortex region or relatively steady vortex regions, the mean velocity and pressure fields are quite Reynolds independent. This is not the case for the statistics though. On the other hand, when concentrated vortices exist (independently from the upstream conditions), Reynolds effects exist even on the mean velocity and pressure fields. The same goes for the Reynolds number dependency on the statistics. There are no reasons that the conclusions drawn on cubes cannot be applied to other 3D bluff bodies.

Eventually, as argued by Schewe [155], it should be kept in mind that if a Reynolds number effect exists, there is most probably a fundamental variation of the topological structure of the wake. It can be added that these structural changes could find an origin in the change of location of the laminar-to turbulent transition.

### 1.3.2.5 Blockage effect

As already mentioned for the 2D step (see paragraph 1.1.2.4) and the 2D cylinders (see paragraph 1.2.2.2), too much obstruction of the test section results in the flow modification. Corrections exist to apply to such coefficients, as reviewed by Cooper [41].

## 1.3.3 Unsteady flow

### 1.3.3.1 Turbulent kinetic energy

Becker et al. [16] observe the maximum turbulent energy within the upper shear layer, around the reattachment region. It reaches values up to 17%, similar to those on the 2D step and cylinders (see respectively paragraphs 1.1.3.1 and 1.2.3.1). Callaud and David [30] show that all three velocity components contribute the high levels of turbulence observed downstream to such 3D bluff bodies. Their measurements reveal turbulent energies locally higher than 20% in the upper shear layer. For parallelepiped of higher aspect ratios, approximately the same values are obtained in the streamwise plane of symmetry of the body, in the wake upper shear layer [94].

### 1.3.3.2 Spectral analysis

For 3D bluff bodies, vortex shedding can be observed under certain conditions. This can occur for non-academic shapes at very high Reynolds numbers and high levels of free-stream turbulence, as observed sometimes downstream of mountains (see figure 1.11). Becker et al. [16] characterize the shedding visualized in the streamwise plane

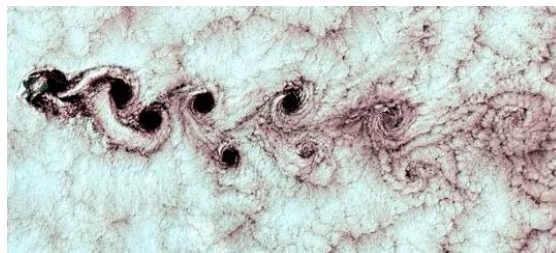


FIGURE 1.11: Von Karman street materialized by clouds downstream of Alexander Selkirk island in the southern Pacific ocean. Image taken by the Landsat 7 satellite in September 1999

of symmetry of a parallelepiped through a Strouhal number of 0.155 at low turbulence level and a Reynolds number of  $2 \times 10^4 \leq Re \leq 7 \times 10^4$ . However, in their spectra, even if no clear peak is visible, a high contribution of the low frequencies (lower than that attributed to vortex shedding) is visible.

The influence of the body aspect ratio is reviewed by Cermak [36] who mentions the Strouhal number measurements (based on the width) of Vickery [180] on prismatic shapes subject to uniform flow. The results are plotted on figure 1.12 and are approximately 0.1. However, when  $b/d < 1$  (namely width/length) or the aspect ratio is

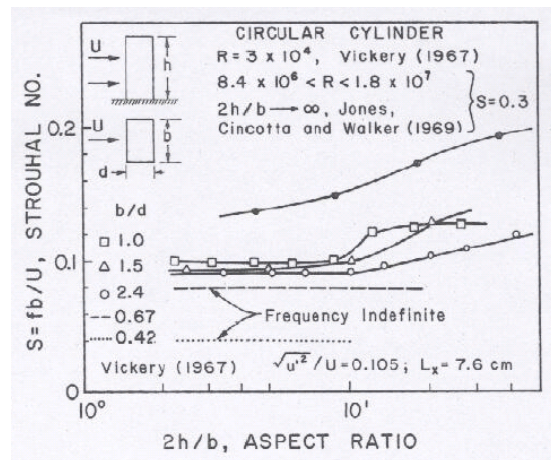


FIGURE 1.12: The effect of building geometry on vortex-shedding frequency in turbulent flow (Cermak [36]).

smaller than 2, a broad-band spectrum is observed and a Strouhal frequency cannot be detected. Cermak [36] suggests that the reattachment of the flow initially separating at the upstream corners could lead to intermittent vortex formation by secondary separation at the downstream corners.

As a comparison, for cubes, the computed and measured Strouhal numbers are around 0.1 [119, 120, 195].

### 1.3.3.3 Coherent structures

In the visualizations of Becker et al. [16] in uniform upstream flow, the vortices in the upper shear layer of the parallelepiped (that has a height to length ratio of 3.5) seem to reach diameters as big as the body height. Similar qualitative results seem to be found by Calluand and David [30] in the same plane but on a parallelepiped with height to length aspect ratio of 0.3.

If, from the understanding of the 2D step and 2D cylinder flows it is possible to have a first impression (false but at least a first impression) of the flow around 3D parallelepiped in the  $y = 0$  and  $z/h = 0.5$  planes, this approach is not sufficient to obtain a full understanding of the 3D instantaneous flow. This is what Kawai et al. [92] and Wang and Zhou [184] tried to visualize experimentally through conditional sampling of their PIV data. This has given them a better understanding of how the arch vortex

is shed: Kawai et al. [92] shows a stretching of one of the two legs of the arch vortex during its shedding.

## 1.4 3D double backward facing step at zero degree sideslip

### 1.4.1 Definition of the Geometry

Within The Technical Cooperation Program (TTCP) AER-TP2 [189] aimed at producing high fidelity flight simulators for shipboard helicopter operations, a Simple Frigate Shape (SFS1) was designed (see figure 1.13(a)). Several variations followed, such as the SFS2 (figure 1.13(b)), SFSC (figure 1.13(c)) and SFST (figure 1.13(d)). To discuss the validity of this geometry simplification, a comparison between the flow computed on a SFS2 and a real type 23 frigate is given by Forrest and Owen [64]: the main flow features are found on both geometries, but the SFS2 remains a simplification.

The geometry is composed of three to four elements as seen on figures 1.13:

- sometimes a forward nose, added to reduce the effects of a massive separation at the upstream face of the body
- a central cuboid, modelling the ship's construction. It will henceforth be referred to as central cuboid
- a backward smaller cuboid of same width as the central one, but of lower height, put behind the first one. As a consequence, two backward facing steps appear. This latter rectangular parallelepiped represents the flight deck. It will henceforth be referred to as backward cuboid
- sometimes, a smaller parallelepiped put on the top of the central cuboid that theoretically represents a ship funnel

A frigate ends up being modelled by a 3D double backward facing step. Some characteristics of 3D bluff bodies and their influencing parameters, etc. have already been overviewed in the previous section 1.3. Since the SFSs are the juxtaposition of such bluff bodies (which makes it a bluff body itself), those characteristics are also found. This section will focus though on the particularity of the flow around this geometry (that is the interaction of the flows around side by side bluff bodies) as well as the main differences obtained between the various SFSs.

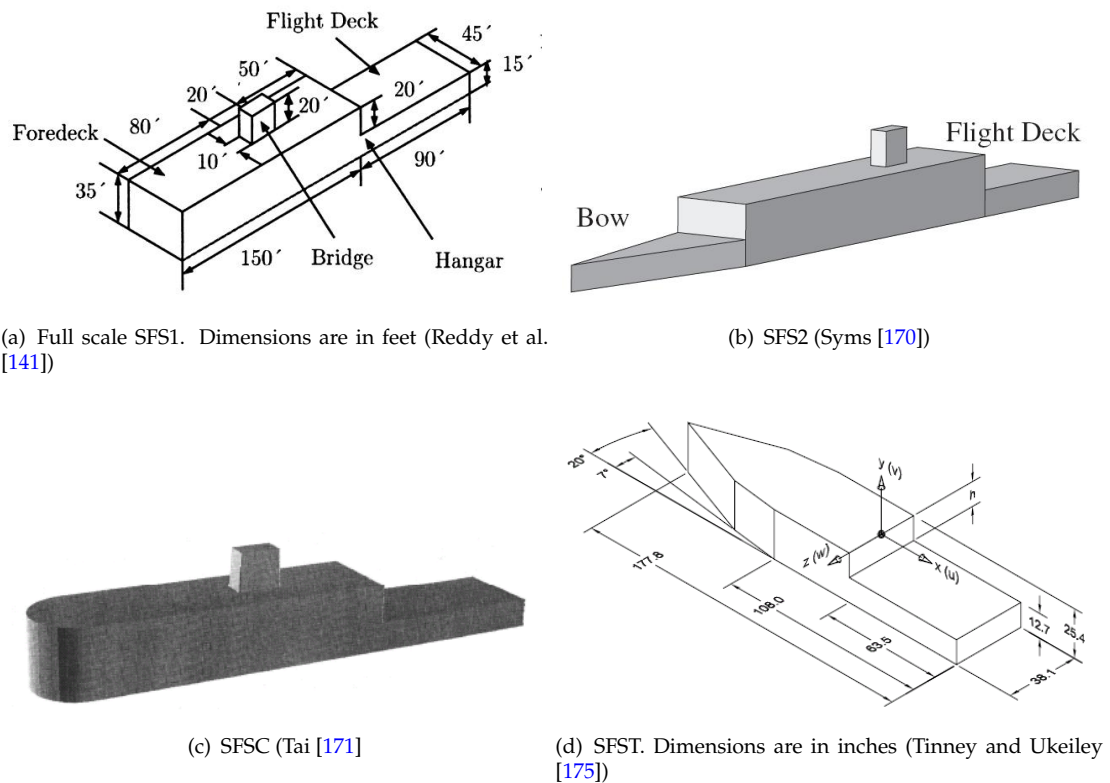


FIGURE 1.13: Several Simplified Frigate Shapes found in the literature

## 1.4.2 Configuration SFS1

### 1.4.2.1 Mean flow description

Cheney and Zan [38] and Zan [197] experimentally studied this flow. Cheney and Zan [38] used smoke and oil-flow visualizations to describe the flow around the SFS1. As for the high length to height ratio parallelepiped (see paragraph 1.3.1 and Kim et al. [94]), the flow separates at the forward face of the body, but reattaches before reaching the first step. The flow separates also around the funnel and downstream of the steps. A primary recirculation bubble is observed over the backward cuboid. As for the parallelepiped, an arch vortex can be observed behind the steps. The arch vortex behind the first step leaves two symmetric footprints on the top of the backward cuboid, as suggested by Cheney and Zan [38]. This is illustrated on figure 1.14(a). Several computational works have been performed on this geometry, in particular RANS computations (Reddy et al. [141], Wakefield et al. [183] and Roper et al. [148, 149]). A quick review of the earliest studies is also found in Wilkinson et al. [189]. In particular, Liu and Long [112] compute a symmetric time-averaged flow, with a reattachment line at about  $1.5h$ . This should be compared with the value of  $2.5$  found experimentally by Cheney and Zan [38]. Questions then remain about the flow pattern obtained at the



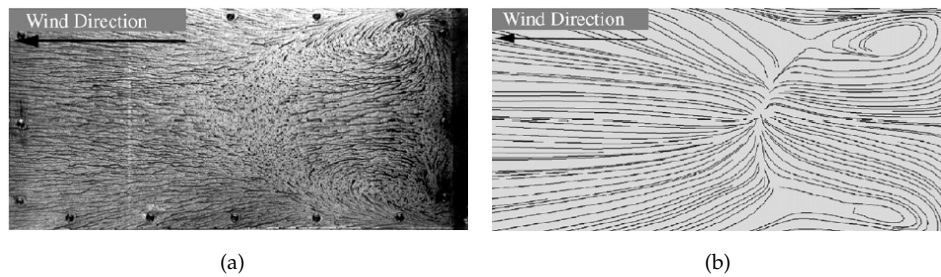


FIGURE 1.14: Surface streaklines of the 1<sup>st</sup> step of the SFS1: (a) experimental (Cheney and Zan [38]), (b) computation (Syms [170])

wall, as suggested by Reddy et al. [141]. In this respect, Zan [198] wrote a note on the interpretation of the surface flow pattern. An unsteady viscous computation was recently performed by Syms [170] using a lattice-Boltzmann approach. The computation compares well with the experiments. Among all the authors referenced above, Syms [170] is the only one who computed the surface pattern that is not strictly symmetric as illustrated on figure 1.14(b). The asymmetry is however not very pronounced.

#### 1.4.2.2 Some characteristics of the unsteady flow

In their computation, Liu and Long [112] observe shedding emanating from the first step. The associated longitudinal turbulence intensities are around 5%, using an inviscid approach. Measurements from Greenwell and Barrett [72] with a LDA device show turbulence levels reaching 40 to 50% at step height levels, peaking at above 60% in the lee of the step. Regarding those extremely high levels of turbulence reached, Greenwell and Barrett [72] suggest that they are related to large-scale unsteadiness in the flow, such as bursting and filling of the recirculation bubble. Further investigation is required before being able to explain those observations.

### 1.4.3 SFS2 geometry

#### 1.4.3.1 Mean flow description

Within the TTCP AER-TP2, experimental data on the SFS2 have been gathered by Lee [104, 105]. Hot-films were used. If the data are not published in the literature, they can indirectly and partially be obtained through their use in CFD validations like in Syms [170], Forrest and Owen [64], Forrest et al. [65, 66]. Those experimental data are also used in the CFD computations of Roper et al. [148, 149], Hodge et al. [78], Kaaria et al. [89, 90] (the last two references are actually using the results from Forrest and Owen [64]). Syms [170] observed an unexpected asymmetry of the time-averaged flow which

is confirmed by the experiments. This asymmetry is seen on the mean velocities and the turbulence intensities as illustrated in figure 1.15. Syms [170] hypothesizes that the

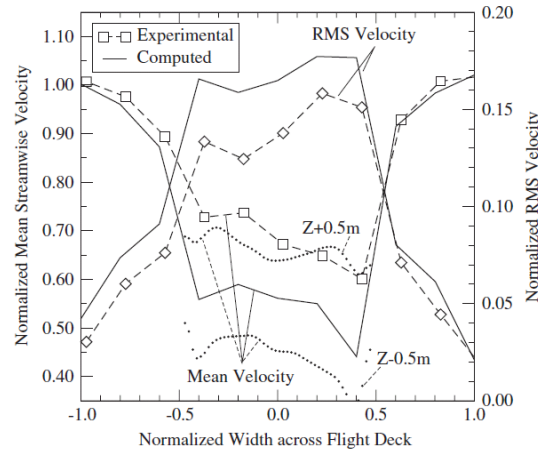


FIGURE 1.15: Mean and RMS streamwise velocities across the backward cuboid of the SFS2, in the vertical plane located at  $1.1h$  downstream of the first step and at step height (Syms [170]).

flow might lock into one side of the nose, since it is long and narrow: the symmetric flow could be unstable or at least a highly fickle one. He mentions the fact that more analysis is required to have a better understanding of this mean flow asymmetry. This feature was however not clearly evidenced in the DES results computed by Forrest and Owen [64].

**Reynolds effect** Forrest and Owen [64] studied the Reynolds number effect on this particular geometry (see paragraph 1.3.2.4 for a more detailed discussion): two computations were performed at  $Re_h = 2.26 \times 10^7$  and  $Re_h = 2.93 \times 10^5$ . It was found that the flow patterns were essentially the same, with some slight differences in the location of features such as reattachment points and vortex cores. To be more precise, the reattachment length varied from  $X_r/h = 2.02$  to  $X_r/h = 2.17$ , that is a relative difference of 7%.

#### 1.4.3.2 Some features of the unsteady flow

**Frequencies involved** Spectral measurements were conducted downstream of the first step. In the wake of the funnel, a slight peak at  $St = 0.12$  (based on the funnel width) is observed, certainly resulting from the shedding behind this geometry [64]. However, at a lower position  $(x/h, y/h, z/h) = (2.24, 0.9, 0.75)$  (see figure 2.1(a) for the definition of the coordinate system), no clear peak is visible. Most of the energy is

found at low frequencies.

Forrest and Owen [64] suggest that the upper shear layer flaps, explaining the unsteadiness of the reattachment point.

**Coherent structures detected** As suggested by the  $\lambda_2$  contour plots of Forrest and Owen [64], coherent structures are observed downstream of the first step. Some are generated by the central cuboid front face, advected and re-energized by the funnel which also generates coherent structures. Behind the first step, the structures are not as energetic as the latter but still exist.

#### 1.4.4 Configuration SFSC

This geometry has only been studied by Tai [171] through a RANS computation. The rounded nose was designed to suppress the flow separation on the lateral sides of the central cuboid. However, a separation is still visible on the upper side, but is not comparable to the massive separation observed on the front face of the SFS1 as described previously. The reattachment length deduced from the plotted figures is about  $1.6h$ . Eventually, contrary to the SFS2 case, Tai [171] computes a symmetric time-averaged flow.

#### 1.4.5 Configuration SFST

The SFST was designed and studied by Tinney and Ukeiley [175]. It is probably the most comprehensive work regarding the unsteady flow features. It is however conducted at a Reynolds number  $Re_h = 9 \times 10^3$ , which is smaller than for all the studies of the 3D double backward facing step described above.

##### 1.4.5.1 Mean flow description

Because the nose induces a pressure that is lower on its top than on its lateral sides, two streamwise vortices at the upper corners are generated (noted 'wing vortex' on figure 1.16). They persist to a minimum to locations  $x/h = 4.5$ . Two counter-rotating vortex pairs are also observed on the top of the backward cuboid, downstream of the saddle point. Tinney and Ukeiley [175] suggest that they are induced by the wing vortices that are pulled towards the low-pressure recirculation region of the flow. Those last two streamwise vortices were not observed behind the parallelepiped. Eventually, the global topology can be seen in figure 1.16, showing the now classic arch vortex and

saddle point. The reattachment point of the primary bubble is measured at  $2.6h$ , which

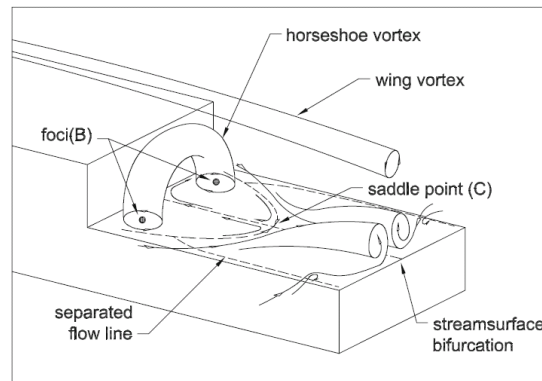


FIGURE 1.16: Perspective view of the flow downstream of the SFST (Tinney and Ukeiley [175]).

is longer than for the other SFSs. The secondary bubble (as discussed in paragraph 1.3) is not visible, probably due to 3D effects or the limitations of the experimental setup.

#### 1.4.5.2 Flow statistics

By comparison to the SFS2 case (see paragraph 1.4.3), while considering the maps of streamlines and turbulence levels (see figure 1.17), questions are raised about the symmetry of the time-averaged flow. This is however not explicitly mentioned by the authors [175]. The highest turbulence longitudinal intensities in the plane of symmetry behind the first step are found in the shear layer and reach values up to 25%. The maximum levels of turbulence production are also found in those areas. However, for the turbulence intensities of the vertical velocity, high levels are also found close to the reattachment region.

#### 1.4.5.3 Coherent structures and frequencies involved

The turbulent structures are particularly concentrated in the plane of symmetry of the body. The advection velocity of the structures ranges between  $0.7U_0$  and  $0.76U_0$ . A Strouhal number of  $St_h = 0.17$  was defined but could not be clearly associated to shedding from the lateral walls. However, a POD analysis suggests that coherent structures are shed in the plane of symmetry of the body, behind the steps, in the upper shear layers. Some even brush the surface after reattachment before being advected downstream.

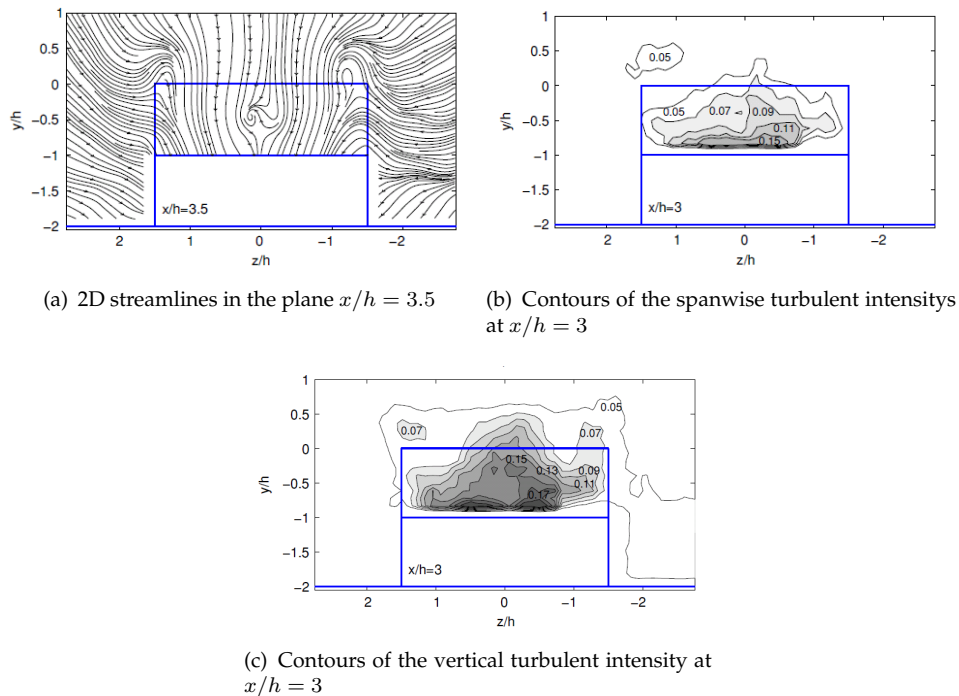


FIGURE 1.17: Some features of the flow in  $x$  planes of the SFST (Tinney and Ukeiley [175])

## 1.5 Summary

This is just an overview of the complexity of the flow characteristics around bluff bodies. Some features of the 2D backward facing step can be found in the streamwise plane of symmetry of a 3D double backward facing step. On the plane normal to this one and at mid-step height, some features of the 2D cylinder can be found. However, the main difference between the 3D double step and other parallelepiped flows is the occurrence of streamwise vortices downstream of the reattachment region as well as a mean flow asymmetry in some cases. If in the literature the studies of 2D steps and other 3D parallelepiped are quite numerous, it is not the case for 3D double steps. The understanding of the unsteady behavior of the flow as well as the description and statistics of the coherent structures in space and time are still ongoing, which justifies the following work. It becomes nonetheless obvious that it is not trivial to elaborate general theories about bluff body flows. Indeed, the steady and unsteady flow features are highly dependant on several parameters such as the geometry itself, the upstream conditions (turbulence levels, boundary layer shape), the blockage coefficients, the Reynolds number and probably even more (Mach number, etc.). Those parameters should therefore be mentioned during all study before drawing any general conclusions.

## Chapter 2

# Experimental and numerical setups

Three experimental campaigns were conducted in three different wind-tunnels: the TEMPO wind-tunnel, the L2 wind-tunnel and a mini-wind tunnel. A RANS computation using the elsA code completes the experiments. Several geometries were tested with different qualitative and quantitative techniques. This chapter will define them, as well as some of the raw data processing tools used.

### 2.1 Defining a common coordinate system

In the present work, the reference frame (see figure 2.1(a)) is defined as below:

- the origin O belongs to the plane of symmetry of the body. It lies at the intersection of the first step face and the top of the backward cuboid
- The x axis belongs to the plane of symmetry of the body and to the top of the backward cuboid. It is oriented towards downstream
- the z axis belongs to the plane of symmetry of the body and to the first step face. It is oriented away from the top of the backward cuboid
- the y axis completes the direct trihedral (O,x,y,z)

For a matter of simplicity, all dimensions are normalized by the first step height h. The new normalized coordinate system is then  $(x', y', z') = (x/h, y/h, z/h)$ .

The geometric drift angle  $\beta_g$  is defined as the oriented angle between the wind tunnel reference axis (noted  $x_{wt}$  in figure 2.1(b)) the model x axis (noted  $x_{model}$  in figure 2.1(b)).  $\beta_g > 0$  means that the nose of the model points to the left while looking into the upstream direction.

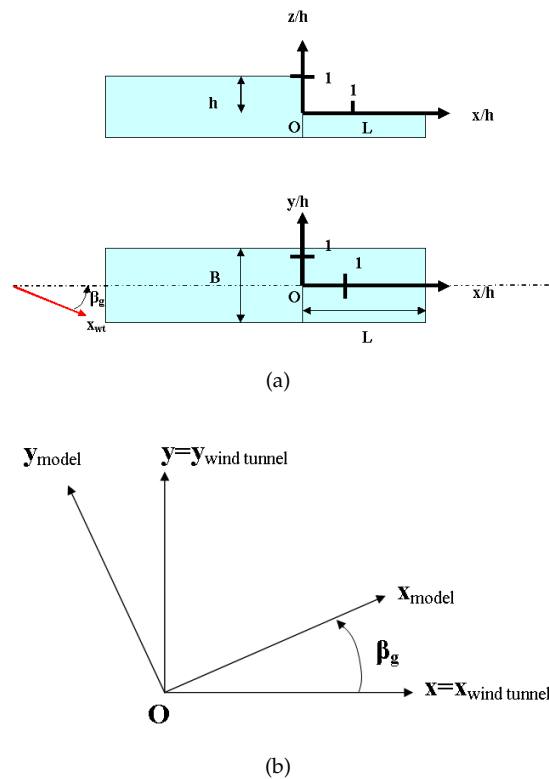


FIGURE 2.1: (a) Coordinate system and (b) definition of the geometric drift angle

## 2.2 Campaign at the TEMPO wind-tunnel

### 2.2.1 The model

The model tested in the TEMPO wind tunnel is based on the SFS1 (see figure 1.13(a)). However, two major modifications were applied: (i) the funnel was removed and (ii) a pyramidal shaped nose was added. It is named SFSO'. The O stands for 'ONERA', since the nose shape was designed in this lab and the prime ' indicates that the funnel was removed. This notation will be kept in the present work, even for the other geometries. The final shape is illustrated on figure 2.2(a). The dimensions are normalized by  $h$ , with  $h = 0.102$  m in those experiments. Eventually, the model was set at the leading edge of a  $2 \times 5$  m<sup>2</sup> table as illustrated in figure 2.2(b). The surface of the table on which the model was mounted was set at 750 mm above the wind tunnel wall. The model and its table were made of hard plywood. They were manufactured explicitly for this series of experiments.

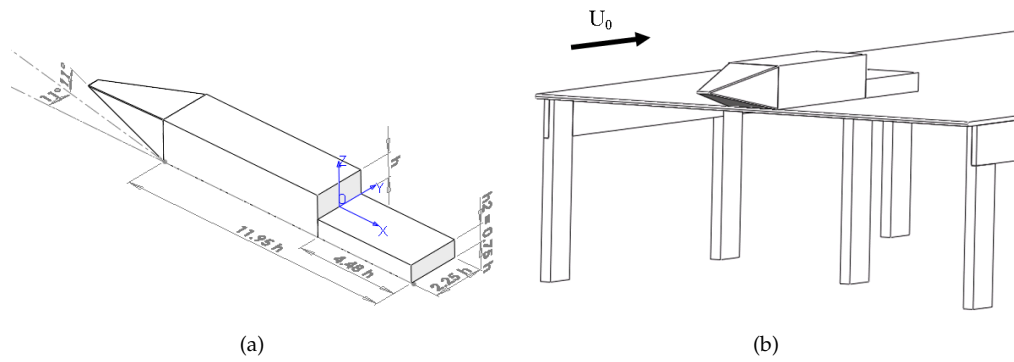


FIGURE 2.2: SFSO': (a) alone and (b) on its table

### 2.2.1.1 Controlling the model drift angle

For most tests, the frigate was set on its table with a series of screws. However, to precisely control the drift angle, an automatic traverse system from DANTEC was used for some tests.

A screw located at  $(x/h, y/h, z/h_2) = (-0.775, 0, -1.0)$  kept the bluff body on its wall without restraining the drifting ( $h_2$  is the second step height). The face of the second step was linked to the traverse system chariot and could translate along the width of the table. The position of the chariot could be programmed with a  $\pm 0.01$  mm accuracy (the clearance in the system is not considered here). Therefore, given a reference drift angle  $\beta_{g0}$ , the uncertainty in determining the relative change in drift angle  $\beta_g - \beta_{g0}$  was around  $0.1''$ .

The table with the model on it was eventually mounted inside the TEMPO wind tunnel.

### 2.2.2 The wind-tunnel

For this test campaign, all the model wake measurements were conducted in the low-speed wind tunnel hosted by TEMPO of the University of Valenciennes. A view of this wind tunnel is shown in figure 2.3.

This wind-tunnel was specifically designed to study the aerodynamics of ground vehicles such as cars and trains. It has a  $2 \times 2$  m<sup>2</sup> square test section ③ that is constant in size over the 10 m of its length. The tunnel is a closed circuit facility with a 6.25 : 1 contraction ratio ① ②, driven by a 200 kW variable-speed propeller ⑤. The wind speed in the test section can be adjusted continuously from 0 to about 60 m/s. A honey comb set at the entry of the collector ①, composed of 10 mm wide cells that are 200 mm long, spatially filters the bigger turbulent structures. At 30 m/s, the turbulent intensity along the empty test section is about 0.5%. A more detailed description of the reference velocity



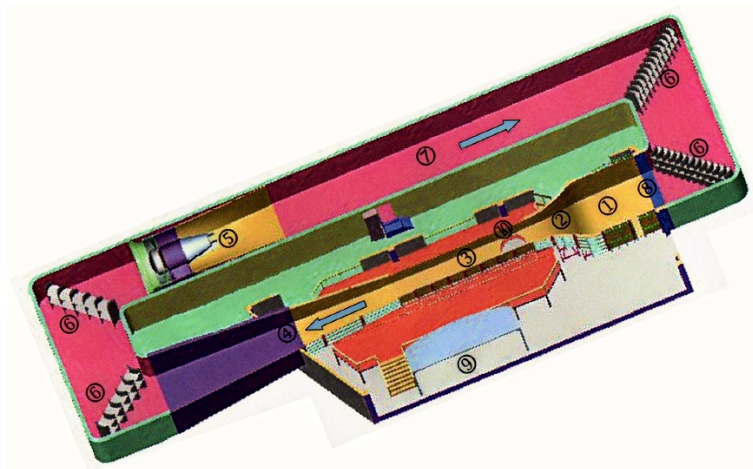


FIGURE 2.3: The TEMPO wind tunnel of Valenciennes

determination is given below. Eventually, in this test campaign, the wind speeds considered induced an experimental Reynolds number  $Re_h$  ranging from about  $8 \times 10^4$  to  $3.6 \times 10^5$ . Based on the central cuboid length, this corresponds to a minimum Reynolds number of  $6 \times 10^5$ .

Because of the table, the model was immersed in a very thin boundary layer that developed on the table, starting at its leading edge. Qualitative smoke visualizations did not show any flow separation at the leading edge.

The return circuit of the wind tunnel is underground ⑦. This keeps the temperature from rising too much during long tests. In the following measurements, temperature variations during tests have been neglected and no temperature correction has been taken into account.

Also, the blockage coefficient of the model at  $\beta_g = 0$ , based on the surface above the table is below 2%. As discussed in the previous chapter, this value was considered small and blockage corrections were not applied. In practice,  $\beta_g$  is determined by measuring the distance between the wind tunnel reference wall and the lateral side of the bluff body at two locations: its front and its end. By estimating at 1 mm the uncertainty of the distance measurement on each sides and knowing the distance between the two measurement locations, the resulting absolute value of  $\beta_g$  is measured with an accuracy superior to 0.05 degree.

### 2.2.2.1 Determining the reference velocity $U_0$

At the TEMPO wind tunnel, the operator actually sets the value  $f_{prop}$  (in Hz) of the wind tunnel propeller rotational speed. Then the relation between  $f_{prop}$  and the true wind speed in the test section must be determined. In practice, it was done through LDA measurements.

In order to measure both the velocity and the turbulence levels, Laser Doppler Anemometry was used. Prior to doing the measurements, a standard smoke generator producing spherical oil particles about  $3\ \mu\text{m}$  in diameter was put inside the closed circuit wind tunnel at the beginning of the diffuser. The smoke generator was set at maximum to generate as many particles as possible. The particles were tracked by a conventional one-dimensional LDA system from DANTEC dynamics<sup>1</sup>. It had 2 continuous laser beams, 2.2 mm in diameter, initially spaced by 39.057 mm and crossing 400.9 mm after the lens, with a 532 nm wavelength (green). The sampling time chosen was 120s. Depending on the free stream velocity, this led from 22000 samples up to more than 211000 samples acquired during 120s.

In the reference frame presented above, the reference velocity was then measured at position  $(x/h, y/h, z/h) = (0.67, 13.6, 2.78)$ . This ensured to be away from the bluff body airwake and away from any wind tunnel boundary layer. The model and its table it was mounted on were then put into the wind tunnel. In the velocity range considered, a linear relation is found between  $f_{prop}$  and  $U_0$ . Appendix B on sampling criteria shows that an estimate of the true mean velocity with a 0.1% uncertainty can be trusted with 99% confidence.

### 2.2.3 Oil flow visualizations

The wind tunnel reference velocity was set higher than for the other tests through  $U_0 = 52.7\text{m/s}$ . Therefore,  $Re_h = 3.5 \times 10^5$ . Two oil mixtures were inspired from recipes found in the literature [82, 193]. In percentage of the total mass, the thicker mixture was composed of 28% titanium oxide, 10% oleic acid and 62% paraffin oil. As for the diluted mixture, the percentages were respectively 15%, 10% and 75%. It was applied on the whole model as uniformly as possible with a paint roller. When the wind blew, the oil was slowly set in motion by the airflow just above the body surfaces. The oil followed the mean flow and drew lines on the model surface, representing the trajectory of a particle of oil mixture. The oil motion depends on its viscosity as well as on the friction velocity. Here, the characteristic time of the oil motion was much greater than that of the airflow. Therefore, the mean surface flow trajectories were drawn. In the following tests, the two mixtures ended up being too thick for the friction velocity considered. Eventually, following the evolution of the oil patterns obtained during the tests, it was arbitrarily decided to let the wind blow ninety-five minutes in the case of the less thick mixture and one hundred and five minutes in the case of the thicker mixture.

A summary of the two tests performed is found in table 2.1.

<sup>1</sup>see <http://www.dantecdynamics.com/Default.aspx?ID=822>, last visit: 05/13/2009

TABLE 2.1: Oil visualization test program

	$Re_h$ [-]	$\beta_g$ [deg]	Oil mixture
Configuration 1	$3.58 \times 10^5$	-0.21	diluted
Configuration 2	$3.58 \times 10^5$	0.21	thick

## 2.2.4 Laser tomography

### 2.2.4.1 Data acquisition

A Phantom V7 high sampling rate camera (up to 6688 fps) was used. The CCD has  $800 \times 600$  pixels. Pixels are squared with a  $22 \mu\text{m}$  side length. Its 2 GB RAM memory allows to take a sequence of more than 4000 frames at this resolution. However, in the following tests, only 100 images were acquired during each sequence. Exposure time could go down to  $2 \mu\text{s}$  thus allowing net images in most situations. A Sigma lens for Nikon AF D was used with a 105 mm focal. The aperture was F2.8. However, high light intensity was required. The flow was illuminated by a laser sheet generated by a continuous Nd:Yag laser (wavelength: 532 nm). The laser optics opened the beam in a few millimeters thick light sheet with a 90 degrees opening angle. The laser was placed about 1.5 m away from the model and illuminated the airflow, seeded with smoke. The laser sheet position is given with an error of a few millimeters. Smoke particles, smaller than  $1 \mu\text{m}$ , were released from a bronze pipe which could be held in any position in space. The operator who held the pipe was outside of the wind tunnel, as well as the conventional smoke generator, linked to the bronze pipe with a plastic tube. A few holes were then drilled through the lateral wooden wall of the wind tunnel. The camera was purchased with a full package including the softwares Phantom Camera Control and Phantom Cine Viewer 663 to trigger the camera, register and view raw videos in a special *.cin* format.

### 2.2.4.2 Data post-processing

The brightness and contrast of the videos acquired in *.cin* format were increased within the Phantom Cineviewer 663 software prior to compression. The 100% compression quality conversion to the *.avi* format at 5 frames per second was done through indeo video 5.10. Sequence images were extracted from *.avi* videos with the Virtual Dub software<sup>2</sup> after RGB filtering. However, single isolated snapshots were directly extracted from *.cin* videos with the Phantom Camera Control software and put in *.jpg* format. No

<sup>2</sup>see <http://www.virtualdub.org/>, last visit 05/14/2009

filtering was then applied, explaining the color difference between the images. Scales and drawings on the images were made using the Paintshop pro 10 software.

### 2.2.4.3 Test program

Smoke visualizations were performed for  $\beta_g = 0.0^\circ$ , at  $Re_h = 9.75 \times 10^4$ , with the laser sheet in the planes:

- $x/h = -0.13$  and  $x/h = 1.6$
- $y = 0$
- $z/h = 0.47$

Some of the acquisition details are given in table 2.2.

TABLE 2.2: Laser tomography visualization test program

Laser sheet Plane probed	Camera		Smoke injection at $(x/h, y/h, z/h) =$	See figure
	$f_s$ [Hz]	Exposure time [ $\mu s$ ]		
$x/h = -0.13$	300	3100	$(-22.4, -1.2, 2.1)$	3.2
$x/h = 1.6$	500	1800	$(0, 0, 0)$	3.27
$y/h = 0$	1000	400	$(0, 0, 0)$	3.28
$z/h = 0.47$	500	1800	$(0, 0, 0)$	3.30
$z/h = 0.47$	300	3100	$(0, 0, 0)$	3.29

## 2.2.5 Hot-wire measurements

### 2.2.5.1 Instrumentation and data acquisition

Experiments were carried out with the model set at  $\beta_g = 0.0^\circ$  and for two reference Reynolds numbers  $Re_h = 9.75 \times 10^4$  and  $Re_h = 1.65 \times 10^5$ . A DANTEC constant temperature hot-wire anemometry (CTA) system was used. The output signal was transferred by an A/D digital card connected to a PC. The STREAMLINE soft supplied by DANTEC was used to acquire and store data. Two single normal wire probe DANTEC 55P15 were used. The sensors of such probes consisted of platinum-tungsten wires. Probe 1 was held by a straight hanger whereas probe 2 was put at the tip of a 90-degree-elbow holder. In any case, no disturbing vibration was observed on the holders. For spectra measurements, their positions were changed manually. For advection velocity determination, probe 2 was set on a manual traverse device allowing micrometrical translations to estimate with good accuracy the distance between the two probes. For

boundary layer probing, only one hot-wire was used and put on the automatic DANTEC traverse device. The device allowed an easy and accurate relative positioning of the wire. The anemometer voltages were calibrated with the velocities using a fifth degree polynomial fit with an accuracy better than 1%. For boundary layer measurements, to ensure that the original calibration curve was maintained during one entire set of hot-wire measurements, the calibration curves were re-checked after each set of measurements covering the entire range of velocities experienced. Shift in calibration was below 0.3%. For both spectra and advection velocity measurements, calibration was not re-checked. Because only time evolution of the signals was initially looked for, regardless of the amplitude.

For the boundary layer probing, the hot wire was automatically set at 33 unevenly spaced positions.  $(x/h, 2y/B, z/h) = (-0.932, 1+\epsilon, 0.33)$  and  $(x/h, 2y/B, z/h) = (-0.932, 1.44, 0.33)$ ,  $\epsilon$  being the normalized distance of the first measurement position to  $y > 0$  side of the model. At each position,  $2^{16}$  samples were acquired at a 1 kHz [resp. 2 kHz] sampling rate for the lowest [resp. highest] reference Reynolds numbers. At a maximum turbulence level of 15%, such sampling rates were enough to have 99% confidence in measuring the mean value with a less than 1% uncertainty (see appendix B).

For the advection velocity determination, two hot wire probes were placed along the body x axis, one behind the other, at a distance  $d$  (see figure. 2.4).

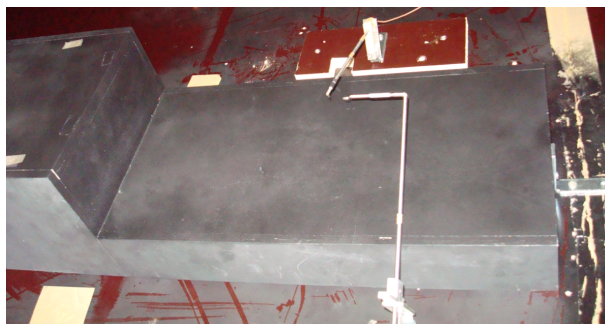


FIGURE 2.4: Positioning of the hot wire probes for mean advection velocity measurements

Their exact positions are reminded in the test program (table 2.3), and illustrated in figure 2.5.

They acquired data simultaneously with sampling parameters chosen after different tests. The two signals were time cross-correlated and the maximum of the cross-correlation coefficient was associated with a particular phase shift  $\tau$ . The cross-correlation coefficient of the signals from the two probes  $x_1$  and  $x_2$  is theoretically defined as:

$$R_{x_1x_2}(\tau) = \lim_{T \rightarrow \infty} \frac{1}{T} \int_0^T x_1(t)x_2(t + \tau)dt \quad (2.1)$$

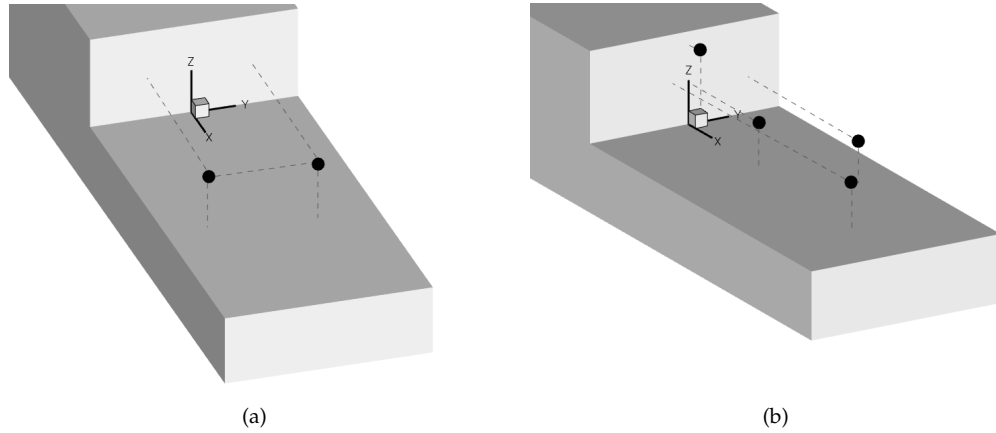


FIGURE 2.5: Positions of the hot-wire probes for (a) spectra measurements and (b) advection velocity determination

In practice, with finite time records, an unbiased estimate of the cross-correlation coefficient is computed as follows [28]:

$$\hat{R}_{x_1x_2}(r\Delta t) = \frac{1}{N-r} \sum_{n=0}^{N-r} x_1(n\Delta t)x_2(n\Delta t + r\Delta t), \quad r = 0, 1, \dots, m \quad (2.2)$$

where  $\tau = r\Delta t$  is the time delay, and  $m$  is the maximum phase lag. In the present study,  $m\Delta t = 10$  ms for the lowest Reynolds number and  $m\Delta t = 5$  ms for the highest Reynolds number.

When the maximum of the cross-correlation coefficient is over 0.4, this means that the upstream hot-wire probe signal is well reproduced on the downstream probe with a time lag  $\tau$ . The average speed at which the information is advected at this position is then  $U_{adv} = d/\tau_m$ , where  $\tau_m$  is the time delay corresponding to the maximum value of the cross-correlation coefficient. Since the signals of the two spatially separated probes are correlated, this means that some flow fluctuations keep part of their characteristics over  $d$ . The information advected between the two probes is then supposed directly related to those vortices. Through this technique, it is then expected to determine the mean advection velocity of the coherent structures.

The sampling frequency has to be high enough to obtain two correlated signals and also to limit uncertainty on peak detection. Added to the uncertainty on  $d$  (below 0.25 mm), and by neglecting the other measurement errors, the advection velocity was estimated with a 7% accuracy. A summary of the test program with some of the acquisition parameters is given in table 2.3. They were all performed at  $\beta_g = 0^\circ$ .

TABLE 2.3: Hot-wire test program

Measure	$Re_h \times 10^{-4}$	Probe ( $x/h, y/h, z/h$ ) =	Acquisition param.		refer to
			$10^{-3} \times f_s$ [Hz]	$N_s$ [-]	
Spectrum	16.5	(2.37,-0.61,0.51)	2	$3 \times 2^{20}$	3.26
	16.5	(2.34,0.58,0.45)			
Advection velocity	9.75	(0.42,-0.06,0.95)	20	$2^{20}$	3.37(b)
	16.5		40		
	9.75	(1.56,-0.03,0.51)	20	$1.8 \times 10^6$	
	16.5		40		
	9.75	(2.51,0.59,0.49)	20	$2^{20}$	
	9.75	(3.59,-0.13,0.51)	20	$2^{20}$	
	16.5		40		
Boundary layer	9.75	(-0.93,1.12,0.33)	1	$2^{16}$	3.1.0.3
	16.5		1		
Calibration	Variable	(0.82,4.02,0.43)	1	$2^{14}$	

### 2.2.5.2 Data processing

Scripts were written in Matlab to compute the spectra. The hot wire signal was first filtered through a Hanning window. Then, using the overlapping and zero-padding techniques, the spectrum was computed with the Welch method [137]. Attention was paid to the number of sub-spectrum computed and ensemble averaged in order to increase the accuracy in the estimated spectrum. This point is discussed in more detail in appendix B.

## 2.2.6 PIV measurements

### 2.2.6.1 Data acquisition

PIV data were acquired using a conventional 2D PIV system from TSI. A standard smoke generator producing spherical oil particles about  $3 \mu\text{m}$  in diameter was put inside the closed circuit wind tunnel at the beginning of the diffuser. This position of the generator was chosen to ensure a seeding as uniform as possible in the whole test section. The seeded flow field was illuminated with two pulsed Nd:Yag lasers, the wavelength being 532 nm. Those lasers could give at a maximum of 15 Hz repetition rate, pulses lasting 10 ns and delivering 20 to 500 mJ each. Standard optical components were used to combine the beams and form a light sheet approximately  $500 \mu\text{m}$  thick. Images of flow tracers were captured with one or two TSI PowerView Plus 2MP cameras at the same time, which have a  $1192 \times 1600$  pixels CCD array. The pixel size

is  $7.4 \times 7.4 \mu\text{m}$ . A pair of Nikon lenses were used with a fixed focal of 50 mm. Also, several values of the Reynolds number were set (see table 2.4 for the test program).

TABLE 2.4: PIV test program

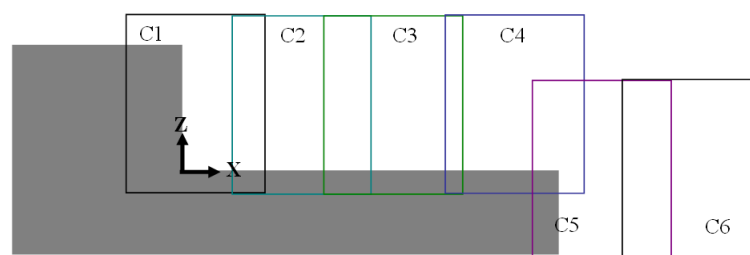
Wind-tunnel and model			Laser			Camera			Raw data		
$Re_h$	$\beta_g$	Position	Plane	$f_{laser}$ [Hz]	pulse sep. [ $\mu\text{s}$ ]	Nb	Position	Aperture	$N_{pairs}$	See figure	
$8 \times 10^4$	0.00	left side	$y/h = 0$	15	25	1	$C_1$	4	535	3.4	
							$C_2$		496		
							$C_3$		468		
							$C_4$		258		
							$C_5$		262		
							$C_6$		423		
$9.75 \times 10^4$	-4.84 -3.95 -2.87 -1.97 -0.86 -0.54 -0.43 -0.32 -0.22 -0.11 0.00 1.78 3.22 -0.22 0.00 0.43 1.29	centered	$z/h = 0.784$	14.5	65	2		5.6	1274	3.10	
			$z/h = 0.5$		40					299	3.6
		manual		1		253	4.2				
		trav. syst.			241						
					275						
					241						
					572						
					559						
					544						
					555						
					938						
					1354						
					257						
		manual			1	1396					
		trav. syst.				610		Hysteresis 4.2			
			528								
			537								
			441								

Using two cameras synchronously was enabled to obtain two instantaneous vector fields over the entire length of the backward cuboid (in that case the number 2 is written in the column *camera Nb* of table 2.4). After recomposition of the two vector fields of the cameras, it was then possible to have one vector field over the whole platform length. Because of the relatively big size of the field, calibration had to be done carefully. That was completed prior to every experiment, by focusing the cameras on a standard  $210 \times 210 \text{ mm}^2$  plane target from TSI that was aligned with the laser sheet. For each experiment, this gave the relation between the object size in pixels in the image and its real size in millimeters in the laser plane. For recomposition issues, the fields of the 2 cameras overlapped, the center on the target belonging to this overlap region (see figure 2.6(b)). Since some points of the target belonged to both fields, it was then possible to give their relative position very accurately (with just a few pixels uncertainty, ie below 1 mm). However, this technique was not used for the measurements in the plane  $y' = 0$  using 6 fields (see figure 2.6(a)): there, the translation of the camera between 2 positions was measured, leading to a higher uncertainty (over 1 mm for C2 and C6 and over 2 mm for C3).

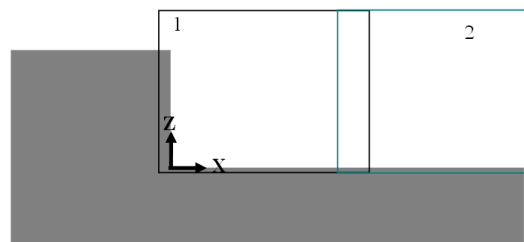
Since the test section is square, for convenience issues, the table on which the model was mounted was either in a vertical position (for measurements in the plane  $y' = 0$  or in a horizontal position for the other measurements. For some measurements in



the plane  $y' = 0$ , the model was closer to the left side wall of the wind tunnel. 'Left side' describes the wind tunnel wall in  $y < 0$  (noted *left side* in table 2.4). The reason was to bring the model closer to the single camera that remained outside the test section increasing the spatial resolution. It also resulted in reduced laser reflections. Laser reflections on the top surface of the backward cuboid caused erroneous velocity vectors computation. Therefore, 6 fields C1 to C6 were needed to map the velocity field over the backward cuboid in the plane  $y' = 0$ . C1 lower left corner was close to the frigate origin whereas that of C4 was closer to the second step face. C2 and C3 were in between. C5 lower left corner was close to the corner of the second step and C6 was obtained after translation of C5 along the  $x$  axis (see figure 2.6(a)). The one



(a) Position of the C1 to C6 PIV fields in the plane  $y' = 0$



(b) Position of the 2 PIV fields in the plane  $y' = 0$

FIGURE 2.6: PIV camera positioning in plane  $y' = 0$

camera higher resolution measurements in the plane  $y' = 0$  were completed by lower resolution 2 cameras measurements in the same plane. As illustrated in figure 2.6(b), the two cameras were positioned aside and acquired images simultaneously. For those measurements, the model was centered on the table (noted *centered* in table 2.4). Unfortunately, laser reflections were stronger than in the 6 fields case. This resulted in false velocity vectors computation within a relatively thick layer over the top surface of the backward cuboid. Therefore, this layer of false vector is partially removed in the results presented in the next chapter. In table 2.4, the time between two pulses (noted *pulse sep.*) was chosen so that a fluid particle would always remain within the interrogation zone during the time separating two pulses. The laser intensity was adjusted with the camera aperture. A higher value of the aperture was preferred to acquire images as clear as possible and ease the processing step (see below). The number of valid

instantaneous fields considered for vector fields averaging is also reported in table 2.4. Measurements in the  $z$  planes were done with 2 cameras acquiring images simultaneously or with 1 camera alone. Their relative positioning is shown in figure 2.7. For some runs, the traverse system to control the drift angle was also used (noted *trav.sys* in table 2.4 or *manual* when the model was placed manually). Except for the last four runs (last four lines of table 2.4), the wind-tunnel was shut down before changing the drift angle. For the last four runs however, the initial position was set manually at  $1.29 \pm 0.1^\circ$ . Then, while the wind-tunnel was still running,  $\beta_g$  was decreased through the translation of the traverse system (see the last four lines of table 2.4).

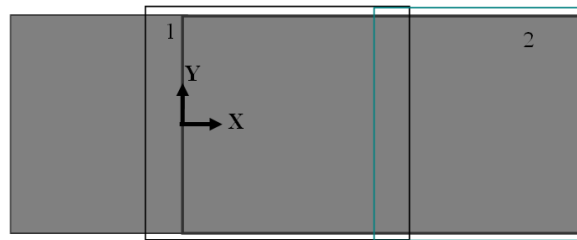


FIGURE 2.7: PIV camera positioning in the  $z$  planes

### 2.2.6.2 Data processing

The Raw images were then processed with different options included within the INSIGHT 3G software [3]. The classic Nyquist PIV grid was used with a 50% spot overlap. Cross-correlation of the two images of a same pair was computed using Fast Fourier Transform. The correlation peak was located using a Gaussian peak engine. For the  $y' = 0$  plane with the 50 mm lens, the interrogation zone was  $16 \times 16$  pixels, allowing thus a spatial resolution of 1.3 mm. For the other experiments, the interrogation zone was  $24 \times 24$  pixels which decreased the spatial resolution to 2.4 mm but also decreased the number of false vectors. A vector was considered locally false when the maximum difference with its reference vector was over 2 pixel units. The velocity components of the reference vector were the median values of the  $3 \times 3$  vectors in the neighborhood. A global validation was also applied by considering false, all vectors which velocity magnitude was greater than 6 times the standard deviation added to the mean velocity. False vectors were replaced by the local mean of the  $3 \times 3$  neighbor vectors using a recursive method. No smoothing of the vectors was applied.

### 2.2.6.3 Data post-processing

**Ensemble averaging and field reconstruction** The vector fields were then averaged in order to obtain the mean velocities and the standard deviation of the velocity. The statistical convergence of those quantities is discussed later on (see appendix B). For measurements in the plane  $y' = 0$ , the averaged fields from C1 to C6 were then put side by side to rebuild a bigger field. A new grid with the same cell size was created and vectors from the new grid were interpolated from vectors of the initial grids using a Krigging method. However, for the other measurements, two cameras were synchronously used giving instantaneous vector fields over the whole top surface of the backward cuboid. Instantaneous vector fields were then put side by side prior averaging. No interpolation was then necessary. For some fields, other statistics moments were computed, such as the Kurtosis and the Skewness. The convergence of such quantities is discussed in more detail in appendix B. Matlab scripts were written especially for this purpose. From the recomposed time-averaged fields, the reattachment length was determined by locating the point where the streamwise velocity close to the wall reaches zero on average. Indeed, the reattachment length is defined as the point where the streamwise friction velocity is zero (see paragraph 1.1.1.3). It can be assumed that the mean streamwise velocity just above the wall also cancels at the reattachment point.

**Turbulence integral length scale computation** A script was also especially written in Python, calling fortran subroutines to compute the autocorrelation coefficients and the turbulent integral length scales from the PIV fields. To decrease the elapsed computational time, the code was parallelized and run on a cluster of 6 cpus. The expression of those physical parameters is developed in chapter 3.

**Coherent structure detection** A script was also thought of for vortex detection. The choice of the detection criteria is also discussed in the next chapter 3.

## 2.3 Campaign at the L2 wind-tunnel

### 2.3.1 Geometries tested

In this campaign, several SFSs models were tested, with  $h = 0.204$  m as defined in figure 2.2(a). Tests were performed on the SFSO', SFSO, SFS1' and SFSC' (see figures 2.2(a) and 1.13 for definition). As a reminder, the prime ' means that the funnel was removed. For some tests, a  $15 \times 15 \times 458$  mm<sup>3</sup> parallelepiped (that is  $0.074h \times 0.074h \times B$ ) was mounted on the top of the central cuboid. It will be referred to as 'perturbator' from now on. It was placed at positions  $x/h = -0.147$  and  $x/h = -0.736$  as seen in figure

2.8. Eventually, one last geometry was tested. It was a regular SFS1' where the central

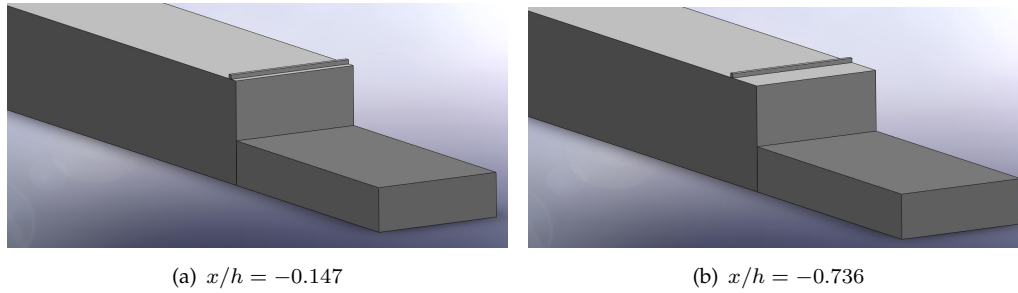


FIGURE 2.8: The two positions of the perturbators on the SFSs

cuboid was shortened along the x axis down to  $1.12h$  (instead of  $7.47h$  for the standard SFS1'). An illustration of this model is given in 2.9. The tests were performed in the L2

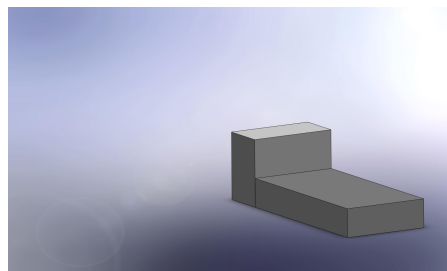


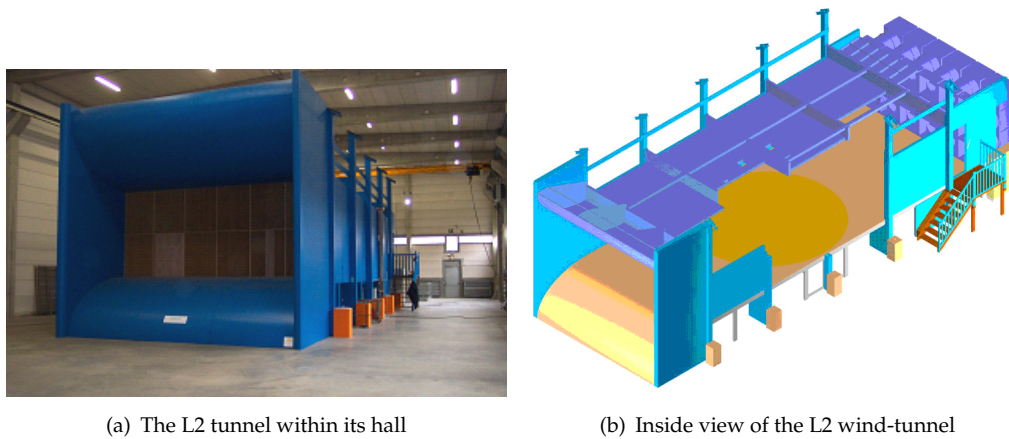
FIGURE 2.9: Definition of the short SFS1'

wind-tunnel.

## 2.3.2 Wind-tunnel

### 2.3.2.1 Overview

The L2 wind-tunnel itself is initially an open loop wind-tunnel. However, since it stands within an industrial hall of  $725 \text{ m}^2$ , the flow that is ejected from the diffuser of the tunnel revolves around the building to be re-injected into the collector. In this respect, some claim it is a closed-loop wind-tunnel (see figure 2.10). The wind-tunnel has a rectangular test-section that is 6 m wide and 2.5 m high that remains constant in size over 13 m in length. At the entry of the tunnel, a collector is mounted. It has the shape of a quarter ellipse 2.5 m long and 1.5 m high. Therefore, the global contraction ratio reaches 1.83:1. The collector is followed by a honeycomb. Downstream of the test section, a small diffuser increases the test section height to 2.8 m in order to leave enough space to fit in the 18 fans. They are put aside in 3 horizontal lines of 6 fans each. The total power installed reaches 125 kW. The fans are controlled by a XBT type programmable automaton. Therefore, every fan can be controlled individually and/or



(a) The L2 tunnel within its hall

(b) Inside view of the L2 wind-tunnel

FIGURE 2.10: The L2 wind tunnel

in pre-defined sequence with other fans, depending on the desired velocity to attain. When the 18 fans rotate at full power, the maximum velocity is 13.85 m/s in the empty test section. It is measured by a pitot tube at 33 cm above the wind-tunnel floor, on the wind-tunnel axis, 1.95 m downstream of the honeycomb. To take into account the effects of the temperature and humidity on the air density, the static pressure as well as the temperature are measured in the undisturbed air in the hall.

A rotating plate (diameter 5.96 m) is integrated into the wind tunnel floor, thus enabling to control the model drift angle. The measured drift angle is set with an over-estimated uncertainty of  $0.1^\circ$ . The center of the rotating plate is at 6.5 m downstream of the honeycomb.

### 2.3.3 Laser tomography visualizations

#### 2.3.3.1 Data acquisition

For the laser tomography visualizations, a similar procedure as the one described in paragraph 2.2.4.1 was conducted. The same laser was also used as in that previous experiment. Only the planes  $z/h = 0.5$  and  $z/h_2 = -0.5$  were visualized ( $h_2$  is the second step height). The smoke was generated by a Safex Nebelsonde NS2. The smoke rod was aligned with the  $x$  axis and the injection was applied on average at the position  $(x/h, y/h, z/h) = (2, 0, 0)$ , from downstream (see figure 2.11). However, to spread the smoke within the whole recirculation area, the rod was moved by the operator at low frequency (below 0.2 Hz) so that its extremity traveled between  $(x/h, y/h, z/h) = (2, -0.5, 0)$  and  $(x/h, y/h, z/h) = (2, 0.5, 0)$ .

A 3CCD SONY DCR VX2000 camera was set on upper wall of the wind-tunnel, at the vertical of the backward cuboid (see figure 2.12). Films between 30 s and 1 minute were

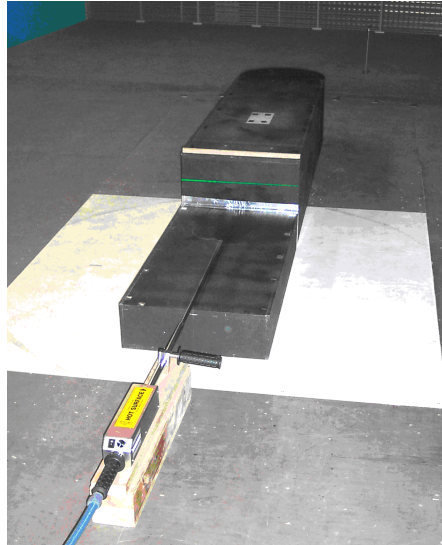


FIGURE 2.11: Smoke injection for the laser tomography visualizations

shot at a 25 Hz frame rate and a 50 ms shutter.

For those tests, only the two first lower lines of fans were switched on while the last

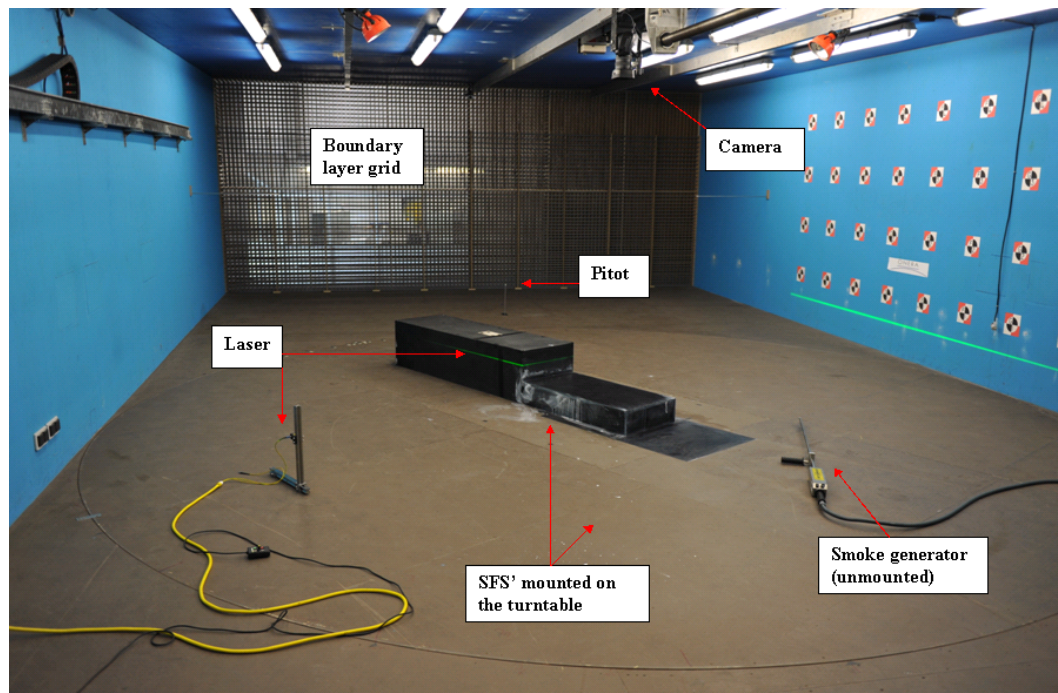


FIGURE 2.12: Position of the camera for laser tomography visualizations

upper line was covered with wooden plates to prevent air circulation through them. This was aimed at lowering the velocity to 8.5 m/s and then ease the laser tomography visualizations.

### 2.3.3.2 Data processing

Movies were saved on miniDV tapes. The tapes were then digitalized in .avi format on a PC via a IEEE 1394 connection and the PINNACLE software. For some movies, all the images were extracted from the .avi file to be processed with Matlab: scripts were written to average all the images of a sequence.

## 2.3.4 Pressure measurements

### 2.3.4.1 Data acquisition

To increase the dynamic pressure of the free stream flow, all the fans were switched on to reach the wind-tunnel maximum free-stream velocity. A PSI ISP8400 device was used to acquire steady pressure signals. It held 6 racks of 16 pressure plugs each. On each rack, 1 plug had to be free to host the static pressure (noted  $p_{ref}$  later on):  $p_{ref}$  was common for each rack and measured inside the test section, on the left lateral wall at position  $(x/h, z/h) = (0, -0.5)$ . The 90 remaining plugs were used for measurements and placed on the model as follows: 90 pressure taps were set on the central and backward cuboids of the tested SFSs. 26 of them were allocated to the lateral sides (13 taps for each sides- see figure 2.13(c)), 12 to the top of the central cuboid (see figure 2.13(a)) and the remaining (52) to the top of the backward cuboid (see figure 2.13(b)). The signals acquired were directly sent to the PC, using the VEE software for processing. The Agilent E1510A software was used to program the acquisition devices. For each test and for each of the 96 pressure taps, 100 data were acquired at 10 Hz. There are two reasons to think this value is enough to estimate the average pressure: (i) a datum was actually already an average of 10 measurements acquired at intervals of 0.1 ms. The actual number of data is then 1000 (ii) 3 m long silicon tubes connected the taps to the acquisition device. There was then, a priori, a big damping effect of the fluctuating pressure signals so that roughly only the time-averaged signal remained. The choice in the sampling parameters is discussed in appendix B.

Prior to starting the campaign, every pressure tap was individually qualitatively tested to verify that none of them was improperly plugged. Also, the PSI 8400 ISP device integrates a calibration system enabling to automatically determine the coefficients of each pressure sensor. Indeed, the generated calibration pressures are measured by a reference sensor within the device. Therefore, the sensors were calibrated twice a day thanks to this standard sensor and the integrated calibration system. Eventually, prior to each measurement, data were acquired with no free-stream velocity in order to have

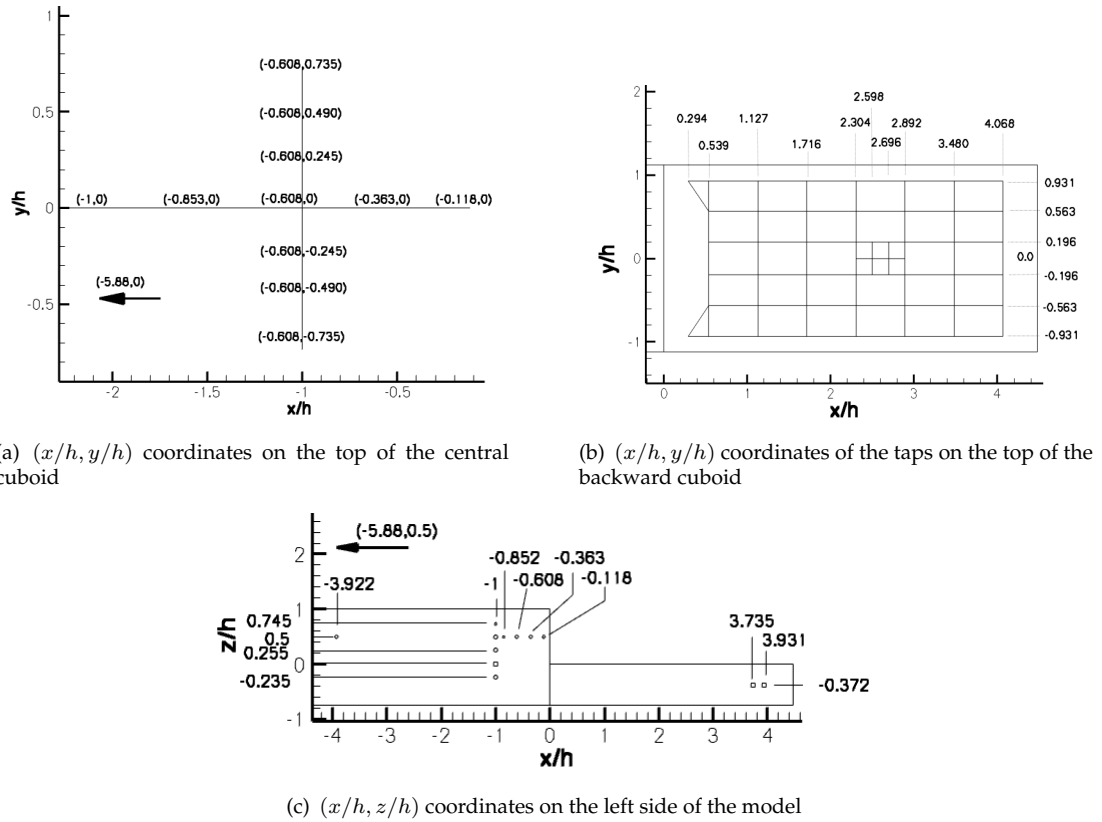


FIGURE 2.13: Position of the pressure taps

a map of 'zeros' (the exponent  $z_1$  will describe this phase). Similarly, the 'zeros' were acquired after each measurement (described by exponent  $z_2$ ).

### 2.3.4.2 Data pre-processing

As a results, pressure coefficients were defined as

$$C_p = \frac{p_i - p_{ref}}{1/2\rho U_0^2} \quad (2.3)$$

In equation 2.3,  $U_0$  is the velocity deduced from the pitot tube measurements and  $p_i$  is the corrected pressure measured at position i, namely  $p_i = p_i^{meas} - 0.5(p_i^{z_1} + p_i^{z_2})$ .  $p_i^{z_1}$  and  $p_i^{z_2}$  are the pressure coefficients measured at position i before and after the run respectively, with  $U_0 = 0$ . The time-average values of  $C_p$  were computed for the 90 locations and mapped using the Tecplot 360 software. Since the blockage coefficient for drift angles between  $-5^\circ$  and  $5^\circ$  was below 2%, no correction as described in Cooper [41] was applied.



### 2.3.5 Atmospheric boundary layer probing

In this section, the reference height is the full-scale equivalent 10 m above sea level. This corresponds to 33 cm above the wind-tunnel wall in the present study.

In order to simulate an atmospheric boundary layer, plastic tubes are lined up horizontally just downstream of the honey comb (see picture 2.12). Their spacing and number has been chosen in order to simulate a mean velocity profile representative of a marine atmospheric boundary layer. Since this profile characterizes the wind-tunnel, it is described in this section. As shown in figure 2.14(a), the velocity profile is well approximated by a  $1/8.5 = 0.12$  power law in most of the height range. This is not far from the generally accepted power coefficient between 0.10 and 0.11 for a marine boundary layer [42, 52, 81].

The turbulence profile in figure 2.14(b) shows values up to 7.6 % close to the wall. This is to compare to the range  $8.3 \leq I_u \leq 10.9$  % at  $z = 10$  m derived from Raupach et al. [139]. Those values depend on the wind-speed. In the wind tunnel,  $U(z_{10}) = 8.5$  m/s for the present profiles drawn. For this velocity, at higher altitude ( $z = 30$  m), Türk and Emeis [177] measured turbulence intensities around 6 %. The turbulence levels in L2 are then between the two. The former profiles were obtained at the vertical of the

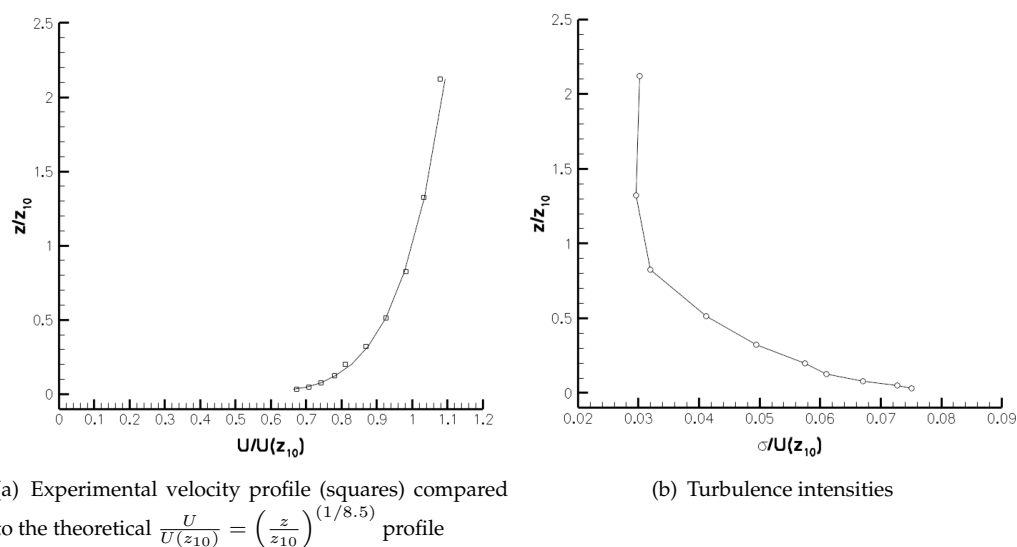


FIGURE 2.14: The L2 wind tunnel simulated atmospheric boundary layer

center of the turntable with a single normal hot-wire probe.  $N_s = 2^{19}$  were acquired at each location at  $f_s = 2^{11}$  Hz. The uncertainty on the estimate of the true mean and mean square values is discussed in appendix B.

## 2.4 Campaign at the mini wind-tunnel

### 2.4.1 Model

The SFSC' (SFSC in figure 1.13(c) with the funnel removed) was the only model tested. It had a step height of 14.57 mm (see figure 2.2(a) for the other dimensions). It was placed on a small  $x \times y$  mm<sup>2</sup> tablet whose leading edge was rounded. The origin of the SFSC' was set on its centerline and 15 mm from the tablet leading edge. The tablet was mounted on a rotating device that could control the drift angle with an estimated 0.1° accuracy (see figure 2.15(a)).

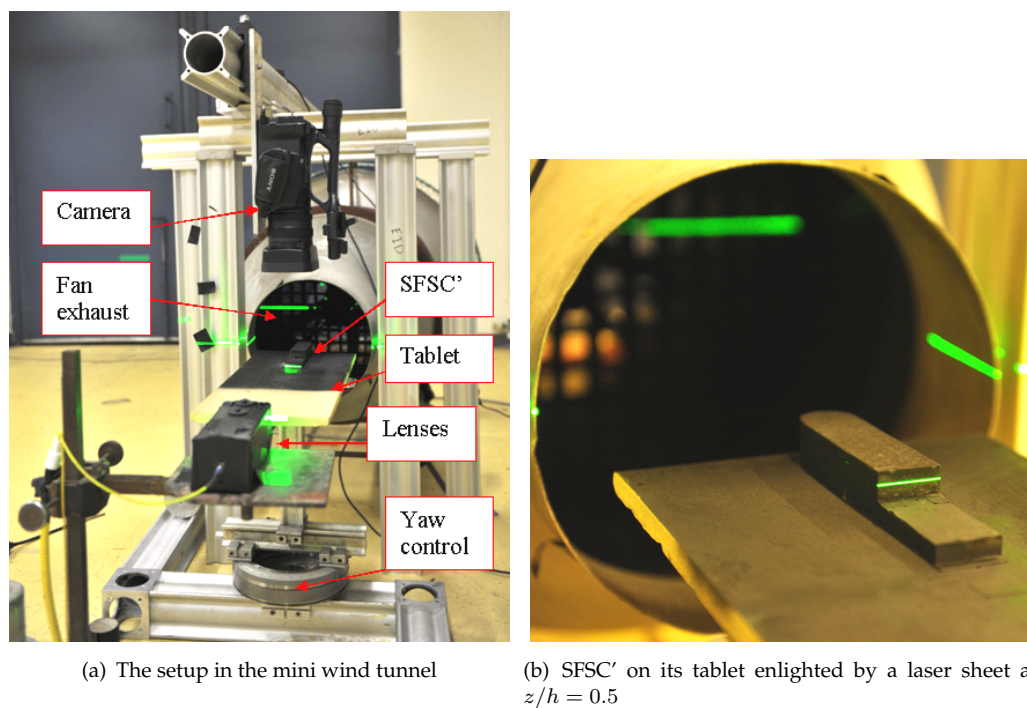


FIGURE 2.15: The mini wind tunnel

### 2.4.2 Wind-tunnel

The mini-wind tunnel has an open test section: in the mainstream direction, the fluid particles encounter first the fan, then a honeycomb, then a contraction vein (with a 2:1 contraction ratio) and eventually the exit, where the model is placed (that is, the model is within a jet-like flow). The velocity profile was determined using the TSI velocicalc, model 8386. This enabled to measure the average, min and max velocities at 30 different locations on the horizontal diameter of the fan, 35 mm ( $= 0.12D$ ,  $D$  being the diameter

of the fan exhaust) downstream from the exit as shown in figure 2.16(a). 15 samples were acquired every 2 seconds. The resulting velocity profile after a power fit is shown in figure 2.16(b). It is similar to a typical jet flow, with the maximum velocity appearing on the wind-tunnel axis. There is therefore a velocity gradient along the width of the model when it is placed on the wind-tunnel axis. The flow is consequently known not to be uniform.

The turbulence intensity was lower than 2.4%. Eventually, as discussed in more detail in appendix B, the number of samples acquired is enough to obtain the mean value with an estimated average uncertainty (due to sampling) of less than 2%. To this uncertainty, must be added the uncertainty in the measurement itself of 3% as announced by the manufacturer. The bars in figure 2.16(b) show the global uncertainty in the velocity measurement. The mainstream velocity was 6.05 m/s at the centerline resulting in a

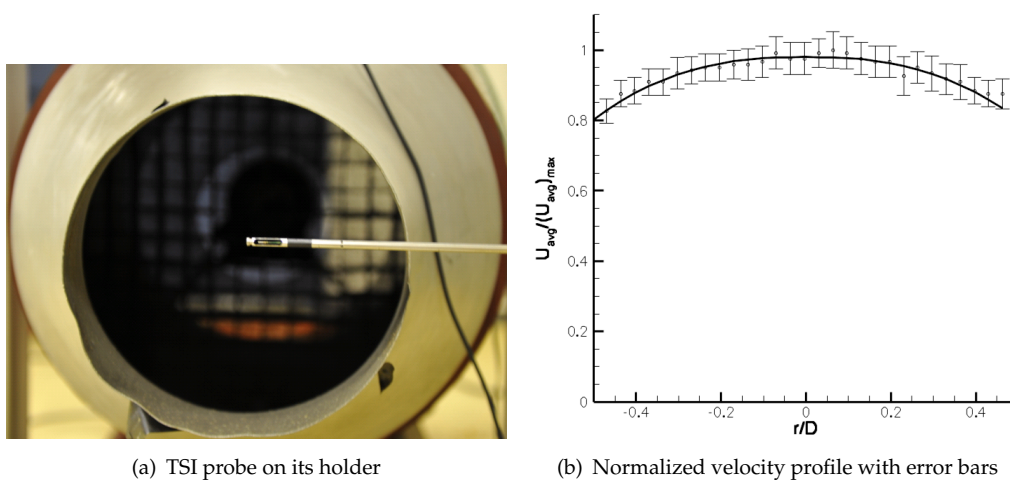


FIGURE 2.16: Probing the mini wind tunnel

Reynolds number  $Re_h = 5.9 \times 10^3$ . In those conditions, smoke visualizations confirmed that the flow did not separate at the tablet leading edge.

## 2.4.3 Laser tomoscopy visualizations

### 2.4.3.1 Data acquisition

As for the experiments described in 2.3.3 the same laser was used to light the flow in the planes  $z/h = 0.5$  and  $z/h_2 = -0.5$  (see figure 2.15(b)). However, two special lenses mounted in a  $200 \times 75 \times 70 \text{ mm}^3$  box and placed just downstream of the tablet were used to generate a very thin laser sheet (figure 2.15(a)).

A negligible mass rate of smoke was injected within the recirculation bubble of the first step, close to the origin of the model. To do so, a small hole ( $\approx h/10$  in diameter) was

drilled through the second cuboid on the centerline, at  $(x/h, y/h, z/h) = (0.45, 0, 0)$  and the smoke pipe was injected from underneath the model. The smoke was produced by Rauchröhrchen smoke tubes from MSA AUER, reference 5019-701, 10065254. Finally a SONY HDR-FX1000 camera was set at the vertical of the backward cuboid (see figure 2.15(a)). Films over 1 minute long were shot at a 25 Hz frame rate and a 250 ms shutter.

### 2.4.3.2 Data processing

Just as for the previous experiments 2.3.3, movies were saved on miniDV tapes. The tapes were then digitalized in .avi format on a PC via a IEEE 1394 connection and the PINNACLE software. Then, all the images were extracted from the .avi file to be processed with python scripts, especially written for this processing and detailed in chapter 4.

## 2.5 Numerical approach

### 2.5.1 Geometry and mesh

A volume of fluid of  $14 \times 2 \times 1.23 \text{ m}^3$  to represent the flow around the SFS1' on its table (figure 1.13(a), funnel removed) was meshed. The model was mounted and centered at  $0^\circ$  drift angle on the lower wall representing the table used for the TEMPO experiments (see section 2.2). However, it was chosen to increase by a factor of three the table length. Choosing a long computational domain was aimed at easing the dissipation of the flow structures in the wake of the steps during their advection and therefore ease computation convergence. The beginning of the mesh started at the beginning of the central cuboid of the SFS1'. The 5 blocks structured mesh was generated with icem cfd, generating 5.6 million cells. The boundary layers on the table and on the faces of the model (except for the step faces) were meshed for Navier-Stokes computations with 33 vertices and with the distance  $d_1$  to the non-slip walls of the first vertex verifying  $d_1^+ = \frac{d_1 \times u_\tau}{\nu} \leq 1$ .

### 2.5.2 Computation parameter

The ONERA code elsA was used for this computation. As described in Cambier and Veillot [31], it can solve the time dependant compressible RANS equations with various turbulence models on structured meshes. Here, the mesh was generated in order

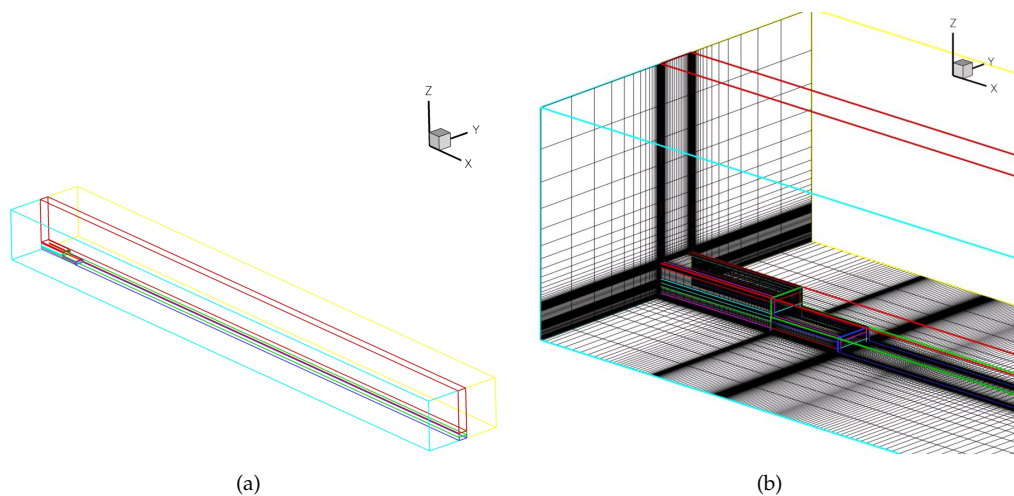


FIGURE 2.17: (a) The computing domain, (b) the structured mesh

to accomplish a RANS computation with the Spalart-Allmaras turbulence model [164]. Therefore, particular boundary conditions required by the turbulence model and the code had to be set: a slip condition was applied to the 3 lateral walls as well as the upper wall of the domain whereas a non-slip condition was applied to the model walls and to the table it was mounted on. A condition on global mass flow conservation at the outlet was applied. The reader should refer to Lazareff [102] for a full mathematical description of those conditions. Eventually, at the entry of the domain, several values were imposed as noted in table 2.5. The turbulence level was chosen following the work of Spalart and Rumsey [165]. The flow was initialized by setting in every cell of

TABLE 2.5: Upstream conditions imposed at the entry of the computational domain

Parameters	Dimension	value
Mach number	[-]	0.2
Total pressure	[Pa]	101325
Total temperature	[K]	300
Turbulence	[-]	$8.2 \times 10^{-4}$
$\nu_t/\nu$	[-]	0.7

the domain the values exposed in table 2.5.

Regarding the numerical resolution of the equations, since the discretized compressible equations are solved, to limit convergence issues, the Mach number was greater than for the experiments. A preconditioning condition was also imposed. Furthermore, a cutoff factor of  $10^{-6}$  was applied to the turbulent viscosity to exclude any negative values. The second order accurate centered scheme from Jameson was used for the spatial discretization whereas the first order backward Euler scheme was applied for the temporal discretization (see Hirsch [77] for more details). The Courant-Friedrichs-Lewy condition was set at 10.

### 2.5.3 Computation convergence

The computation was performed on a single NEC SX-8R processor. It was stopped after 2200 iterations performed in multigrid mode over 3 grids. At that time, the residuals had decreased by 3 orders of magnitude as illustrated on figure 2.18. It was verified

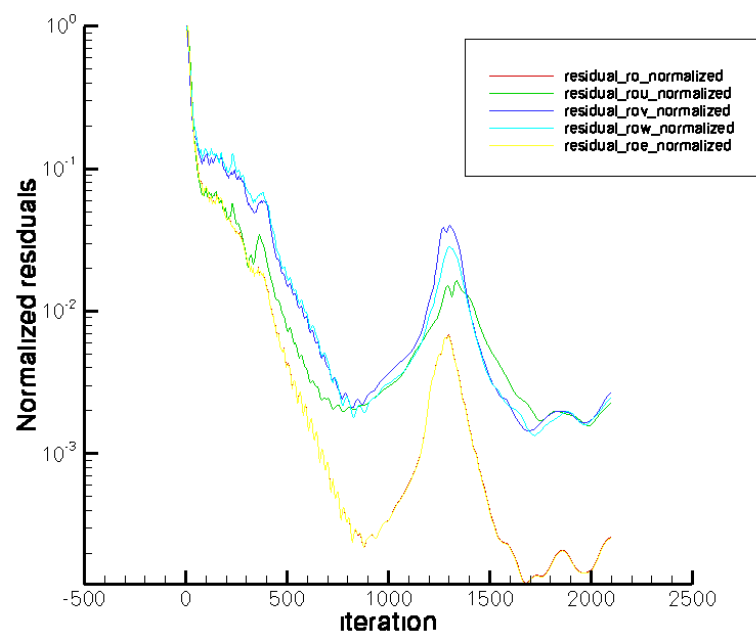


FIGURE 2.18: Evolution of the residuals against the number of iterations performed

that the flow was smooth in the vicinity of the outlet.

The data computed were then processed and analyzed with Tecplot.



## Chapter 3

# Flow description downstream of a 3D double backward facing step at zero degree sideslip

The first step for the study of the aerodynamics of a 3D backward facing double step was to get a better understanding of the flow behind the step. The experimental study was first expected to give a description of the mean flow. In particular, the goal was to see if the asymmetry mentioned in section 1.4.3 ([170]) could also be observed under specific conditions. Then, intentions were to complete the very few studies of other authors on the unsteady flow. To do so, a specific simplified geometry was designed to obtain upstream of the first step a flow as uniform as possible. Then, the model was tested in the TEMPO subsonic wind-tunnel using qualitative flow visualizations (laser tomography and oil-flow visualizations) as well as quantitative PIV velocity field measurements. The data set was completed by hot-wire anemometry measurements. Data could then be processed to extract the main statistics of the flow as well as some of its unsteady features.

### 3.1 Geometry design

#### 3.1.0.1 Aims

In order to compare the results with other authors (see 1.4), the geometry had to be similar to the existing simplified frigate shapes. However, the issue with the regular SFS1, SFS2 and SFSC (see figure 1.13) lies in the nose shape and the presence of a funnel. Indeed, as shown by smoke visualizations in Cheney and Zan [38], the flow



massively separates around the funnel of the SFSs. So is the case at the bow of the SFS1 [38], the SFS2 [64] and, to a smaller extent, on the upper face of the nose of the SFSC [171]. Those separations lead to mean velocity defect, vortex shedding and high levels of turbulence. This breaks the uniformity of the flow upstream of the first step which complicates the understanding of what happens downstream of the first step.

Solutions were then looked for in order to obtain a flow as uniform as possible upstream of the first step. In this respect, ideally no perturbation from upstream would influence the flow behind the step and the aerodynamic phenomena resulting from the step could be isolated.

### 3.1.0.2 Approach

The simplest change was to remove the funnel which is a great source of perturbation. Then, attention was paid to other main sources of perturbations, namely the nose and its surroundings. Several geometries were therefore designed and their properties were checked and compared through CFD simulations. However, only the retained geometry, the SFSO', is described here.

On the SFS1 and SFS2, the massive flow separation results from the bluff aspect of the nose. A streamlined nose is then required. The rounded nose of the SFSC is a good solution for the side wall flow but this geometry induces a sharp edge on the top surface, leading to flow separation. A geometry was then conceived to have at constant  $x$  sections the same pressure on each side of the model. This required having the sides of the nose open with the same angle. This angle was chosen equal to  $11^\circ$  to find a compromise between a short model (requiring a wide open angle) and limited flow separation at the joint nose/central cuboid (requiring narrower open angle). However, if the model was directly wall-mounted into the wind-tunnel, (i) it would be immersed within the few centimeters thick boundary layer developing on this wall and (ii) the symmetry within the flow would be broken since it could not go over and under the model in a similar manner. This could be overcome by using a table: by mounting the model at the leading edge of the table as shown in figure 2.2(b), the flow can also escape under the model, between the wind tunnel wall and the bottom of the table. This should ensure a relatively symmetric flow on all sides of the model. To remove the model from the boundary layer developing on the wind tunnel wall, the table was stepped up by 750 mm, that is  $3/8$  of the test section height. This is more than necessary but it was thought useful to manipulate the model.

To isolate the flow behind the step, it was tried to limit the influence of the parameters discussed in section 1.3.2 (Reynolds number, blockage coefficient, free-stream turbulence, etc.). Therefore, the Reynolds number was chosen sufficiently high (over  $5 \times 10^5$

based on the length of the central cuboid) to ensure the development of a turbulent boundary layer on the sides of the model [156] and therefore limit Reynolds number effects. Also, the blockage coefficient was kept small (below 2%). As for the free stream turbulence, the TEMPO wind-tunnel was chosen to remove the influence of high turbulence levels on the flow. The choice of this geometry is not to be a high fidelity representation of the full-scale flow, but a simplified shape aimed at understanding the aerodynamics of the 3D backward facing double step. The flow was then probed to check the validity of the design.

### 3.1.0.3 Experimental validation

In order to see if the nose shape and the table were well-designed to produce a relatively uniform flow upstream of the first step, oil-flow visualizations were performed as well as a hot-wire probing of the boundary layer.

**Oil flow visualizations** As exposed in section 2.2.3, they were conducted at  $Re_h = 3.58 \times 10^5$ . To see if the friction lines were well-aligned with the model centerline and if no streamwise vortices were generated at the edges of the central cuboid, oil was spread all over the central cuboid and the nose. The results show at about  $0.196 h$  downstream of the beginning of the central cuboid that the oil draws on each face of the model a line normal to the  $x$  axis (see the pink line on figure 3.1(a)). Upstream of this line, the oil is relatively uniformly spread like on the nose, whereas downstream of this line, white lines along the  $x$  axis can be seen. It is not obvious that this represents a reattachment line. Therefore, those visualizations do not confirm that the flow separates at the joint between the nose and the central cuboid. However, those results (see figure 3.1(b)) show that the oil trajectories are along the  $x$  axis around the edges of the central cuboid. Therefore, there is no solid evidence of mean edge vortices. The mean flow seems to be relatively smooth on the three faces of the body.

To complete those tests, the flow in  $x/h = -0.13$  plane was visualized by means of

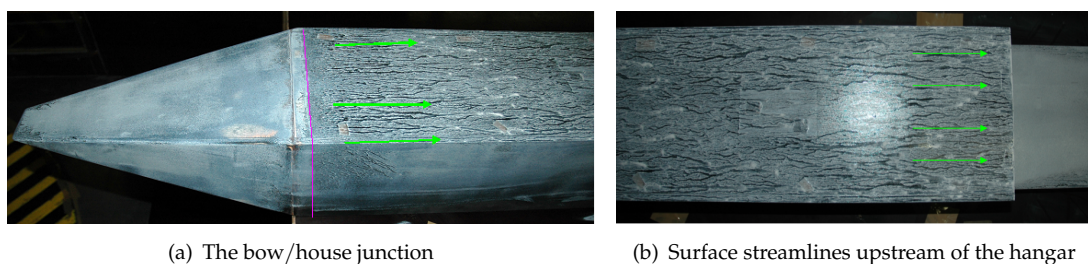


FIGURE 3.1: Oil visualizations over the central cuboid of the SFSO'

laser tomography. The video shot in this plane seems to show random turbulence at

the edges. The video is a succession of images such as that in figure 3.2. Those vi-

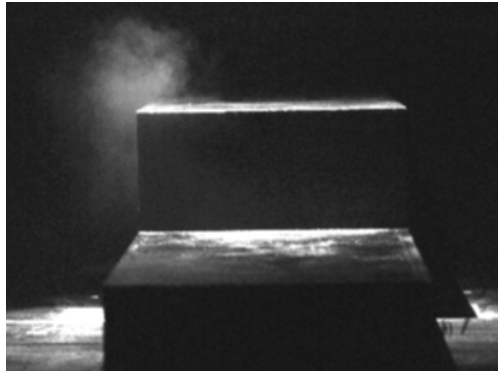


FIGURE 3.2: Flow visualization in the plane  $x/h = -0.13$

ualizations do not show any strong streamwise vortices at the edges: because of the centrifugal force of such vortices, the smoke would be ejected from the vortex core which would be characterized by a black hole in the video.

Eventually, the oil flow and laser tomography visualizations seem to confirm qualitatively that the flow upstream of the first step is relatively uniform. This is partially verified quantitatively.

**Quantitative characterization of the upstream boundary layer** To quantify the effect of the nose and the table on the quality of the flow, the boundary layer was probed with a single hot-wire anemometer normal to the side of the central cuboid. The time-averaged velocity profile obtained is not too far from what is observed in a turbulent boundary layer developing on a flat plate, namely in a zero-pressure gradient turbulent boundary layer [60].

Those oil flow visualizations and boundary layer probing thus seem to confirm that the nose and the table enable to generate a relatively uniform flow upstream of the first step. To confirm this in a more rigorous manner, more locations within the lateral and upper boundary layers should have been probed with the hot-wire, or even PIV should have been applied extensively. However, the point was more to confirm that the geometry did not induce vortices or extra turbulence upstream of the step. It is then possible to focus on the time-averaged and unsteady features of the flow downstream of the step.

### 3.2 Time-averaged flow

There are several ways of probing the time averaged-flow. In the following section, the oil-flow visualizations and PIV measurements are presented.

### 3.2.1 Oil flow visualizations

A first step is to characterize the mean recirculation area. It was expected that oil-flow visualizations could give information regarding the reattachment length and general flow topology, vortex apparition (etc.) behind the step. There is a limit to the method though: the flow pattern on the face of the step (that was vertical) will not be interpreted. Indeed, as seen in chapter 1, the velocities there are expected to be smaller than 20% of the value of the upstream velocity. A quick estimate shows that the friction stress on a particle of oil spread on the vertical face has about the same intensity as the gravity force. Therefore the pattern is not representative of only the friction forces. However, this is not the case on the horizontal surface of the backward cuboid. The flow pattern is then interpreted on the upper face of the backward cuboid. The result is shown on figure 3.3, green lines show surface streamlines. The arrows show the mean direction of the flow just above the surface. Those arrows diverge on either side of the pink lines, whereas they converge towards the blue lines. In those figures, lines are noted L. Some singular points where the shear stress and the velocity are zero are noted S (see [193] for singular points classification). Vortex footprints are noted V and zones delimited by lines are noted Z. The main zones, as described in section 1.4.2, are found here: in zones Z4 to Z6, the flow coming from the shear layers go away from the first step. In zones 4 and 5, the lateral shear layers are curved towards the body centerline. However, the friction lines go away from it. This might be the consequence of streamwise corner vortices. The recirculation bubble in Z1 is also observed. It is parabola shaped. The parabola summit is not very well defined, probably due to the airflow unsteadiness just above the top surface of the backward cuboid. It is estimated, with an uncertainty lower than 10%, to be around  $X_R/h = 2.8$ . Within the recirculation bubble, in zone Z1, backflow goes from the reattachment region towards the first step. A very slight asymmetry is visible, with the vortex V1 (centered in  $(X_{V_1}/h, Y_{V_1}/h, z/h) = (0.4, 0.5, 0)$ ) being slightly bigger than the vortex V2. This was thought to be the consequence of the not perfectly zero drift angle (it was actually set at  $\beta_g = -0.21$ ). The center of the vortex V2 is not as easy to locate as for  $V_1$ . Eventually, considering the singular points classification of Hunt et al. [82], it seems like there are two attachment nodal points which are foci ( $V_1$  and  $V_2$ ) and a nodal non-foci attachment point (at reattachment). S1 and S2 seem to be two separation saddle points. In zone Z7, there might be a saddle attachment point. The other singular points (if they exist) are difficult to detect. A summary of the vortex characteristics at the wall is given in table 3.1. When reaching the step face,

TABLE 3.1: Some features at the surface of the flow behind the first step

$Re_h$	$X_R/h$	$X_{V_1}/h$	$Y_{V_1}/h$	$D_1/h$	$X_{V_2}/h$	$Y_{V_2}/h$	$D_2/h$
$3.54 \times 10^5$	2.8	0.4	0.5	0.3	0.4	-0.6	0.3

the flow seems to separate: some of it revolves around the vortex V1 whereas the rest is enrolled around V2. Flow in zone Z7, just at the corner of the first step, also seems to be going away from the step face, towards the recirculation zone before bifurcating towards vortices V1 or V2. Is this zone Z7 the footprint of a secondary bubble as can be seen behind other bluff bodies (see chapter 1)? Other information must be gathered to have a better understanding of the 3D flow topology. Therefore, PIV measurements were conducted.

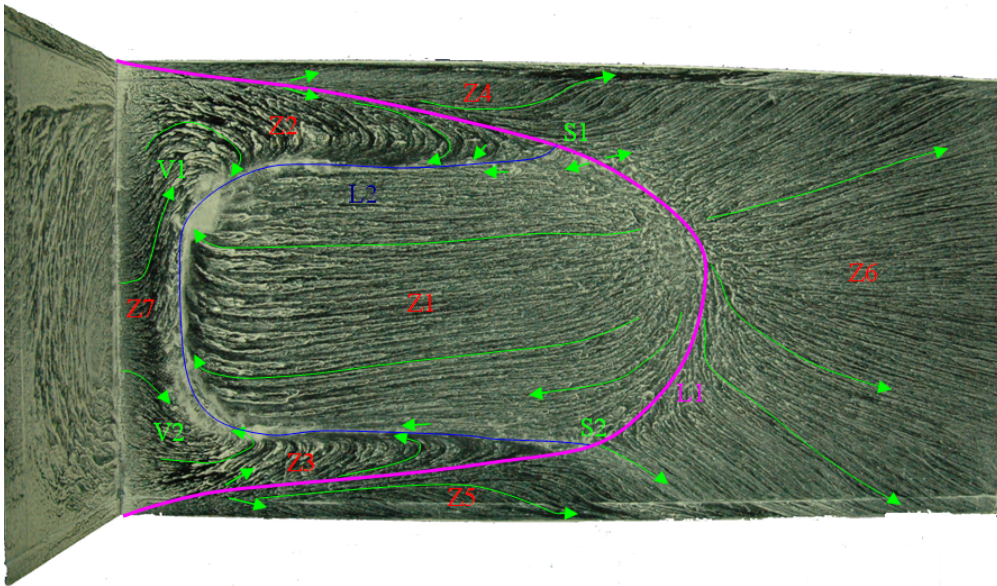


FIGURE 3.3: Surface oil flow visualization on the top surface of the backward cuboid

### 3.2.2 PIV measurements

Based on the literature overview (see chapter 1), because of the presence of the recirculation bubble and of the arch vortex on such bluff bodies, it was thought that the most interesting information would be obtained through the plane of symmetry ( $y/h = 0$ ) and in its normal plane slicing the first step mid-height ( $z/h = 0.5$ ). Those planes were then probed.

#### 3.2.2.1 Plane of symmetry of the model $y = 0$

The oil visualizations suggested the existence of a secondary bubble. The time-averaged description of the  $y = 0$  plane could confirm this. Studying this plane should also reveal the position of the reattaching point, the upper shear layer and the recirculation bubble in general. Therefore, a high resolution global field was obtained from 6 smaller fields as explained in section 2.2.6. The streamlines in figure 3.4 confirm the existence of

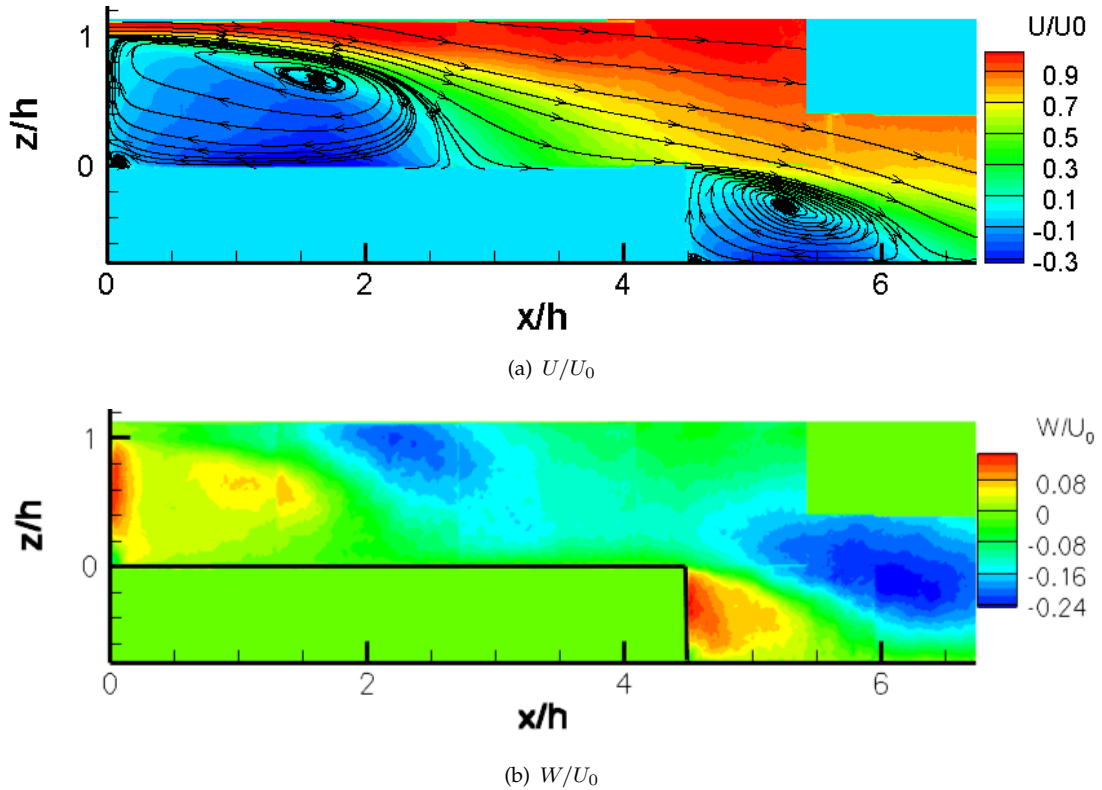


FIGURE 3.4: Streamlines and streamwise and spanwise velocity contour levels in the high resolution  $y' = 0$  plane at  $Re_h = 8 \times 10^4$

such a secondary bubble at the corner of the steps. From those fields, the flow topology behind the first step shows a primary and secondary recirculation bubble: as for the 2D step 1.1, the flow separates at the upper corner to form a slightly curved shear layer where high streamwise velocity gradients are found. To give an idea of the strength of this gradient, the velocity goes from  $U/U_0 = 0.09$  at  $(x/h, z/h) = (0.2, 0.95)$  to  $0.92$  at  $(x/h, z/h) = (0.2, 1.05)$ . As a consequence, this will certainly be a region of high unsteadiness as it will be described later. The shear layer closes to the recirculation bubble by showing a sharper curvature towards the wall. There, outside the shear layer, in a region centered on  $(x/h, z/h) = (2.3, 0.9)$ , the downward velocities consequently reach high values, up to 22% of the upstream velocity (see figure 3.4(b)). This leads to local mean flow angles with the wall of up to  $-13^\circ$ . The shear layer eventually impinges the wall at the reattachment zone. The reattachment zone separates the flow going away from the step with the flow going towards the step. As a matter of fact, the backward flow within the recirculation bubble reaches high velocity values, as high as 35% of the upstream velocity. The recirculation bubble can therefore not be named as a dead zone (see section 1.1).

This description of the flow behind the first step can qualitatively be made behind the second step. However, quantitatively, the reattaching length and the position of the centers of rotation of the bubbles are quite different behind the two steps (subscripts  $F_1$

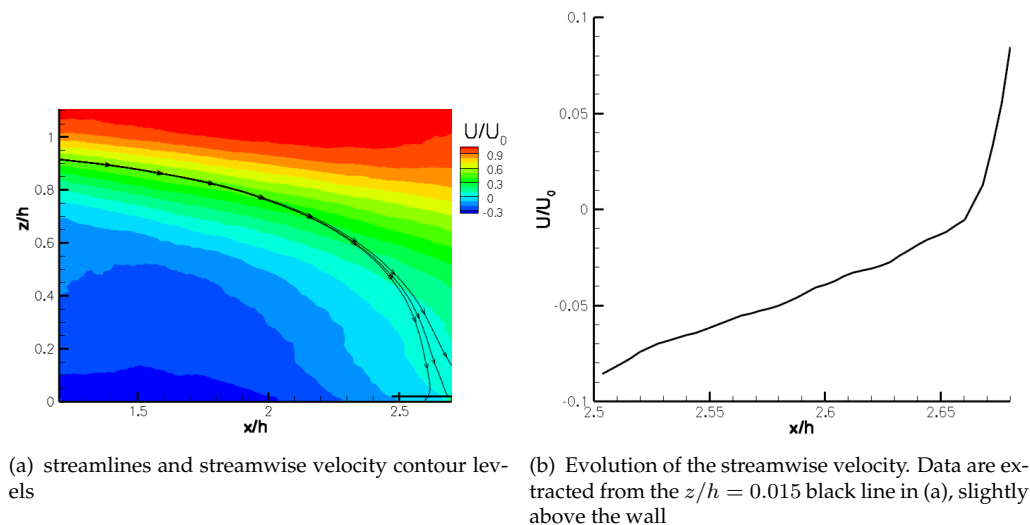


FIGURE 3.5: Determining the reattachment length behind the first step  $Re_h = 8 \times 10^4$

and  $F_2$  respectively stand for the primary and the secondary bubbles and  $X$  and  $Z$  are the coordinates of the centers). This is shown in table 3.2: in particular, the recirculation bubble is bigger behind the first step. This difference on the reattachment lengths is not explained by the measurement uncertainty though, since it is estimated around 0.02 h. Furthermore, the value obtained through this method, as illustrated in figure 3.5(b), matches that obtained through the oil flow visualizations 3.1. The difference behind both steps can be explained by the different upstream conditions and geometries. Indeed, the lengths obtained here are somewhat higher than all the other reattachment lengths obtained by the other authors (see chapter 1) in different conditions. The geometry shape is most probably directly responsible for those differences.

TABLE 3.2: Characteristics of the recirculation bubbles behind both steps

Step	$Re_h$	$X_R$	$X_{F_1}$	$Z_{F_1}$	$X_{F_2}$	$Z_{F_2}$
Step1	$8 \times 10^4$	2.66 h	1.629 h	0.668 h	0.096 h	0.043 h <sub>2</sub>
Step2	$8 \times 10^4$	$L + 2.36 h_2$	$L + 1.05 h_2$	$(-1 + 0.593) h_2$	$L + 0.092 h_2$	$(-1 + 0.024) h_2$

To have a better understanding of the whole flow topology, in particular the shape of the recirculation bubble in space, the constant  $z$  planes were then analyzed.

### 3.2.2.2 Constant $z$ planes

A first plane was probed at  $z/h = 0.784$ , which is of interest for the issue of helicopter launch and recovery since the rotor plane can be at this height (figure 3.6). Since the streamlines do not wind up in any way, this suggests that the  $z/h = 0.784$  plane does not slice the arch vortex legs. However, since the streamlines are not monotonic,

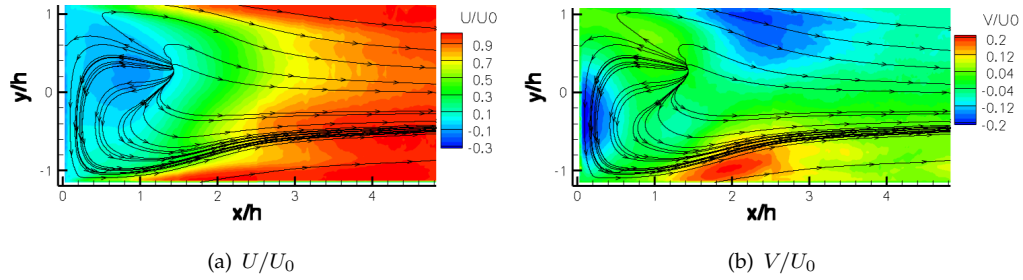


FIGURE 3.6: Streamlines and velocity contour levels in the plane  $z/h = 0.784$ ,  $Re_h = 9.75 \times 10^4$

the  $z/h = 0.784$  probably slices the top of the arch vortex. This means that the latter stretches between  $z/h = 0$  and a little higher than  $z/h = 0.784$ . A lower plane must be analyzed though to check when the legs are sliced. It should also be mentioned that the streamlines in this plane do not draw a symmetric pattern which reveals some asymmetry of the time-averaged flow. This justifies the study of other constant  $z$  planes.

In the plane  $z/h = 0.5$  (see figures 3.7(a) and 3.7(b)), the mean flow topology can first be described by two shear layers downstream of the edges. This is to be compared with cylinder flows 1.2.1. The shear layers are also curved towards the centerline, generating spanwise velocities (oriented towards the centerline) reaching values up to 20% of the upstream velocity. The highest values are concentrated in two regions outside the shear layers, centered around  $(x/h, y/h) = (2.4, 0.89)$  and  $(x/h, y/h) = (2.4, -0.96)$ . This leads to local mean flow angles (with the centerline) of up to  $18^\circ$  (in absolute value), which can be relevant for the issue of launch and recovery. However, the velocities are not symmetrically distributed, as shown by the asymmetric contour levels of those figures. This feature is more than striking when the streamlines are drawn (see figure 3.7(c)). Even though the geometric drift angle is zero, the time-averaged flow is far from the expected symmetric solution. The phenomenon observed here is probably of the same kind as the asymmetry described on the SFS2 by Syms [170] and detailed in section 1.4.3.

This mean flow asymmetry is characterized by different shapes and sizes of the mean vortices: considering the notations of figure 3.3, one big vortex ( $V_2$ ) is seen on the  $y < 0$  side of the image (located at position  $(X_{V_1}/h, Y_{V_1}/h)$ ) whereas a narrower but stretched one ( $V_1$ ) is seen on the other side ( $y > 0$ , located at position  $(X_{V_2}/h, Y_{V_2}/h)$ ). Even if  $V_1$  is not circular, a diameter  $D_1$  is defined for this vortex as its width. For  $V_2$ , its diameter is just twice the distance between the center of  $V_2$  and the step face. Those values are reported in table 3.3. It should be mentioned that the vortices observed in the plane  $z/h = 0.5$  are slices of the mean arch vortex. Two remarks follow this: (i) in parallel with figure 3.6, it is eventually assumed that the beginning of the top region of the arch vortex extends between  $z/h = 0.5$  and  $z/h = 0.784$  as illustrated in figure 3.8. (ii) The



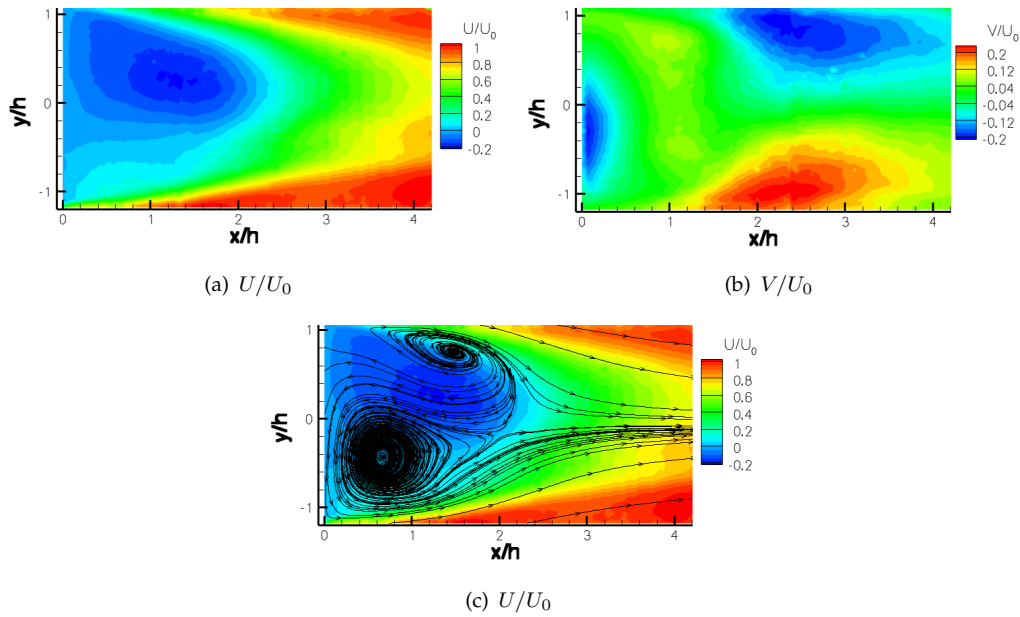


FIGURE 3.7: Streamlines and velocity contour levels in the plane  $z/h = 0.5$ ,  $Re_h = 9.75 \times 10^4$

TABLE 3.3: Characteristics of the vortices in the plane  $z/h = 0.5$

$Re_h$	$X_{V_1}/h$	$Y_{V_1}/h$	$D_1/h$	$X_{V_2}/h$	$Y_{V_2}/h$	$D_2/h$
$9.75 \times 10^4$	1.485	0.748	0.48	0.666	-0.429	1.32

center of  $V_1$  is quite similar in the plane  $z/h = 0.5$  as in the plane  $y = 0$  (see table 3.2). However, there is a strong offset with the position of  $V_2$  in the plane  $z/h = 0.5$ . This is more easily visualized in the 3D image of the flow in figure 3.9 : the left leg of the arch vortex must be steeply inclined to link the centers in the  $z/h = 0.5$  and  $y = 0$  planes.

This time-averaged analysis reveals the mean topology of the flow. Features of the arch

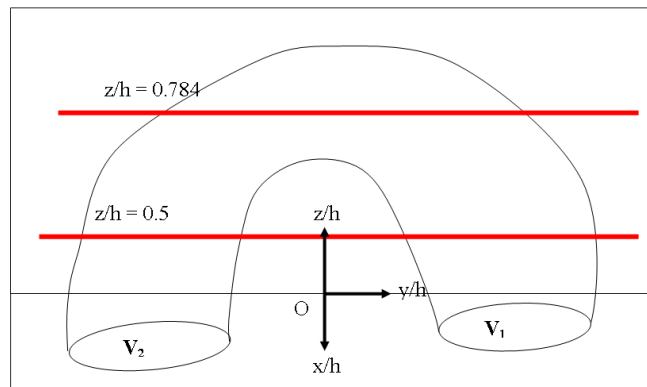


FIGURE 3.8: Estimated Position of the  $z$  planes relative to the estimated arch vortex shape

vortex, secondary bubble and reattachment length have been given. However, mean flow asymmetry is observed. Is it a consequence of the flow unsteadiness ? Does the

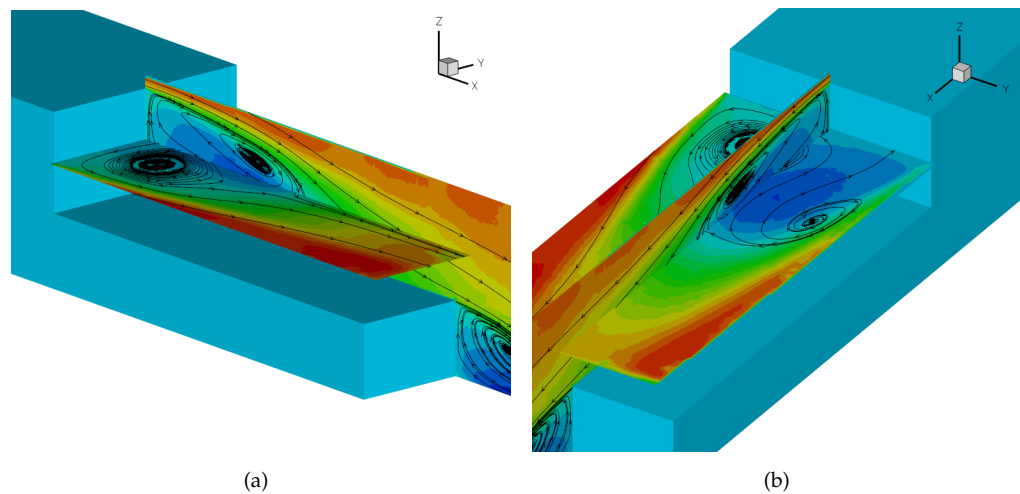


FIGURE 3.9: 3D view of figures 3.4(a) and 3.7(c)

time averaging lead to such fields? To look for some answers, it is necessary to study the unsteady behavior of the flow.

### 3.3 Some features of the unsteady flow

The unsteady flow is globally characterized by its statistic moments. The regions of high turbulence intensities and production are then looked for (see appendix A for definition). A POD analysis aims at understanding the aerodynamic phenomena associated to those flow features. Those approaches do not consider the time as a parameter though. Therefore, to obtain the frequencies associated to those phenomena, spectra are computed and the frequencies are compared to those obtained via high speed flow visualizations. Eventually, some features of the coherent structures are analyzed.

#### 3.3.1 Time independent analysis

##### 3.3.1.1 Plane $y = 0$

**Statistic moments** The lower resolution PIV snapshots (see figure 2.6) are used to present some of the turbulence statistics in the plane  $y = 0$  (see figure 3.10). Although the resolution is not as high as in figure 3.4 for those fields, more instantaneous snapshots were acquired, leading to more converged statistics.

As expected from the high velocity gradients, the maximum levels of turbulence are found in the upper shear layer. The streamwise turbulence reaches 25% at about one step height upstream of reattachment, around  $(x/h, z/h) = (1.92, 0.8)$ . On the opposite,

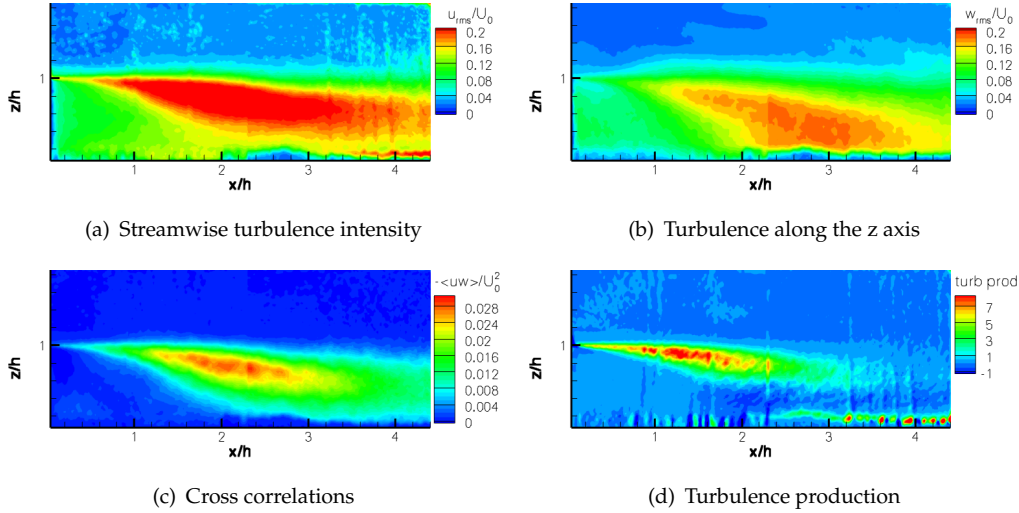


FIGURE 3.10: Turbulence intensity and turbulence production in the plane  $Y = 0$ ,  $Re_h = 9.75 \times 10^4$

the maximum values of  $w_{rms}/U_0$  ( $\leq 18\%$ ) appear closer to the wall and downstream of reattachment, about  $(x/h, z/h) = (2.86, 0.46)$ . They are similar to the levels observed on a 2D backward facing step (see 1.1.3.1). Nevertheless, the velocities are not the most correlated there (see figure 3.10(c)). Indeed, the maximum of correlation appears closer to the maximum of streamwise turbulence intensity, around  $(x/h, z/h) = (2.33, 0.73)$ . A value of  $2.9 \times 10^{-2}$  is reached there, which is more than what is observed on a 2D step 1.1.3.1.

The high rms values though are not necessarily associated to energy transfer from the mean flow to the fluctuating flow. Hence, let us define the turbulence production as  $-\langle u_i u_l \rangle S_{il}$  (the equations are developed in appendix A). Turbulence is produced when this term is positive. In that case, this should occur in the upper shear layer, with a peak located around  $(x/h, z/h) = (1.3, 0.9)$  (see figure 3.10(d)), which is not where the maximum rms values are observed. On the contrary, there is a region spanning over one step height upstream and downstream of reattachment, at about 0.4 step height that shows negative turbulence production: kinetic energy from the fluctuating flow is transferred to the mean flow. The peak is visible around  $(x/h, z/h) = (2, 0.4)$ , with an absolute value that is however 10 times smaller than that in the upper shear layer. It should be mentioned though that the zone of negative turbulence production matches that of high  $w_{rms}/U_0$  with low correlation between  $u$  and  $w$ .

Those different locations in turbulent production and intensities suggest different aerodynamic behavior. In order to have a better understanding, other statistical quantities are computed.

In particular, the forward-flow intermittency factor  $\Pi_x$  is defined: it is the fraction of realizations during which the flow at a given position goes in the  $x > 0$  direction

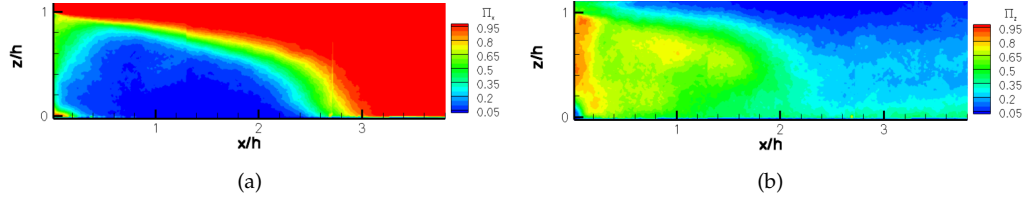


FIGURE 3.11: Forward (a) and upward (b) flow intermittency factors in the plane  $y = 0$  at  $Re_h = 8 \times 10^4$

[158, 159, 166].

$$\Pi_x(M) = \frac{1}{N_s} \sum_{i=1}^{N_s} coeff(i, M) \quad (3.1)$$

where

$$\begin{cases} coeff(i, M) = 1 \text{ if } U \geq 0 \text{ for snapshot } i \text{ at position } M, \text{ and} \\ coeff(i, M) = 0 \text{ otherwise} \end{cases} \quad (3.2)$$

This means that  $\Pi_x = 0.5$  denotes the most unstable state. As shown in figure 3.12, the most unstable point is the reattachment point. In a more general way, the shear layers are the most unstable regions. Furthermore, as shown on figure 3.11(a), this factor is equal to 0 for  $1 < x/h < 2$  close to the wall and slightly above it. This reveals that only reverse flow occurs here. Therefore, if an analogy can be made with the 2D step flow (see 1.1), if large scale vortical structures exist within the recirculation bubble and are advected downstream, they leave the bubble well above the surface in the region  $1 < x/h < 2$ . The analogy with the 2D case can go further : a growth of the secondary bubble is not excluded since a second unstable point is found downstream of the secondary bubble, around  $x/h = 0.24$ ; the flow is either reverse or forward for  $0 \leq x/h \leq 1$ . Along the  $z$  direction (see figure 3.11(b)), the conclusion remains unchanged: an unstable point where the upward-flow intermittency factor  $\Pi_z = 0.5$  is observed at  $z/h = 0.12$ . This suggests the possibility for this secondary bubble to grow. Figure 3.11(a) should be compared to that obtained on the 2D step by Spazzini et al. [166]. Just above the reattachment point, the velocities are upward-oriented 30% of the time, characterized by  $\Pi_z = 0.3$ . In 2D, Shi et al. [159] would attribute such features to the complex interaction between the reattaching large-scale vortical structures and the flapping upper shear layer.

If such phenomena occur, then the velocity distribution functions would most probably not be Gaussian, as it is often the case for turbulent flows. Is the turbulence production related to vortex shedding? Do the maximum  $w_{rms}/U_0$  and negative turbulence production reveal some kind of shear layer flapping? Is the behavior close to that of a 2D step in this plane? It is expected that the energy associated to those 2 phenomena are

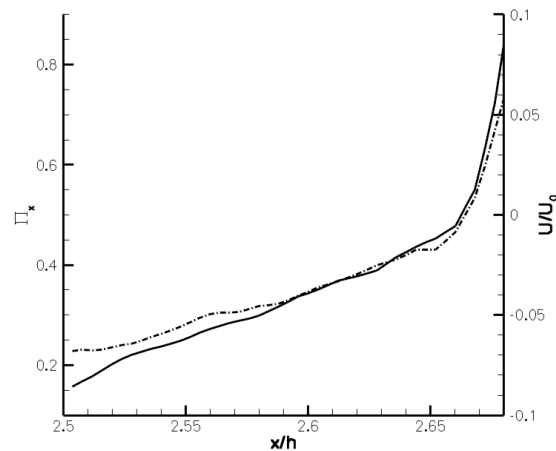


FIGURE 3.12: Evolution of the mean streamwise velocity (dashed) and the forward flow intermittency factor (solid). Data are extracted from the  $z/h = 0.015$  black line drawn on figure 3.5(a)

different. In this respect, in order to differentiate them, a POD analysis was conducted.

**POD analysis** The method employed is described in appendix C. The convergence curves 3.13 show that many modes are required to retrieve 99% of the energy of the fluctuating flow. This is much more than for the academic laminar flow behind cylinders for example, where the fluctuating flow can be described using only a few modes [43]. The sum of the energy of the first 4 modes reaches only 28% of the total energy

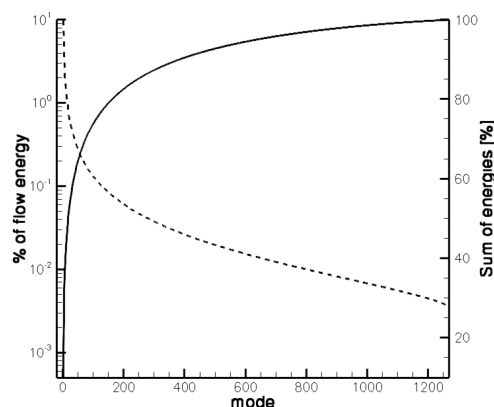


FIGURE 3.13: POD energy of the modes (dashed) and sum of the mode energy (solid)

of the fluctuating flow, which is not sufficient to precisely describe it. They are however shown in figure 3.14. Even if the interpretation of such modes should be done with great care, it seems like mode 1 (in figure 3.14(a)) describes a global up and down movement of the fluctuating flow around the average field. Is this the illustration of some flapping of the upper shear layer? It is furthermore the most energetic mode. However, do the next modes illustrate the shedding within the upper shear layer? Interpreting the modes much further would be dangerous. However, those 4 first modes seem to

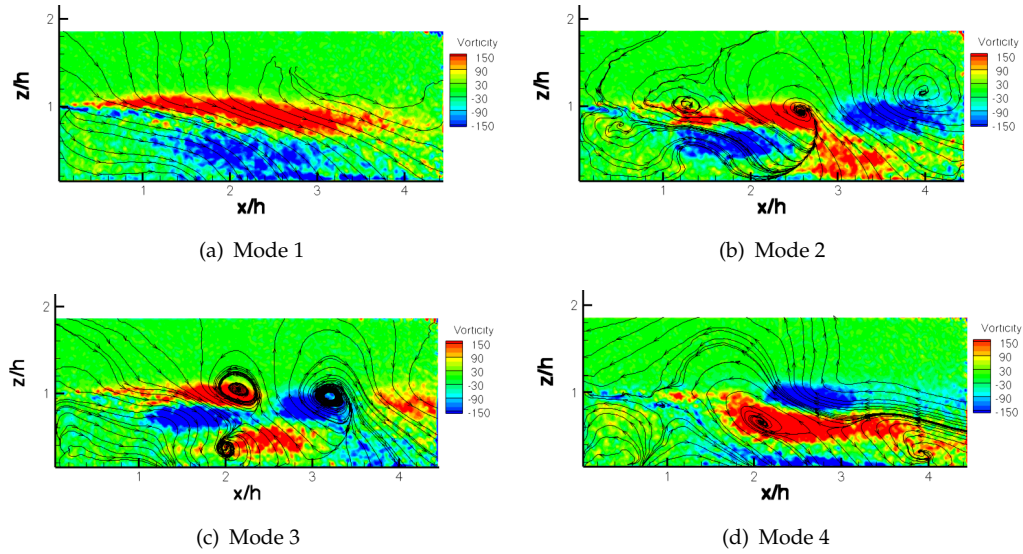


FIGURE 3.14: Streamlines and longitudinal velocity contour levels of the first 4 POD modes in the plane  $y = 0$  at  $Re_h = 9.75 \times 10^4$

explain the two phenomena expected from the statistic analysis: they would claim for the upper shear layer flapping and for vortex shedding. If this is the case, the higher order statistic moments or even the probability density functions of the velocities should most certainly not be Gaussian (like most of the time actually).

**Distance to Gaussian turbulence** A Gaussian function is defined by its mean value  $U_i$  and its standard deviation  $\sigma_i$ . Therefore, to see if a phenomenon is non-Gaussian, the statistic moments higher than two must be computed. This defines the third and fourth order moments, namely the Skewness  $\gamma_x = \frac{\langle u^3 \rangle}{\sigma_x^3}$  and the kurtosis (or flatness factor)  $\beta_x = \frac{\langle u^4 \rangle}{\sigma_x^4}$ . They are written here for the velocity  $u$  but can similarly be written for the velocity  $w$ :  $\gamma_z = \frac{\langle w^3 \rangle}{\sigma_z^3}$  and  $\beta_z = \frac{\langle w^4 \rangle}{\sigma_z^4}$  respectively. Maps of skewness and kurtosis are therefore given in figures 3.15. As shown in appendix B, the statistic convergence of those moments is not well established and the data interpretation should be more qualitative than quantitative. It can be seen that in most regions of the flow, the skewness and kurtosis values differ from the Gaussian case. In particular, away from the wall and away from the free-stream region, the extreme non-zero skewness values appear above the shear layer, at about 1.2 step height, for  $x/h \geq 2h$  (see figures 3.22(a) and 3.22(b)). The same goes for the kurtosis in figures 3.22(c) and 3.22(d). Those kind of values are found in turbulent boundary layers away from the walls.

As pointed out previously, since they are third and fourth order statistic moments, a huge amount of samples is required for the estimated values to converge towards the true value (see appendix B). The maps presented here do not have enough samples to give an accurate quantitative estimate of the skewness and kurtosis. This is illustrated

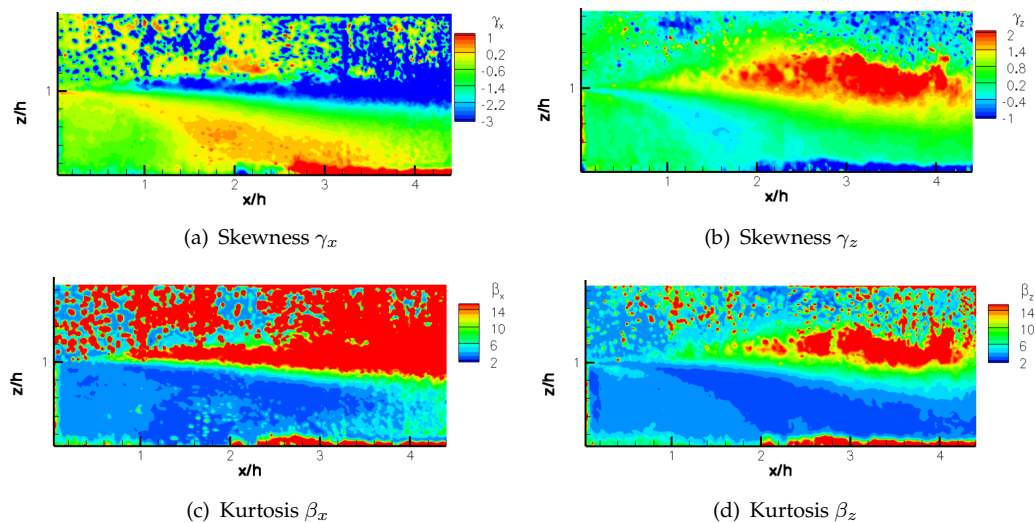


FIGURE 3.15: Estimated values of Skewness and kurtosis in the plane  $y = 0$  at  $Re_h = 9.75 \times 10^4$

by the scattered data in the PIV maps of figures 3.15: it is particularly pronounced in the free stream ( $z/h > 1$ ) where the standard deviation is much lower than in the other regions of the flow. Therefore, a qualitative conclusion, only, should be drawn from those fields: the flow is not Gaussian in most regions. The quantitative interpretation of the data, in particular in table 3.4, should be done with great caution, if at all. An

TABLE 3.4: Skewness and kurtosis at some locations in the plane  $y = 0$  at  $Re_h = 9.75 \times 10^4$ . Locations are illustrated in figure 3.16

Location	$\gamma_x$ Skewness	$\gamma_z$ Skewness	$\beta_x$ kurtosis	$\beta_z$ kurtosis
1: (0.0,1.67)	1.28	0.16	15.14	8.31
2: (1.98,1.67)	0.01	0.39	3.29	4.60
3: (3.0,1.67)	-2.79	0.34	65.60	12.25
4: (1.3,0.9)	-0.36	0.24	2.87	2.59
5: (1.92,0.8)	-0.26	0.38	2.69	2.52
6: (2.0,0.4)	0.33	-0.13	3.61	3.70
7: (2.3,0.9)	-1.62	1.28	5.52	4.94
8: (2.33,0.73)	-0.23	0.48	2.59	2.69
9: (2.86,0.46)	0.19	0.14	2.70	2.60
10: (3.0,1.1)	-2.36	1.82	26.81	12.88
11: (3.0,1.0)	-3.69	1.97	25.32	10.36
12: (3.0,0.9)	-2.37	1.48	11.17	7.32
13: (3.0,0.6)	-0.27	0.58	2.47	3.11
14: (3.0,0.4)	0.29	0.17	3.51	2.85
15: (3.0,0.3)	0.50	0.08	4.93	2.90
Gaussian	0.0	0.0	3.0	3.0

alternative to discussing non-Gaussian aspect of the statistics is then drawing the probability density functions. It could also help understand if this distance to non-Gaussian

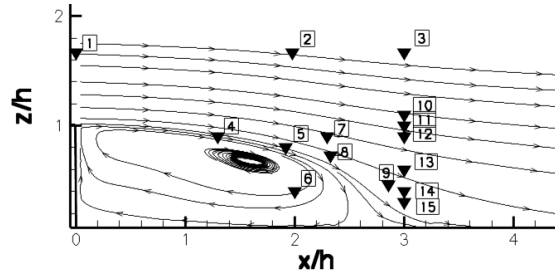


FIGURE 3.16: Illustration of the positions where the skewness, kurtosis and PDF are extracted in the plane  $y = 0$

statistics is due to intermittent flow or other features.

The PDF (probability density function)  $p$  is defined as:

$$p(z) = \frac{N_z}{N_{\text{total}} \text{Width}} \quad (3.3)$$

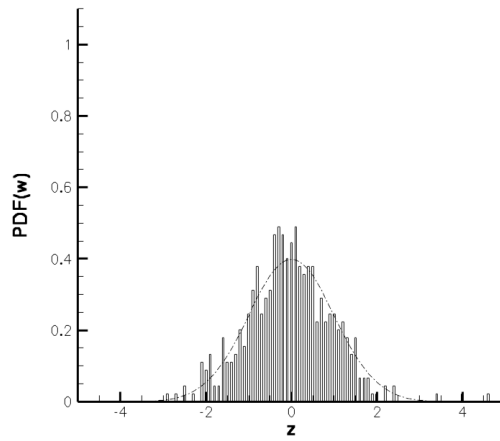
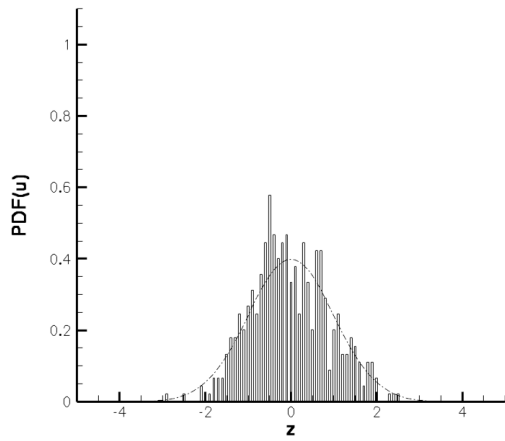
where  $N_z$  is the number of samples where the reduced velocity  $z = \frac{U_i(t) - U_i}{\sigma_i}$  for the velocity  $U_i = U, V, W$  falls into the range  $[z, z + \text{Width}]$ . It was chosen here  $\text{Width} = 0.1$ . The uncertainty on the estimate of the PDF is discussed in appendix B. To quantify the distance to Gaussian statistics, the PDF is compared to the normal distribution defined as :

$$p(z) = \frac{1}{\sqrt{2\pi}} e^{-z^2/2} \quad (3.4)$$

The PDFs are computed at the particular aforementioned locations (reported in table 3.4 and illustrated in figure 3.16), namely in the free-stream flow and where the turbulence peaks are observed. Results are shown in figures 3.17. For the discussion, two reference PDFs are shown in figures 3.17(a) and 3.17(b) at location (0.0, 1.67). This point is in the free-stream flow 3.1. It is therefore only affected by the wind-tunnel turbulence. The other locations, however, are either in the wake or within the recirculation bubble. By comparing their PDFs with the reference PDFs, the effect of the step can be shown.

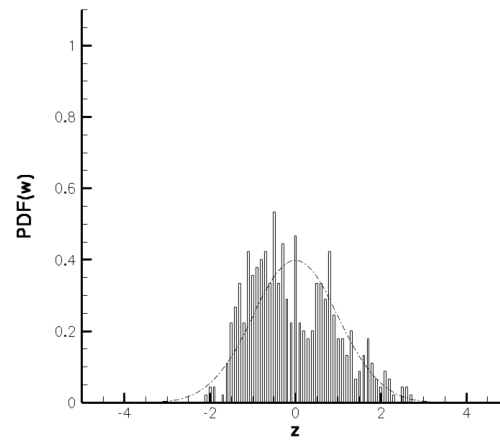
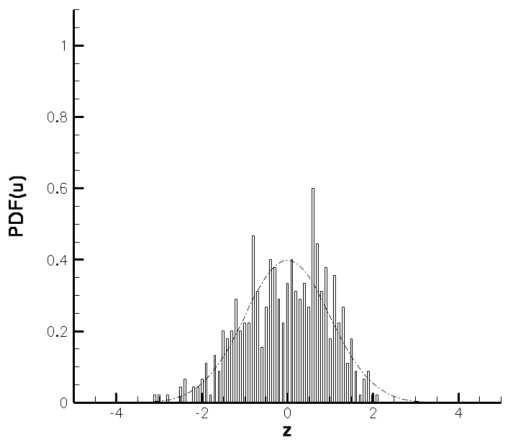
The reference PDFs are actually not too far from a normal distribution for the two velocity components, even though PDF(u) has a positive skewness (see figure 3.17(a)). The distribution diverges from the normal one at the location of maximum  $(u_{rms})_{max}$ : if the shape is not very skewed, it seems to have two distinct peaks on each side of  $z = 0$  (see figure 3.17(c)). This is even more pronounced on the PDF(w) in figure 3.17(d). A camel back shaped distribution is representative of a bimodal distribution. Would this translate the effect of vortex shedding and shear layer flapping? A third type of distribution is also observed as illustrated in figure 3.17(e): it is skewed with a narrow peak. However, a few very large amplitude events occur ( $z < -2$ ). This is however not as visible on the w velocity (see figure 3.17(f)). What is this due to? Since the flow is highly 3D, scanning the  $z/h = 0.5$  plane could help interpret those features observed.





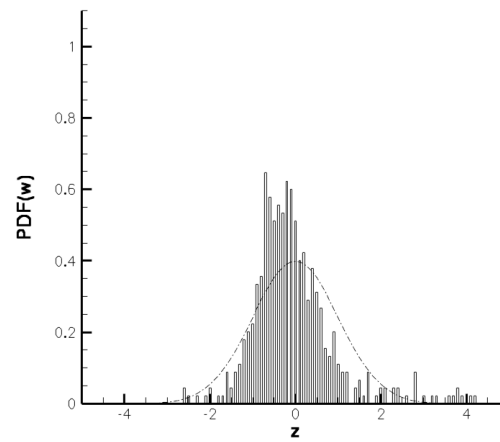
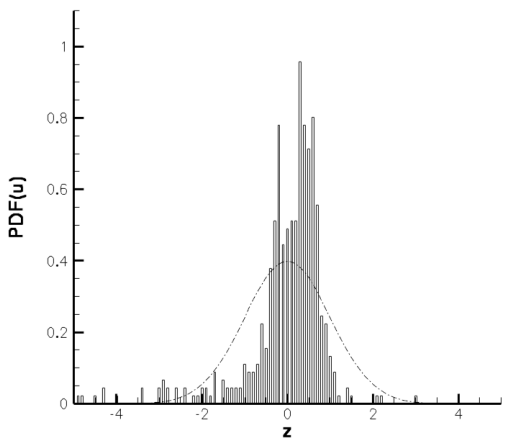
(a) 1:  $(x/h, z/h) = (0, 1.67)$ : free-stream turbulence

(b) 1:  $(x/h, z/h) = (0.0, 1.67)$ : free-stream turbulence



(c) 5:  $(x/h, z/h) = (1.92, 0.8)$ :  $(u_{rms})_{max}$

(d) 5:  $(x/h, z/h) = (1.92, 0.8)$ :  $(u_{rms})_{max}$



(e) 12:  $(x/h, z/h) = (3.0, 0.9)$ : bubble wake

(f) 12:  $(x/h, z/h) = (3.0, 0.9)$ : bubble wake

FIGURE 3.17: Estimated probability density functions (bars) compared to the normal distribution (dash dot line) at different locations in the plane  $y = 0$  at  $Re_h = 9.75 \times 10^4$ . Positions are illustrated in figure 3.16

### 3.3.1.2 Plane $z/h = 0.5$

The same analysis as in the plane  $y = 0$  is conducted in the plane  $z/h = 0.5$ .

**Statistic moments** In this plane, as described previously, there are two shear layers. As expected, high levels of turbulence are found there. To give some figures, values of  $v_{rms}/U_0$  reach 13% in both shear layers. However, the values of streamwise turbulence is about 50% higher in the  $y > 0$  shear layer than in the other one. The shear layers are not the only regions of high turbulence though: above the reattachment region, the flow is also highly fluctuating. Indeed, slightly downstream of the reattachment region and above the centerline (around  $(x/h, y/h) = (2.8, 0.2)$ ),  $v_{rms}/U_0$  values up to 18% are observed. The highest values of  $u_{rms}/U_0$  values are found elsewhere: values up to 18% are distributed in two regions after reattachment, one a bit under the centerline (centered on  $(x/h, y/h) = (2.8, -0.1)$ ) and the other one much above it (centered on  $(x/h, y/h) = (2.8, 0.6)$ ). As for the  $y = 0$  plane, the two fluctuating velocities are not the most correlated in the area of high  $v_{rms}/U_0$  values.

The turbulence is also produced in those shear layers. However, the intensity is twice as strong in the  $y > 0$  shear layer as in the other one, with values smaller than in the shear layer of the  $y = 0$  plane. Unfortunately, the quality of the PIV data in this plane is poor for this processing. Since it is scattered data, only qualitative interpretation should be made. A small zone of negative turbulence production is also visible between the  $y > 0$  shear layer and the centerline, extending to a rather circular region centered above the reattachment area. As for the  $y = 0$  plane, the absolute values of negative turbulence production here are smaller than the positive ones. As for the  $y = 0$  plane, one can ask if the region around reattachment flaps not only in the  $z$  direction, but also along the  $y$  axis.

The asymmetry observed in this experiment on the streamwise mean and RMS values (see figure 3.19) should be compared to those observed by Syms [170] in figure 1.15. However, it should be reminded that Syms [170] extracted data on the line at  $z/h = 1$  whereas it was done here a little lower into the shear layer at  $z/h = 0.814$ . This could explain the higher RMS values observed. The shape of the graph is nonetheless similar in both cases.

It should be mentioned that the turbulence production is computed from in-plane velocity components. It is shown though that the flow is highly 3D, which suggests that this 2D approach for turbulence production localization is very restrictive. A dual plane 2D3C PIV approach for example should have been accomplished to compute the 3 velocity components and 3 velocity gradients in the plane to confirm or not those

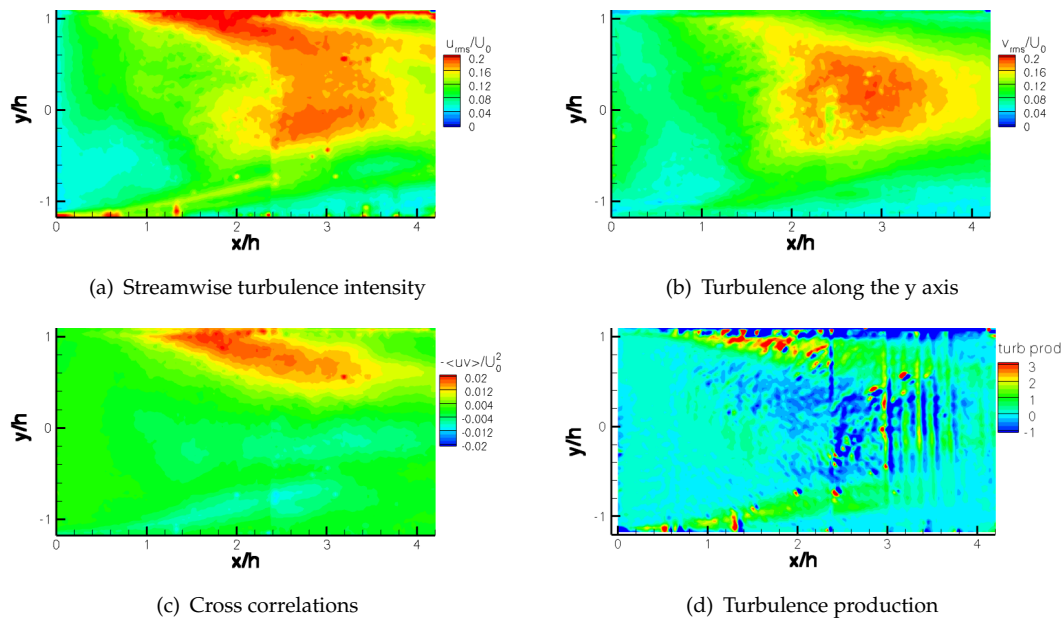


FIGURE 3.18: Turbulence intensities and turbulence production in the plane  $z/h = 0.5$ ,  $Re_h = 9.75 \times 10^4$

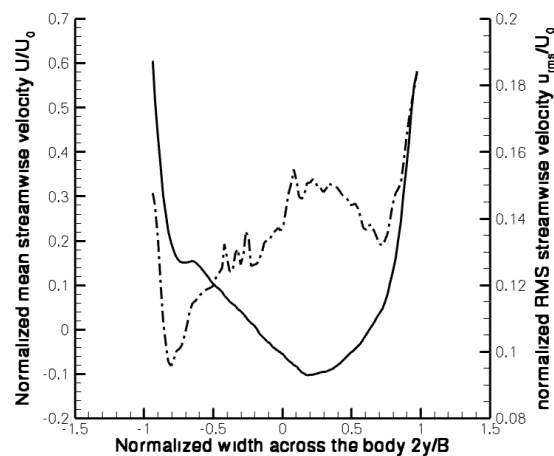


FIGURE 3.19: Mean (solid) and RMS (dashed) streamwise velocities along the line  $(x/h, z/h) = (1.12, 0.814)$

results. However, the results are sufficient to observe an imbalance in turbulence intensities and production between the two shear layers. This suggests they do not behave identically. Is there more intense vortex shedding in the  $y > 0$  shear layer than in the other one? This requires further investigation, in particular concerning the intermittency factors.

In figure 3.20(b), a region close to the step can be seen, where the flow goes towards  $y < 0$  ninety nine percent of the time. However, the values of the  $v_{rms}$  in figure 3.18(b) suggest that this is not a steady region. Unsteadiness is also visible on the centerline, downstream of the recirculation bubble, where the  $y$  velocity changes its sign evenly. The rms values (see figure 3.18(b)) suggest that those changes are quite high, with 15%

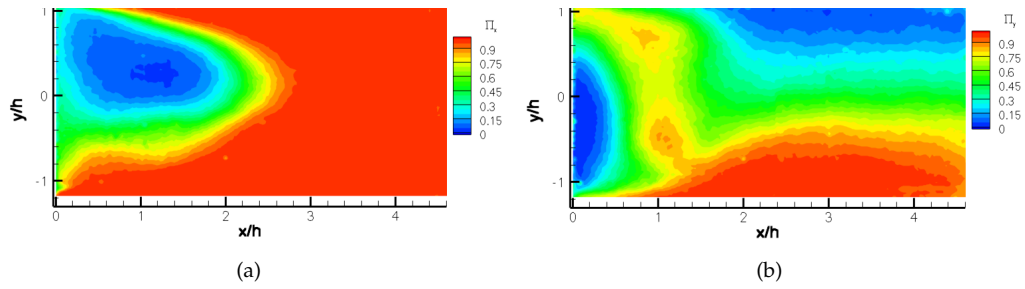


FIGURE 3.20: Forward (a) and sideways (b) flow intermittency factors in the plane  $z/h = 0.5$  at  $Re_h = 9.75 \times 10^4$

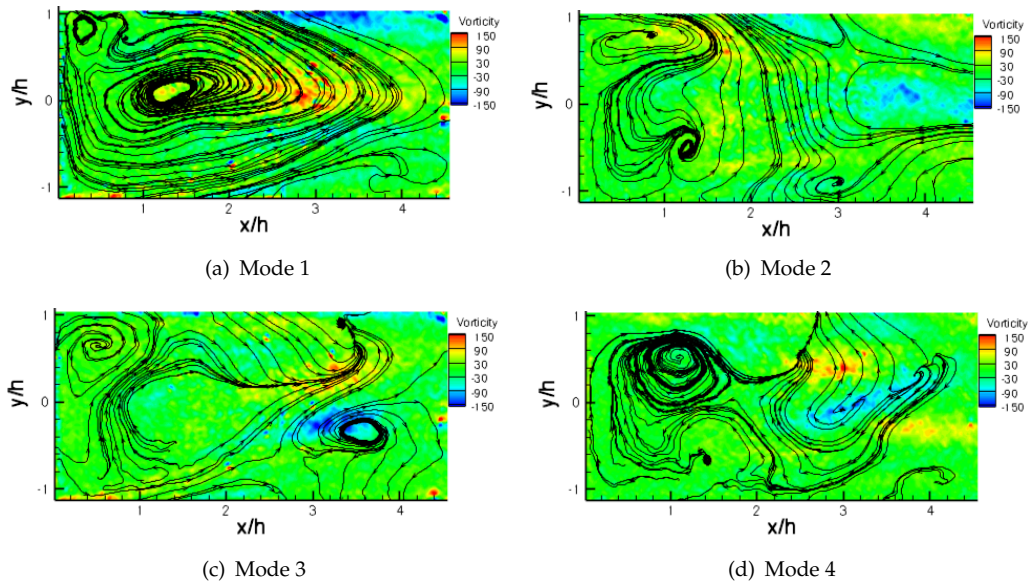


FIGURE 3.21: Streamlines and longitudinal velocity contour levels of the first 4 POD modes in the plane  $z/h = 0.5$  at  $Re_h = 9.75 \times 10^4$

of the upstream velocity. Is this due to a sideways flapping of the bubble, vortex shedding or something else? In order to answer this question, a POD analysis was conducted.

**POD analysis** Contrary to the other plane (see figure 3.14), the first 4 modes in the plane  $z/h = 0.5$  (figure 3.21) do not illustrate any obvious aerodynamic phenomenon. Therefore, no hazardous interpretation of the modes will be attempted. However, an obvious comment can be made: the modes are not symmetric, contrary to the academic cylinder flow for example [43, 134, 135]. This suggests that, like the time-averaged flow 3.2.2.2, the fluctuating flow does not have a symmetric behavior. This confirms the already non-symmetric turbulence statistics results presented above 3.3.1.2. This reveals the complexity of the unsteady flow in this plane. The POD analysis does not seem to be directly efficient to extract the main unsteady flow features in this plane. The

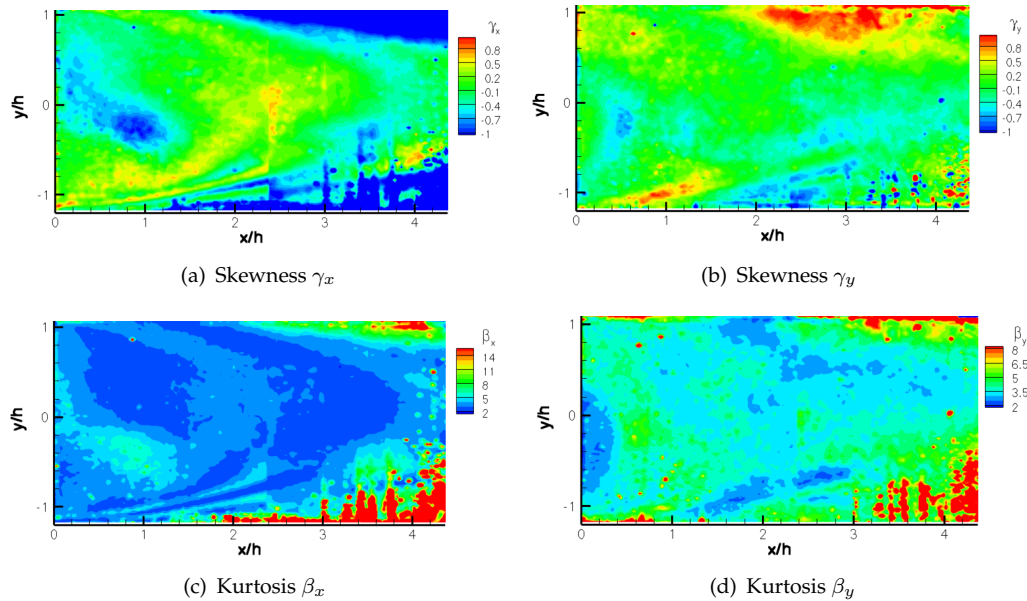


FIGURE 3.22: Estimated values of Skewness and kurtosis in the plane  $z = 0.5$  at  $Re_h = 9.75 \times 10^4$

distribution functions are then computed at some places to see if more several distinct phenomena can be highlighted in this plane.

**Distance to Gaussian turbulence** The same analysis as in paragraph 3.3.1.1 is conducted. The estimates of the skewness and the kurtosis are also biased due to the limited amount of samples. Therefore, the same conclusion should be drawn as in the  $y = 0$  plane : there are also regions of non-Gaussian statistics. Because of the bias, it is unsure to conclude that the difference to Gaussian statistics is not as pronounced at the locations probed in the  $z/h = 0.5$  plane (as suggested by table 3.5) as those in the  $y = 0$  plane (as suggested by table 3.4). However, qualitatively, the regions where the statistics are the farthest from Gaussian are not as clear as in the  $y = 0$  plane.

The PDF shows this deviation to Gaussian statistics better: in particular, the bi-

TABLE 3.5: Skewness and kurtosis at some locations in the plane  $y = 0$  at  $Re_h = 9.75 \times 10^4$ . Locations are illustrated in figure 3.23

Location	$\gamma_x$ Skewness	$\gamma_y$ Skewness	$\beta_x$ kurtosis	$\beta_y$ kurtosis
1: (2.8,0.2)	0.24	-0.17	3.00	3.13
2: (2.8,0.6)	-0.12	0.44	2.80	3.21
3: (1.8,0.95)	-0.28	0.30	2.62	2.65
4: (1.8,-0.9)	-0.01	0.13	2.42	2.50
Gaussian	0.0	0.0	3.0	3.0

modality is obvious on both the  $u$  and  $v$  velocities as shown in figures 3.24(b), 3.24(c), 3.24(d) and 3.24(e). This is the side of the model where the stretched mean vortex  $V_1$

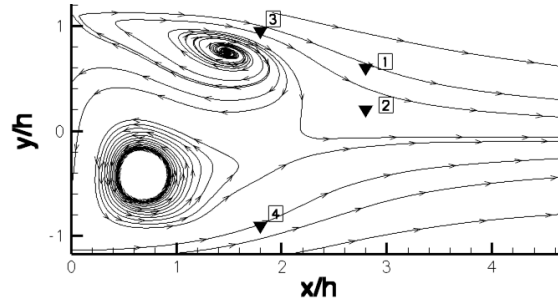


FIGURE 3.23: Illustration of the positions where the skewness, kurtosis and PDF are extracted in the plane  $z/h = 0.5$

is observed (refer to paragraph 3.2.2.2). On the centerline or on the side of the other vortex, the PDF is slightly skewed (figures 3.24(a) and 3.24(f)) but does not show such a bimodal distribution. Is the bimodal distribution associated to one same or two distinct phenomena? Is it just an aperiodic phenomenon? Further investigation of the unsteady flow is then required to hope answering such questions. A spectral analysis was then performed.

### 3.3.2 Frequencies involved

As illustrated on figure 3.25 (and detailed in section 2.3), the spectra were computed at two locations. The results are plotted in figure 3.26. A peak at  $St_h = 0.08$  can be seen for the two positions probed. This value is almost twice as small as that obtained on the SFST by Tinney and Ukeiley [175]. Since it is not mentioned at what location their measurements were performed, it is difficult to interpret this difference. Indeed, to compare with cylinder flows, the frequency measured at the centerline where the counter-rotating vortices are observed is twice as big as that measured more on the side, where only one of the two counter-rotating vortices is observed. This could be an explanation. It also depends on the height where it is measured [8], the aspect ratio of the step [133], the Reynolds number 1.2.2.4. The half width of the peak, defined as the Strouhal range where  $\frac{E_1(St_h)}{\text{var}(U)} \geq \frac{1}{2} \left[ \frac{E_1(St_h)}{\text{var}(U)} \right]_{MAX}$  for  $St_h \geq 0.08$  is between 0.02 and 0.035 for positions (1) and (2) respectively (defined in figure 3.26). No harmonics of the  $St_h = 0.08$  peak are clearly visible.

The other half width of the peak (on the side  $St_h \leq 0.08$ ) cannot be determined because of the high energies appearing at the lower Strouhal numbers. This shows that at the locations probed, the flow is dominated by low frequencies: most of the fluctuating flow energy is contained between  $0 \leq St_h \leq 0.12$ . Higher values appear at location (2) than at location (1). Is this a consequence of the flow asymmetry observed previously? Also what aerodynamic phenomenon do those frequencies correspond to? Is the  $St_h = 0.08$  related to a vortical type motion in the upper shear layer, like in the

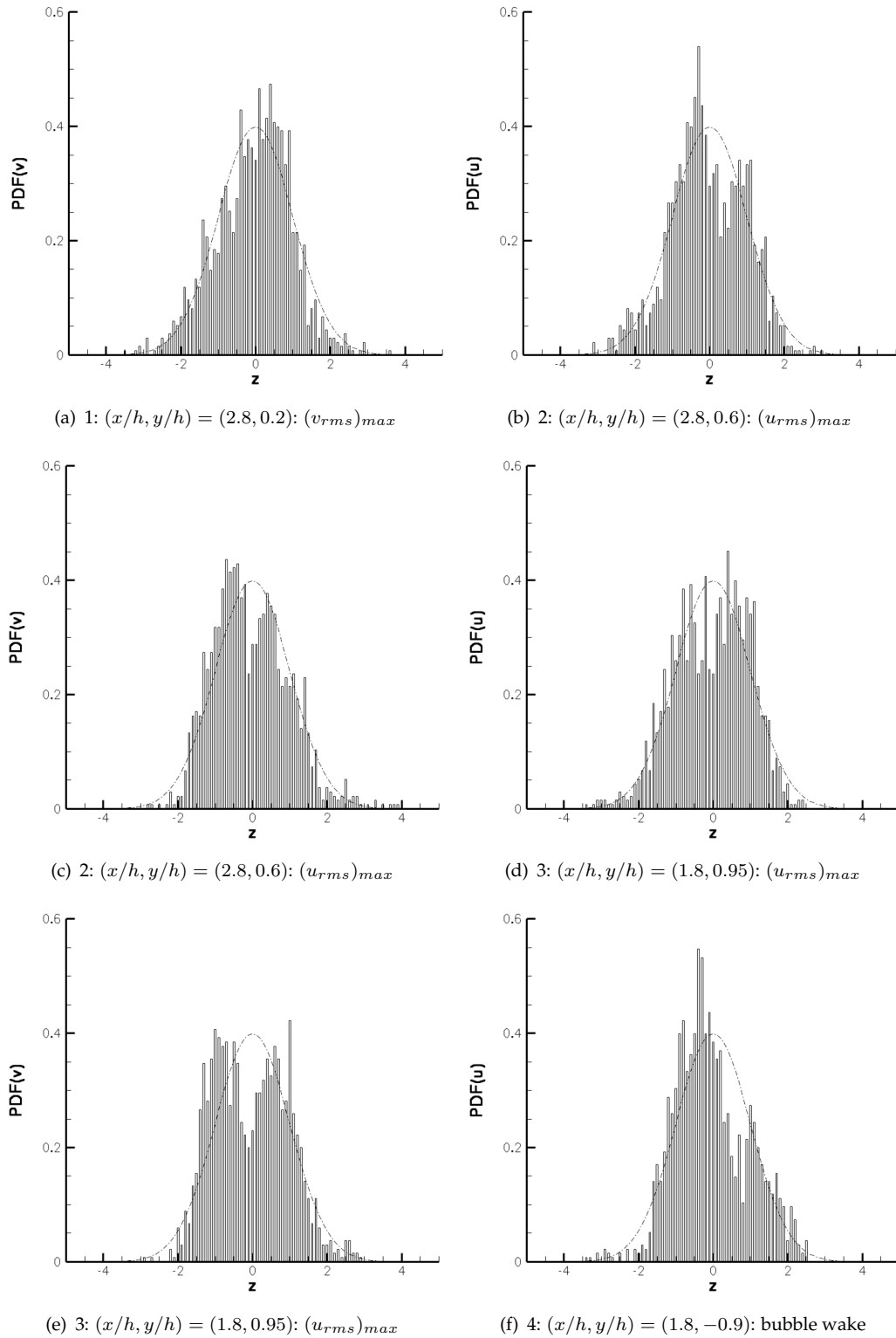


FIGURE 3.24: Estimated probability density functions (bars) compared to the normal distribution (dash dot line) at different locations in the plane  $z/h = 0.5$  at  $Re_h = 9.75 \times 10^4$ . Positions are illustrated in figure 3.23

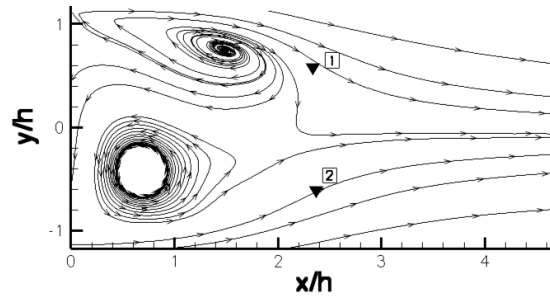


FIGURE 3.25: Illustration of the positions where the spectra were computed, in the vicinity of the plane  $z/h = 0.5$ . In black, the velocity streamlines

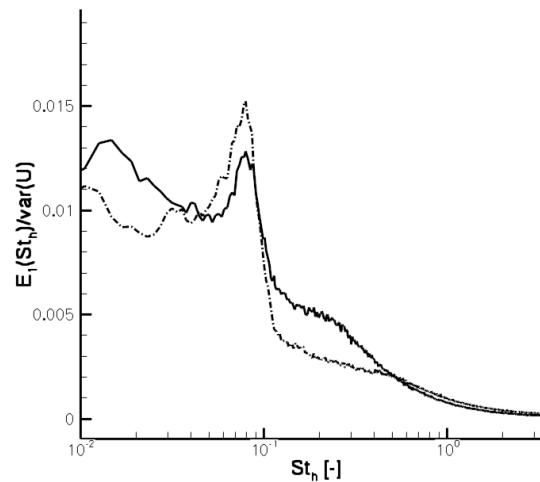


FIGURE 3.26: Normalized spectra at positions 2 :  $(x/h, y/h, z/h) = (2.37, -0.61, 0.53)$  (solid line) and 1 :  $(x/h, y/h, z/h) = (2.34, 0.58, 0.45)$  (dashed line) for  $Re_h = 1.675 \times 10^5$ . Positions are illustrated in figure 3.25

2D case where a comparable Strouhal number  $St_h = 0.07$  is observed (see paragraph 1.1.3.1)? Or is it related to vortex shedding from the model lateral walls? If this is the case, the model width  $B$  should be considered to compute the Strouhal number. This one becomes  $St_B = 0.18$ , which is a more common value for bluff bodies (see 1). Or is this Strouhal number related to the flapping of the upper shear layer? In order to try to answer those questions, the flow was directly visualized through time-resolved laser tomography.

### 3.3.3 Interpreting the unsteady phenomena

#### 3.3.3.1 Comparing with laser tomography results

Since a high frame rate camera was used for those laser tomography visualizations, information about the flow unsteadiness can be gathered. It is expected to complete the



hot-wire measurements regarding the main aerodynamic phenomena. Therefore, several planes were visualized.

**Plane  $x/h = 1.6$**  The centrifugal force of a vortex takes the smoke away from its core. Then, streamwise vortices can be spotted in the  $x/h = 1.6$  laser plane by looking for the holes such as in figure 3.27(a). It should be remembered that this plane is upstream of the reattachment, probably slicing the arch vortex (see table 3.3 for the vortex leg location). The position of such a hole in the plane  $x/h = 1.6$  can be tracked over time such as in figure 3.2. The same hole is surrounded by a red line. This streamwise vortex is not stationary. It can be seen in figure 3.27 going downwards from about mid-step height down to the surface. As an order of magnitude, it takes about  $t^+ = 3.5$  to cover the distance. If the phenomenon is assumed to be periodic and if the time to go downward is supposed to be the same as the time going upward, this would correspond to a Strouhal number  $St_h = 0.15$ .

A streamwise vortex was also observed on the SFST: it is also located on the model centerline, but in a more downstream  $x$  plane however. Are those streamwise vortices on the SFST and SFSTO' related to the same phenomenon? This is not obvious since purple lines, in figure 3.27(n), show that this vortex is not alone. Inspired by the work of Wang and Zhou [184] on a prism and illustrated in figure 1.10, are those streamwise vortices in the  $x/h = 1.6$  plane just slices of the arch vortex being shed? This could also explain that those vortices are not alone. Therefore, the up and down movement of the streamwise vortex would just represent a forward-backward motion of the arch vortex leg being sliced. If this was the case, analyzing the  $x$  plane videos could then help characterize the phenomenon associated with the arch vortex motion. A 3D picture of the flow should greatly help understand the spatial topology of the flow and in particular this unsteady feature.

**Vortex Shedding in the plane  $y = 0$**  It has been attempted to follow over time the vortices expected to be shed in the upper shear layer and discussed in section 1.4. A representative sequence of pictures in this plane is shown in figures 3.28 (The reference frame is on figure 3.28(r)). In figures 3.28, smoke puffs are surrounded by a red line. Their advection is followed over time. If figure 3.28(r) is representative of the others, the distance between two smoke puffs is about one step height. The puff that is the closest to the step takes about  $t^+ = 1.63$  to cover the one step distance. A probe located at a fixed position would then observe a puff passing by, every  $t^+ = 1.63$ . This corresponds to  $St_h = 0.6$ . This value is more than three to four times higher than that obtained through the spectra or by Tinney and Ukeiley [175] on the SFST. The uncertainty estimated on the location of the puffs is below 0.1h. The uncertainty on  $t$  (for

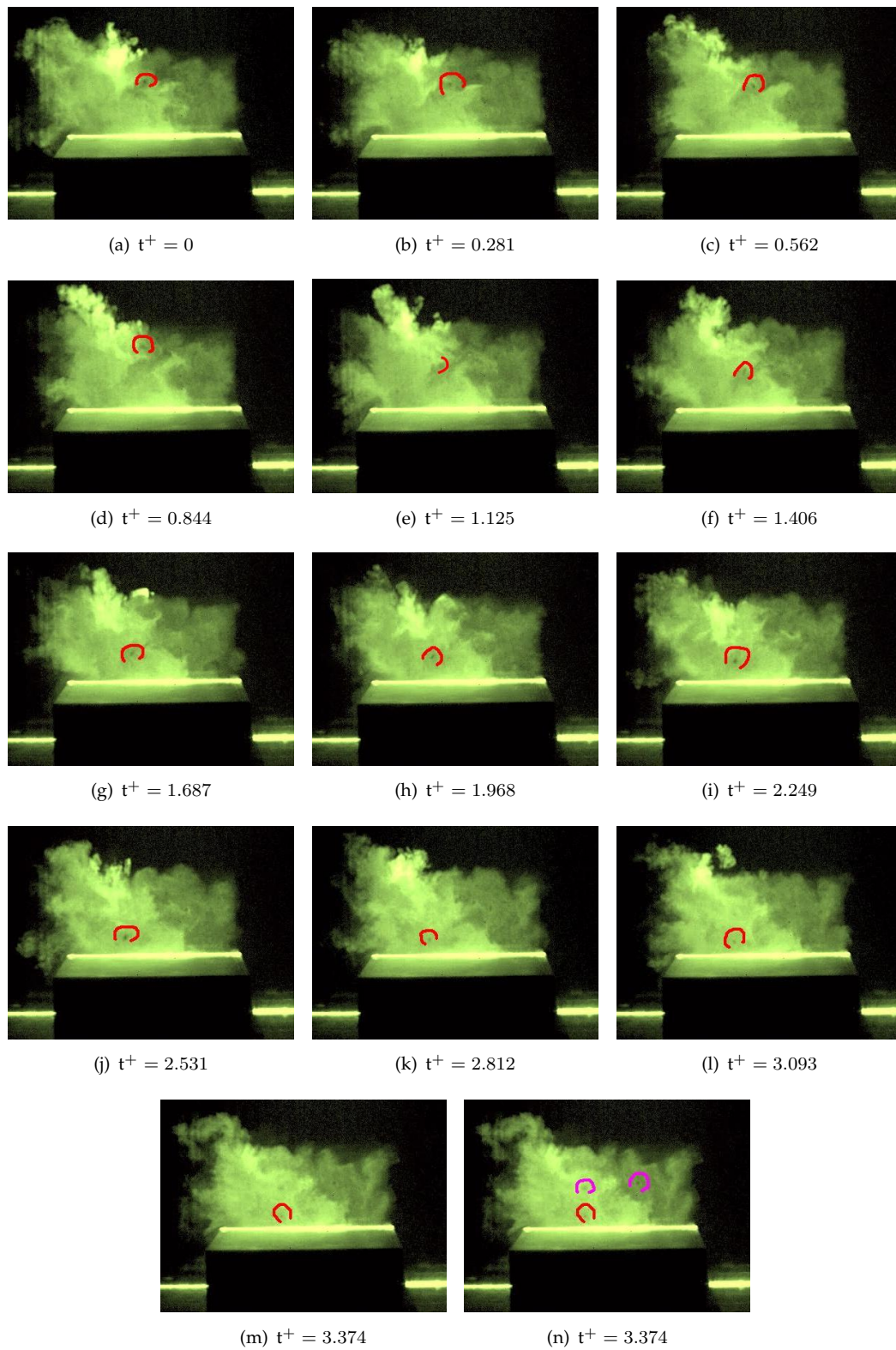


FIGURE 3.27: Time evolution of streamwise vortices in the plane  $x/h = 1.6$  at  $Re_h = 9.75 \times 10^4$

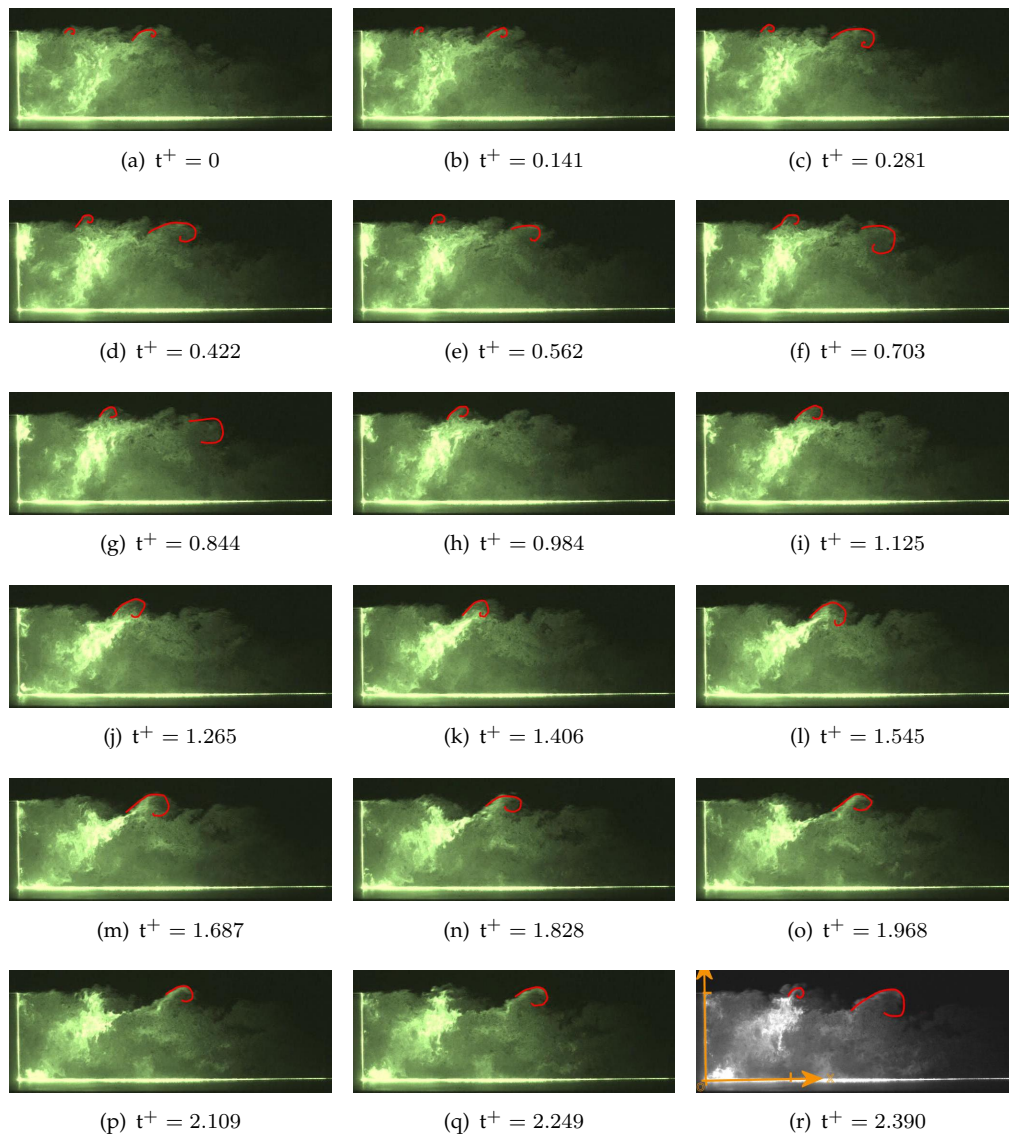


FIGURE 3.28: Time evolution of shear layer smoke puffs in the plane  $y/h = 0$  at  $Re_h = 9.75 \times 10^4$

one period) is less than 3 ms leading to an overestimated uncertainty of  $St_h$  around 0.3. There is still a factor of 2 between the values. Other explanations could be: (i) what was thought to be a vortex is not (ii) this sequence is not representative of all the sequences (iii) the peak in the spectra is not associated to the shedding of the upper shear layer. As a matter of fact, it is difficult to assess that the red surrounded smoke puffs in those figures are actual vortices. Indeed, the pictures are quite similar to that obtained by Becker et al. [16] in the case of non-periodic flow. If the flow is not perfectly periodic, this sequence could then also not be representative of the others. However, if the detected smoke puffs are vortices, from figure 3.28(l), they would have a typical size of  $h/4$  around  $x/h = 1.5$  whereas they would be much smaller more upstream in the shear layer. This would suggest vortex pairing in the upper shear layer as

observed in a 2D simple backward facing step 1.1. Further investigation to understand this ambiguity is required.

**Plane  $z/h = 0.47$ : vortex Shedding** The same ambiguity occurs in the  $z/h = 0.47$  plane : smoke puffs can be tracked over time but it is difficult to assert if they are actual vortices. By watching the videos, some stretched vortices can be seen as shown in figure 3.29).

If those puffs are actual vortices, a Strouhal number can be defined by conducting the

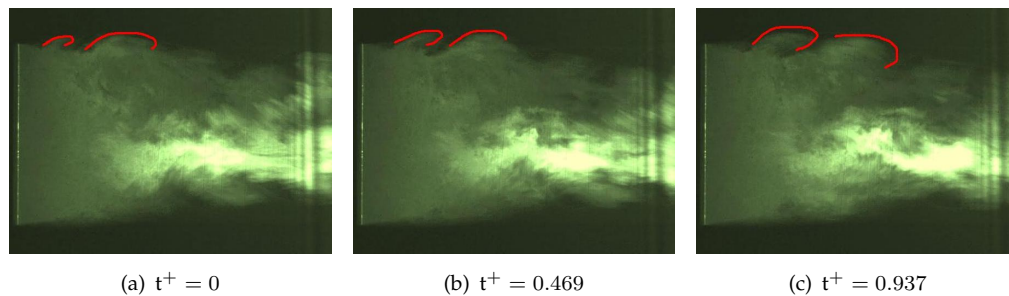


FIGURE 3.29: Time evolution of shear layer smoke puffs in the plane  $z/h = 0.47$  at  $Re_h = 9.75 \times 10^4$

same analysis as for the  $y = 0$  plane (refer to paragraph 3.3.3.1) : the distance between two puffs as in figure 3.29(c) is about  $0.47 h$ . Given an advection velocity of about  $0.7 U_0$  yields  $St_h = 1.5$ . This is more than twice as much the result obtained in the  $y = 0$  plane which was already more than any Strouhal number measured with the hot-wire probes.

However, by looking closer at the videos, stronger burst-like events seem to occur with bigger smoke puffs being advected downstream. A representative sequence is illustrated in figure 3.30. From those figures,  $0.1 \leq St_h \leq 0.2$  with an average of  $St_h = 0.13$ . The flow was qualitatively observed and events could have been missed. If not due to a pseudo-periodic feature of the flow, the dispersion in the results could also be due to a mis-interpretation of the pictures. The Strouhal computed here is closer to that obtained with the spectrum. It is difficult to ascertain though that the peak in the spectrum describes the vortex shedding in the shear layer.

Eventually, the flow visualizations in all the planes showed the difficulty to associate a frequency to an aerodynamic phenomenon. The main difficulty in interpreting the visualizations is to confirm that the smoke puffs are actual vortices. They are not well defined in space and time. Also, they are even less visible in the  $y < 0$  shear layer of the  $z/h = 0.47$  plane. A more quantitative study is then required to detect the vortices.

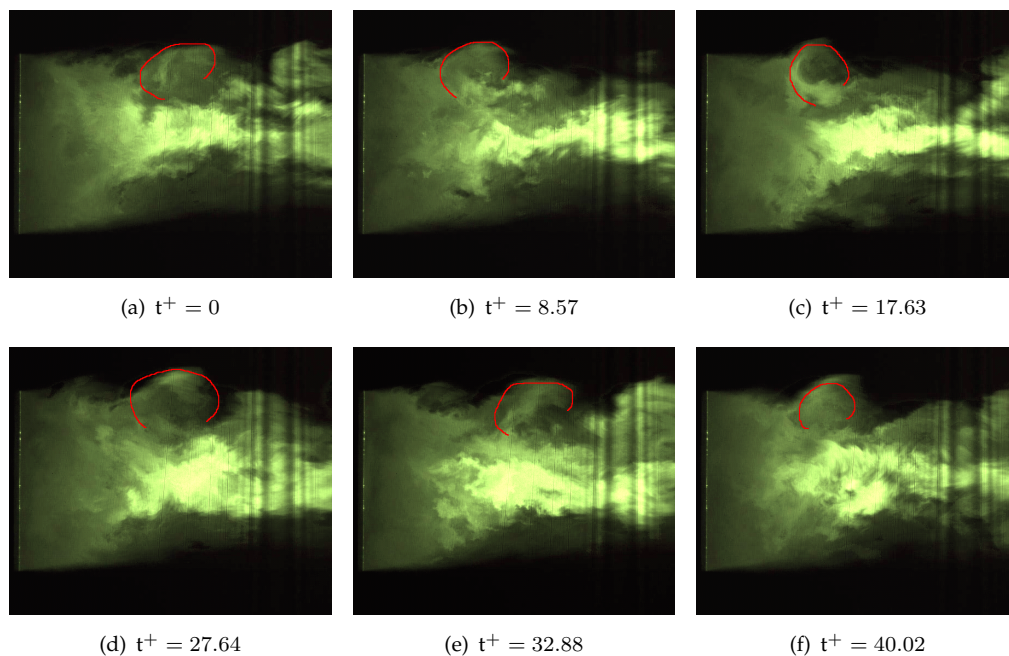


FIGURE 3.30: Time evolution of shear layer smoke puffs in the plane  $z/h = 0.47$  at  $Re_h = 1.65 \times 10^5$

### 3.3.4 Coherent structures in the flow

#### 3.3.4.1 Spatial cross-correlations

A first step towards the study of coherent structures can be done by computing the two-points spatial correlation tensor. The interest of this tensor, in particular for the study of near wall turbulence from PIV data has been shown for example by Stanislas et al. [167] and Lin [111]. The spatial auto-correlation and spatial cross-correlation discussed below were computed from the fluctuating velocity components on the 2D PIV data. They are defined as follows [28]:

Two-dimensional two point correlation function :

$$R_{u_i u_j}(\Delta x_1/h, \Delta x_2/h) = \frac{\langle u_i(x_1/h, x_2/h) u_j(x_1/h + \Delta x_1/h, x_2/h + \Delta x_2/h) \rangle}{\sigma_{u_i} \sigma_{u_j}} \quad (3.5)$$

In equation 3.5,  $u_i$  and  $u_j$  are any of the fluctuating velocity components available ( $u, v$  or  $w$ ).  $x_1$  and  $x_2$  are defined by  $(x_1/h, x_2/h) = (x/h, z/h)$  in the plane  $y = 0$  and  $(x_1/h, x_2/h) = (x/h, y/h)$  in the plane  $z/h = 0.5$ .  $\sigma_{u_i}$  is computed at position  $(x_1/h, x_2/h)$  whereas  $\sigma_{u_j}$  is computed at position  $(x_1/h + \Delta x_1/h, x_2/h + \Delta x_2/h)$ . From this equation, the streamwise one-dimensional two-points correlation function is obtained by setting  $\Delta x_2/h = 0$ . The other one dimensional two-points correlation functions are obtained by setting  $\Delta x_1/h = 0$ . From those measurements, it is possible to define a size associated to those coefficients.

### 3.3.4.2 Turbulence spatial integral length scale

From the previous two-dimensional two point correlation functions, a spatial integral length scale is defined as follows:

$$L_x^+/h = \int_0^{\infty} R_{uu}(x/h + n, 0) dn \quad (3.6)$$

In practice, it is not possible to integrate from 0 to  $\infty$  in equation 3.6. The integration domain must be bounded. Following O'Neill et al. [129], the integration domain was chosen to range from 0 to the value where the autocorrelation function falls to  $1/e$  (where  $1/e \approx 0.37$ ). Equation 3.6 can also be written with  $x/h - n$ : the integration is then performed in the upstream direction. Eventually, to take into account upstream and downstream integral length scales, the streamwise integral length scale is defined as

$$L_x/h = \frac{n^+ L_x^+/h + n^- L_x^-/h}{n^+ + n^-} \quad (3.7)$$

In equation 3.7,  $n^+$  and  $n^-$  are the values of  $n$  for which  $R_{uu}(x/h + n, 0)$  and  $R_{uu}(x/h - n, 0)$  respectively reach  $1/e$ . If they are both equal to zero, then  $L_x = 0$ . Similarly, a spanwise integral length scale  $L_{x_2}/h$  is defined as

$$L_{x_2}/h = \frac{n^+ L_{x_2}^+/h + n^- L_{x_2}^-/h}{n^+ + n^-} \quad (3.8)$$

where  $n^+$  and  $n^-$  are the values of  $n$  for which  $R_{uu}(0, x_2/h + n)$  and  $R_{uu}(0, x_2/h - n)$  respectively reach  $1/e$ . In this equation,  $L_{x_2}^+/h$  for example is defined as

$$L_{x_2}^+/h = \int_0^{\infty} R_{uu}(0, x_2/h + n) dn \quad (3.9)$$

Maps of the integral length scales are given in figures 3.31 and 3.32. In the  $y = 0$  plane, the biggest streamwise integral length scales (about  $h/2$ ) are found in the upper shear layer, in a region centered on  $(x/h, z/h) = (2.3, 0.7)$ . This is the region of maximum  $\langle uw \rangle$  correlation, as discussed before. High turbulent length scales are also found within the recirculation bubble, in the region centered on  $(x/h, z/h) = (0.65, 0.79)$ . As for the other integral length scale, the highest values (up to  $h/5$ ) are located downstream of reattachment, between  $(x/h, z/h) = (3.2, 0.77)$  and  $(x/h, z/h) = (4.3, 0.77)$  (see figure 3.31(b)). Those high integral length scales behind the step result exclusively from the step flow and are not influenced by the free-stream flow since the values there are close to zero. This translates that large scale vortices are expected behind the step and downstream of reattachment.

As for the  $z/h = 0.5$  plane, the highest values of streamwise integral length scales are found in a band a little under the centerline that goes through the recirculation bubble.

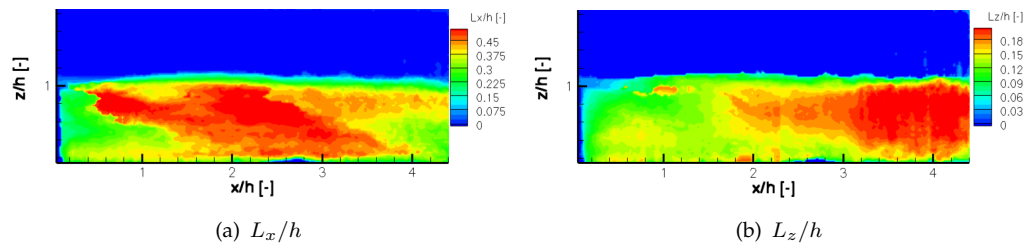


FIGURE 3.31: Spatial turbulence integral length scales in the plane  $y = 0.5$  at  $Re_h = 9.75 \times 10^4$

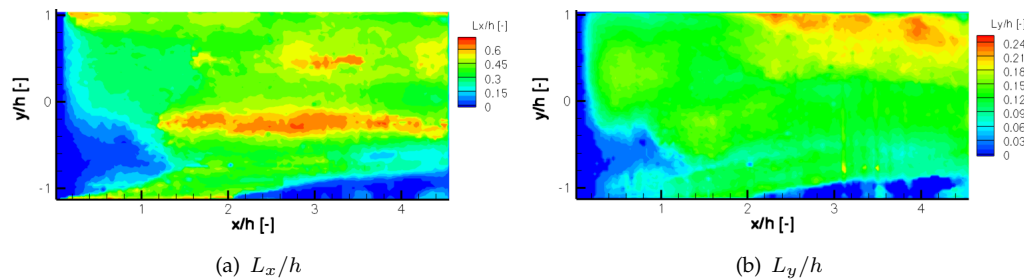


FIGURE 3.32: Spatial turbulence integral length scales in the plane  $z/h = 0.5$  at  $Re_h = 9.75 \times 10^4$

It stretches between  $(x/h, y/h) = (1.4, -0.25)$  and  $(x/h, y/h) = (4.0, -0.27)$ . Values up to  $0.55 h$  are reached there (see figure 3.32(a)). This spot is also related to the highest absolute values of  $\langle uv \rangle$ . Is this band where high scale vortices are shed?

Another spot is also centered a little downstream of reattachment, at mid-step height (centered on  $(x/h, y/h) = (3.1, 0.45)$ ). Lower values of the spanwise length scale are found ( $\leq h/4$ ). They occur in the wake of the stretched mean vortex, in the  $y > 0$  area (see figure 3.32(b)). Very low values are found in the wake of the bigger mean vortex (in the  $y < 0$  area). Does this mean no vortex appears in this region? Another method using vortex detection is needed to answer this question. In addition to the size, the autocorrelation coefficients can also give an idea of the shape of the vortices, as analyzed by Lin [111] in a boundary layer flow. Figure 3.33(a) is representative of the autocorrelation maps computed: the iso-contours for the autocorrelation coefficient are slightly stretched along the  $x$  axis. Do the integral length scales computed this way give an average size of the large scale coherent structures observed in the flow? As a comparison, a structure detection criterion is used in the following section. It will also help understand where the vortices are located.

### 3.3.4.3 Statistic study of the coherent structures

**Detection criteria** There exist several criteria to detect vortices in the flow. As exposed by Jeong and Hussain [84], some criteria such as the  $Q$  and  $\lambda_2$  criteria are based

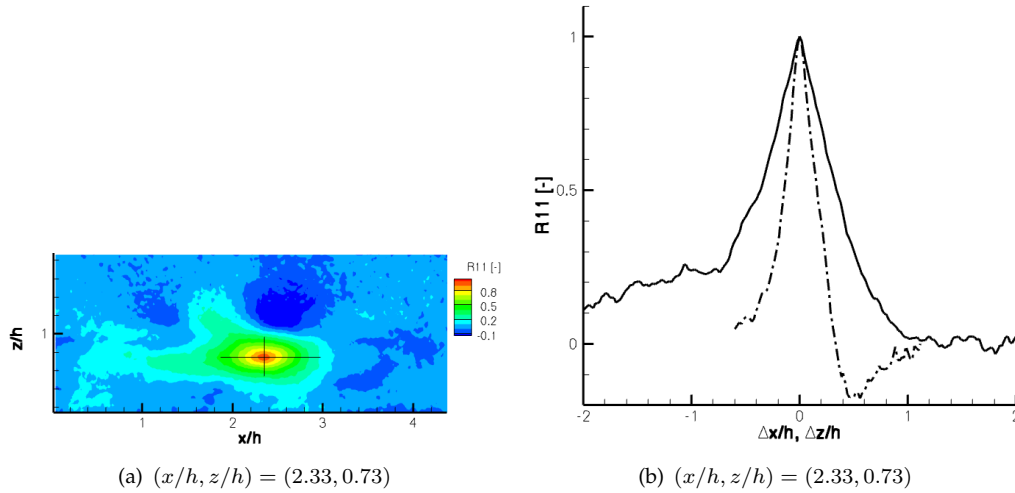


FIGURE 3.33: Streamwise autocorrelation coefficient along the  $x$  (solid) and the  $z$  (dot dashed) axis in the plane  $y = 0.5$  at  $Re_h = 9.75 \times 10^4$ . Data from the graphs (b) and (d) are extracted from the black line in (a) and (c) respectively

on the velocity gradients. This leads to some difficulties in case of PIV fields since:

- velocities are only measured on a plane whereas the flow is three dimensional. Therefore only 4 of the 9 velocity gradients can be computed in case of 2D2C PIV.
- velocity gradients of the instantaneous fields can be highly noisy

This is why Graftieaux et al. [71] propose 2 other criteria for PIV data:  $\Gamma_1$  and  $\Gamma_2$ . In what follows, the  $\Gamma_1$  criterion is used to detect coherent structures. Let  $P$  be a fixed point in the measurement domain. The dimensionless scalar function  $\Gamma_1$  at  $P$  is defined as:

$$\Gamma_1(P) = \frac{1}{S} \int_{M \in S} \frac{(\mathbf{PM} \wedge \mathbf{U}_M) \cdot \mathbf{z}}{\|\mathbf{PM}\| \cdot \|\mathbf{U}_M\|} dS = \frac{1}{S} \int_S \sin(\theta_M) dS \quad (3.10)$$

where  $S$  is a two dimensional area surrounding  $P$ ,  $M$  lies in  $S$  and  $\mathbf{z}$  is the unit vector normal to the measurement plane.  $\theta_M$  represents the angle between the velocity vector  $\mathbf{U}_M$  and the radius vector  $\mathbf{PM}$ .  $\Gamma_1$  is a dimensionless scalar taking values between -1 and 1. Those criteria are representative of the ratio of the deformation rate over the rotation rate. If the flow is incompressible, an analytical study based on the Lamb-Oseen vortex model shows that a vortex is detected when the absolute value of the criterion is greater than or equal to  $2/\pi$  [71]. Furthermore, the sign of  $\Gamma_1$  is directly related to the rotation sign of the vortex. Eventually, Castelain [33] illustrates the advantages of the  $\Gamma_1$  criterion over the vorticity criterion.

In practice, to process PIV snapshots, equation 3.10 is discretized as follows:

$$\Gamma_1(P) = \frac{1}{N} \sum_S \frac{(\mathbf{PM} \wedge \mathbf{U}_M) \cdot \mathbf{z}}{\|\mathbf{PM}\| \cdot \|\mathbf{U}_M\|} = \frac{1}{N} \sum_S \sin(\theta_M) \quad (3.11)$$



where  $N$  is the number of points  $M$  inside  $S$ . Then, the surface  $S$  must be properly chosen for accurate vortex detection. If  $S$  is too large, then velocities at locations  $M$  that are not correlated with the velocity at location  $P$  will be taken into account, which could alter the result. Therefore,  $S$  must be adapted to the flow. Several tests were performed in the present study. Using the  $\Gamma_1$  criterion, no influence of the side length of  $S$  was observed for values between 4 and 16 PIV mesh steps. A side length of 10 PIV mesh steps for surface  $S$  was then chosen, corresponding to  $0.23h$  and  $0.19h$  for the data in the  $z/h = 0.5$  and  $y = 0$  planes respectively. This weak effect of the parameter  $N$  on the location of the maximum value of  $\Gamma_1$  was already mentioned by Graftieaux et al. [71].

**Using spatially filtered snapshots** The  $\Gamma_1$  criterion was applied to the raw data in the planes  $y = 0$  and  $z/h = 0.5$ . Large and small structures are expected to be detected. However, it is thought that the larger scale coherent structures should be found in the case of vortex shedding. They should also present higher levels of energy. Therefore, the detection criterion was applied to spatially filtered instantaneous PIV fields using POD (see appendix C). For both the  $y = 0$  and  $z/h = 0.5$  planes, 110 and 200 modes were respectively considered to approximate the snapshots and retrieve 75% of the fluctuating flow energy. In a second time, the same was done using 37 and 77 modes respectively to retrieve 60% of the fluctuating flow energy in both planes (as discussed later on in section 5.2.2, this value is interesting for the launch and recovery of helicopters). Examples of the  $\Gamma_1$  criterion applied to typical snapshots (raw and POD filtered) are found in figure 3.34. From figure 3.34, where high values  $\Gamma_1$  are found, the streamlines often wind up, which seems to confirm that a vortex has been detected. In both planes, POD filtering smoothes the snapshots, as shown by the streamlines. Also, some vortices detected in the unfiltered data disappear in the filtered snapshots, revealing there are low in energy. However, to conclude about the position of the vortices, more snapshots must be analyzed. Therefore, a statistic study was applied on the snapshot series of both planes.

**Trajectory of the vortices** In both planes, the  $\Gamma_1$  criterion was applied to each snapshot of the series. Then, probability density functions were computed:  $p_n$  determines the probability to find a vortex rotating in a clockwise manner at a given position of the PIV field.  $p_{n_{max}}$  is the maximum value of the probability function. In practice, let  $N_{n_{max}}$  be the maximum number of vortices rotating in a clockwise manner and found in a same position of the PIV field. Let also  $N_n$  be the number of vortices rotating in a clockwise manner and found in a given position of the PIV field. Then  $p_n/p_{n_{max}} = N_n/N_{n_{max}}$ . Similarly,  $p_p/p_{p_{max}}$  is defined for the vortices rotating in an anti-clockwise manner. The probability functions are computed on the initial PIV mesh

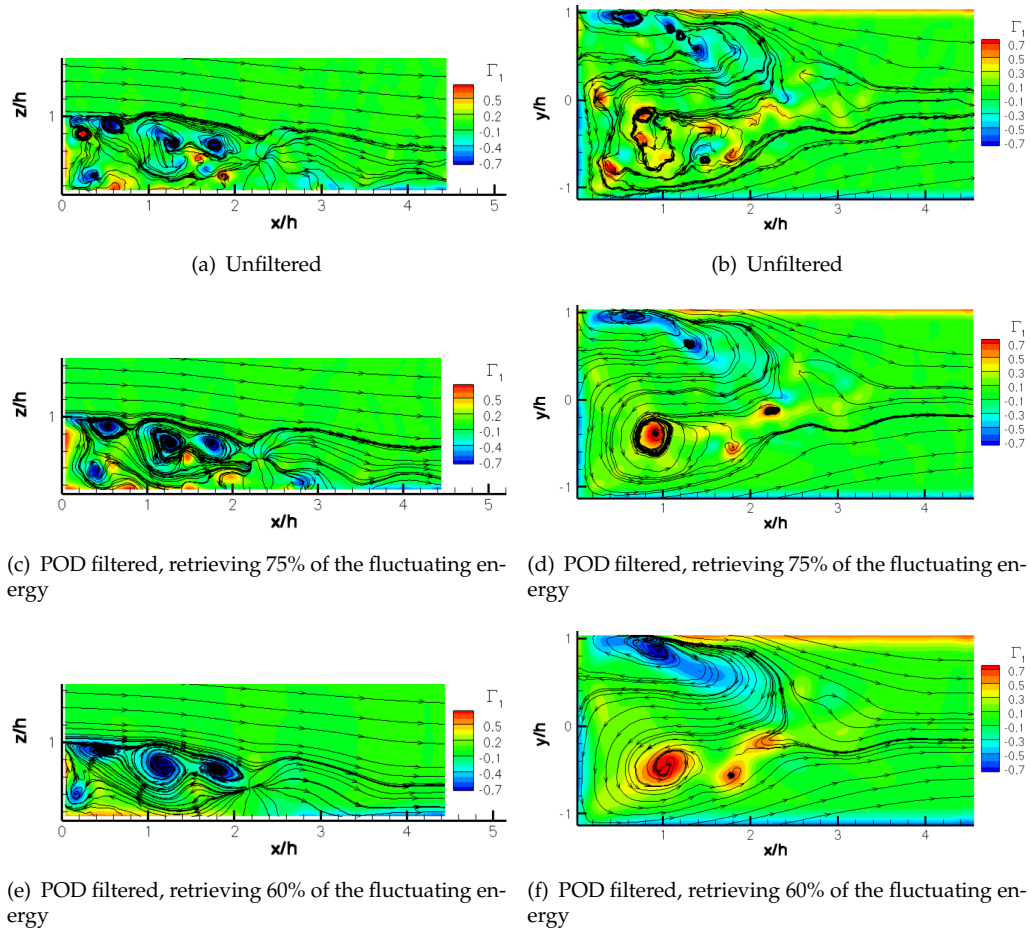


FIGURE 3.34: Coherent structures detection in the planes  $y = 0$  ((a),(c),(e)) and  $z/h = 0.5$  ((b),(d),(f)) at  $Re_h = 9.75 \times 10^4$  using the  $\Gamma_1$  criterion. In black, the 2D streamlines

and results are plotted in figures 3.35 and 3.36 for the planes  $y = 0$  and  $z/h = 0.5$  respectively. In both planes, no vortex is detected in the high speed regions, downstream of reattachment. This does not mean however that there are none. It is more a drawback of the  $\Gamma_1$  criterion. This criterion is nonetheless sufficient to detect the vortices generated within the shear layers. In the plane  $y = 0$ , most of the clockwise-rotating vortices are concentrated in the shear layer and some of them reach the wall around the reattachment area (see figures 3.35(a), 3.35(c) or 3.35(e)). Most of them are high energy vortices as the effect of POD filtering is not strong on the maps obtained (see figures 3.35 and 3.36). A small amount of anti-clockwise vortices are concentrated behind the step (around  $(x/h, z/h = 0.5, 0.2)$ ). Are they shed from the secondary bubble? The area of higher probability to find those vortices suggests a trajectory in the  $y = 0$  plane going vertically from the lower wall to the shear layer while going upwards close to the step. Then, such vortices seem to be taken away from the step with the shear layer. A further investigation should confirm this scheme.

In the  $z/h = 0.5$  plane, the clockwise rotating vortices are found in the  $y > 0$

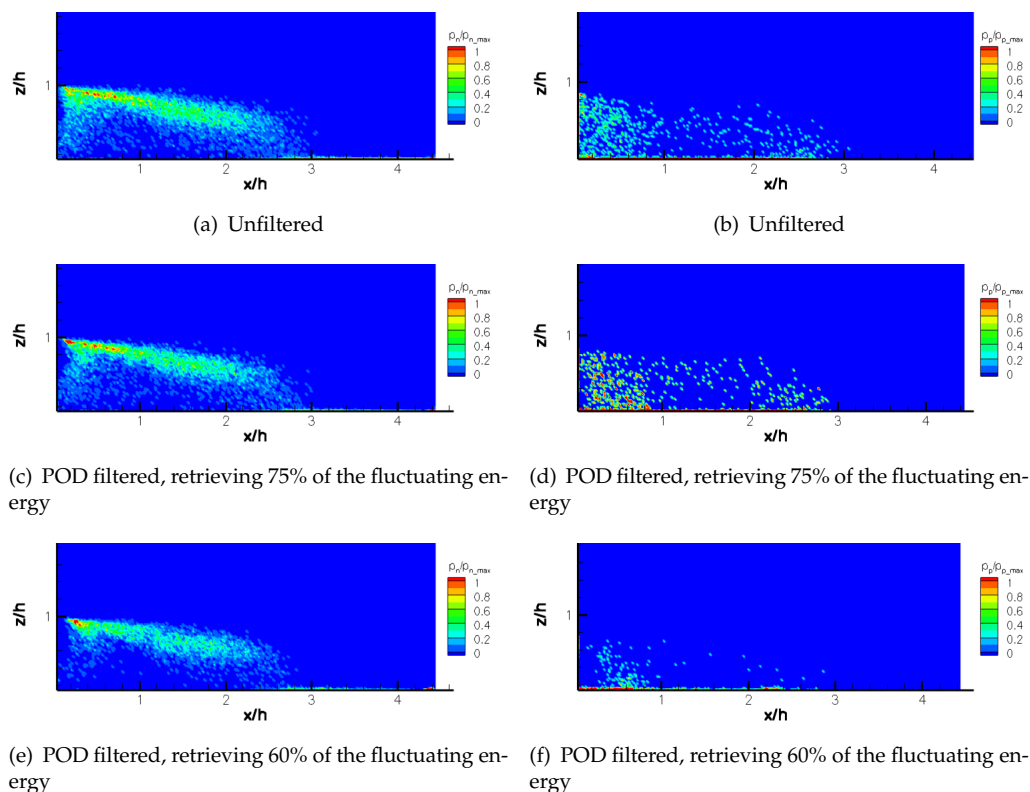


FIGURE 3.35: Maps of the normalized probability to find vortices in the plane  $y = 0$  at  $Re_h = 9.75 \times 10^4$  using the  $\Gamma_1$  criterion

shear layer. They are concentrated in a band as it is the case in the shear layer of the  $y = 0$  plane. However, this is not the case in the  $y < 0$  shear layer of the  $z/h = 0.5$  plane. On that side of the model, there are two areas of highest probability to find an anti-clockwise rotating vortex. The first area is centered on position  $(x/h, y/h) = (0.67, -0.42)$ . This corresponds to the position of the center of the bigger vortex  $V_2$  as described in table 3.3. On the other hand, the second area is a band centered on  $(x/h, y/h) = (2, -0.4)$ . Those two areas do not seem to be well connected (see figures 3.36(b), 3.36(f) or 3.36(f)). Therefore, this raises questions about the generation and behavior of those anti-clockwise rotating vortices: is the vortex  $V_2$  shed? If so, shouldn't the two areas be well connected? If not, then are the shed vortices of the second area generated by the  $y < 0$  shear layer? Here again, further investigation is needed before conclusions can be drawn with confidence.

Eventually, this is another confirmation that the unsteady behavior of the flow is not symmetric (in the plane  $z/h = 0.5$ ). In the plane  $z/h = 0.5$ , on the  $y > 0$  model side, the vortices detected in the shear layer seem to be generated similarly as in the shear layer of the  $y = 0$  plane. When time-averaged, those vortices give rise to a stretched vortex (see figure 3.9). This shedding process does not seem to be the case in the plane  $z/h = 0.5$ , at least regarding the vortex  $V_2$ , which, when time-averaged, is not stretched

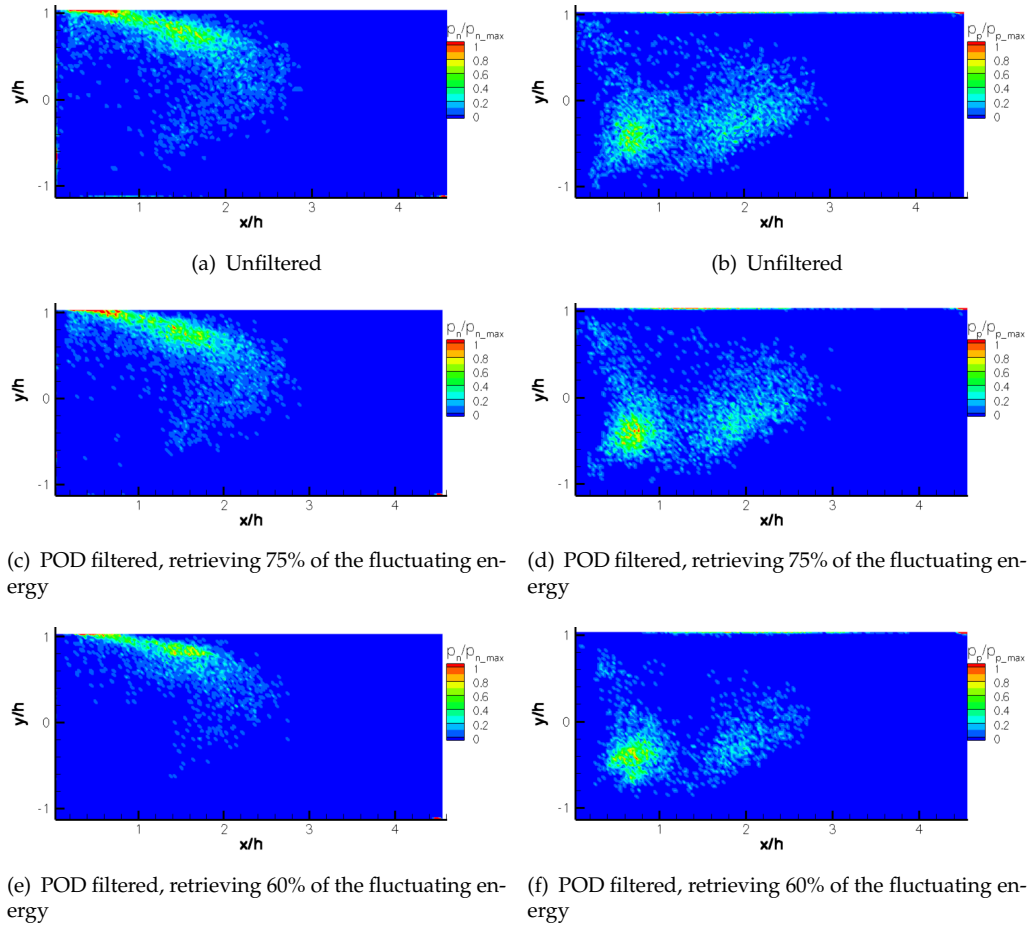


FIGURE 3.36: Maps of the normalized probability density to find vortices in the plane  $z/h = 0.5$  at  $Re_h = 9.75 \times 10^4$  using the  $\Gamma_1$  criterion

(see figure 3.9). Further investigation is needed to get a good understanding of the 3D unsteady behavior of the flow.

**Advection velocity** The average advection velocity of the vortices shed between  $0 \leq x/h \leq 2$  in the plane  $y = 0$  was first estimated through the laser tomography visualizations. Even if the smoke puffs are not actual vortices in figures 3.28, their advection velocity can be determined. From those figures, one can determine that a puff covers a distance  $d/h = 1.38$  in  $t^+ = 2.249$ , that is  $\frac{U_{adv}}{U_0} = \frac{d}{U_0 t} = \frac{d/h}{t^+} = 0.6$ . The uncertainty on this measure is relatively high though, since the center of the puff cannot be easily located. Also, this analysis should be done on many sequences to have a fairly good ensemble average. Since this operation can hardly be automated, it was decided to estimate the advection velocity through hot-wire measurements.

The average advection velocity of the coherent structures was measured at different positions behind the first step as illustrated in figure 3.37(a) (for a better visualization of the positions, their projections on the step face were previously given in figure

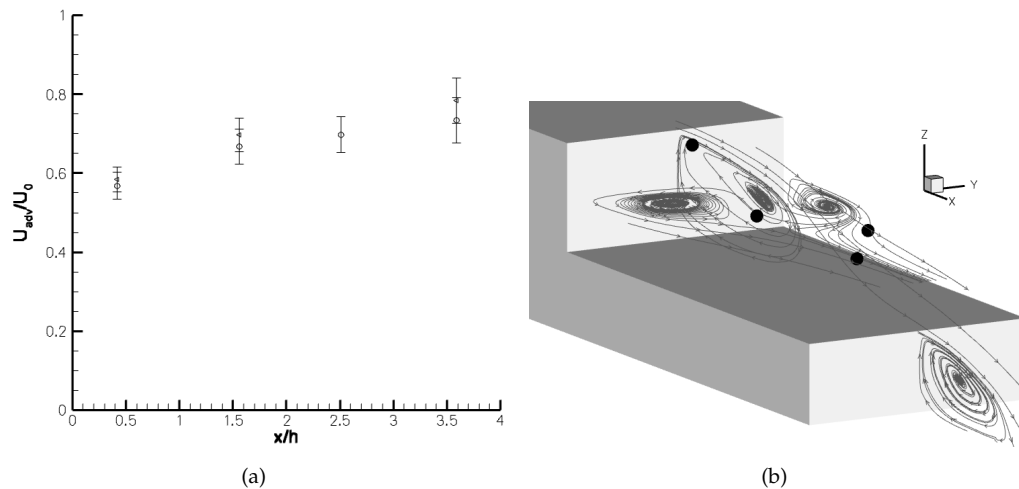


FIGURE 3.37: (a) Mean advection velocity of the coherent structures in different positions behind the first step at Reynolds number  $Re_h = 9.75 \times 10^4$  (circle) and  $Re_h = 1.65 \times 10^5$  (triangle). (b) illustration of the positions probed

2.5(b)). The results obtained for two upstream velocities are shown in figure 3.37(b). On the SFST, Tinney and Ukeiley [175] have computed advection velocities ranging from  $0.7 U_0$  at  $(x/h, y/h, z/h) = (3, 0, 0.8)$  to  $0.76 U_0$  at  $(x/h, y/h, z/h) = (6, 0, 0.8)$ . On the SFSO', at higher Reynolds number, those values vary from  $0.6 U_0$  at  $(x/h, y/h, z/h) = (0.417, 0, 0.51)$  to  $0.75 U_0$  at  $(x/h, y/h, z/h) = (3.588, 0, 0.49)$  with an estimated uncertainty lower than 10%. If the measuring locations and the geometries are different in the two experiments, the advection velocities are of the same order of magnitude. Both tests show that the advection velocity increases along the  $x$  axis, implying that the flow structures accelerate during their advection as they reach the high speed region of the flow.

#### 3.3.4.4 Reynolds effect

In this chapter, results of experiments performed at different Reynolds numbers were presented. The ratio of the highest Reynolds numbers over the smallest is less than a factor of 2. Evolution against the Reynolds number of reattachment length and Strouhal numbers is negligible. It is then assumed that the Reynolds number effect is not a major issue on either the mean or the unsteady flow features in the range considered here. This explains why data are compared despite different Reynolds numbers.

### 3.4 Summary

Global conclusions were drawn on the steady and unsteady flow characteristics behind a 3D backward facing double step at zero degree sideslip and high Reynolds number. Complementary qualitative and quantitative experimental methods were confronted. In particular, they confirm the mean flow asymmetry observed by Syms [170]. However, no explanation results from the data gathered here. A sensibility study should be performed to see if the asymmetry changes side with a different drift angle. If the asymmetry does have some cause/consequences on the unsteady behavior and for the launch and recovery issue, this feature could be more than relevant. This is why the next chapter focuses on this particularity of the flow.



## Chapter 4

# Analyzing the mean flow asymmetry downstream of 3D double backward facing steps around the zero degree sideslip angle

In the previous chapter, despite the geometrical zero degree sideslip angle and the symmetric geometry, an asymmetric mean flow downstream of the first step was observed. This feature was already mentioned by Syms [170] on the SFS2 but has remained unexplained. However, this could have an impact on the launch and recovery of helicopters. Therefore, attention is paid to this phenomenon. In particular, is the mean flow asymmetry a stable phenomena appearing for a wide range of drift angles? Is it inherent to 3D double backward facing step flows? To answer those questions, a parametric study was conducted. First of all, the influence of the drift angle around the zero degree sideslip angle was investigated on the SFSO'. Then, the influence of the upstream conditions on the flow was studied. In this respect, several geometries were tested at different Reynolds numbers, in different wind-tunnels. Both experimental and numerical approaches were adopted.



## 4.1 Mean flow sensitivity to variations of the drift angle

### 4.1.0.5 Oil flow visualization

To see the influence of the drift angle on the mean flow, a first qualitative approach was conducted, using oil-flow visualization. The same procedure as in 3.2.1 was adopted, except for the geometric drift angle that was set to  $\beta_g = 0.21^\circ$  (opposite sign of the case described in 3.2.1). The pattern obtained is shown in figure 4.1. Contrary to the other

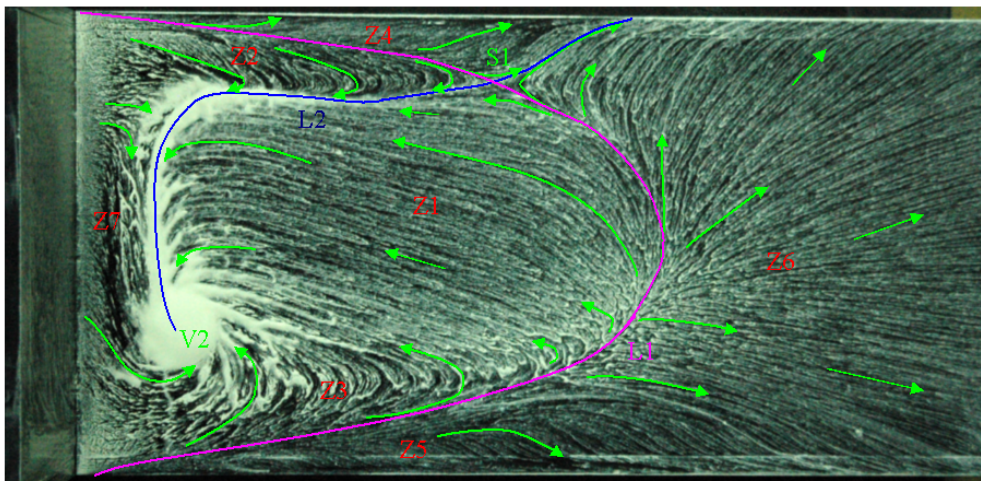


FIGURE 4.1: Surface oil flow visualization on the top surface of the backward cuboid at  $\beta_g = 0.21^\circ$

drift angle tested (see figure 3.3), the asymmetry here is more pronounced. The pattern at the surface is more like the projection on the surface of the flow in the  $z/h = 0.5$  plane (see figure 3.7(c)). Indeed, vortex  $V_2$  (on the  $y < 0$  side) is much bigger than vortex  $V_1$  (on the  $y > 0$  side of the model). As a matter of fact, it is difficult to locate the center of vortex  $V_1$ , since it is stretched. This picture seems to reveal a different behavior on both sides of the model: vortex  $V_2$  seems to be the center of rotation of the fluid just above the surface, within the recirculation bubble. In this respect, no convergence line (in blue) can be drawn between zone Z3 and Z1 on the  $y < 0$  side, contrary to the  $y > 0$  side where it is drawn. Eventually, considering the singular points classification of Hunt et al. [82], it seems like there is one attachment nodal point which is foci ( $V_2$ ), one separation saddle point (S1), the other singular points (if they exist) being not clearly visible. In particular, the reattachment saddle point is barely visible. It is strange though that the surface pattern at  $\beta_g = 0.21$  (see figure 4.1) is not the symmetric of the pattern obtained for  $\beta_g = -0.21$  (see figure 3.3). This requires more drift angle testing. Since the asymmetry was already observed in the  $z/h = 0.5$  plane, it was chosen to conduct this sensitivity study through PIV measurements. Therefore, the degree of asymmetry could be quantified, as long as a quantitative criteria is defined.

#### 4.1.0.6 PIV

PIV was performed in the  $z/h = 0.5$  plane. The experimental setup was the same as in the previous chapter 3 except for one detail: a traverse system was mounted in order to control precisely the model drift angle (see 2.2.1.1 for details on the setup). The flow was then analyzed for several drift angles around  $\beta_g = 0^\circ$ . The wind tunnel was shut down during the change in drift angle. Eventually, three representative PIV fields (for positive, almost zero and negative drift angles) are illustrated in figure 4.2. For drift angles  $0^\circ \leq \beta_g \leq 5^\circ$ , all the PIV fields are very similar to the field obtained at  $\beta_g = 0^\circ$  and already presented in figure 3.7. From now on, this field will be labeled  $A_1$ .  $A_1$  is characterized by a big vortex (time-averaged) on the  $y < 0$  side and a stretched one on the other side. On the contrary, for geometric drift angles  $-5^\circ \leq \beta_g \leq -0.7^\circ$ , all the PIV fields are quite similar to a field henceforth referred to as  $A_2$ . If a mirror was placed in  $y = B/2$  of the field  $A_1$ , then  $A_2$  would be the symmetric of  $A_1$  with respect to the mirror. However, for drift angles  $-0.7^\circ \leq \beta_g \leq 0^\circ$ , the field is not as asymmetric. This can be quantified by introducing the  $\Phi$  angle:  $\Phi$  is defined as the angle between the  $y_{model}$  axis and the (purple) line passing through the centers of the two vortices  $V_1$  and  $V_2$  (for the coordinate and vortices definitions, refer to 2.1(b) and 3.2.1 respectively). Therefore, the greater  $\Phi$  in absolute value, the greater the asymmetry. This level of asymmetry is then measured by studying the evolution of the  $\Phi$  angle against  $\beta_g$ . A small correction is applied by adding  $\beta_g$  to  $\Phi$  to measure the angle with the y axis, not the  $y_{model}$  axis. As illustrated in figure 4.2, it comes that the  $\Phi + \beta_g$  angle is very high for  $-5^\circ \leq \beta_g \leq -0.7^\circ$ , with values exceeding  $20^\circ$ . By symmetry of the fields, the  $\Phi + \beta_g$  values are very low, under  $-20^\circ$ , for  $0^\circ \leq \beta_g \leq 5^\circ$ . In the very narrow band in-between, namely  $-0.7^\circ \leq \beta_g \leq 0^\circ$ ,  $\Phi$  varies brutally by more than  $-60^\circ$ . Despite the use of the traverse system enabling very small changes in drift angles, the symmetric flow was not obtained. The field the closest to symmetric presents an angle  $\Phi = -13.4^\circ$ .

This graph illustrates that the geometric drift angle should have been a little less than zero to expect obtain the symmetric mean flow. Indeed, if a curve interpolates the experimental data points,  $\Phi = 0$  would be expected at about  $\beta_{g0} = -0.2^\circ$ . From this remark, the aerodynamic drift angle  $\beta_a$  is defined as :

$$\beta_a = \beta_g - \beta_{g0} \quad (4.1)$$

Perfect experimental conditions should give rise to  $\beta_{g0} = 0^\circ$ . However, imperfections in the model geometry and the non-uniformity of the flow are certainly the major causes of this difference. Furthermore, this non zero  $\beta_{g0}$  value explains why the oil visualization obtained for  $\beta_g = -0.21$  is not the symmetric of the flow pattern obtained for  $\beta_g = 0.21$  (see figures 3.3 and 4.1 respectively). Those values suggest that  $\beta_a$  was just

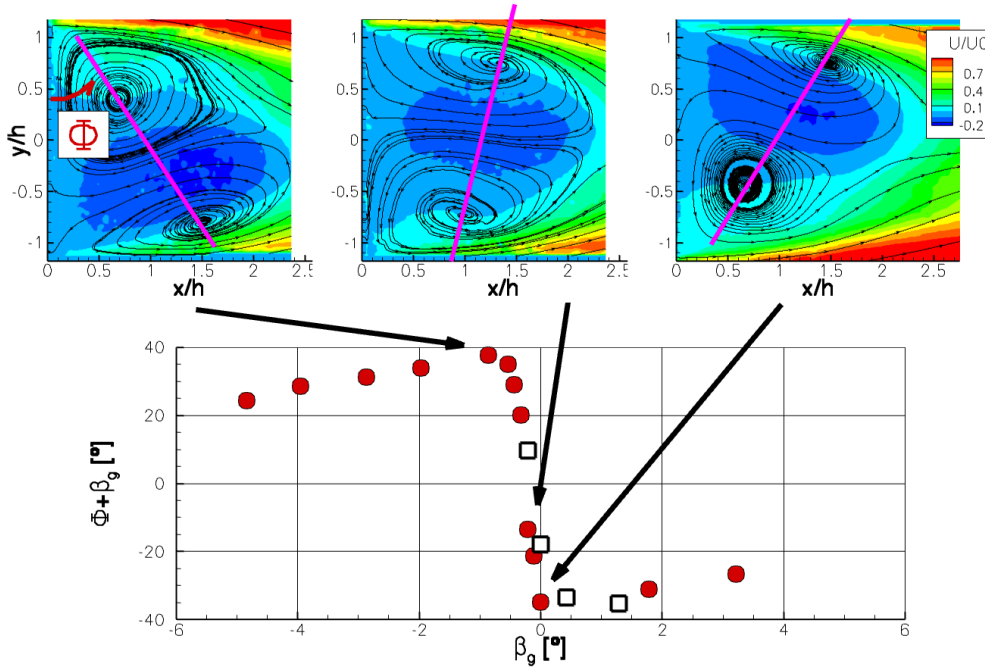


FIGURE 4.2: PIV on the SFISO' in the  $z/h = 0.5$  plane: evolution against the drift angle of streamlines and iso-contour of  $U/U_0$  without (red circles) and with the hysteresis test (squares).  $Re_h = 9.75 \times 10^4$

slightly negative for the  $\beta_g = -0.21$  oil flow visualization. It can already be seen on figure 3.3 that the flow already slightly tends towards configuration  $A_2$  with a bigger vortex on the  $y > 0$  side of the model. The symmetric mean flow seems then difficult to obtain. Is it impossible?

Syms [170], whose computations did not hold a priori such geometric imperfections, computed the asymmetric mean flow. This other argument suggests that the flow is probably unstable at exactly  $\beta_a = 0^\circ$  and tends towards either  $A_1$  or  $A_2$ . Eventually, is the symmetric flow an unstable solution of the flow? Are  $A_1$  or  $A_2$  two stable solutions? If this is the case, a consecutive question arises: consider for example the flow in configuration  $A_1$ , assumed to be a stable solution; if the drift angle  $\beta_a$  continuously evolves towards zero, with the relative wind velocity remaining constant in strength, will the flow switch to  $A_2$  after passing  $\beta_a = 0$  or will it remain in the  $A_1$  configuration until it reaches a critical value of  $\beta_a$ ? In other words, is there an hysteresis effect? To answer this question, the wind-tunnel was run continuously with the drift angle being changed remotely after each run, using the traverse system. The first drift angle was chosen positive and the three following ones were smaller, making sure the last one was smaller than  $\beta_{g_0}$ . The results are plotted in figure 4.2 (black squares): the data of this test follow very well the trend of the data obtained by setting the relative wind-speed to zero after each run. In this respect, it was thought from those data that the hysteresis effect was negligible, if not inexistent. Therefore, the full hysteresis cycle

was not completed.

Eventually, the mean flow asymmetry has been observed for both the SFSO' and the SFS2. Is this phenomenon the result of particular upstream conditions? Is it inherent to double backward facing step flows? Some parameters were then changed to see their influence on the mean flow asymmetry.

## 4.2 Influence of the upstream conditions on the mean flow asymmetry

### 4.2.1 Approach

Let us assume that there are two main families of parameters that could influence the mean flow sensitivity to the drift angle : (i) the upstream conditions and (ii) the step geometry. The influence of the two families of parameters is not necessarily exclusive. This part focuses on the upstream conditions. An analysis is then conducted so as to cover most of the possible upstream conditions.

Any modification upstream of the step should have an influence on the characteristics of the boundary layer separating at the first step edges. The boundary layer is characterized by several global parameters: the velocity outside the boundary layer and at the wall, the different thicknesses relative to the step height and the ratio between those thicknesses. To those parameters must be added the structure of the turbulence globally characterized by turbulence levels and spectrum. An extensive study of those parameters would lead to a huge amount of tests. Therefore, to limit the number of tests, some hypotheses were made, resulting from some observations : the PIV measurements in the  $z/h = 0.5$  plane show a slightly greater mean velocity on the side of the big vortex than on the side of the stretched vortex. It was then proposed that :

**Hypothesis 1** : *a mean velocity difference between the lateral sides of the central cuboid induces the mean flow asymmetry*

In what follows, the mean velocity difference between the lateral sides of the central cuboid is noted  $\Delta U$ . Another hypothesis was made, considering the results from Syms [170] obtained on the SFS2 : this geometry has a funnel on the top surface of the central cuboid, upstream of the step. As shown by Forrest and Owen [64], it induces a lot of turbulence. Since the mean flow was also observed on the SFSO', the other hypothesis holds :

**Hypothesis 2** : *the mean flow asymmetry is little influenced by the characteristics of the upper upstream boundary layer*

To verify hypothesis 1, only the difference in the lateral walls' mean velocity should be varied, the other parameters remaining constant. The choice of the nose should control this condition: it is thought that the relative sharp edges of the SFSO' and SFS2 noses fix the stagnation point away from the model centerline. This would induce a velocity greater on one side than on the other. It is thought that removing those edges would help fix the stagnation point as close to the model centerline as possible, for drift angles close to zero: the rounded nose of the SFSC' should be well-suited for this. Considering the flow around a cube where the stagnation point is close to the centerline, it is possible that no nose, like in the SFS1 case, has the same effect as the rounded nose of the SFSC.

To verify hypothesis 2, the characteristics of the upper boundary layer must be varied while the mean flow asymmetry is observed. In practice, it was thought it could be controlled using a square section cylinder mounted on the central cuboid top surface, its length aligned with the  $y_{model}$  axis. Its dimensions were chosen equal to B in length and  $D/h = 0.0735$  in height. According to Shi et al. [159], since the reattachment behind such cylinders is between 5 and 7 cylinder heights, two types of boundary layers could be generated : (i) attached and (ii) separated, by placing the cylinder upstream of the step at  $x/D = -10$  and  $x/D = -2$  respectively. In table 4.1, the use of the cylinder in both positions is noted (b) and (c) respectively. It should be mentioned that the SFS1' should induce (b) type boundary layers on each of its 3 faces without the need to use the cylinder. The same would go with the top face of the SFSC', due to the flow separation at the nose. The funnel was also added in some cases to increase the turbulence levels. The (a) stands for flat-plate-like boundary layer types. This is found on the three sides of the SFSO' (see chapter 3) and the lateral sides of the SFSC' [171].

The test matrix is then reported in table 4.1: on a same line, the velocity difference on

TABLE 4.1: Configuration tested

	C1	C2	C3
L1	SFSO' (aaa)	SFSO' (aba)	SFSO' (aca)
L2		SFSC' (aba)	SFSC' (aca)
L3		SFS1' (bbb)	SFS1' (bcb)

the sidewalls is expected to be fixed by the nose. This aims at showing the influence of the upper boundary layer on the asymmetry. Not all the possible upper boundary layers are considered though (such as SFSO' (bbb), SFSO' (cbc), etc.). However, if hypothesis 1 is valid, those tests are not necessary. Column C2 shows the influence of  $\Delta U$  for a type a sidewall boundary layer. It also shows the influence of a type b lateral

boundary layer at fixed  $\Delta U$ . Column C3 aims at showing the influence of  $\Delta U$  for a type a boundary layer and also shows the influence of type a and b boundary layers for a given  $\Delta U$ . Those seven configurations enable to modify one parameter at a time. However, they are not sufficient to assert whether or not those parameters behave dependently. This would require more tests.

More tests should also be carried out to see the influence of the geometry shape on the asymmetry. This will not be the focus of the present study. Only the configurations of table 4.1 were then tested in the L2 wind tunnel. This wind-tunnel was also chosen in order to see the influence of other parameters on the mean flow asymmetry : for the other results presented previously, the model was mounted on a table within a low turbulence uniform flow at  $Re_h = 9.75 \times 10^4$ . Here, in the L2 wind-tunnel, the model is directly mounted on the lower wall of the wind-tunnel: it is immersed in a simulated atmospheric boundary layer. Another consequence is that no flow can go under the model, which will certainly break the flow uniformity upstream of the step. The Reynolds number is set a little higher at  $Re_h = 1.15 \times 10^5$ . Therefore, if the asymmetry is also observed under those conditions on the SFSO', this will mean that there is no influence of simulated atmospheric boundary layer nor increase in Reynolds number nor non uniformity of the upstream flow.

The results are presented below.

## 4.2.2 Experimental results

### 4.2.2.1 Verifying the test cases

The first stage consists in verifying that the proposed test cases in table 4.1 enable to obtain the expected boundary layer characteristics and  $\Delta U$ . To do so, smoke visualization was performed on the different configurations.

**Probing the boundary layers on the model walls** The flow separation on the SFS1 has already been sufficiently described in Cheney and Zan [38]. The flow separation on the upper face of the central cuboid and its attachment on the sidewalls is illustrated in figure 4.3. As for the SFSO', the flow is attached on the upper and sidewalls as illustrated in figure 4.4.

The last figures show the effect of the cylinder on the upper wall boundary layer: separation and reattachment before the step for the cylinder placed at  $x/D = -10$  (figure 4.5(a)) and separation without reattachment when it is placed at  $x/D = -2$  (figure 4.5(b)). The effect of the nose and cylinder on the boundary layers developing on the upper and sidewalls is confirmed through those smoke visualizations. Only the

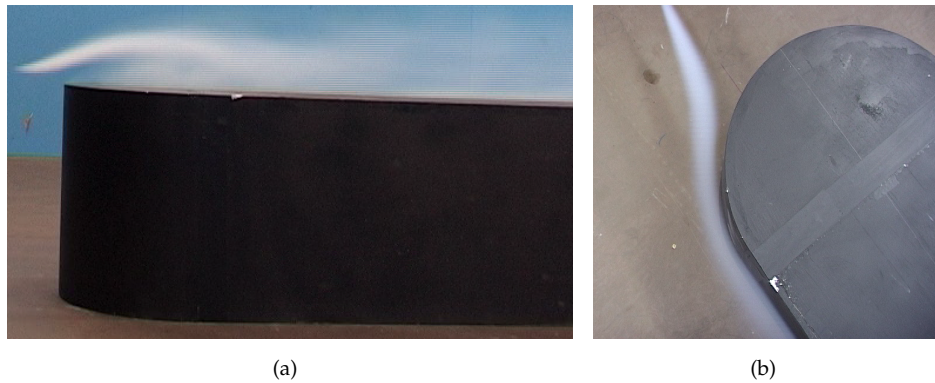


FIGURE 4.3: SFSC': flow is detached on the upper wall (a), attached on the lateral walls (b)

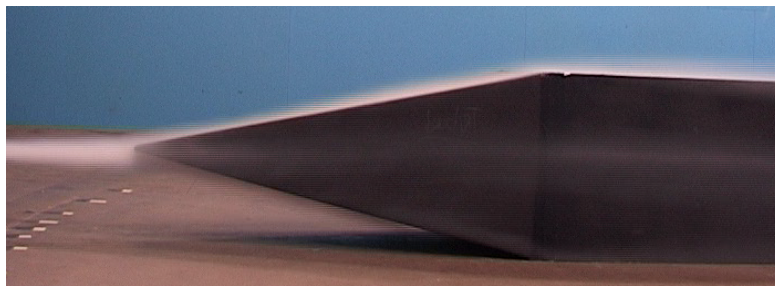


FIGURE 4.4: Attached flow on the upper and sidewalls of the SFSCO'

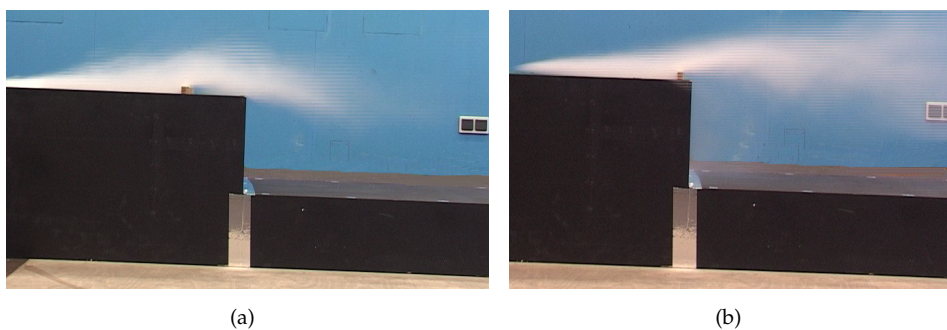


FIGURE 4.5: Effect on the upper boundary layer of the cylinder placed upstream of the first step at (a)  $x/D = -10$  and (b)  $x/D = -2$

difference in velocity could not be determined through this qualitative approach. A quantitative method was then adopted.

**Determining  $\Delta U$**  According to the equations for flat-plate zero pressure gradient boundary layers [156], at first order, the pressure is constant through the boundary layer at constant  $x$  locations ( $x$  being the direction of the development of the boundary layer). Outside the boundary, where  $U = U_e$ , it is relevant to consider the inviscid flow approximation. Furthermore, since the Mach number is well below 0.3, the incompressible flow approximation is also valid. The conditions are then met to apply

Bernoulli's equation on a streamline:

$$p_0 + \frac{1}{2}\rho U_0^2 = p(x) + \frac{1}{2}\rho U_e^2(x) \quad (4.2)$$

Eventually, if the free-stream flow is considered irrotational, then equation 4.2 is not only valid on a streamline, but everywhere in the flow. In particular, applying equation 4.2 on both sides of the model yields:

$$p_{(y>0)} + \frac{1}{2}\rho U_{(y>0)}^2 = p_{(y<0)} + \frac{1}{2}\rho U_{(y<0)}^2 \quad (4.3)$$

Let be  $\Delta Cp = Cp_{(y>0)} - Cp_{(y<0)}$ . Putting the velocities on one side of the equality and the pressures on the other side, dividing by  $U_0$  and eventually doing a first order Taylor expansion in  $\Delta Cp$  yields:

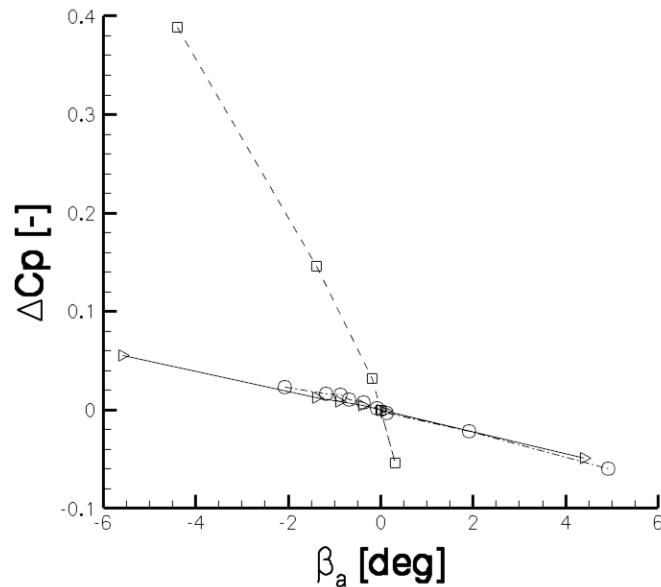
$$\frac{\Delta U}{U_0} = \frac{U_{(y>0)} - U_{(y<0)}}{U_0} = -\frac{2(p_{(y>0)} - p_{(y<0)})}{\rho(U_{(y>0)} + U_{(y<0)})U_0} = -\frac{\Delta Cp}{2}(1 + \mathcal{O}(\Delta Cp)) \quad (4.4)$$

As is shown in figure 4.6(a), since  $\Delta Cp \ll 1$  (except for the SFS1'), then  $\frac{\Delta U}{U_0} \approx -\frac{\Delta Cp}{2}$ . The direct consequence is that  $\Delta U/U_0$  is rather small for the SFSO' and SFSC' case, less than 1% for  $|\beta_a| < 2^\circ$ .  $\beta_a$  is defined in this graph such that  $\beta_a = 0$  when  $\Delta Cp = 0$ . This small difference in  $\Delta U$  between the SFS1' and SFSO' cases suggest that if their stagnation point is not the same, at least their effect on  $\Delta U$  is negligible. On the contrary,  $\Delta U$  is much higher for the SFS1', whereas a similar behavior as for the SFSC' was expected. An explanation for this would probably be that the pressure taps on the SFS1' are located in an area that is affected a lot by the massive flow separation occurring at the beginning of the central cuboid. Therefore, for the SFS1', pressure coefficients closer to the step should be plotted, where the flow has reattached on the model sidewalls. This will be done later on. Indeed, graph 4.6(a) aimed at quantifying the effect of the nose on  $\Delta U$  and required pressure measurements the closest to the nose. It eventually shows that the effect of the rounded and pyramidal shaped noses on  $\Delta U$  is similar. Therefore, the idea that  $\Delta U$  would be increased by using the SFSO' instead of the SFSC' proves to be wrong. Is the asymmetry still visible on the SFSC' then, not disapproving hypothesis 1?

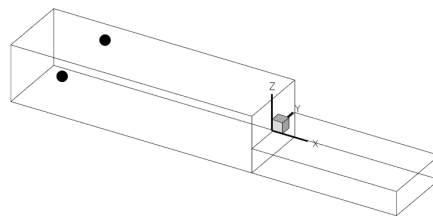
#### 4.2.2.2 Laser tomography visualizations

As a reference case, and to compare with the previous test campaign, the flow over the SFSO' was first visualized. A representative instantaneous image is shown in figure 4.7. By watching the videos shot, it is obvious to see the mean flow asymmetry on the SFSO' at  $|\beta_g| > 2^\circ$ : the majority of the snapshots show a big vortex on one side and





(a)



(b)

FIGURE 4.6: (a)  $\Delta C_p = C_{p_{y>0}} - C_{p_{y<0}}$  against  $\beta_a$  at position  $(x/h, z/h) = (-5.88, 0.5)$  (illustrated in figure(b)) at  $Re_h = 1.8 \times 10^5$  for the SFSO' (triangles), SFSC' (circles) and SFS1' (squares)

one or several smaller vortices on the other side. For a given drift angle, the big vortex is visible most of the time on the same side of the model. To give a mean picture of the flow, an ensemble average on the luminosity was then attempted on the snapshots of a given series. This proved unsuccessful since the smoke rod was not fixed during the tests and therefore, there was no concentration of smoke (and then luminosity) in a particular area (of either the big or the stretched vortex). The videos were then watched one by one and conclusions regarding the mean flow asymmetry was reported in table 4.2 : 'Yes' means that the asymmetry is clearly visible whereas the question marks means that the video does not allow to conclude with total confidence. It should be mentioned that in a few videos, the asymmetry on both sides is visible, as if the flow jumped from one solution  $A_1$  to the other  $A_2$ . This feature will be investigated in more detail in section 4.3. To overcome this ambiguity, a complementary quantitative approach using pressure measurements was adopted.

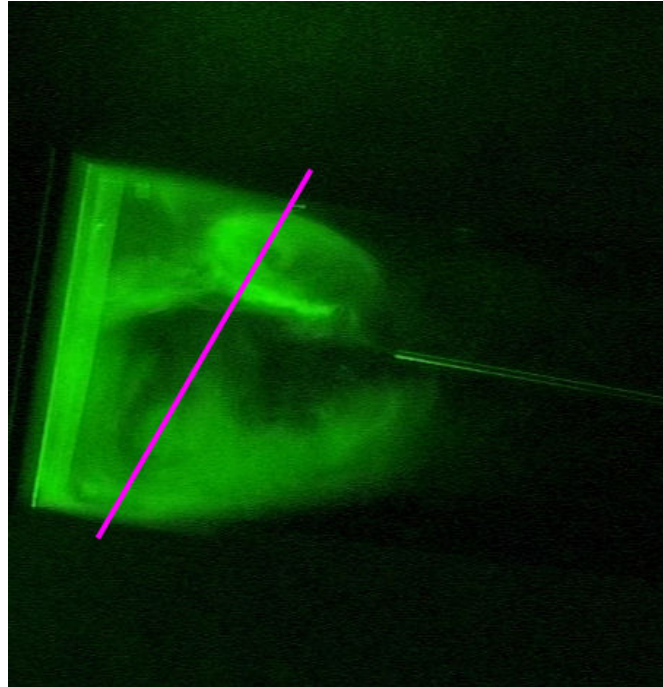


FIGURE 4.7: Representative snapshot of the flow in the  $z/h = 0.5$  plane when the mean flow asymmetry is observed

TABLE 4.2: Configurations of apparition of the mean flow asymmetry

Baseline geo.	clean (a or b)	cyl. at $x/D = -10$ (b)	cyl. at $x/D = -2$ (c)	funnel (c)
SFSO'	Yes	Yes	Yes	Yes
SFSC'		Yes	Yes	
SFS1'	Yes		?	

#### 4.2.2.3 Pressure coefficient measurements

A few pressure taps were set on the top surface of the backward cuboid (see description in section 2.3): this was aimed at locating the reattachment region in particular, which is supposed to be associated to a maximum of static pressure [38]. From the oil flow visualizations, it was observed that the reattachment point did not seem to be on the model centerline when an asymmetry occurred 4.1. Therefore, it was thought that the maximum pressure coefficient would not be on the centerline. Pressure taps were then put closer to one another in the reattachment area. The corresponding  $C_p$  maps in figures 4.8 illustrate this phenomenon for the SFSO' at several drift angles: the location of the maximum  $C_p$  makes a  $0.4 h$  step for a  $1^\circ$  change in drift angle. Indeed, the position goes from  $(x/h, y/h) = (2.89, 0.2)$  at  $\beta_g = -0.3^\circ$  to  $(x/h, y/h) = (2.89, -0.2)$  at  $\beta_g = 0.7^\circ$ . There is however an uncertainty in determining this position, directly related to the mesh size of the pressure taps. However, for  $\beta_g \neq 0.2^\circ$ ,  $C_{p_{max}}$  is not located on the centerline pressure tap. Therefore, if  $0.4 h$  is an overestimation of this change in position, this suggests that its minimum value is  $0.2 h$  ( $0.2 h$  is the mesh size). However, if

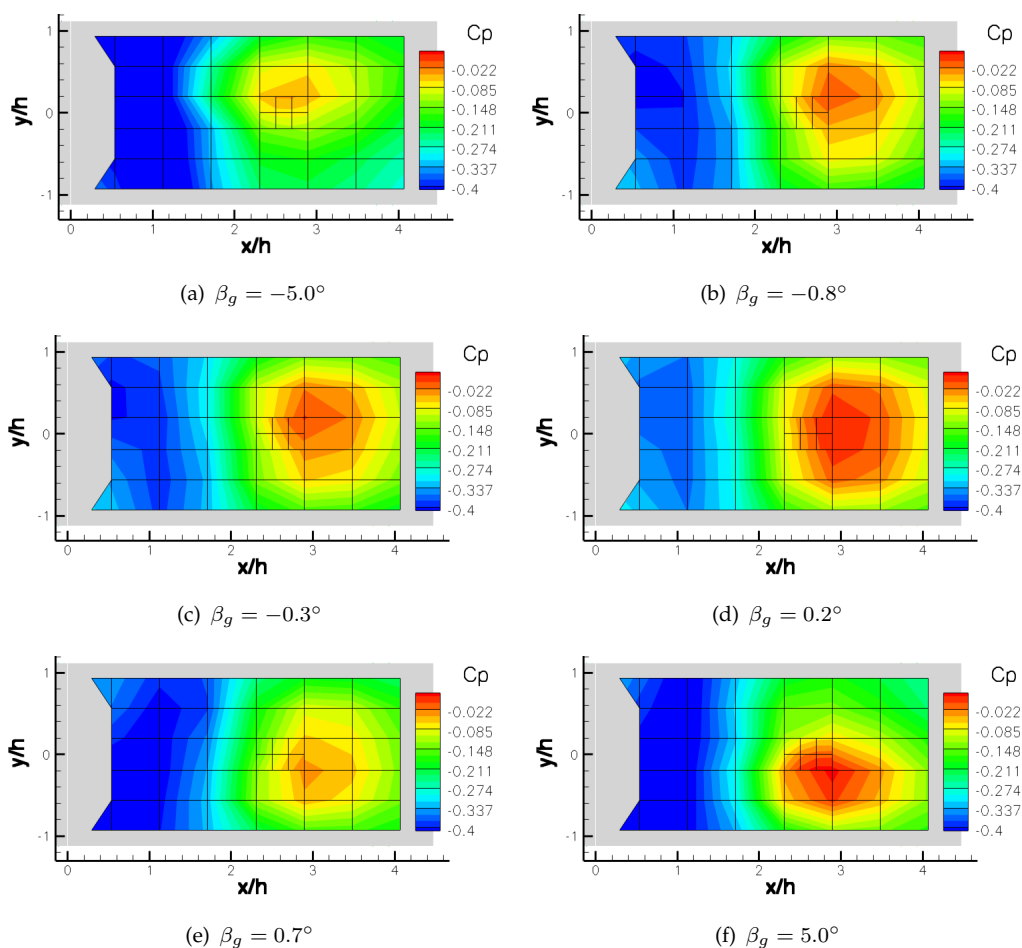


FIGURE 4.8: Maps of pressure coefficients over the top surface of the SFSO' backward cuboid at several drift angles

this point only followed the mainstream, a change of  $1^\circ$  would correspond to a change of  $0.05 h$  along the  $y$  axis for the point initially located on the centerline at  $x/h = 2.9$ . This suggests the  $0.2 h$  shift observed is directly related to the mean flow asymmetry. Contrary to the PIV measurements in the  $z/h = 0.5$ , a symmetric pressure map could be obtained for the SFSO' (see figure 4.8(d)). From this figure, the reattachment length can be determined with the same uncertainty of  $0.2 h$ :  $X_R/h = 2.9 \pm 0.2$ . This confirms the value obtained in the different experimental conditions of chapter 3. The symmetric pattern could not be obtained on the other two configurations (see figures 4.9 and 4.10). The behavior is the same for the SFSC' as for the SFSO'. The reattachment length is similar in both cases (and is 1.8 times greater than what was computed by Tai [171] with the funnel). The reattachment length is smaller on the SFS1' than on the other geometries with  $x_R/h = 2.3 \pm 0.2$ . This confirms the value obtained experimentally by Cheney and Zan [38] on the SFS1.

Eventually, from those tests, the hypothesis made previously can be argued: since the mean flow asymmetry is observed for all the configurations tested (except for the SFS1'

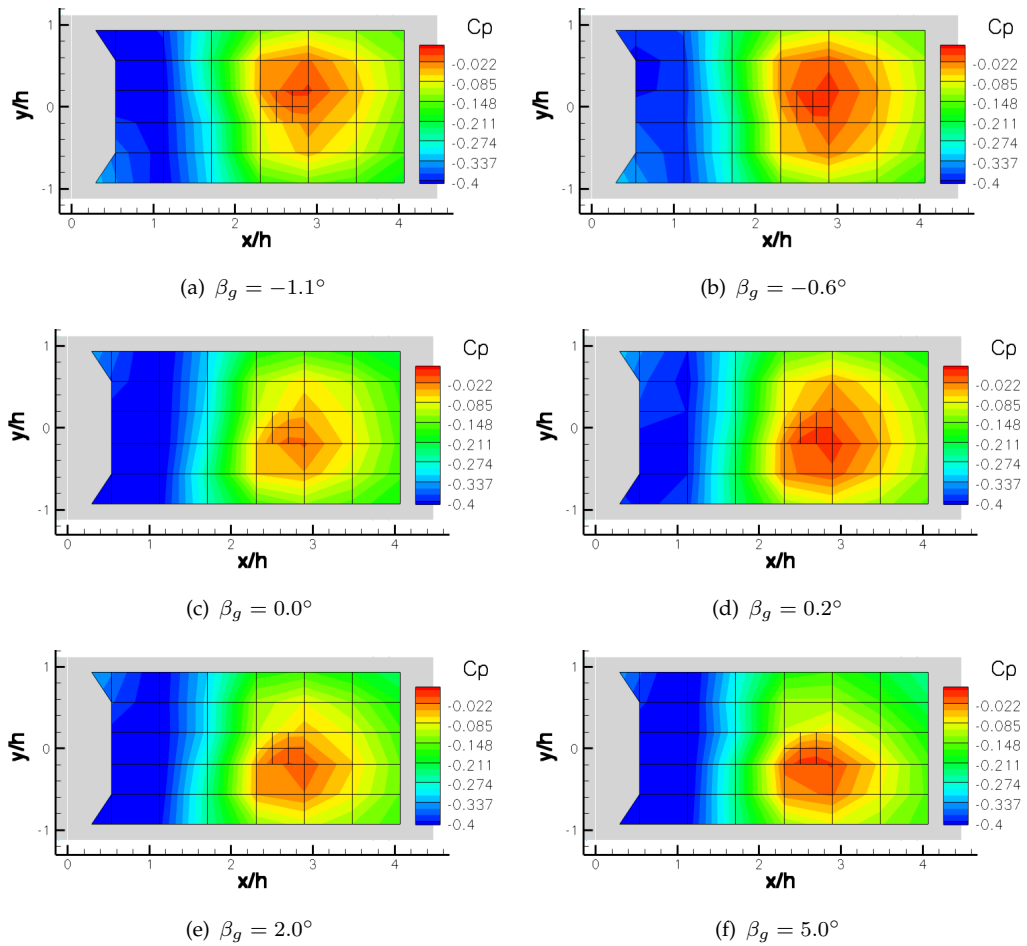


FIGURE 4.9: Maps of pressure coefficients over the top surface of the SFSC' backward cuboid at several drift angles

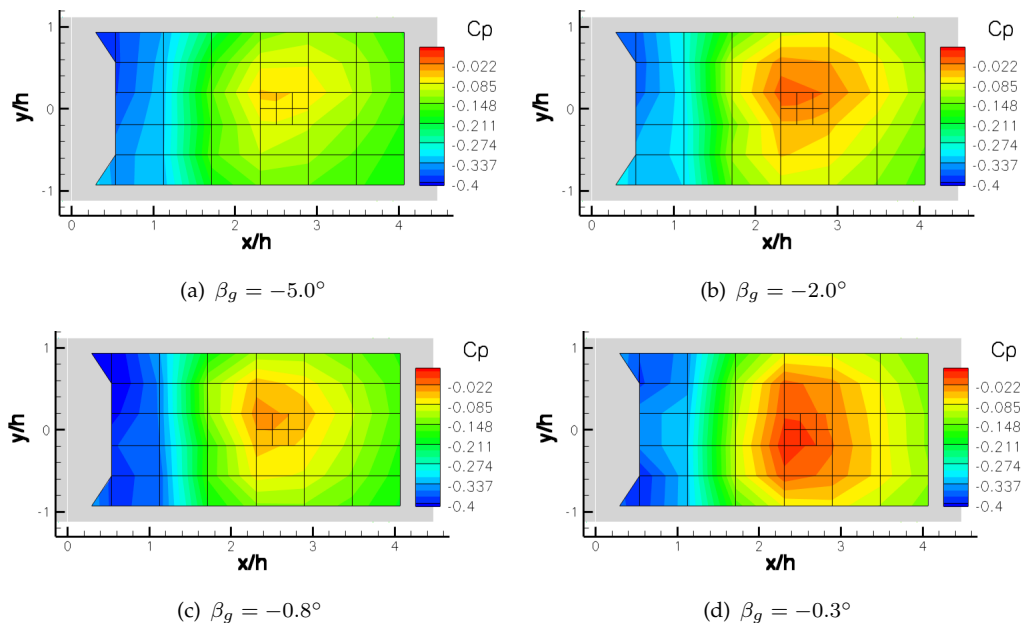


FIGURE 4.10: Maps of pressure coefficients over the top surface of the SFS1' backward cuboid at several drift angles

(bcb) where an uncertainty remains), the phenomenon is perhaps independent of the characteristics of the upper boundary layers tested. Hypothesis 2 seems then to be justified to a certain extent. However, regarding hypothesis 1, this is not so sure. Indeed, on a parallelepiped, a mean flow asymmetry is not observed (see section 1.3). However, when the backward cuboid is set behind the central cuboid (giving rise to a SFS'), then the asymmetry appears. This suggests an opposite formulation for hypothesis 1 :

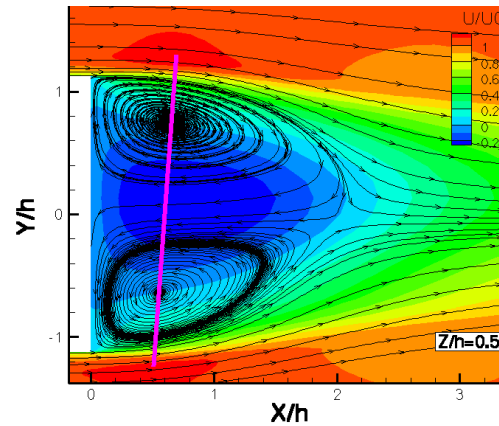
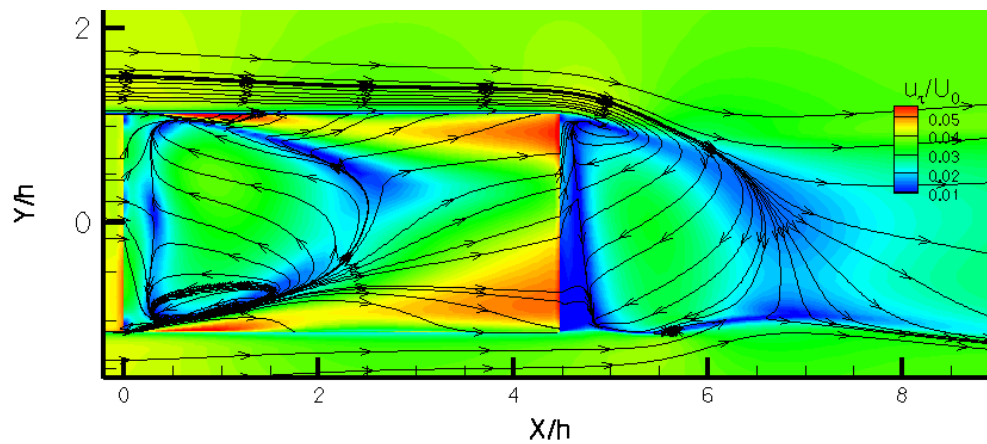
**Hypothesis 1'** : *The mean flow asymmetry is induced by the step geometry itself, with little influence of the upstream conditions*

A protocol must be conceived to verify this new hypothesis.

### 4.2.3 Numerical approach

To be completely sure there is no influence of the nose on the apparition of the mean flow asymmetry, ideally, there should be perfectly uniform conditions upstream of the first step. It is utopist to expect to achieve perfectly uniform conditions. However, this is theoretically possible through CFD. By starting the computational domain at the beginning of the central cuboid and by setting uniform conditions there, the influence of the nose is removed. By setting the drift angle at  $\beta_g = \beta_a = 0^\circ$ , this setup could also give some clues about the stability of the symmetric solution. If indeed the asymmetric mean solution appears in those conditions, this would mean that (i) the nose has no direct influence on the result and (ii) the symmetric mean solution is unstable. Since the study focuses on the mean flow, it was thought that a RANS computation would be sufficient.

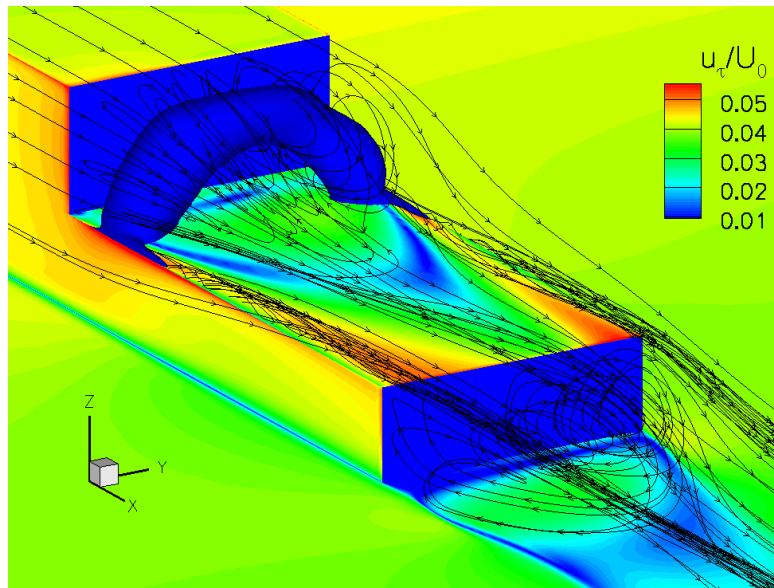
**Results** At mid-step height, a very small asymmetry is visible (see figure 4.11(a)). The  $\Phi$  angle reaches  $-3.4^\circ$ , which is smaller than the experimental values obtained (see figure 4.2). However,  $\Phi$  increases (in absolute value) the closer the z planes get to the surface: there, the asymmetry is more pronounced, as seen on figure 4.11(b). The surface pattern behind the first step is similar to the experimental flow visualizations of figure 4.1. Contrary to the experimental results presented above, CFD can give a 3D image of the flow topology as illustrated in figure 4.12(a). The arch vortex is relatively symmetric, as expected from figure 4.11(a). Only close to the surface, its leg located on the  $y > 0$  side narrows down : indeed, streamlines show that on average, fluid particles emanating from the  $y < 0$  step edge go around the recirculation bubble, close to the surface, and enter the bubble in a  $y > 0$  ordinate. Then, they wind up around the  $y > 0$  arch vortex leg all the way to the  $y < 0$  leg, close to the surface. It goes

(a) Longitudinal velocity and streamlines in the  $z/h = 0.5$  plane

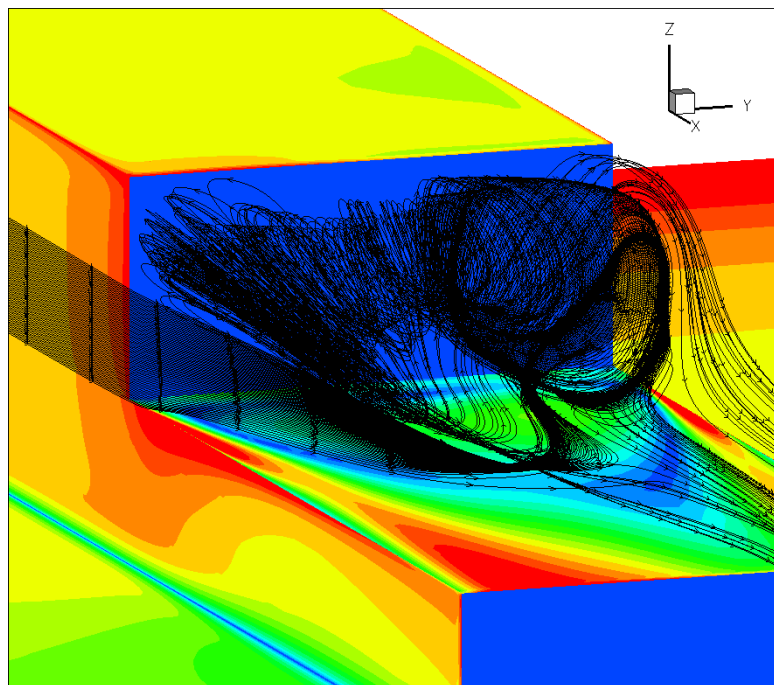
(b) Friction lines and friction velocity contours at the surface

FIGURE 4.11: Observing the mean flow asymmetry using CFD at  $Re_h = 4.9 \times 10^5$ 

around the arch vortex one last round, following the centerline, and escapes from the upper shear layer (see figure 4.12(a)). The path followed by fluid particles is then quite complex and asymmetric and is not influenced by the upstream conditions. Is the  $\Delta U$  observed experimentally due to the step flow itself? The  $\Delta C_p$  were then extracted on two horizontal lines, respectively positioned at first step mid-height ( $z/h = 0.5$ ) and at second step mid-height ( $z/h_2 = -0.5$ ) on the model lateral walls, as illustrated in figure 4.13(b). The results are plotted in figure 4.13(a). Since the computation gives an asymmetric mean flow, the pressure coefficients are compared with the experimental data obtained on the SFSO' and SFSC' at small positive drift angles. The data from the SFS1' are not presented since the flow on the model sidewalls is separated and therefore not comparable to those attached flows. The numerical results fit very well the experimental data (with  $\Delta C_p$  for the SFSO' and SFSC' being very close to one another as already observed in figure 4.6(a)). The trend of  $\Delta C_p$  between the scattered experimental data can then be extrapolated from the CFD data with a relatively good confidence. It is then shown that  $\Delta C_p$  is close to zero at the beginning of the central cuboid on the  $z/h = 0.5$



(a) The arch vortex is represented by an isocontour of  $C_p = -1.286$



(b) Streamlines emanating from the  $y < 0$  lateral step edge

FIGURE 4.12: Observing the mean flow asymmetry using CFD. 3D streamlines and friction velocity contours at the surface

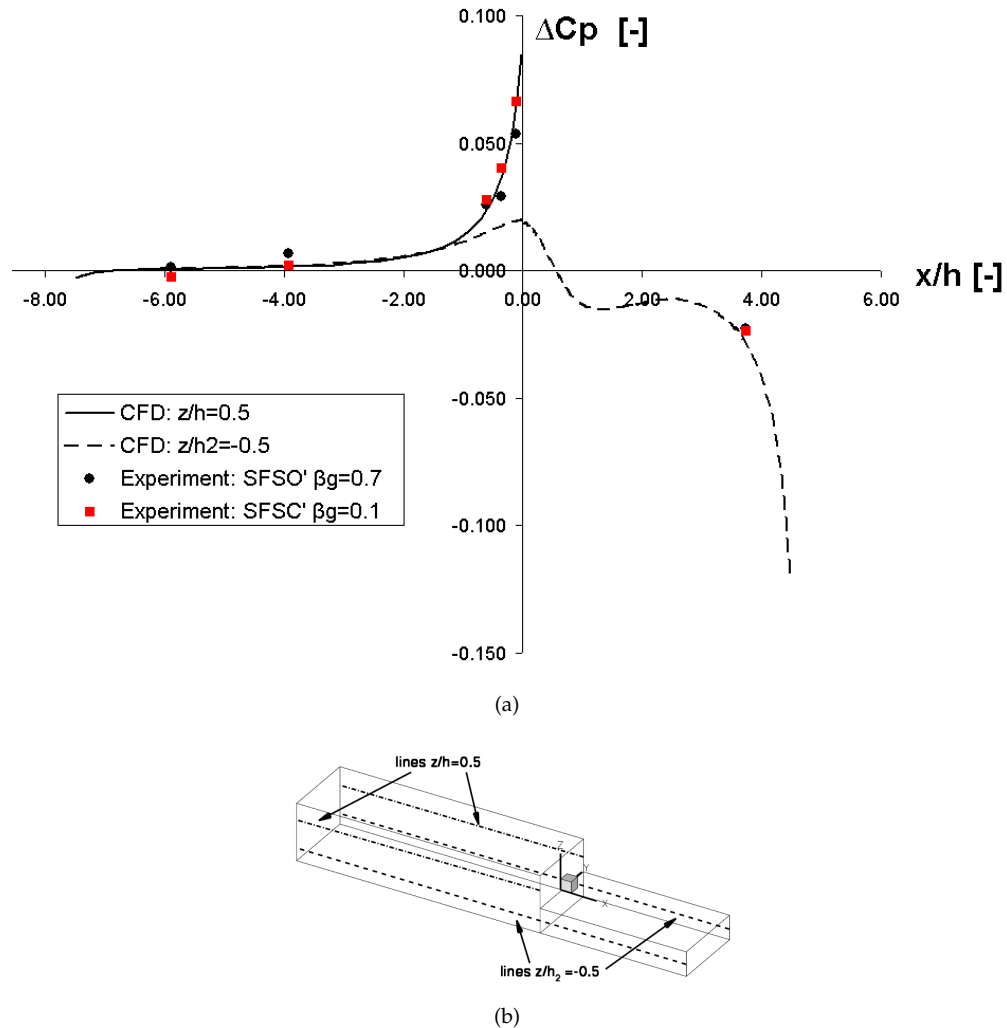


FIGURE 4.13: (a) Comparison of the  $\Delta C_p = C_{p_{y>0}} - C_{p_{y<0}}$  obtained through CFD and experiments on the SFSC' and SFSO' at positive drift angle. (b) Lines where the data are extracted

line.  $\Delta C_p$  then increases while getting close to the step where, at the edge,  $\Delta C_p$  reaches 0.08. According to equation 4.4, this corresponds to  $\Delta U/U_0 \approx -4\%$ . It should be emphasized that the flows behind the two steps have an opposite behavior : the pressure coefficients confirm the surface flow patterns observed in figure 4.11(b). There, the bigger vortex appearing on the  $y < 0$  side behind the first step is visible on the  $y > 0$  side behind the second step. As for the positive values of  $\Delta C_p$  occurring before the first step, they give rise to negative values between the two steps. An explanation for this phenomenon can probably be found in the streamwise vortices developing on the two top edges of the backward cuboid. Indeed, behind the first step, because of lower pressure within the recirculation bubble than on the model sidewalls, the flow tends to go from the sidewalls towards the top surface  $z/h = 0$ . This results in the formation of 2 streamwise vortices. As an illustration, the streamwise vortex on the  $y < 0$  edge is represented in figure 4.14. The consequence of those vortices is the widening of the



stream tube. For example, the streamline that passes through the second step corner, namely at  $(x/L, y/B, z/h_2) = (1, -0.5, 0)$ , starts at about second step mid-height at the beginning of the central cuboid, namely at  $(x/L, y/B, z/h_2) = (1, -0.5, -0.54)$ . Given the constant mass flow in the flow tube bounded by the walls and this streamline, an increase in the tube section while getting closer to the second step induces a decrease in velocity (and an increase in pressure according to equation 4.2). However, on the step edge on the  $y < 0$  side, the velocity is greater at separation than on the other side. This is related to a slightly lower pressure on the  $y < 0$  side of the recirculation bubble than on the other side for low  $x$  values. As a consequence, there is a small offset in the pressure distribution between the two sides, which leads to the  $\Delta C_p$  evolution up to  $x/h = 3$  (see figure 4.15). For  $x/h \geq 3$ , there seems to be the influence of the second step on the pressure distribution.

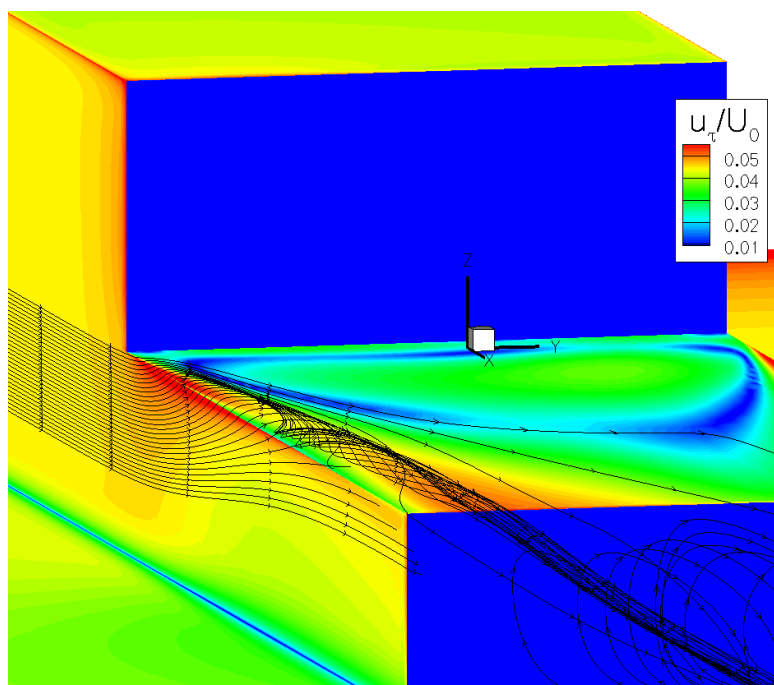
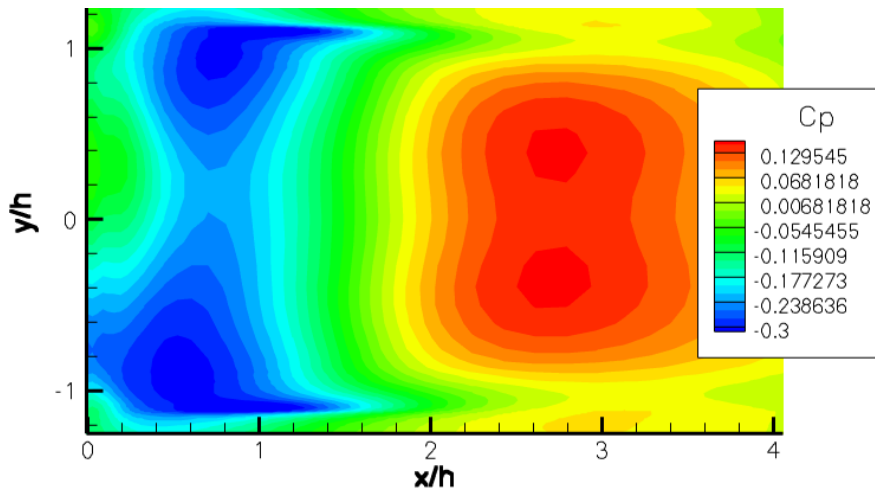


FIGURE 4.14: Visualization of the  $y < 0$  streamwise vortex through 3D streamlines. In color: normalized friction velocity contours levels

This computation seems to confirm hypothesis 1' for the conditions tested. It suggests that the mean flow asymmetry is inherent to such step geometries. Is there however a restriction on the upstream conditions? Obviously, if the flow is massively separated to the extent it does not reattach on the backward cuboid, a mean flow asymmetry is unlikely to occur since the interaction between the reattaching flow and the second backward cuboid would be weak. It was verified by laser tomography on a modified SFS1': the model was shortened along the  $x$  axis down to  $1.12h$  (instead of  $7.47h$  for the standard SFS1' as seen in figure 2.9). The results show no mean flow asymmetry. So

FIGURE 4.15:  $C_p$  coefficients in the  $z/h = 0.02$  plane

there are some restrictions on hypothesis 1'. Are there any other restrictions, regarding the Reynolds number for example ?

#### 4.2.3.1 Reynolds effect

As already mentioned in chapter 1, the Reynolds number can dictate whether or not a phenomenon will appear. The flow topology can be dramatically changed depending on the Reynolds number. The case of a sphere (figure 1.7), would be a classic example. It is then legitimate to ask if this mean flow asymmetry is a Reynolds number effect. To give a partial answer to this question, a low-Reynolds number experimental setup was designed ( $Re_h = 5.9 \times 10^3$ ). Since the previous results have shown that the mean flow asymmetry occurs for the SFSC' or the SFSO', mounted or not on a table, the SFSC' was chosen, because it is easier to manufacture. It was then set on a small table. Laser tomoscopy visualizations were used. As shown in a representative picture of the flow in figure 4.16, the smoke concentrates on the side of the big vortex. It is then easy to differentiate the snapshots where the big vortex is on the  $y > 0$  side from those where it is on the other side.

Those tests eventually confirmed that the mean flow asymmetry also appears at that lower Reynolds number.

Now that this flow feature has been observed under many different conditions, is there an explanation for it?

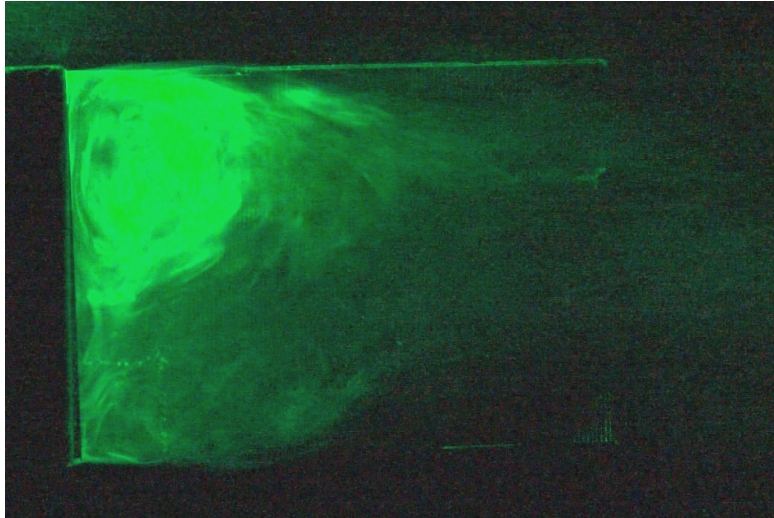


FIGURE 4.16: A representative snapshot from laser tomography in the  $z/h = 0.5$  plane of the SFSC' at  $Re_h = 5.9 \times 10^3$

### 4.3 The asymmetry is the consequence of a bi-stable flow

#### 4.3.1 Discrimination of the snapshots into 2 categories

By looking at some instantaneous flow fields (snapshots), it seems like a majority of them from both PIV and tomography data can be sorted into two distinct categories: fields from category 1 show among others a big vortex on the  $y < 0$  side with one or several smaller vortices in the shear layer on the right side. The opposite goes for fields from category 2 showing among others a big vortex on the  $y > 0$  side with one or several smaller vortices in the shear layer on the  $y < 0$  side. This is illustrated on figures 4.17 and 4.16. For the PIV fields, snapshots were then split into two equally-sized zones on each side of the centerline (the contour of those two zones are noted  $C_1$  and  $C_2$  in figure 4.18). It was thought that if the big vortex is in zone 1 for example, then the velocity circulation on  $C_1$  should be greater than on  $C_2$ , that is  $\Delta\Gamma > 0$  in equation 4.5.

$$\Delta\Gamma = \int_{C_1} \vec{v} \cdot d\vec{l} - \int_{C_2} \vec{v} \cdot d\vec{l} \quad (4.5)$$

This method was successfully verified on a particular series of snapshots sorted manually.

The family discrimination is comparable for the laser tomography snapshots, on the smaller model: for a category 1 snapshot, the smoke is mostly visible on the left side of the picture whereas, for category 2 snapshots, it is mostly seen on the right side of the picture. Therefore, by comparing the light intensity on the left and right sides of the snapshot (after removing to all the snapshots a reference picture taken before the smoke was applied), it can also be sorted into category 1 or 2. A small minority of

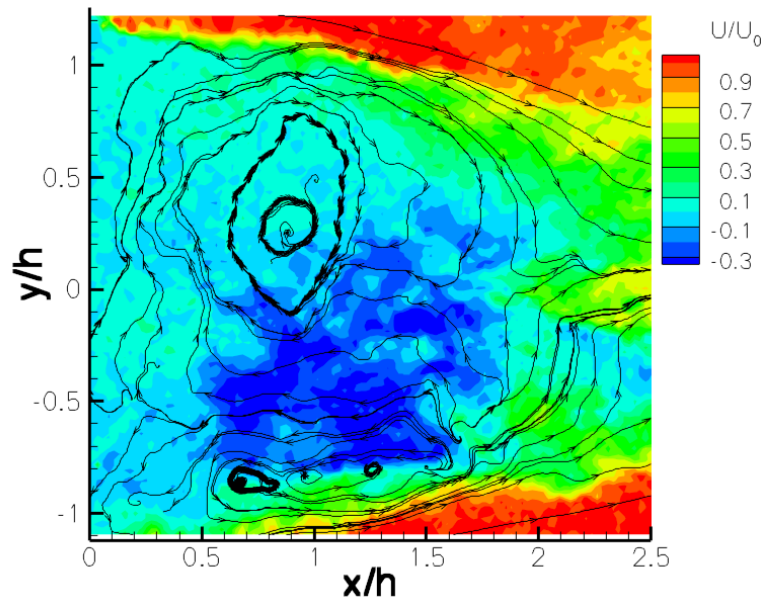
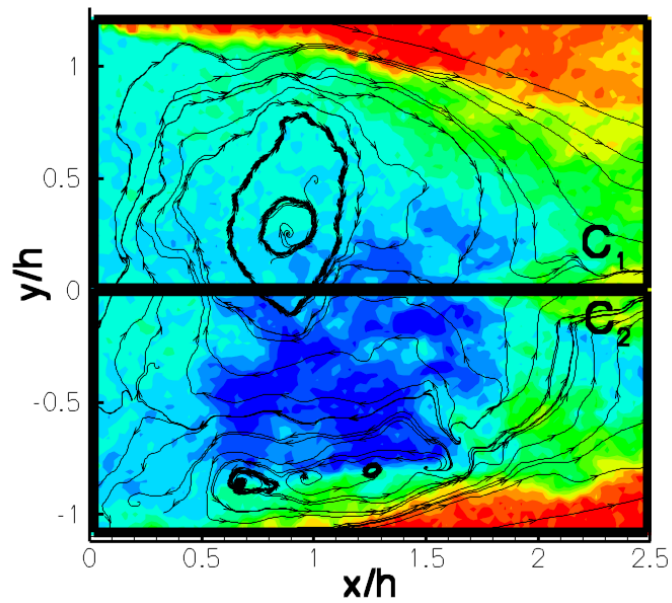


FIGURE 4.17: Velocity streamlines and contour levels on a representative PIV snapshot

FIGURE 4.18: The 2 control contours  $C_1$  and  $C_2$  for the computation of the circulation on snapshot 4.17

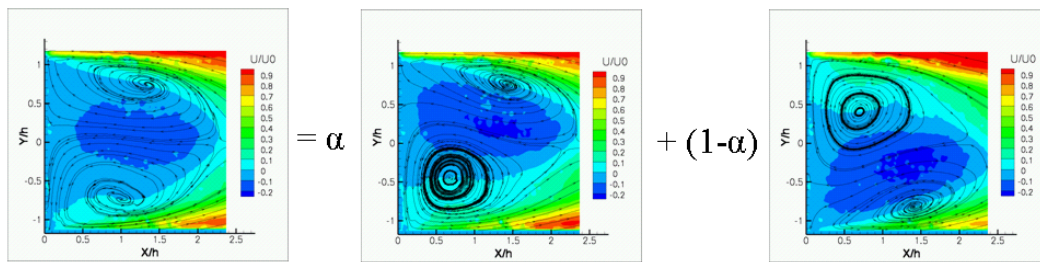


FIGURE 4.19: An average field  $A$  decomposed as the weighted sum of solutions  $A_1$  and  $A_2$ . Here,  $\alpha = 33\%$  and  $\beta_a = 0.04^\circ$

snapshots (<7 % of the total number of snapshots of a given series, for all the series processed) can not be clearly discriminated. They are therefore not taken into account in what follows. The average field obtained from category 1 snapshots give the field  $A_1$  and that from category 2 give the field  $A_2$  as seen in figure 4.19. It is observed that any average field  $A$  from figure 4.2 is a weighted sum of the 2 average fields  $A_1$  and  $A_2$  from both categories:  $A = \alpha A_1 + (1 - \alpha) A_2$  with  $0 \leq \alpha \leq 1$  (see figure 4.19).  $\alpha$  is  $\beta_a$

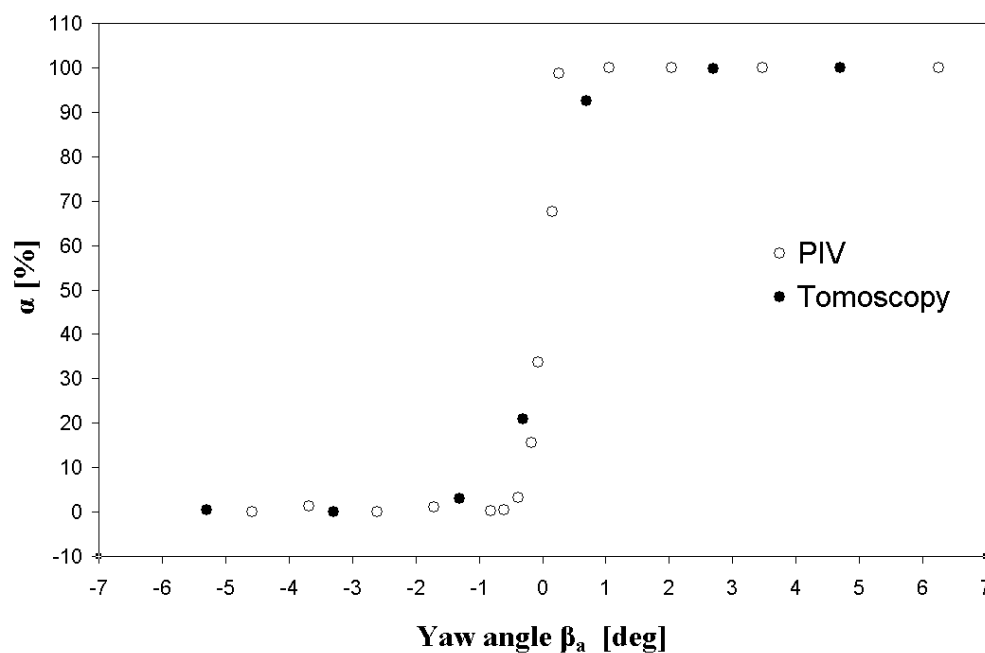


FIGURE 4.20: Proportion of type I snapshots against  $\beta_a$  for the PIV measurements on the SFSO' at  $Re_h = 9.75 \times 10^4$  and the tomoscopy snapshots on the SFSC' at  $Re_h = 5.9 \times 10^3$

dependent and evolves similarly for both PIV and laser tomoscopy tests as shown in fig. 4.20. For  $|\beta_a| > 2^\circ$  there is almost only one solution observed whereas the closer  $\beta_a$  gets to zero, the more often the 2 solutions occur. This evolution of  $\alpha$  with  $\beta_a$  eventually explains that of  $\Phi$  with  $\beta_g$  as shown in figure 4.2.

### 4.3.2 Occurrence of the two solutions in an intermittent manner

It must be mentioned that for most drift angles, many successive snapshots usually belong to one same category. Therefore, it is assumed that  $A_1$  and  $A_2$  are two distinct averaged solutions of the flow field. Also, the flow switches randomly from one solution  $A_1$  to the other  $A_2$  and vice versa. If  $T$  is the time period when one solution is found ( $T$  takes random values), the shortest normalized period of time  $T^+ = TU_0/h$  observed in the different PIV and laser tomoscopy tests is 54, if exclusively periods longer than 1 snapshot are considered. At  $\beta_a = 0$ , the flow then seems to be intermittent. Many data would be required to give proper statistics on the phenomenon. An extensive statistic study will therefore not be given here. However, it should be emphasized that in the videos observed on the mini SFSC', the flip-flop could occur over 3 images and sometimes between 2 images. Since the camera frame rate was 25 Hz and the velocity of 6.05 m/s, it means that the flip-flop characteristic time can go under 15 and can reach 50. Finally, two solutions have been evidenced. Contrary to the symmetric solution, they seem to be stable. The flow can then be called bi-stable.

Is there an explanation for this phenomenon?

### 4.3.3 Some clues towards an explanation of the bi-stability

Such bi-stable flows have already been described in the literature. The closest geometry where such a mean flow asymmetry was computed is the cavity over a train roof [109]. The 3D double forward facing step is the other similar geometry where the asymmetry was computed: Prevezer et al. [138] never obtained the symmetric mean solution. They experimentally verified that the symmetric flow seems to be unstable. No explanation was proposed though for either study. On a different geometry, namely an axisymmetric forebody at high angles of attack, Champigny [37] reviewed some experimental and numerical studies on the mean flow asymmetry and suggested an explanation for the phenomenon. It would be of inviscid origin, related to the unstable character of the flow. As for the SFS flows, it was also shown on those forebodies that the upstream flow is not responsible for these asymmetries: it is generally accepted that microscopic irregularities of the forebody trigger this process of axisymmetric vortices. This explanation might not be suitable for the present flows. Mean flow asymmetry also appears in internal duct flows with symmetric sudden expansion [6]. Fearn et al. [59] computed the flow in 2D and predicted that the unique stable solution loses stability at a critical value of Reynolds number (about 40) via a symmetry-breaking bifurcation. Above this value, there are 3 solutions, of which the original symmetric solution is unstable.

There might also be a bifurcation in the SFSs flows above a Reynolds number obviously lower than  $Re_h = 5.9 \times 10^3$ . The reason why at  $\beta_a = 0^\circ$  the flow switches randomly from one solution to the other could be a consequence of small perturbation in  $\beta_a$ , which is inevitable experimentally. Numerically, this could be triggered by truncation error.

The reason why there are at least 3 solutions on the SFS1' and not on simple parallelepiped (see section 1.3) is then related to the difference between those two geometries: the backward cuboid. The backward cuboid is characterized by an upper face where the flow reattaches, which is not too big a difference with the wall a parallelepiped is mounted on. The difference lies on (i) the lateral edges and faces where the two streamwise vortices develop and (ii) the back edge and face of the second step where separation occurs. Small tests were then performed on the SFSC' in the mini-wind tunnel to try to understand the cause of the bi-stability. This is a fundamental preliminary step if flow control is to be considered later on.

#### 4.3.3.1 The effect of the second step on the bi-stability

Considering the CFD results that show that the flow behind both steps is rather symmetric to one another, it was thought that the asymmetry behind the first step is self-sustained by the asymmetry behind the second step. If this is the case, controlling the asymmetry on the second step would therefore control the asymmetry on the first step. A splitter plate was then set vertically along the  $x_{model}$  axis, at the corner of the table and the second step vertical wall. There was no effect on the asymmetry behind the first step. Then, the splitter plate angle with the  $x_{model}$  axis was varied by more than  $10^\circ$  (see figure 4.17). This also had no effect on the flow asymmetry behind the first step. This suggests that the second step has no influence on the asymmetry behind the first step. Therefore, the asymmetry seen on  $\Delta C_p$  just before the second step (see figure 4.13(a)) is certainly the consequence of the bi-stability behind the first step: it is a priori in this case not self-sustained by the second step. The effect of the streamwise vortices was then investigated.

#### 4.3.3.2 The effect of the streamwise vortices on the bi-stability

To see the influence of those vortices on the bi-stability, efforts were made to control the strength of one of the two vortices. To do so, the splitter plate used in the previous test (see figure 4.21) was then set horizontally at different positions : (i) close the second step to influence the end of the vortex (see figure 4.22(a)) and (ii) close to the first step to influence the start of the vortex (see figure 4.22(b)). No influence in case (i) was observed. However, the transition from the  $A_1$  to the  $A_2$  solution, called the

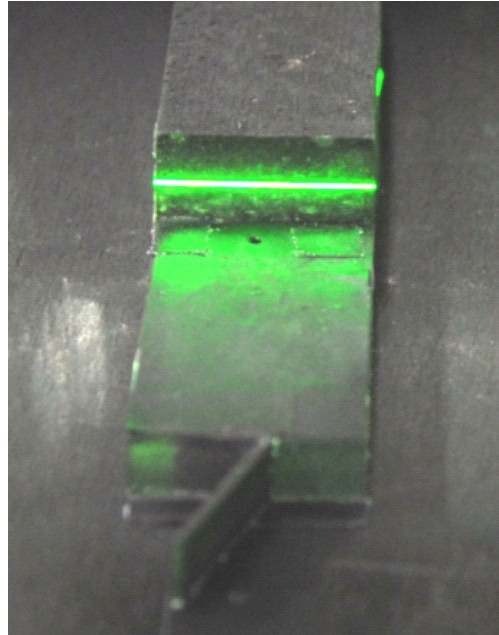


FIGURE 4.21: Inclined splitter plate behind the second step of the SFSC' at  $Re_h = 5.9 \times 10^3$

flip-flopping, is delayed to  $\beta_a = 3^\circ$  in case (ii). Modifying the origin of the streamwise vortex seems to have a bigger impact than modifying its end. Following this, the flat plate was replaced by a smaller winglet set with an angle of attack. The angle of attack was chosen so that the winglet tip vortex would rotate in opposite direction to the original streamwise vortex and then could counter it (see figure 4.22(c)). The effect was that the flip-flop now occurred for  $\beta_a = -2^\circ$ , which has an opposite sign to the flat plate case. When the winglet is set upstream of the step (see figure 4.22(d)), its effect on the bi-stability is removed.

Eventually the effect of the flat plate is the same as that of a cylinder placed vertically on the model sidewall at  $x/h = -0.68$  (see figure 4.23) : the flip-flop phenomenon appears for  $\beta_a = 4^\circ$ .

Those tests suggest a correlation between the characteristics of the streamwise vortices at their birth and the drift angle to which the flip-flop phenomenon occurs. The bi-stability has not been removed though. Those are preliminary tests. They should be pushed further to better understand the origins of this bi-stability.

#### 4.4 Summary

The mean flow asymmetry observed around the zero-degree drift angle is actually the consequence of the flow being bi-stable. The symmetric solution seems to be unstable and the flow, through a flip-flop phenomenon, switches randomly from one solution



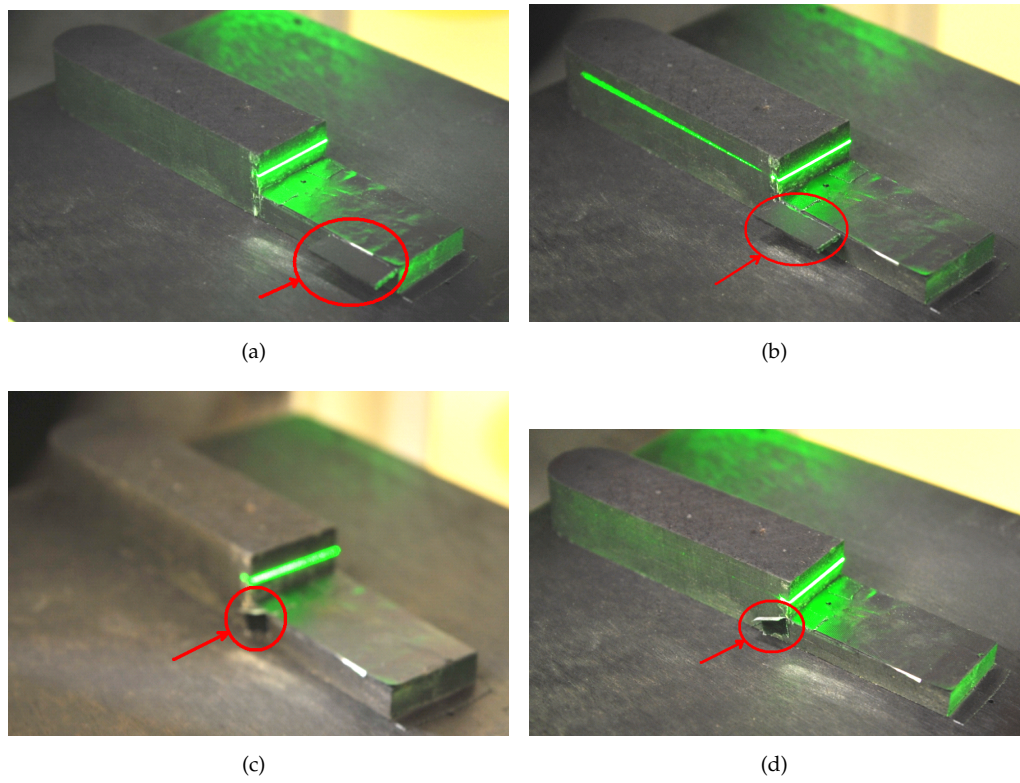


FIGURE 4.22: Some control devices put on the SFSC' to test the influence of the stream-wise vortices on the bi-stability at  $Re_h = 5.9 \times 10^3$

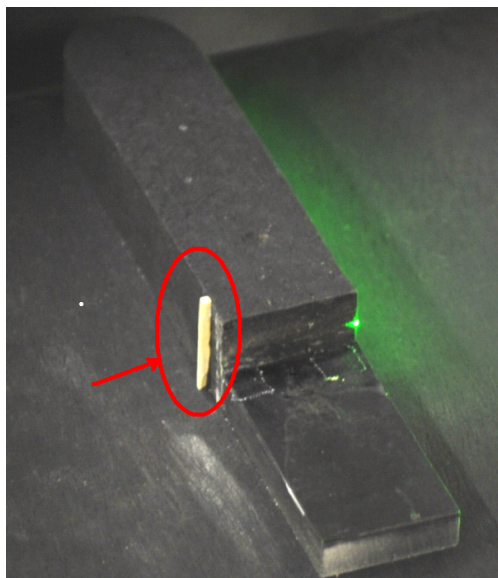


FIGURE 4.23: Control device on the lateral wall, upstream of the first step of the SFSC' at  $Re_h = 5.9 \times 10^3$

to the other at zero sideslip angle. The bi-stability has been observed under many different conditions : it is Reynolds number independent in the range  $5.9 \times 10^3 \leq Re_h \leq 4.9 \times 10^5$  (wind-tunnel and CFD computation). It is furthermore not affected by higher levels of free-stream turbulence nor while the model is immersed within a simulated atmospheric boundary layer. In a word, the bi-stability seems to be relatively independent of the upstream conditions, whether attached or slightly separated flow takes place on the model upper wall. As a consequence, this suggests the bi-stability is inherent to 3D double backward facing step flows for a wide range of upstream conditions. Those results were presented both in a national [75] and an international congress [76]. A technical brief has also been submitted to the ASME Journal of Fluids Engineering. However, a more extensive study should be conducted to see under what geometric conditions this bi-stability is independent of the upstream conditions. The origins of this flow feature should also be investigated to a further level. The present tests seem to reveal a correlation between the mean flow asymmetry and the streamwise vortices developing on the backward cuboid. Its understanding should help develop control devices in a second stage. But should this flow feature be controlled? What is the impact of the bi-stability on the launch and recovery of helicopters?



## Chapter 5

# **Some issues of the flow bi-stability on the launch and recovery of helicopters on ships. Recommendations for future work**

This final chapter aims at discussing the consequences of the observed flow characteristics on the issues related to the helicopter/ship dynamic interface. One major goal is indeed to simulate the impact of such flows on the helicopter flight. To do so, the flow features that affect the helicopter flight dynamics have to be well understood. Then, when the degree of fidelity required has been determined, a modeling method must be chosen. To do that, the limits of each must be understood. In particular, some questions must be answered : is the RANS approach sufficient ? Must the interaction between the helicopter rotor wake and the frigate airwake be simulated ? If the helicopter flight qualities need be improved, what kind of flow control should be adopted ? The following chapter does not claim to fully answer such questions. Based on the previous chapters, it is sooner aimed at showing the future possibilities of dealing with issues related to launch and recovery of helicopters on ships.

### **5.1 The impact of the bi-stability on the flight of helicopters. Comparison with the impact of the other flow features**

A flow is considered unfavorable for pilots when it pushes their helicopters to their power/cyclic/lateral/pedal limits and/or when the induced pilot workload is too high.

Jones et al. [86] subdivided the sources of pilot workload into two components : guidance and stabilization. The first one is associated to low frequency stick controls whereas the second one is related to high frequency stick movements. In general, the workload due to guidance is a consequence of the mean flow, whereas the workload related to stabilization is due to turbulence. As for the helicopter limits in command displacement, they can be reached both because of strong gusts and mean winds in the downward and sideward directions. Therefore, criteria have been established over the past years. It is checked here if the extreme allowable values for those criteria are reached with the flow described in the previous chapters. In particular, it is towards an understanding if the bi-stability is a critical phenomenon to the launch and recovery of helicopters on ships.

### 5.1.1 Impact of the mean flow

As mentioned by Saunders [153], wind shear can lead to difficulties in following a pre-selected glide path. This is why it has long been recognized as a source of control problems for pilots and as a contributing factor in landing accidents for all classes of aircraft. For helicopter flight, a moderately strong inversion means a difference of 5 m/s per 100 m. When the helicopter faces a mean velocity decrease while descending, it feels (i) a decrease in airspeed magnitude and (ii) an increase in rotor angle of attack. The general effect of (i) is to decrease lift and drag whereas the effect of (ii) is the opposite. No general results can then be stated. As a comparison, vertical velocity gradients above 1 m/s per 1 m are found in the SFSO' shear layer (see 3.2.2.1). This is 20 times higher than a moderately strong inversion. The effect is probably not neutral and there could be dangerous consequences if a fair portion of the rotor blades entered the recirculation bubble.

Another criteria that was used concerned the maximum acceptable downwind absolute value. A recommendation was made for a limitation on the allowable vertical component of the wind speed over the helideck at main rotor height. This limit was set to 0.9 m/s for wind speeds up to 25 m/s [187]. This allowed a maximum wind vector slope of  $2^\circ$  (in absolute value). It was based on simple theory that suggests that, in absence of ground effect, a thrust margin of at least 3% would be required to overcome the effects of this magnitude of gust and maintain a hover over the deck in zero wind. On the SFSO', the maximum wind vector slope reaches  $13^\circ$  at most (see 3.2.2.1) which is much above the recommended value. Angles higher than  $2^\circ$  are also found over the landing target, at  $2/3$  of the helideck length. The flow would then be very unfriendly. However, this last criteria might not be well-suited since it is based on an analysis of pilot/helicopter response to sudden 'vertical gust'. It is therefore very much an analysis

of a transient situation in a temporal sense. Moreover, this criteria considers particular helicopters (mass, size, etc.). After being used over 17 years, a later study showed that it could be removed since it was already taken into account within the turbulence criteria ([5]), which is now described.

### 5.1.2 Impact of the unsteady flow

The turbulence criteria was initially developed for helicopter launch and recovery on offshore platforms. There, Rowe and Hawson [150] could correlate the vertical turbulence intensity with the pilot workload. Among other parameters, this value depends on the helicopter rotor load and size. For example, for the Sikorsky S-76 of 4.7 tons, the standard deviation of the vertical velocity measured in the rotor plane in hover flight over the helideck should not overcome 1.75 m/s [150]. This threshold value is pushed between 2.5 and 3 m/s on the 3 spatial axis for Merlin helicopters recovering on a type 23 frigate [178]. On the SFSO', at  $U_0 = 14.34$  m/s, the vertical velocity standard deviation in the shear layer is lower than 2.58 m/s. If this is acceptable for a Merlin at this speed, it might be problematic at higher upstream velocities and/or for smaller helicopters. However, this is a very global approach and does not take into account the characteristics of the turbulence, namely the length scales and frequencies involved.

This is why an alternative criterion is based on spectra analysis: from the temporal signals of the pilot controls, spectra are computed [1, 5]. As shown by Jones et al. [86], the low frequency stick movements are related to guidance whereas the high frequency movements are related to stabilization. It is believed that the higher the workload, the higher the frequencies of the stick movements. As a consequence, the higher the energy at high frequencies, the higher the pilot workload. Then a relation must be found between the pilot stick activity, the atmospheric turbulence and the helicopter response. In fact, since the atmospheric turbulence input is a continuous perturbation of the lifting surface dynamic pressure and angle of attack, Van Gool [179] suggests that it has a similar effect as the pilot stick input. He argues in this sense that any analysis which is affected by the pilot stick motion will be affected by atmospheric turbulence. It might then be legitimate to relate the helicopter response to atmospheric turbulence to its response to the pilot stick movements. And some softwares like CIFER ® compute the helicopter transfer functions, namely the helicopter movements against the amplitude and frequency of the control stick movements. Such functions, for example, have been established for the MQ-8 UAV by Colbourne et al. [40] or on smaller models like the Raptor by Bhandari et al. [18]. This confirms that the helicopter response to atmospheric turbulence depends, among other parameter, on its mass and size. Nevertheless, from McRuer [118], the common frequency range of interest for the study of

manned helicopter handling qualities can be defined : it is generally assumed to be [0.2, 2 Hz]. According to the similarity laws (see appendix A), it is then expected to find the same Strouhal numbers at full scale as on the model. If the free-stream velocity is the same for both, namely 20 m/s, the frequency range [0.2, 2 Hz] corresponds to a Strouhal number range  $St_h$  of [0.06, 0.6] on a FREMM like frigate (see figure 5.1). From the spec-



FIGURE 5.1: FREMM: the next generation frigate of the French Navy with its helicopter

tra computed in section 3.3.2 , about 50 % of the total fluctuating energy is contained in this range. This is not negligible. 40 % is contained in the higher frequencies.

If considering the frequencies is an improvement to establish a criterion from only the turbulence intensities, it is however not sufficient. As demonstrated by Van Gool [179], to model the helicopter response correctly to turbulence, it is also necessary to take into account the turbulence coherency : response to random turbulence is not accurate enough. Wilkinson et al. [190] has not contradicted this. It is then important to have a good idea of the characteristic length scales of the turbulent structures. For the SFSO', the spatial turbulence length scale was shown to be of the order of 0.2 to 0.5 step height. The vortex size must be compared to the helicopter rotor radius. The effect of such structures will then depend on the helicopter size relative to the ship size.

Then, as the impact of mean winds, turbulence intensities, frequencies and length on the helicopter behavior has just been discussed, so should the impact of the bi-stability.

### 5.1.3 Application to the impact of the bi-stability

In the spectra presented in section 3.3.2, the contribution of the bi-stability is not included. For those measurements indeed,  $\beta_g = 0^\circ$ , which corresponds to  $\alpha = 99\%$  in figure 4.20. In this respect, the average field is  $A_1$  (see figure 4.19). Let us imagine that the flow flip-flops from  $A_1$  to  $A_2$ . There is however no proper Strouhal number associated to this phenomenon since it was shown to be intermittent. Nevertheless, as seen in section 4.3.2, the normalized time it takes for the flow to switch from one solution to

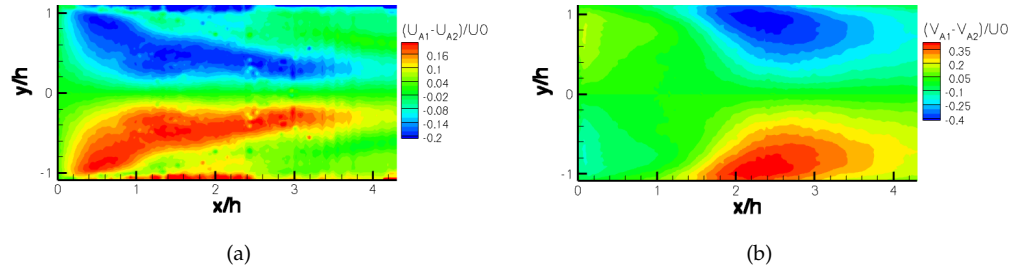


FIGURE 5.2: Change in mean velocity in the plane  $z/h = 0.5$  at  $Re_h = 9.75 \times 10^4$  resulting from the flow flip-flopping

the other can go below 15. This corresponds to a Strouhal number  $St_h \geq 0.07$ . Characteristic times of up to 50 have also been observed, corresponding to  $St_h \approx 0.02$ . Since the range of interest for helicopters spreads between  $0.06 \leq St_h \leq 0.6$  for a frigate as big as a FREMM, the flip-flop phenomenon could induce pilot workload. To do so, the velocity fluctuations induced by this phenomenon might not be negligible.

At first sight, it is assumed that the change in velocity felt by a helicopter at a given position is of the order of the difference in mean velocity between the two solutions  $A_1$  and  $A_2$ . The normalized U and V velocity differences are then computed on the SFSO' and plotted in 5.2(a) and 5.2(b) respectively.

Levels up to 0.2 and 0.3 are reached for  $(U_{A1} - U_{A2})/U_0$  and  $(V_{A1} - V_{A2})/U_0$  respectively. For an upstream velocity of 20 m/s, this corresponds to a change in velocity amplitude of about 4 m/s for U and 6 m/s for V. Then, if it is justified to define a turbulence intensity as the change in mean velocity, namely the switch from a solution  $A_1$  to a solution  $A_2$ , the levels reached would overcome the threshold value of 2.5 to 3 m/s obtained on Merlin helicopters recovering on type 23 frigates [178]. This would suggest that the impact of the bi-stability on helicopter launch and recovery on ships is not negligible.

It should also be emphasized that at sea, the ship is never at zero degree drift angle: there can often be changes from positive to negative values when the ship tries to sail towards the relative wind. Since the bi-stability is very sensitive to drift angle, it is then not impossible that the flow often switches from mode  $A_1$  to mode  $A_2$ . To avoid this, a change in launch and recovery procedure would recommend that the ship drift angle should be strictly non zero with a given margin to ensure the occurrence of exclusively one solution. This would then cancel all the effects due to the apparition of flip-flopping. It should be mentioned that the bi-stability was observed qualitatively with laser tomography in the L2 wind tunnel on a  $1/100^{th}$  scale FREMM. This goes in favor that the bi-stability is not a phenomenon only found on simple academic geometries but could be of interest for full scale frigates. However, before updating the operational launch and recovery procedures, the impact of the bi-stability on helicopter flight dynamics should be further investigated.



To sum up, according to the different metrics presented above to quantify pilot workload, the present study confirms that the aerodynamic environment above frigate flight decks is very hostile. The helicopter rotor diameter compared to the frigate hangar height as well as its mass are two major parameters that will dictate how critical the influence of the ship airwake will be on the helicopter flight dynamics. One way of predicting the helicopter behavior is to simulate it. However, this requires an accurate simulation of the ship airwake. The next section deals with this issue in view of the results that have been presented so far.

## 5.2 Simulating frigate airwakes in case of bi-stability

In general, the simulation of frigate airwakes requires respecting certain fidelity standards. Those are globally discussed by Padfield and White [130] and Wilkinson et al. [190]. In this respect, the previous section suggests that there are some flow features that must be simulated in priority to accurately predict the helicopter flight dynamics critical to launch and recovery. Those are :

- (i) the mean velocity values and gradients
- (ii) the (large scale) turbulence intensities in the helicopter range of interest, namely [0.2,2Hz]
- (iii) the turbulence characteristic length and coherency related to the frequency range [0.2, 2Hz]
- (iv) the flow bi-stability around  $0^\circ$

So far, the easiest way to obtain those data in three dimensions and implement them into simulators has been achieved using CFD. However, such computations should be confronted, and validated with high quality experimental data. Considering the possible existence of bi-stable flows on ships, the interpretation of the experimental data should be done with care as exposed below.

### 5.2.1 Accurately interpreting the experimental validation database : the issue of data averaging in case of bi-stable flows

The zero degree drift angle is usually a reference case in the study of flows around bluff bodies. The several cases exposed in chapter 1 illustrate this statement. However, as shown in the previous chapter 4, this test case is critical for 3D double backward

facing steps because of the bi-stability. The aim here is to discuss the validity and the validation of this test case at zero degree sideslip when only the raw averaged data are presented.

Indeed, if  $A_1$  and  $A_2$  are two stable solutions of the flow, is  $A = \alpha A_1 + (1 - \alpha)A_2$  also a solution of the flow for  $0 < \alpha < 1$ ? This raises the question of uniqueness of the equations that describe the phenomenon.

Existence and uniqueness of the full Navier-Stokes equations (NSE) remains an open question to the point that the demonstration of existence and smoothness of the NSE is one of the millennium problems<sup>1</sup>. However, when some restrictions are introduced into those equations, some mathematical demonstrations exist regarding existence and uniqueness. For example, it has been proved that solutions of the steady incompressible NSE exist and are unique [67]. There are nonetheless restrictions regarding existence and uniqueness of the solutions of the steady-state equations of a turbulence model for incompressible fluids. Using the Smagorinsky turbulence model, Paré [132] shows the existence of the solution but the uniqueness only for values high enough of the kinematic viscosity. He concludes that the bigger the turbulent viscosity added is, the bigger the uniqueness range must be. A comment can then be made regarding the validation of RANS computations from an experimental database: if, for given initial and boundary conditions, the solution of the RANS equations is unique, then  $A_1$ ,  $A_2$  and the probably unstable symmetric solution are not solutions of the same problem. That means that there must be a numerical approximation or difference in the computation that makes the boundary conditions slightly different at some point. In this respect,  $A = \alpha A_1 + (1 - \alpha)A_2$  cannot be solution of the same RANS problem for all  $0 < \alpha < 1$ . Under those conditions, the experimental averaged data obtained by PIV, hot-wire, pressure taps or any other device at zero degree sideslip where flip-flopping occurs could not be a validation case for RANS computations. Those experimental averaged data would therefore not be solutions of the RANS equations. Comparison could only be done after discrimination of the solutions in the experimental dataset.

On the other hand, given an initial and boundary conditions, if several solutions of the RANS equations exist (the aforementioned result suggest that non-uniqueness is not impossible depending on the fluid and turbulence model viscosities), then the same conclusion is not that straight-forward; it will therefore not be drawn.

Whatever the former theoretical result is, at zero degree sideslip, since the flow flip-flops randomly, there must be a reasonable amount of flip-flopping events to converge towards the value  $\alpha = 0.5$ . This is related to a large sampling time that is not always reached in practice. Therefore, two experiments, or computations, may not lead to the same values of  $\alpha$ . For example, it was probably by chance that Syms [170] computed the mean flow asymmetry on the same side as for the experiments on the SFS2. Also,

<sup>1</sup>[http://www.claymath.org/millennium/Navier-Stokes\\_Equations/](http://www.claymath.org/millennium/Navier-Stokes_Equations/) last visit: 2010/08/26

it can be by chance that Cheney and Zan [38] visualized a symmetric flow on the SFS1 helideck. They may as well have observed the  $\alpha = 0.5$  flow which might also not be representative of the unstable symmetric solution of the RANS equations. The same goes for the pressure measurements obtained in the present study on the SFSO' (see 4.8). This possible lack in reproducibility does not go in favor of trustful validation cases at zero degree sideslip. There are then two alternatives : (i) compare the discriminated data according to the two solutions and (ii) compare the flow at a non zero sideslip angle.

Eventually, this raises questions about the validity of RANS computations to simulate such flows. In particular, the approach consisting of computing the flow on half a geometry [148, 149] and therefore obtaining a symmetric solution is probably not relevant for such bi-stable flows. This symmetric solution seems to be unphysical, because it is unstable.

Another limitation of the RANS computations is that they only give access to the mean flow and some turbulence statistics. No information about the time-dependant flow features can be extracted from such computations, in particular the flip-flop property. This is one of the reasons why Kulin [9] and Syms [169] already mentioned that RANS computations might not be sufficient for ship airwake prediction. They consequently proposed the use of more sophisticated models.

However, if the bi-stability leads to some challenges in the field of flow simulation, this property can be used to decrease the number of drift angles computed and/or tested. This is the subject of the next section.

## 5.2.2 Using the bi-stability property for data reduction

It has been shown that at  $\beta_a = 0$ , there are two averaged fields  $A_1$  and  $A_2$  that describe the flow. Moreover, the topology for  $A_1$  is qualitatively still the same regardless of the drift angle as long as  $1^\circ \leq \beta_a \leq 5^\circ$ . This is not the case after  $8^\circ$  where a third vortex appears, as seen in figure 5.3. Therefore, an improvement on today's flow models would be to take into account the bi-stability by fully describing solution  $A_1$  for example at  $5^\circ$  with an unsteady approach.  $A_2$  would then be easily obtained as the symmetric field of  $A_1$ . Eventually, any solution for  $-5^\circ \leq \beta \leq 5^\circ$  would be constructed as the succession of the unsteady  $A_1$  and  $A_2$  solutions. Flip-flop would be random, as long as  $\alpha$ , the proportion of the occurrences of  $A_1$ , is respected. Some work would still have to be done to construct transient snapshots that lead from  $A_1$  to  $A_2$  in a continuous manner. There, an unsteady computation at zero degree sideslip would help if it could compute this flow property. This is however not obvious, considering the work of Forrest and Owen [64] who did not observe the mean flow asymmetry despite a DES computation. An

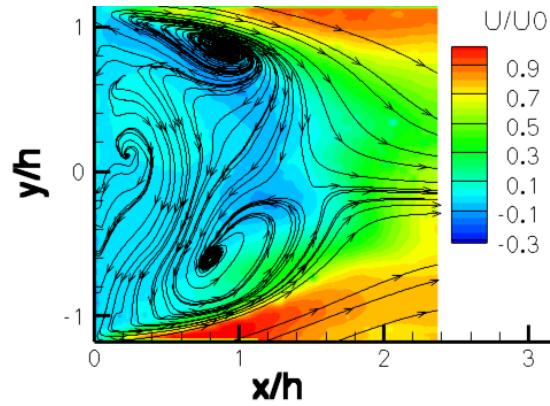


FIGURE 5.3: 2D streamlines and contour levels of the normalized streamwise velocity in the plane  $z/h = 0.5$  at  $\beta_g = 8.7^\circ$

alternative would be the experimental approach ; but three dimensional time-resolved data acquisition in a large volume of fluid is not trivial and it is still an ongoing subject of research [97]. Eventually, simulating the bi-stability in 3D seems to remain an uneasy task.

As for the description of one solution  $A_1$  for example, there are two main ways of completing it : (i) using CFD and (ii) through experiments. Both approaches have their advantages and drawbacks. Time-accurate CFD computations such as DES or LES [152] could give most of the needed information. The problem is the validity and validation of such computations: they are not straight-forward, as illustrated for example by Polsky et al. [136]. High quality experimental data are required and 3D unsteady data would be helpful.

This could partially be achieved by scanning the flow with two dimensional three components PIV. Since the data in the different planes would obviously not be acquired at the same time, they could not be correlated. One way to correlate them would be to put some pressure taps on the model surface to have reference time-resolved pressure signals. By phase averaging the data in each plane and knowing their common phase, a 3D unsteady picture of the flow could be obtained. The basic idea of this method has been used, for example, by Perrin et al. [134], Wang and Zhou [184], De Kat et al. [47], Kawai et al. [92]. This requires the existence of a periodic phenomenon in the flow (the frequency will be noted  $f_{ref}$  from now on). This phase averaging also plays the role of a filter, and only the aerodynamic frequencies below  $f_{ref}$  are reproduced. This approach can be of interest for the launch and recovery of helicopters on ships if  $f_{ref}$  is of the order of the maximum frequency of interest for the helicopter flight dynamics, namely around 2 Hz (at full scale).

It should be emphasized that time-resolved PIV data might not be necessary for this task. By using POD, the modes can be computed regardless of the time. The difficulty is then to determine over time the POD coefficients for each mode. When the number

of necessary modes is low, the evolution of the POD coefficients can be found analytically, as done by Chiekh et al. [39] in the wake of a flat plate. However, for ship airwake simulation, more modes are necessary. From the POD analysis performed in paragraph 3.3.1.1, 77 modes are required to model 60% of the total fluctuating flow energy (in the plane  $z/h = 0.5$ ). And as discussed previously, this is the amount of energy contained in the full scale range of interest [0, 2 Hz] (see section 5.1.2). Knowing that the higher the mode number, the lower its energy, then only the 77 first modes would be useful for the launch and recovery issue (this is in a way similar to LES filtering [58]). Then, determining the 77 time-dependant POD coefficients could be done with the help of a sufficient number of pressure probes combined with the use of LSE [22]. This is also source of inspiration for the field of research [134, 151, 174, 176].

If the method was proved to be effective, it could be thought to be applied to full-scale ships : from the POD modes obtained through CFD or model scale experiments and by acquiring pressure signals in real time at a sufficient number of locations over the flight deck, a picture of the turbulent field could be sent in real time to the helicopter pilot. Since pilots are interested in understanding the unsteady flow they are flying through, this kind of information could be relevant for them. It could also be useful for flow control.

A last perspective of such approach finds its interest in the fundamental understanding of the flow itself : if the time dependant POD coefficients can be determined, would it be possible, by selecting a range of consecutive POD modes, to isolate, visualize and then better understand some flow features independently of the others ? For example, by choosing certain consecutive POD modes, could it be possible to isolate a flapping phenomenon from a vortex shedding ?

A few promising perspectives emanate from the isolation of the bi-stability. However, before looking further into them, the validity of the one-way approach should be discussed.

### 5.2.3 Bi-stability and the limits of the one-way coupling approach

So far, in the present study, the analysis of the flow related to launch and recovery of helicopters on ships has always considered that the helicopter did not modify the ship airwake. However, does the bi-stability and other flow characteristics appear in presence of a helicopter? Then, the circumstances under which the helicopter modifies the flow are still to be determined. If the influence is negligible, this would justify the previous analysis and the future studies exclusively dealing with the ship airwake alone. The interaction between the helicopter and the ship airwake has therefore been studied by a few authors, experimentally and numerically. By simply adding a helicopter

fuselage into a ship airwake was shown to already have an influence on the flow obtained around a ship without helicopter [122]. Furthermore, the effect of the rotor was investigated. By comparing with the rotorless case [107], Lee and Zan [106] showed the effect of the rotor on the fuselage loads of a helicopter hovering over a frigate helideck. It was concluded that to conduct a proper evaluation of ship airwake effects on a helicopter fuselage in a wind tunnel, the incorporation of a correctly-scaled main rotor in the simulation is essential. A computation by Landsberg et al. [98] with an actuator disk also concluded that the rotor has an impact on the flow features. The helicopter was however not trimmed. This detailed was then considered by Bridges et al. [26] who performed a CFD computation with full interaction between a CFD and a flight dynamics code. It was shown that the one-way coupling method can predict a level of pilot workload equal to, or greater than that of the fully coupled method for the cases simulated. The addition of the rotor downwash to the CFD solution in the fully coupled method showed that vortices in the airwake that have a significant effect in one-way coupling may have either a similar effect or a lessened effect if the vortices are pushed away from the helicopter. In a word, the full coupling does not seem to be mandatory for pilot workload prediction in the conditions simulated. If the global results are unchanged, there are however some changes in the flow topology. This was computed by Alpman et al. [11] and Tattersall et al. [173]. The three approaches used an inviscid flow approximation. In case of low upstream velocities down to zero, the influence of the rotor is obviously important, as shown by Lee and Silva [108].

The different studies presented above draw different conclusions depending on what parameter is considered. The issue of the one-way coupling validity should then be further investigated, in particular around the zero degree drift angle at relatively high upstream velocities. This is why a first attempt was conducted in parallel to the present study at the ONERA L2 wind-tunnel. In those experiments, a model helicopter was mounted on a balance and fixed downstream a parallelepiped [51]. The dimensions were chosen so that it would be representative of a frigate hangar. Different tests were performed with and without the geometry, with zero and non-zero relative wind velocities in order to isolate and quantify several effects such as ground effect, rotor airwake recirculation and ship/rotor airwake interaction. This study goes beyond the scope of the present work and the interested reader should refer to [51] for the detailed results. Those results actually suggested a pursuit in such tests for two reasons : (i) the data acquired could give an alternative to the CFD approach used in the flight simulators and (ii) the validity of the one-way coupling with, in particular, the apparition of the bi-stability and the other flow features in presence of a helicopter rotor could be verified.

It should also be checked if the ship motion influences those flow features. A preliminary study by Biskaduros [19] recommends indeed further investigation on the subject

of ship motion.

There still remains some work to do then, to check under what circumstances and on what parameters the one-way coupling approach is valid. The rotor downwash could indeed locally modify the flow but globally, compared to the one-way coupling, the full-coupled approach could have no effect on pilot workload predictions. This could be a relevant questioning if flow control is considered since it deals with local flow features.

### 5.3 Bi-stability and flow control

If it can be proved that the bistability still occurs when a helicopter rotor is placed in the flow, and if its impact on launch and recovery can be confirmed, then it may be interesting to control this flow feature. The control must be applied so that the flow is improved. This requires defining the notion of flow improvement: for helicopter operations in the maritime environment, according to section 5.1, improving the flow would mean decreasing the impact of its characteristic features that contribute to high pilot workload. At first sight, this would mean reducing mean velocity gradients, side- and down winds as well as high levels of turbulence. In particular, the contribution in the spectra of the frequencies belonging to  $[0,2 \text{ Hz}]$  should be reduced, and big coherent structures of the size of a rotor radius should be downsized. A review on this specific topic was especially conducted by Maurel [117] in the frame of this study. However, flow control cannot be fully treated as long as questions remain on the existence of the bi-stability, the other flow features and the impact of the rotor on the whole.

Putting this issue aside, a flow control device that would limit the problems related to separated flows was suggested: the flat vertical hangar doors would be replaced by rounded ones as shown in figure 5.4. An appropriate blowing device placed in the

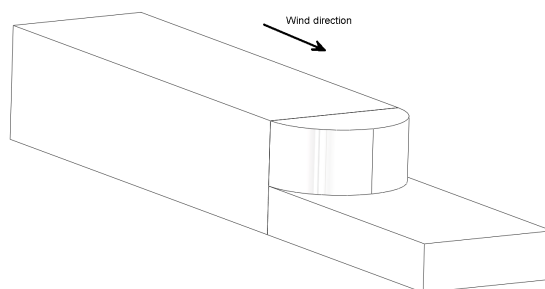


FIGURE 5.4: A proposition of active flow control device for ship airwake

right place would keep the flow from separating on the frigate sidewalls using Coanda effect. At high headwinds, the recirculation bubble would then be almost inexistent, thus limiting the mean vertical velocity gradients. The lateral mean velocity gradients

would however still exist but would make the landing spot on the centerline a stable position for the helicopter. Furthermore, the accelerating flow on the centerline would increase the mean longitudinal velocity. As a consequence, the helicopter power margin available would also be increased. However, such a configuration would generate a shear layer on the horizontal surface above the hangar. This would result in the generation of streamwise vortices that could also affect the helicopter flight dynamics, even if, according to Whitehouse et al. [188], their impact might not be as strong as on airplanes. Eventually, the high longitudinal airspeeds would push the rotor airwake downstream and therefore justify to some extent the one-way coupling approach for flight simulations.

These are only suggestions that should be further investigated. Also, the feasibility of integrating such devices on a real frigate should be considered because of other operational issues not related to aerodynamics, such as the interaction with electronic devices, weapons, etc.

## 5.4 Summary

Preliminary estimates tend to indicate that the flow bi-stability (flip-flopping) should be considered for the issue of helicopter launch and recovery on ships. This would suggest, for example, to modify the launch and recovery procedure in order to avoid this flip-flopping and therefore decrease pilot workload. However, more investigation is required before changing those well-established procedures. To do so, the impact of the bi-stability on helicopter flight dynamics could be simulated. This requires high fidelity models of the ship airwake. An approach could be to generate experimental data. Some directions are proposed in this way for obtaining experimental 3D unsteady data that could also be used for unsteady CFD validations as long as care is taken in data interpretation. However, flight simulators require quickly available data. In this respect, some orientations through a POD/LSE method are proposed that would reduce the required number of data needed. Ideally, such an approach would go beyond the field of flight simulation since it could help have a better understanding of the physics of the flow by isolating each feature independently. However, such methods consider that the ship motion and the interaction between the helicopter and ship airwake is negligible. Before pushing such works any further, the first mandatory step would be to quantify those interactions on the parameters of interest. This step is also a necessity if flow control is being considered, except in the case where the idea proposed in the last section is investigated.





# Conclusion

The present study has highlighted some steady and unsteady flow features of a particular 3D backward-facing double step. The geometry is the arrangement of three elements: a small parallelepiped put behind a bigger one with a pyramidal shaped nose placed in front of it. It was designed to isolate the flow characteristics behind the first step from the influence of upstream artifacts such as funnels or blunt noses. By placing the geometry at the leading edge of a table set in the low speed, low turbulence TEMPO wind tunnel, a relatively uniform flow could be obtained upstream of the first step. This was verified qualitatively by means of laser tomography and quantitatively by probing the boundary layer developing on the model lateral wall, upstream of the first step. The boundary layers were fully turbulent, ensured by considering high Reynolds numbers ranging from  $8.75 \times 10^4$  to  $3.54 \times 10^5$  (based on the step height). Then, the time-averaged flow behind the step could be described, still at zero degree drift angle. The friction lines were observed at the surface of the second cuboid using oil flow visualizations. It revealed the time-averaged footprints of an arch vortex within the well drawn backflow area. The patterns were nonetheless not perfectly symmetric. This feature was better observed using PIV in the plane slicing the first step mid-height: in this plane, at zero degree sideslip, the mean flow is asymmetric. A particular originality of this work has then been to investigate this phenomenon. To do so, a sensitivity study relative to the drift angle was performed. It has shown that a very slight change in drift angle towards  $\beta > 0$  leads to a strongly asymmetric solution, whereas a slight change towards  $\beta < 0$  leads to another strongly asymmetric solution, which is the mirror image of the first one. However, when the drift angle is very close to zero, the mean flow is also very close to symmetric. By analyzing the instantaneous Particle Image Velocimetry (PIV) fields in the plane slicing the first step mid-height, two families of snapshots were evidenced: in the first group, a big vortex is visible on one side of the model whereas in the second group, the big vortex is seen on the opposite side. It has then been observed that for most drift angles close to zero, many successive snapshots usually belong to one same category. It is then thought that the mean field obtained after averaging all the snapshots of a given family represents a stable solution of the flow. In this case, the

flow is bi-stable, with, at zero degree sideslip, the flow switching intermittently from one solution to the other. The symmetric time-averaged solution is then expected to be unstable. However, at exactly zero degree sideslip, the two solutions should a priori occur with the same probability, leading, on average, to a symmetric pattern after an infinite period of time. However, mathematical demonstrations from the literature suggest that this symmetric pattern may not be solution of the steady state equations of a turbulence model for incompressible fluids. Therefore, it may be necessary to discriminate the two solutions before using the experimental time-averaged data as a validation database for CFD results, especially steady state RANS computations.

A parametric study was then conducted in order to isolate some conditions under which this flow bi-stability occurs. It was not affected by most of the parameters tested: it is independent of the Reynolds-number in the range  $5.9 \times 10^3 \leq Re_h \leq 3.54 \times 10^5$ . Tests were then performed in another facility (ONERA L2 wind-tunnel) to observe the influence of a simulated atmospheric boundary layer on the bi-stability: the mean velocity gradient and higher levels of free-stream turbulence, up to 7%, has no effect on the result. Other tests suggest that the bi-stability is relatively independent of the upstream conditions, whether attached or slightly separated flow takes place on the model upper wall. Changing the nose for a rounded one or even removing it did not have any effect on the phenomenon. This was confirmed by a RANS computation with the computational domain starting after the nose and where uniform inlet conditions were set: the mean flow downstream of the first step shows an asymmetry, suggesting that the upstream conditions have no influence on the phenomenon. As a consequence, if the parameters tested are sufficiently numerous, it seems that the flow bi-stability is inherent to 3D double backward facing step flows for a wide range of upstream conditions.

This mean flow asymmetry has some consequences or causes on the unsteady flow and was therefore studied. The behavior of the unsteadiness is also asymmetric: this is shown by the various statistic moments computed in the plane slicing the first step mid-height. It is also confirmed by the asymmetric Proper Orthogonal Decomposition (POD) modes in that plane. They furthermore do not seem to represent any academic unsteady behavior like vortex shedding, as it would be observed downstream of a cylinder. Understanding the unsteady aerodynamic phenomena in this plane has not been completely achieved, despite the use of high speed laser tomography visualizations and the  $\Gamma_1$  structure detection criterion applied to the PIV snapshots: if vortex shedding seems to occur on one side of the model, it is hard to conclude what exactly happens on the opposite side. The rear end of the recirculation area also seems to be unsteady. This is more easily evidenced in the plane of symmetry of the model: there, the first POD mode suggests a flapping movement of the upper shear layer which contributes to the reattaching point unsteadiness. The other first modes may represent vortex shedding

in the upper shear layer which would also modify the position of the reattaching point. Vortex shedding was observed using high speed laser tomoscopy visualizations and structure detection using the  $\Gamma_1$  criterion. The size of the large scale structures were estimated through the integral length scales and reach values up to one step height. Such values are also found in the wake of the step, downstream of the recirculation area, suggesting advection of large scale structures. The average advection velocity of those vortices was measured with two hot-wire probes. The vortices are shown to accelerate during their advection. Eventually, the unsteady phenomena are characterized behind the first step and on both sides of the model by a Strouhal number of  $St_h = 0.08$ , based on the step height and the upstream velocity.

The understanding of this flow remains incomplete: firstly, the origins of the bi-stability must be further investigated. Preliminary tests suggest that it may be a consequence of the second parallelepiped behind the first step, but may not be influenced by the second step. Future work should then focus on the longitudinal vortices generated at the edges of that second parallelepiped. Also, the influence of the aspect ratios of that geometry on the bi-stability should be analyzed. Secondly, an unsteady CFD computation of the flow could help understand its 3D unsteady behavior. This could be of great help if high fidelity flight simulators or even flow control were considered.

This may indeed be useful, since rough estimates using criteria of the literature suggest that the flow bi-stability, and in particular when the flow switches from one solution to the other, may be a phenomenon to take into account as far as the launch and recovery of helicopters on frigates is concerned. However, such results consider that the ship airwake affects the helicopter flight but not inversely, namely the rotor airwake does not modify the ship airwake. The first step to any further work should then be to check if this flow bi-stability still remains when a helicopter rotor is involved. Some experimental tests on a rotor model could be performed in this way. If the bi-stability still occurs and if it has been proved to be a relevant issue to helicopter operations in the maritime environment, then it should be accounted for in helicopter flight simulators. The circumstances under which the rotor wake has a negligible influence on the ship airwake alone should also be highlighted.

Eventually, if the bi-stability of the flow has been highlighted here as well as some of its consequences on the launch and recovery of helicopters on ships, the understanding of such complex flows remains incomplete. This is even more true when a rotor is involved. The question is broad and further research needs to be conducted.



# Appendix A

## Basic theoretical background

In this appendix, some theoretical notions that were used in the previous chapters will be developed here. It is not meant to be a course on fluid mechanics. For detailed demonstrations, the reader should refer, for example, to Batchelor [14] or Schlichting and Gersten [156] for the general equations and to Sedov [157] and Rebuffet [140] for the similarity theory.

### A.1 Simplified Navier-Stokes equations (NSE)

This section aims to present some approximations leading to the simplified NSE. This will enable to define some basic similarity parameters that have been mentioned along the previous chapters.

In the scope of this work, since the size of the model is much greater than the mean free path of the fluid particles and since the Mach number is lower than 0.3 everywhere in the flow, some assumptions will be made. Hereafter, it is assumed that the continuum as well as the incompressible flow approximations are valid. It is also assumed that there are no volume forces acting on fluid particles other than the pressure, viscous and inertial forces: since there is no free-surface in the fluid, the gravity force is not taken into account.

Under those hypotheses, the time-space evolution of a continuum fluid can be described by simplified Navier-stokes equations. Those equations translate the general laws of continuum mechanics, namely conservation of mass, energy and linear momentum. The advantage of the incompressible flow approximation is that the energy and momentum equations are therefore uncoupled, namely the velocity field can be determined only by the momentum and continuity equations (or mass conservation equation). In the Eulerian representation, they are expressed below [63]:

$$\operatorname{div}(\mathbf{u}) = 0 \quad (\text{A.1a})$$

$$\frac{\partial \mathbf{u}}{\partial t} + (\mathbf{u} \cdot \nabla) \mathbf{u} - \nu \Delta \mathbf{u} + \frac{1}{\rho} \nabla p = 0. \quad (\text{A.1b})$$

## A.2 Normalized NSE and similarity laws

A better physical interpretation is to consider the normalized Navier-Stokes equations. For this purpose, a reference length  $L_*$ , a reference velocity  $U_*$ , a reference pressure  $p_*$ , a reference time  $t_*$  and a reference viscosity  $\nu_*$  are introduced. For  $i = 1, 2, 3$ , this defines the reduced variables  $x_i = L_* x_i^+$ ,  $u_i = U_* u_i^+$ ,  $p = p_* p^+$ ,  $t = t_* t^+$  and  $\nu = \nu_* \nu^+$ . The normalized density is equal to 1 due to the incompressible flow approximation. By substituting those variables into equations A.1, the normalized NSE become:

$$\operatorname{div}^+(\mathbf{u}^+) = 0 \quad (\text{A.2a})$$

$$St \frac{\partial \mathbf{u}^+}{\partial t^+} + (\mathbf{u}^+ \cdot \nabla^+) \mathbf{u}^+ - \frac{1}{Re} \Delta^+ \mathbf{u}^+ + Eu \nabla^+ p^+ = 0. \quad (\text{A.2b})$$

The superscript  $^+$  means that the quantity is differentiated against the reduced variable  $x_i^+$ . This introduces some dimensionless numbers:

$$St = \frac{L_*}{t_* u_*} = \frac{\text{characteristic advection time}}{\text{characteristic time of the unsteady phenomenon}} \quad (\text{A.3})$$

$$Re = \frac{u_* L_*}{\nu_*} = \frac{\text{inertial volume forces}}{\text{viscosity volume forces}} \quad (\text{A.4})$$

$$Eu = \frac{p_*}{u_*^2} = \frac{\text{pressure volume forces}}{\text{inertial volume forces}} \quad (\text{A.5})$$

$$(\text{A.6})$$

Usually, for incompressible flows,  $p_* = \rho_* u_*^2$  can be chosen, leading to  $Eu = 1$ . Otherwise, the speed of sound and the ratio of the thermal capacities  $\gamma$  can be introduced, which yields to  $Eu = \frac{1}{\gamma M^2}$  where  $M = \frac{u}{a}$  is the Mach number and  $a$  the speed of sound in the reference conditions.

The similarity laws come directly from those normalized equations. Take two flows, one on the model and one on the full scale (subscript  $(\cdot)_m$  and  $(\cdot)_f$  respectively). The two flows are similar if (i) they respect the same reduced initial and boundary conditions and (ii) they are solutions of the same equations, namely the normalized simplified NSE above. Those normalized equations are identical if the reduced variables are the same on the model and at full scale, and also if  $(St)_m = (St)_f$  and  $(Re)_m = (Re)_f$

and  $(M)_m = (M)_f$ . In general, it is not possible to fulfill those last three conditions simultaneously. In the present study, it was not possible to respect the Reynolds number. Its effect was already discussed in chapter 1.

### A.3 RANS equations and budget equations

The role of this section is to set the equations leading to the definition of the turbulence production mentioned in section 3.3. The following development is taken for the most part from Cousteix [44].

Let the time-dependant velocity  $\mathbf{u}$  be decomposed into a mean  $\mathbf{U} = \langle \mathbf{u} \rangle$ , and  $\mathbf{u}'$  the fluctuation (the same goes for the pressure):

$$\mathbf{u} = \mathbf{U} + \mathbf{u}' \quad (\text{A.7a})$$

$$\mathbf{p} = \mathbf{P} + \mathbf{p}' \quad (\text{A.7b})$$

Substituting this new expression for  $\mathbf{u}$  into the simplified NSE (A.1) and by averaging the result, leads to the Reynolds Averaged Navier-Stokes equations (RANS equations):

$$\frac{\partial U_l}{\partial x_l} = 0 \quad (\text{A.8a})$$

$$\frac{\partial U_i}{\partial t} + U_l \frac{\partial U_i}{\partial x_l} + \frac{1}{\rho} \frac{\partial P}{\partial x_i} - \nu \frac{\partial^2 U_i}{\partial x_l^2} + \frac{\partial \langle u'_i u'_l \rangle}{\partial x_l} = 0 \quad (\text{A.8b})$$

$\langle u'_i u'_l \rangle$  is representative of the influence of the turbulence on the mean flow. In terms of energy, the exchange term between the mean and fluctuating flow can be expressed. To do so, the momentum equation in A.1 is multiplied by  $\mathbf{u}$ . Taking the average and using the continuity equation yields:

$$\begin{aligned} \frac{D}{Dt} (K + k) + \frac{\partial}{\partial x_l} \left( \frac{\langle u'_i u'_i u'_l \rangle}{2} + \langle u'_i u'_l \rangle U_i \right) = -2\nu \langle s'_{il} s'_{il} \rangle \\ -2\nu S_{il} S_{il} + \frac{\partial}{\partial x_l} \left( -\frac{1}{\rho} P U_l + 2\nu U_i S_{il} - \frac{1}{\rho} \langle p' u'_l \rangle + 2\nu \langle u'_i s'_{il} \rangle \right) \end{aligned} \quad (\text{A.9})$$

where  $K = (U_i U_i)/2$ ,  $k = (\langle u'_i u'_i \rangle)$  are the kinetic energies of the mean and fluctuating flows respectively,  $S_{il} = \frac{1}{2} \left( \frac{\partial U_i}{\partial x_l} + \frac{\partial U_l}{\partial x_i} \right)$  and  $s'_{il} = \frac{1}{2} \left( \frac{\partial u'_i}{\partial x_l} + \frac{\partial u'_l}{\partial x_i} \right)$  are the deformation tensors of the mean and fluctuating flows respectively.  $\frac{DK}{Dt} = \frac{\partial K}{\partial t} + U_l \frac{\partial K}{\partial x_l}$  expresses the rate of change of  $K$  at a point that moves with the mean flow.

The budget energy for  $K$  can also be obtained by multiplying by  $U_i$  equation A.8b. This



leads to:

$$\frac{DK}{Dt} = \langle u'_i u'_i \rangle S_{ii} - 2\nu S_{ii} S_{ii} + \frac{\partial}{\partial x_l} \left( -\frac{1}{\rho} P U_l + 2\nu S_{il} U_i - \langle u'_i u'_i \rangle U_i \right) \quad (\text{A.10})$$

By subtracting, the equation for  $k$  becomes:

$$\begin{aligned} \frac{Dk}{Dt} = & - \langle u'_i u'_i \rangle S_{ii} - 2\nu \langle s'_{il} s'_{il} \rangle \\ & + \frac{\partial}{\partial x_l} \left( -\frac{1}{\rho} \langle p' u'_l \rangle + 2\nu \langle u'_i s'_{il} \rangle - \frac{\langle u'_i u'_i u'_i \rangle}{2} \right) \end{aligned} \quad (\text{A.11})$$

The term  $-\langle u'_i u'_i \rangle S_{ii}$  is the power of the deformation of the Reynolds stress tensor. It appears in both kinetic energy budget equations but with an opposite sign. Therefore, it represents the exchange of energy between the mean and the fluctuating flow. In general, this term is positive, meaning that the mean flow gives some of its energy to the fluctuating flow: this is why it is called the term of turbulence production.

In section 3.3, this quantity was multiplied by  $h/U_0^3$  so that it would be a dimensionless quantity.

## Appendix B

# Sampling parameters of a stationary ergodic random process

In the previous chapters, some uncertainty on the estimate of the statistic moments such as the mean and mean square values, Skewness, Kurtosis and spectrum were given without any justification. This appendix gives a non-exhaustive development that enables to quantify the uncertainty. For more details, the reader should refer to the work of Bruun [28], the basis of most of this appendix.

### B.1 Theory of uncertainty estimates

This uncertainty comes from the fact that the time-series considered are not infinite. Indeed, for example, the true mean value  $\bar{X}$  of a stationary ergodic continuous random process  $x(t)$  is defined as:

$$\bar{X} = \lim_{T \rightarrow \infty} \frac{1}{T} \int_0^T x(t) dt \quad (\text{B.1})$$

Of course, when only a finite sample of the signal is taken, namely T does not tend to infinity, then the value computed is the estimated mean value, noted with a hat:

$$\hat{X} = \frac{1}{T} \int_0^T x(t) dt \quad (\text{B.2})$$

A theory has been developed that can evaluate how far the estimated mean value  $\hat{X}$  is from the true value  $\bar{X}$  and with how much confidence this result can be taken. To do so, a main assumption is made: the probability density function (PDF) of the random signal approximates a Gaussian distribution. To apply this to the mean value, for example,  $\hat{X}$  is supposed to be a random variable: if many measurements of  $\hat{X}$  are

made for a given T,  $\hat{X}$  will take random values that are around the true mean value  $\bar{X}$ . According to the assumption of Gaussian behavior, the distance to the true mean is known through its PDF: the measured mean value  $\hat{X}$  (true value,  $\bar{X}$ ), will statistically fall within the interval

$$\bar{X} - z_{\alpha/2}\sigma[\hat{X}] < \hat{X} < \bar{X} + z_{\alpha/2}\sigma[\hat{X}] \quad (\text{B.3})$$

with a probability of  $(1 - \alpha)\%$ . In equation B.3,  $z_{\alpha/2}$  is the value of  $z = \frac{\hat{X} - \bar{X}}{\sigma[\hat{X}]}$  for which its probability equals to  $1 - \alpha/2$ . Also, the variance of  $\hat{X}$  is

$$\text{var} [\hat{X}] = \sigma^2[\hat{X}] \quad (\text{B.4})$$

where  $\sigma[\hat{X}]$  is the standard deviation of the measured mean value,  $\hat{X}$ . This yields to the relative uncertainty

$$\text{Error}_{\hat{X}}(\alpha) = \frac{\hat{X} - \bar{X}}{\bar{X}} = z_{\alpha/2}\varepsilon[\hat{X}] = z_{\alpha/2}\frac{\sigma[\hat{X}]}{\bar{X}} \quad (\text{B.5})$$

(as long as  $\bar{X} \neq 0$ ).

The same goes for the relative uncertainty on the measured mean-square value of the fluctuating part of the signal:

$$\text{Error}_{\hat{x}^2}(\alpha) = \frac{\hat{x}^2 - \bar{x}^2}{\bar{x}^2} = z_{\alpha/2}\varepsilon[\hat{x}^2] = z_{\alpha/2}\frac{\sigma[\hat{x}^2]}{\bar{x}^2} \quad (\text{B.6})$$

(as long as  $\bar{x}^2 \neq 0$ , namely always for an unsteady signal).

A conservative estimate of the uncertainty for the variance of the autocorrelation coefficient can be given by the uncertainty for the variance of  $\hat{x}^2$ . As for the cross-correlation, the uncertainty for the variance of the highest mean square value of the two signals that are being cross-correlated is a conservative estimate.

The difficulty is now to compute the error. As mentioned before, it depends on the confidence required on the results. Indeed, the higher the confidence in the estimate of the uncertainty (namely small values for  $\alpha$ ), the wider the interval of confidence  $z_{\alpha/2}$ . The relation between  $\alpha$  and  $z_{\alpha/2}$  is given in table B.1.

The next step then is to determine  $\varepsilon$ , in other words the variance of the measured value of interest. It can be expected that the greater T, the closer to the true value the measured value gets. In practice, the time signals are not continuous but samples. If the former equations are still valid, this feature must be taken into account in the following. If  $N_s$  is the number of samples of the signals, supposed to be statistically independent (that is acquired every 2 integral time scales  $2T_1$  -see section B.3), it can be shown that the standard deviation of the measured values of interest takes the values recalled in

TABLE B.1: A Gaussian probability density distribution

$(1 - \alpha)$ [%]	$z_{\alpha/2}$ [-]
100	$\infty$
99	2.57
98	2.33
95	1.96
90	1.65

table B.2.

Regarding spectra,  $n_d$  is introduced: the error is indeed reduced by computing an ensemble of estimates from  $n_d$  different subrecords of same length. The corresponding error is written in table B.2.

Eventually, Bruun [28] gives the mean square error  $\epsilon^2$  for the probability density function  $p(x)$ :

$$\epsilon^2[\hat{p}(x)] \approx \frac{1}{NWp(x)} + \frac{W^4}{576} \left[ \frac{p''(x)}{p(x)} \right]^2 \quad (\text{B.7})$$

Equation B.7 shows that there are conflicting requirements on the window width  $W$ : a large value of  $W$  is needed to reduce the error related to the first term whereas a small value of  $W$  has the same effect on the second term. Therefore,  $W \leq 0.2\sigma_i$  is usually chosen to limit the normalized bias error in probability density measurements (less than 1% for approximately Gaussian random data). In the results presented in figures 3.17 and 3.24, a width of  $0.1\sigma_i$  was chosen. However, because of the difficulty to estimate  $p''$  in equation B.7, the bias error was not computed, but expected to be relatively low according to the former criterion. Several values of  $W$  were tested and led qualitatively to the same shape as those presented, which was sufficient for the approach adopted herein.

TABLE B.2: Expression of the error estimates for various quantities

Quantity	$\sigma[\text{Quantity}]$	$\epsilon[\text{Quantity}]$	$Error_{\text{Quantity}}(\alpha)$
mean $\hat{X}$	$\sigma_x/\sqrt{N}$	$\frac{1}{\sqrt{N}} \frac{\sigma_x}{X}$	$\frac{z_{\alpha/2}}{\sqrt{N}} \frac{\sigma_x}{X}$
mean square $\hat{x}^2$	$\sigma_x^2/\sqrt{N}$	$\frac{1}{\sqrt{N}}$	$\frac{z_{\alpha/2}}{\sqrt{N}}$
Skewness $\hat{x}^3/\sigma_x^3$	$\sqrt{6/N}$	$\sqrt{\frac{6}{N}} \frac{\sigma_x^3}{x^3}$	$z_{\alpha/2} \sqrt{\frac{6}{N}} \frac{\sigma_x^3}{x^3}$
Kurtosis $\hat{x}^4/\sigma_x^4$	$\sqrt{96/N}$	$\sqrt{\frac{96}{N}} \frac{\sigma_x^4}{x^4}$	$z_{\alpha/2} \sqrt{\frac{96}{N}} \frac{\sigma_x^4}{x^4}$
Spectrum $\hat{G}_x(f)$	$G_x(f)\sqrt{n_d}$	$\frac{1}{\sqrt{n_d}}$	$\frac{z_{\alpha/2}}{\sqrt{n_d}}$

Some comments should be made concerning the values in this table B.2: in general, the turbulence intensity  $\frac{\sigma_x}{X}$  is smaller than 1 and therefore, the uncertainty on the mean value is less than that on the mean square value. It should be emphasized that in practice,  $\frac{\sigma_x}{X}$  is computed from the measured value and is therefore not the true value.

This induces another error. Although it does not make much of a difference for the error estimate of the mean, it is not so true for the error estimate of the skewness and the Kurtosis. Moreover, even if  $N_s$  is large, the standard deviation becomes very large with higher statistic moments and the uncertainty grows consequently. This method is therefore not very precise for the uncertainty estimation of those third, fourth and higher order moments. Also, because the signal is composed of sample data, care must be taken when defining the statistic moments.

## B.2 Unbiased estimates of the statistic moments for the normal law

The definition of the statistic moments from sample data can introduce a bias if it is not done properly. Therefore, in order not to introduce an additional error, the former defined measured statistic moments must be computed from the following formula:

$$\hat{X} = \frac{1}{N_s} \sum_{n=1}^{N_s} X(n) \quad (\text{B.8})$$

for the mean and for the mean square:

$$\hat{x}^2 = \frac{1}{N_s - 1} \left[ \sum_{n=1}^{N_s} X^2(n) - N_s \hat{X}^2 \right] \quad (\text{B.9})$$

As for the skewness, it was computed in the previous chapter from the third order moment as follows:

$$\hat{x}^3 = \frac{1}{N_s} \left( \sum_{n=1}^{N_s} X^3(n) - 3\hat{X} \sum_{n=1}^{N_s} X^2(n) + 2N_s \hat{X}^3 \right) \quad (\text{B.10})$$

Leading to the unbiased estimate of the Kurtosis:

$$\hat{x}^4 = \frac{(N_s + 1)N_s}{(N_s - 1)(N_s - 2)(N_s - 3)} \sum_{n=1}^{N_s} (X(n) - \hat{X})^4 - 3 \frac{(n-1)^2}{(n-2)(n-3)} \quad (\text{B.11})$$

## B.3 Choosing the acquisition parameters

As mentioned before, the previous results were obtained on the assumption that the records are statistically independent. This requires to choose carefully the acquisition

frequency  $f_s$ , the sampling time  $T$  and the number of samples  $N_s$ . Those three quantities are related through  $N_s = T \times f_s$ . It can be shown that the optimum sampling criterion to achieve this is:

$$f_s = 1/(2T_I) \quad (\text{B.12})$$

where  $T_I$  is the integral time scale at that measurement point, defined by

$$T_I = \int_0^\infty \rho_u(\tau) d\tau \quad (\text{B.13})$$

where  $\rho_u$  is the autocorrelation coefficient function defined by

$$\rho_u = \frac{R_u(\tau)}{\sigma_u^2} \quad (\text{B.14})$$

and

$$R_u(\tau) = \lim_{T \rightarrow \infty} \int_0^\infty u(t)u(t + \tau)dt \quad (\text{B.15})$$

In practice, the integration range for  $R_u$  is finite and was already discussed in section 3.3.4. Also,  $T_I$  is estimated and then checked experimentally. Of course, to measure  $T_I$ , there must be enough samples between 0 and  $2T_I$  otherwise the two signals will be statistically uncorrelated and the autocorrelation coefficients will be close to zero almost everywhere.

Eventually, the number of independent samples is maximum when the confidence required in the measured value is maximum as well as the turbulent intensity. It is then better to overestimate the latter in order to overestimate  $N_s$ . As for  $f_s$ , for a given number of samples, sampling much more slowly will extend the measuring time without any significant increase in accuracy, whereas a faster sampling rate will increase the uncertainty because the samples will no longer be statistically independent. The sampling criteria were then chosen in this manner. In the following section, some uncertainty estimates are given for the different measurements performed.

## B.4 Application to the experimental database

### B.4.1 TEMPO free-stream velocity and turbulence

For the LDA measurements presented in section 2.2.2.1, the integral length-scale of turbulence is estimated to be smaller than the honey comb cell size of 10 mm. To determine the turbulence integral time scale, Taylor's convected, frozen-turbulence-pattern hypothesis is applied [28]:

$$\frac{\partial}{\partial x} = -\frac{1}{\bar{U}} \frac{\partial}{\partial t} \quad (\text{B.16})$$

This procedure relates the longitudinal variation to the temporal variation at a point, by assuming the convection of ‘frozen’ turbulent structures past the measurement point with the mean velocity. The integral time scale can be estimated from

$$L_u^x = \bar{U}T_I \quad (\text{B.17})$$

In the present case,  $T_I = L_u^x/U_0$ , which reaches a maximum of 5 ms for the minimum value of  $U_0$ . In order to have statistically independent samples, the sampling period must be greater than 10 ms which is the case. All samples then are not independent. The maximum number of statistically independent samples is  $N_s = T/(2T_I) = 120/(2 \times 0.005) = 12000$  which is reached for every series of measurements. Overestimating a maximum longitudinal intensity of 5% leads to the results of table B.3 for all the velocities probed.

TABLE B.3: Uncertainty in the estimate of the true mean and mean square values in the TEMPO wind tunnel. Empty test-section

Quantity	Confidence [%]	$Tu_{max}$ [%]	$N_s$	Uncertainty [%]
mean	99	5	12000	0.1
mean square	99	5	12000	2.4

#### B.4.2 PIV measurements

The turbulence integral length scales determined in section 3.3.4 give values smaller than a step height  $h$ . For a rough estimate of the integral time scale, considering  $U_0$  as the mean velocity inserted into equation B.17 gives an integral time scale smaller than 10 ms. The sampling frequency  $f_s$  must then be smaller than 50 Hz to obtain statistically independent samples. This was the case in the experiments with  $f_s = 15$  Hz.

Since the mean value cancels at some locations, it is more convenient to define the uncertainty estimate  $\Delta U/U_0$ , where  $\Delta U$  is the maximum uncertainty estimate on the velocity in the field.  $\Delta U/U_0$  must be compared to 1, the value of the normalized velocity in the free-stream. The PIV fields in figure 4.2 do not present the same amount

TABLE B.4: Uncertainty in the estimate of the mean value for the PIV measurements

Plane	see fig.	$Re_h \times 10^{-4}$	Confidence [%]	$Tu_{max}$ [%]	$N_s$	$\Delta U/U_0$ [-]
$y = 0$	3.2.2.1	8	99	25	468	0.03
$y = 0$	3.3.1	9.75	99	25	1274	0.02
$z/h = 0.784$	3.2.2.2	9.75	99	20	299	0.03
$z/h = 0.5$	4.2	9.75	99	25	179	0.05
$z/h = 0.5$	4.2	9.75	99	25	1354	0.02

of data. The maximum uncertainty  $\Delta U/U_0$  varies inbetween 0.02 and 0.05 depending on the fields. It is emphasized that this is the maximum uncertainty of the true mean value. In most of the field, the turbulence value is well below those reported in table B.4. Therefore, the true mean value can be considered to be relatively in fact well estimated.

The uncertainty however grows for the higher order moments, as illustrated in table B.5. In this table, since the skewness can equal to zero, the error that is defined is just the absolute value of the difference between the measured and the true skewnesses, namely Error Skewness  $= \frac{\hat{x}^3 - x^3}{\sigma^3} = z_{\alpha/2} \sqrt{\frac{6}{N}}$ .

TABLE B.5: Uncertainty in the estimate of higher order moments for the PIV measurements at  $Re_h = 9.75 \times 10^4$

Plane	$z/h = 0.5$ (see fig. 3.3.1.2)	$y = 0$ (see fig. 3.3.1.1)
$\left(\sigma_x^4/\overline{x^4}\right)_{avg}$	0.25	0.25
$N_s$	1354	1274
Confidence [%]	95	95
Error mean square [%]	5.3	5.5
Error Skewness [-]	0.13	0.14
Error Kurtosis [%]	25	25

### B.4.3 Hot-wire anemometry data

#### B.4.3.1 Boundary layer probing at the L2 wind tunnel

The same development as for section B.4.1 can be applied to the measurements presented in section 2.3.5. Considering the turbulence integral length scales are representative of the coherent structures being shed behind the tubes of the grid, the coherent structures are expected to reach a few millimeters in size. This leads to an optimal sampling frequency around 200 Hz. For those measurements,  $T = 256$  s and  $f_s = 2^{11} > 200$  Hz. There are then about  $N_s = 51000$  statistically independent samples. The consecutive uncertainties on the estimates are recalled in table B.6.

TABLE B.6: Uncertainty in the estimate of the true mean and mean square values in the L2 wind tunnel. Empty test-section

Quantity	Confidence [%]	$Tu_{max}$ [%]	$N_s$	Uncertainty [%]
mean	99	9	51000	0.1
mean square	99	9	51000	1.1



### **B.4.3.2 Boundary layer probing on the SFISO'**

The same development goes for the velocities measured in the boundary layer of the SFISO' (see 3.1). Here the uncertainty on the mean square is around 1% and even less for the mean value.

### **B.4.3.3 Spectrum**

The number of subrecords for the spectrum plotted in figure 3.26 reaches 1569. This leads to an uncertainty of about 6.5% on the energy measured at each frequency smaller than half the sampling frequency. In this estimate, the influence of the window is not taken into account.

## **B.4.4 Pressure measurements**

For the pressure measurements at L2, only steady measurements were performed. The high frequencies are, a priori, damped within the silicon tubes. However, in the worst case, if it is assumed that the signal measured is unsteady, with normalized turbulence about 20%, the uncertainty on the measured  $C_p$  does not exceed 5%. This is thought to be an overestimate.

## **B.5 Remarks on uncertainty determination**

The method presented here was used in the previous chapters. It should be kept in mind that it exclusively determines the uncertainty on the estimation of the true values to be measured. If it can be a non-negligible part of the global uncertainty, it is most likely not the global uncertainty on the measure. To get the global uncertainty, the other sources of errors should be taken into account. They are numerous. The reader should simply bear in mind that the absolute global uncertainty on the determination of the true quantities to be determined is greater or equal to the uncertainties estimated by the present method.

# Appendix C

## POD

The present description is deeply inspired from Montigny-Rannou [121] that reviews, among others, the work from Berkooz et al. [17] and Holmes et al. [79]. The main ideas of the theory are recalled below. For the proofs that are not given, the reader should refer to [121].

The Proper Orthogonal Decomposition (POD) is also known under the Karhunen-Loève decomposition, principal components analysis, singular system analysis or singular value decomposition. Given an ensemble of results belonging to a vector space, the idea behind POD is to determine an optimal sub-space of smaller dimension. This optimality is defined in the sense that the error due to the projection on this sub-space is minimal. In practice, optimality refers to the energy. The problem is then to find an orthogonal basis of vectors in a sub-space where a random vector takes its values, such that the elements belonging to this space can be expressed in an optimal way from the first  $N$  vectors of the basis (if the first  $N$  modes are the most energy containing ones, then the maximum energy is kept). To solve this optimization problem, let us consider a Hilbert space  $\mathcal{H}$ , with the inner product  $\langle \cdot, \cdot \rangle$  and the associated norm  $\|\cdot\|$ .  $\mathcal{H}$  is an ensemble of square-integrable functions on the domain  $\Omega$  where the fluid evolves. In our case of PIV fields,  $\Omega$  is the slice of the flow where the velocities are measured. Those functions can have vector values.

**Mathematical definition of the problem** Given an ensemble of data  $\{u^k \in H | k = 1, \dots, M\}$ , provided by experiments or computations, the goal is to find a sub-space  $\mathcal{S}$  of  $\mathcal{H}$ , with finite dimension  $N < M$  such that

$$E(\|u - P_s u\|) \tag{C.1}$$

is minimal.  $P_s$  is the orthogonal projection on the sub-space  $\mathcal{S}$  and  $E$  is an average operator on  $k$ . In our case,  $\{u^k\}$  is the ensemble of snapshots of a given serie. In what follows, the notation  $\{u^k\} = u$  is adopted. Also, the average  $E$  can be an arithmetic or weighted average but it is supposed to be linear. Therefore, it commutes with the inner product:

$$E(\langle u^k, v^k \rangle) = \langle E(u^k v^k) \rangle \quad (\text{C.2})$$

Let us consider  $\{\Phi_j \in \mathcal{H} | j = 1..N\}$  an orthonormal basis of the sub-space  $\mathcal{S}$ . The orthogonal projection on  $\mathcal{S}$  is defined as:

$$P_s \{u^k\} = P_s u = \sum_{j=1}^N \langle u, \Phi_j \rangle \Phi_j \quad (\text{C.3})$$

It can be noted that minimizing  $E(\|u - P_s u\|)$  on  $\mathcal{S}$  is equivalent to maximizing  $E(\|P_s u\|^2)$  on  $\mathcal{S}$ . This also corresponds to maximizing in relation with the orthonormed functions  $\Phi_j$  the quantity:

$$\sum_{j=1}^N E(|\langle u, \Phi_j \rangle|^2) \quad (\text{C.4})$$

This optimization problem leads to an eigenvalue problem:

$$K\Phi = \lambda\Phi \quad (\text{C.5})$$

where  $K = E(u \otimes u^*)$  is the Esperance of a tensorial product,  $u^*(.) = \langle ., u \rangle$  the dual vector for  $u$  and  $\otimes$  the tensorial product defined as the linear transformation within  $\mathcal{H}$  by  $(u \otimes u^*)\Psi = uu^*(\Psi) = u \langle \Psi, u \rangle$  for all  $\Psi \in \mathcal{H}$ . Also, by taking the inner product, it leads to

$$\lambda = E(|\langle u, \Phi \rangle|^2) \quad (\text{C.6})$$

$K$  is defined and positive ( $\lambda \geq 0$ ), the functions  $\Phi_j$  which maximize the initial functional (see equation C.4) are the eigenfunctions corresponding to the  $N$  highest  $K$  values. Since  $K$  is self-adjoint, the eigenfunctions can be chosen orthonormal.

**POD theorem** As a result, this theorem actually proves that, given a dataset  $\{u^k \in H | k = 1, ..M\}$ , the sub-space  $\mathcal{S}$  with dimension  $N < M$  that minimizes  $E(\|u - P_s u\|)$  has an orthonormal basis  $\{\Phi_j \in \mathcal{H} | j = 1..N\}$  where  $\Phi_j$  are solutions of  $K\Phi_j = \lambda\Phi_j$ , with  $K = E(u \otimes u^*)$ , where  $\lambda_1 \geq \lambda_2 \geq \lambda_N > 0$  are the highest eigenvalues for  $K$ . The eigenfunctions  $\Phi_j$  are called the POD modes.

The eigenvalue  $\lambda_k$  physically represents the average energy captured by the eigenmode  $\Phi_k$ .

**Determining the POD modes** To simplify the eigenvalue problem (equation C.5), Sirovich [160] introduced the snapshot method. It is based on the property that every POD mode  $\Phi_m$  can be expressed as the linear combination of the snapshots:

$$\Phi_m = \sum_{k=1}^M c_k^m u^k \quad \text{for } m = 1, \dots, N \quad (\text{C.7})$$

Considering that the average operator  $E(\cdot)$  is the classical ensemble average on the  $M$  snapshots  $u^k$  and by introducing equation C.7 into C.5, the eigenvalue problem reduces to

$$\sum_{j=1}^M \frac{\langle u^j, u^k \rangle}{M} c_j = \lambda c_k \quad \text{for } k = 1, \dots, M \quad (\text{C.8})$$

This can be written in matricial form  $Uc = \lambda c$  where  $c^T = (c_1, \dots, c_N)$  and  $U$  is the  $N \times N$  matrix defined by its coefficients  $U_{ij} = \frac{\langle u^j, u^i \rangle}{M}$ .  $U$  is self-adjoint for the inner product  $\langle a, b \rangle = M \sum_j a_j \bar{b}_j$  and therefore the eigenfunctions  $c$  are orthogonal.

**Decomposition and approximation** Using the previous demonstrations, once the POD modes have been determined, every snapshot  $u^k$  can be projected on the POD basis as follows:

$$u^k(x, t) = \sum_{j=1}^N a_j(t) \Phi_j(x) \quad \text{for } k = 1, \dots, M \quad (\text{C.9})$$

The POD modes  $\phi_j$  are time independent, whereas the POD coefficients  $a_j$  are time-dependant. The POD coefficients are not correlated.

If the number of POD modes equals the number of snapshots, namely  $N = M$ , then a projected snapshot is the exact replica of the initial snapshot. However, once  $N < M$ , then a projected snapshot is an approximation of the initial one.

Depending on what phenomenon must be retrieved and on what amount of fluctuating energy should be kept, a small amount of modes can be sufficient to approximate snapshots.

In practice, the POD code implemented in the DaVis 7.2 PIV software [2] was used in the present study.



# Bibliography

- [1] (2004) Helicopter turbulence criteria for operations to offshore platforms. Tech. Rep. CAA paper 2004/03, Civil Aviation Authority
- [2] (2007) DaVis FlowMaster Software Manual for DaVis 7.2, item number: 1105011-4. LaVision GmbH
- [3] (2008) Insight 3G: data acquisition, analysis, and display software platform. User's guide 1980511/ Revision G. TSI Inc.
- [4] (2008) Lecture series - Atmospheric Boundary Layer Flows in air pollution modelling, VKI, Brussels, Belgium
- [5] (2008) Offshore helideck environmental research. Tech. Rep. CAA paper 2008/02, Civil Aviation Authority
- [6] Abbott D, Kline S (1962) Experimental investigations of subsonic turbulent flow over single and double backward-facing steps. *ASME Journal of basic engineering* 84:317–325
- [7] Adachi T (1997) Effects of surface roughness on the universal Strouhal number over the wide Reynolds number range. *Journal of Wind Engineering and Industrial Aerodynamics* 69:399–412
- [8] Adaramola M, Akinlade O, Sumner D, Bergstrom D, Schenstead A (2006) Turbulent wake of a finite circular cylinder of small aspect ratio. *Journal of Fluids and Structures* 22(6-7):919–928
- [9] AGARD (ed) (1998) Fluid dynamics problems of vehicles operating near or in the air-sea surface, vol RTO meeting proceedings 15, Amsterdam
- [10] Aider J, Danet A (2006) Large-eddy simulation study of upstream boundary conditions influence upon a backward-facing step flow. *Comptes rendus-Mécanique* 334(7):447–453

- [11] Alpman E, Long L, Bridges D, Horn J (2007) Fully-Coupled Simulations of the Rotorcraft/Ship Dynamic Interface. In: Annual forum proceedings- American Helicopter Society, American Helicopter Society, Inc., vol 63, p 1367
- [12] Anderson G (1989) Mapping the Airwake of a Model DD-963 Along Specific Helicopter Flight Paths. Master's thesis, Naval postgraduate school, Monterey
- [13] Armitt J (1968) The effect of surface roughness and free stream turbulence on the flow around a model cooling tower at critical Reynolds numbers. In: Proceedings of a Symposium on Wind Effects on Buildings and Structures, Loughborough University of Technology, England
- [14] Batchelor G (2000) An introduction to fluid dynamics. Cambridge Univ Press
- [15] Bearman P, Morel T (1983) Effect of free stream turbulence on the flow around bluff bodies. *Progress in Aerospace Sciences* 20(2-3):97–123
- [16] Becker S, Lienhart H, Durst F (2002) Flow around three-dimensional obstacles in boundary layers. *Journal of Wind Engineering & Industrial Aerodynamics* 90(4-5):265–279
- [17] Berkooz G, Holmes P, Lumley J (1993) The proper orthogonal decomposition in the analysis of turbulent flows. *Annual Review of Fluid Mechanics* 25(1):539–575
- [18] Bhandari S, Colgren R, Lederbogen P, Kowalchuk S (2005) Six-DoF Dynamic Modeling and Flight Testing of a UAV Helicopter. In: AIAA Modeling and Simulation Technologies Conference and Exhibit
- [19] Biskaduros J (1987) Flow Visualization of the Airwake of an Oscillating Generic Ship Model. Master's thesis, Naval postgraduate school, Monterey, California
- [20] Blevins R (1984) Applied fluid dynamics handbook. Van Nostrand Reinhold Company
- [21] Blocken B, Carmeliet J (2004) Pedestrian Wind Environment around Buildings: Literature Review and Practical Examples. *Journal of Building Physics* 28(2):107
- [22] Borée J (2003) Extended proper orthogonal decomposition: a tool to analyse correlated events in turbulent flows. *Experiments in Fluids* 35(2):188–192
- [23] Brackbill C (2000) Helicopter rotor aeroelastic analysis. PhD thesis, The Pennsylvania State University
- [24] Bradshaw P, Wong F (1971) The reattachment and relaxation of a turbulent shear layer. *Journal of Fluid Mechanics* 52(01):113–135

- [25] de Brederode V, Bradshaw P (1972) Three-dimensional flow in nominally two-dimensional separation bubbles. I. Flow behind a rearward-facing step. Imperial College, Aeronautical Report 72(19)
- [26] Bridges DO, F J, Horn, Alpman E, Long LN (2007) Coupled Flight Dynamics and CFD Analysis of Pilot Workload in Ship Airwakes. In: AIAA Atmospheric Flight Dynamics conference, American Institute of Aeronautics and Astronautics, Hilton Head, SC
- [27] Brooks CJ (1992) Canadian Forces Helicopter Ditchings 1952-1990. In: Agard conference proceedings 532, Cesme, Turkey, pp 37.1–37.12
- [28] Bruun H (1995) Hot-wire anemometry: principles and signal analysis. Oxford University Press
- [29] Buresti G (1998) Vortex shedding from bluff bodies. In: Riera, Davenport (eds) Wind Effects on Buildings and Structures: Proceedings of the Jubileum Conference on Wind Effects on Buildings and Structures, Balkema, Porto Alegre, Brazil, pp 61–96
- [30] Calluaud D, David L (2004) Stereoscopic particle image velocimetry measurements of the flow around a surface-mounted block. *Experiments in Fluids* 36(1):53–61
- [31] Cambier L, Veuillot J (2008) Status of the elsA CFD Software for Flow Simulation and Multidisciplinary Applications. In: 46th AIAA Aerospace Science Meeting and Exhibit, Reno. AIAA, vol 664
- [32] Carico G, Fang R, Finch R, Geyer Jr W, Krijns H, Long K (eds) (2003) Helicopter/-ship qualification testing, Flight Test Techniques Series, vol 22, Research and Technology Organisation, North Atlantic Treaty Organisation, Defense Technical Information Center, DOI ISBN92-837-1093-2
- [33] Castelain T (2006) Contrôle de jet par microjets impactants. Mesure de bruit rayonné et analyse aérodynamique. PhD thesis, École Centrale de Lyon
- [34] Castro I, Dianat M (1983) Surface flow patterns on rectangular bodies in thick boundary layers. *Journal of Wind Engineering and Industrial Aerodynamics* 11(1-3):107–119
- [35] Castro I, Robins A (1977) The flow around a surface-mounted cube in uniform and turbulent streams. *Journal of Fluid Mechanics* 79(02):307–335
- [36] Cermak J (1976) Aerodynamics of buildings. *Annual Review of Fluid Mechanics* 8(1):75–106



- [37] Champigny P (1994) Side forces at high angles of attack. Why, when, how? Recherche aérospatiale pp 269–269
- [38] Cheney B, Zan S (1999) CFD code validation data and flow topology for the technical co-operation program AER-TP2 simple frigate shape. Tech. Rep. LTR-A-035, NRC-CNRC
- [39] Chiekh M, Michard M, Grosjean N, Bera J (2004) Reconstruction temporelle d'un champ aérodynamique instationnaire à partir de mesures PIV non résolues dans le temps. In: 9<sup>e</sup> Congrès Francophone de Vélocimétrie Laser
- [40] Colbourne J, Tischler M, K R (2001) Flight Control Design for an Unmanned Rotorcraft Program with a Rapid Development Schedule. In: American Helicopter Society, 57<sup>th</sup> Annual Forum, American Helicopter Society International, Inc.
- [41] Cooper K (1998) Bluff-Body Blockage Correction in Closed and Open Test Section Wind Tunnels. In: Wind tunnel wall corrections, Advisory Group for Aerospace Research and Development. North Atlantic Treaty Organization, NTIS, Springfield, VA, AGARD-AG-336
- [42] Counihan J (1975) Adiabatic atmospheric boundary layers : a review and analysis of data from the period 1880-1972. Atmospheric Environment 9:871–905
- [43] Couplet M (2005) Modélisation POD-Galerkine réduite pour le contrôle des écoulements instationnaires. PhD thesis, Université Paris 13
- [44] Cousteix J (1989) Turbulence et couche limite. Cepadues editions
- [45] Croisier G (1998) Etude de l'écoulement en aval d'une marche descendante confinée par différentes méthodes optiques quantitatives. Numéro d'ordre: 2245, Université des sciences et technologies de Lille
- [46] De Ferrier B, Langlois B (1998) Simulation tools in the calculation of aircraft-ship interface operational limits. In: AGARD (ed) Fluid dynamics problems of vehicles operating near or in the air-sea surface, Research and Technology Organization, vol RTO meeting proceedings 15, pp 10–10
- [47] De Kat R, Humble R, Van Oudheusden B (2010) Time-resolved PIV study of a transitional shear-layer around a square cylinder. In: Leweke T, Williamson C (eds) IUTAM Symposium on Bluff body wakes and vortex-induced vibrations
- [48] Delcayre F (1999) Etude par simulation des grandes échelles d'un écoulement décollé: la marche descendante. PhD thesis, Institut National Polytechnique de Grenoble

- [49] Depardon S, Lasserre J, Brizzi L, Borée J (2006) Instantaneous skin-friction pattern analysis using automated critical point detection on near-wall PIV data. *Measurement Science and Technology* 17:1659
- [50] Depardon S, Lasserre J, Brizzi L, Borée J (2007) Automated topology classification method for instantaneous velocity fields. *Experiments in Fluids* 42(5):697–710
- [51] Desse J, Gilliot A, Herry B, Le Roy J, Mialon B, Monnier J, Paquet J, Pruvost M, Rodriguez O (2009) Etudes sur ressources générales RGF au DAAP/MMHD en 2009. Tech. Rep. RT 2/14595 DAAP, Onera
- [52] DMI (2002) The simulation of a typical ocean wind. Danish Maritime Institute
- [53] Driver D, Seegmiller H, Marvin J (1987) Time-dependent behavior of a reattaching shear layer. *AIAA journal* 25(7):914–919
- [54] Durst F, Tropea C (1981) Turbulent backward-facing step flows in two-dimensional ducts and channels. In: 3rd turbulent shear flow symposium
- [55] Eaton J, Johnston J (1980) Turbulent flow reattachment: an experimental study of the flow and structure behind a backward-facing step. Tech. Rep. MD-39, Stanford university
- [56] Eaton J, Johnston J (1981) A review of research on subsonic turbulent flow reattachment. *AIAA Journal* 19(9):1093–1100
- [57] Eaton J, Johnston J (1981) Low-frequency unsteadiness of a reattaching turbulent shear layer. In: *Proceedings of the Third International Symposium on Turbulent Shear Flows*, Davis, CA, pp 162–170
- [58] Farge M, Schneider K, Pellegrino G, Wray A, Rogallo R (2003) Coherent vortex extraction in three-dimensional homogeneous turbulence: Comparison between CVS-wavelet and POD-Fourier decompositions. *Physics of Fluids* 15:2886
- [59] Fearn RM, Mullin T, Cliffe KA (1990) Nonlinear flow phenomena in a symmetric sudden expansion. *Journal of Fluid Mechanics* 211:595–608
- [60] Fernholz H, Finley P (1996) The incompressible zero-pressure-gradient turbulent boundary layer: An assessment of the data. *Progress in Aerospace Sciences* 32(4):245–311
- [61] Ferrier B, Ludwig D, Carico D, Duncan J (2006) Simulated Dynamic Interface Testing as a Tool in the Forecasting of Air Vehicle Deck Limits and Deck Landing Aids. In: Society AH (ed) Annual forum proceedings, American Helicopter Society, Inc., vol 62, p 210

- [62] Ferrier B, Duncan J, Carico D (2007) Validation of Simulated Dynamic Interface Testing as a Tool in the Forecasting of Air Vehicle Deck Limits and Deck Landing Aids. In: Society AH (ed) Annual forum proceedings, American Helicopter Society, Inc., vol 63, p 1338
- [63] Foias C (2001) Navier-Stokes equations and turbulence. Cambridge Univ Pr
- [64] Forrest J, Owen I (2010) An investigation of ship airwakes using Detached-Eddy Simulation. *Computers & Fluids* 39:656–673
- [65] Forrest J, Hodge S, Owen I, Padfield G (2008) An investigation of ship airwake phenomena using time-accurate CFD and piloted helicopter flight simulation. 34th European Rotorcraft Forum
- [66] Forrest J, Hodge S, Owen I, Padfield G (2008) Towards fully simulated ship-helicopter operating limits: the importance of ship airwake fidelity. In: AHS International, 64th annual forum, Montréal, Canada
- [67] Galdi G (1994) An introduction to the mathematical theory of the Navier-Stokes equations: Linearized steady problems. Springer-Verlag
- [68] Gartshore I (1984) Some effects of upstream turbulence on the unsteady lift forces imposed on prismatic two dimensional bodies. *Journal of Fluids Engineering* 106:418
- [69] Giry P, Courcoux P, Taillemite J (1992) Accidents d'Helicoptere Au Dessus de l'Eau dans la Marine Nationale: Etude Epidemiologique sur la Periode 1980-1991. In: Agard conference proceedings 532, Cesme, Turkey, pp 38.1–36.8
- [70] Goldschmidt V, Bradshaw P (1973) Flapping of a plane jet. *Physics of Fluids* 16:354
- [71] Graftieaux L, Michard M, Grosjean N (2001) Combining PIV, POD and vortex identification algorithms for the study of unsteady turbulent swirling flows. *Measurement Science and Technology* 12:1422–1429
- [72] Greenwell D, Barrett R (2006) Control of Ship Air Wakes using inclined screens. In: 32<sup>nd</sup> European Rotorcraft Forum
- [73] Healey J (1992) Establishing a database for flight in the wakes of structures. *Journal of Aircraft* 29(4):559–564
- [74] Healey JV (1987) The prospects for simulating the helicopter/ship interface. *Naval Engineers Journal* 99(2):45–63

- [75] Herry B, Keirsbulck L, Labraga L, Paquet JB (2009) Caractérisation de l'écoulement derrière une double marche descendante 3D. In: Congrès français de mécanique, 24-25 août, Marseille, France
- [76] Herry B, Keirsbulck L, Labraga L, Paquet JB (2010) Mean flow asymmetry downstream of a 3d double backward facing step. In: IUTAM Bluff Body and Vortex Induced Vibrations 6, 22-25 June, Capri Island, Italy
- [77] Hirsch C (2007) Numerical computation of internal and external flows: fundamentals of computational fluid dynamics. Elsevier
- [78] Hodge S, Zan S, Roper D, Padfield G, Owen I (2009) Time-Accurate Ship Airwake and Unsteady Aerodynamic Loads Modeling for Maritime Helicopter Simulation. *Journal of the American Helicopter Society* 54:022,005
- [79] Holmes P, Lumley J, Berkooz G (1998) Turbulence, coherent structures, dynamical systems and symmetry. Cambridge University Press
- [80] Hoxey RP, Reynolds AM, Richardson GM, Robertson AP, Short JL (1998) Observations of Reynolds number sensitivity in the separated flow region on a bluff body. *Journal of Wind Engineering and Industrial Aerodynamics* 73:231–249
- [81] Hsu SA, Meindl EA, Gilhousen DB (1994) Determining the Power-Law Wind-Profile Exponent under Near-Neutral Stability Conditions at sea. *American Meteorological society* 33(6):757–765
- [82] Hunt J, Abell C, Peterka J, Woo H (1978) Kinematical studies of the flows around free or surface-mounted obstacles; applying topology to flow visualization. *Journal of Fluid Mechanics* 86(1):179–200
- [83] Iaccarino G, Ooi A, Durbin P, Behnia M (2003) Reynolds averaged simulation of unsteady separated flow. *International Journal of Heat and Fluid Flow* 24(2):147–156
- [84] Jeong J, Hussain F (1995) On the identification of a vortex. *Journal of Fluid Mechanics* 285:69–94
- [85] Johns M (1988) Flow Visualization of the Airwake Around a Model of a DD-963 Class Destroyer in a Simulated Atmospheric Boundary Layer. Master's thesis, Naval postgraduate school Monterey
- [86] Jones J, Padfield G, Charlton M (1999) Wavelet analysis of pilot workload in helicopter low-level flying tasks. *Aeronautical Journal* 103(1019):55–63

- [87] Jones M, Newman S (2007) A Method of Reducing Blade Sailing through the Use of Trailing Edge Flaps. In: Society AH (ed) Annual forum proceedings, American Helicopter Society, Inc., vol 63, p 411
- [88] Jovic S (1998) Recovery of reattached turbulent shear layers. *Experimental thermal and fluid science* 17(1-2):57–62
- [89] Kaaria C, Forrest J, Owen I, Padfield G (2009) Simulated aerodynamic loading of an SH-60B helicopter in a ship's airwake. 15th AIAA/CEAS Conference
- [90] Kaaria C, Forrest J, Owen I, Padfield G (2009) Simulated aerodynamic loading of an SH-60B helicopter in a ship's airwake. In: 35th European Rotorcraft Forum, Hamburg, Germany
- [91] Kareem A (1990) Measurements of pressure and force fields on building models in simulated atmospheric flows. *Journal of Wind Engineering and Industrial Aerodynamics* 36:589–599
- [92] Kawai H, Okuda Y, Ohashi M, Tamura T (2010) Wake structure behind 3D square prism in shallow boundary layer flow. In: Leweke T, Williamson C (eds) IUTAM Symposium on Bluff body wakes and vortex-induced vibrations
- [93] Keller J (2001) Analysis and control of the transient aeroelastic response of rotors during shipboard engagement and disengagement operations. PhD thesis, The Pennsylvania State University
- [94] Kim K, Ji H, Seong S (2003) Flow structure around a 3-D rectangular prism in a turbulent boundary layer. *Journal of Wind Engineering & Industrial Aerodynamics* 91(5):653–669
- [95] Kochin N, Kibel I, Roze N (1964) *Theoretical hydrodynamics*. Interscience publishers
- [96] Krajnovic S, Davidson L (2002) Large-Eddy Simulation of the Flow Around a Bluff Body. *AIAA Journal* 40(5):927–936
- [97] Kreizer M, Liberzon A (2010) Three-dimensional particle tracking method using FPGA-based real-time image processing and four-view image splitter. *Experiments in Fluids* 49(4)
- [98] Landsberg A, Boris J, Sandberg W, Young T (1995) Analysis of the Nonlinear Coupling Effects of a Helicopter Downwash with an Unsteady Airwake. AIAA Paper pp 95–0047

- [99] Laneville A (1973) Effects of turbulence on wind induced vibrations of bluff bodies. PhD thesis, University of B.C., Vancouver, Canada, 129 pp.
- [100] Larose G, D'Auteuil A (2006) On the Reynolds number sensitivity of the aerodynamics of bluff bodies with sharp edges. *Journal of Wind Engineering and Industrial Aerodynamics* 94:365–376
- [101] Larose GL, D'Auteuil A (2008) Experiments on 2d rectangular prisms at high reynolds numbers in a pressurised wind tunnel. *Journal of Wind Engineering and Industrial Aerodynamics* 96(Issues 6-7):923–933
- [102] Lazareff M (2006) elsA Theoretical manual. Onera, version.edition 2.0.05 edn
- [103] Lee B (1975) The effect of turbulence on the surface pressure field of a square prism. *J Fluid Mech* 69(part 2):263–282
- [104] Lee R (2003) SFS 2 Code Validation Data Update. In: TTCP AER TP 2 Dynamic Interface Workshop, Patuxent River, USA
- [105] Lee R (2003) SFS2 mean flows & intensities, unpublished data provided by the National Research Council of Canada
- [106] Lee R, Zan S (2005) Wind Tunnel Testing of a Helicopter Fuselage and Rotor in a Ship Airwake. *Journal of the American Helicopter Society* 50(4):326–337
- [107] Lee R, Zan S, et al. (2004) Unsteady aerodynamic loading on a helicopter fuselage in a ship airwake. *Journal of the American Helicopter Society* 49:149
- [108] Lee Y, Silva M (2010) CFD Modeling of Rotor Flowfield Aboard Ship. In: 48th AIAA Aerospace Sciences Meeting Including the New Horizons Forum and Aerospace Exposition, Orlando, Florida
- [109] Lemarié C (2004) Etude du refroidissement et du positionnement d'équipements ferroviaires embarqués en toiture. PhD thesis, Université de Valenciennes et du Hainaut Cambrésis
- [110] Lim H, Castro I, Hoxey R (2007) Bluff bodies in deep turbulent boundary layers: Reynolds-number issues. *Journal of Fluid Mechanics* 571:97–118
- [111] Lin J (2006) Etude détaillée des structures cohérentes de la zone tampon de la turbulence de paroi à l'aide de données de PIV stéréoscopique. PhD thesis, Université des Sciences et Technologies de Lille
- [112] Liu J, Long L (1998) Higher order accurate ship airwake predictions for the helicopter/ship interface problem. In: American Helicopter Society 54th annual forum, American Helicopter Society, Inc., Washington, DC, pp 58–70

- [113] Lu Z, Laneville A (1988) Study of effect of incidence, ratio of depth to height and turbulence on pressure distribution on prisms. *Acta Aerodynamica Sinica* 6:232–236
- [114] Mair W, Maull D (1971) Bluff bodies and vortex shedding—a report on Euromech 17. *Journal of Fluid Mechanics* 45:209–224
- [115] Martinuzzi R, Tropea C (1993) The flow around surface-mounted, prismatic obstacles placed in a fully developed channel flow. *Journal of Fluids Engineering* 115(1):85–92
- [116] Maull D, Young R (1974) Vortex shedding from a bluff body in a shear flow. In: *Flow-induced structural vibrations*, Springer-Verlag, Berlin, A 75-15253 04-39, pp 717–729
- [117] Maurel L (2008) Contrôle des structures d'écoulement sur une marche descendante. Master's thesis, Université de Valenciennes et du Hainaut Cambrésis
- [118] McRuer D (1994) Interdisciplinary interactions and dynamic systems integration. *International Journal of Control* 59(1):3–12
- [119] Meinders E, Hanjali K (1999) Vortex structure and heat transfer in turbulent flow over a wall-mounted matrix of cubes. *International Journal of Heat and Fluid Flow* 20(3):255–267
- [120] Meinders E, Hanjalic K, Martinuzzi R (1999) Experimental study of the local convection heat transfer from a wall-mounted cube in turbulent channel flow. *Journal of Heat Transfer* 121:564
- [121] Montigny-Rannou F (2009) Construction de modèles réduits. Méthode POD. Formation professionnelle continue de l'Office National d'Études et de Recherches Aérospatiales
- [122] Multiple (2007) Investigation of Airwake control for safer Shipboard Aircraft operations. Tech. Rep. RTO-TR-AVT-102 AC/323(AVT-102) TP/107, Research and Technology Organisation North Atlantic Treaty Organisation
- [123] Nakamura Y (1993) Bluff-body aerodynamics and turbulence. *Journal of Wind Engineering and Industrial Aerodynamics* 49(1-3):65–78
- [124] Nakamura Y, Ozono S (2006) The effects of turbulence on a separated and reattaching flow. *Journal of Fluid Mechanics* 178:477–490
- [125] Nakamura Y, Ohya Y, Ozono S (1988) The effects of turbulence on bluff-body mean flow. *Journal of Wind Engineering and Industrial Aerodynamics* 28(1-3):251–259

- [126] Namiranian F, Gartshore I (1988) Direct measurements of oscillating lift on a rigid square section cylinder in a turbulent stream. *Journal of Wind Engineering and Industrial Aerodynamics* 28(1-3):209–218
- [127] Narayanan M, Khadgi Y, Viswanath P (1974) Similarities in pressure distribution in separated flow behind backward-facing steps. *Aeronautical Quarterly* 25:305–312
- [128] Okajima A (1982) Strouhal numbers of rectangular cylinders. *Journal of Fluid Mechanics* 123:379–398
- [129] O’Neill PL, Nicolaides D, Honnery D, Soria J (2004) Autocorrelation Functions and the Determination of Integral Length with Reference to Experimental and Numerical Data. In: 15th Australasian Fluid Mechanics Conference The University of Sydney, Sydney, Australia
- [130] Padfield G, White M (2005) Measuring simulation fidelity through an adaptive pilot model. *Aerospace Science and Technology* 9(5):400–408
- [131] Papadopoulos G, Ötügen M (1995) Separating and reattaching flow structure in a suddenly expanding rectangular duct. *Journal of Fluids Engineering* 117:17
- [132] Paré C (1992) Existence, uniqueness and regularity of solution of the equations of a turbulence model for incompressible fluids. *Applicable Analysis* 43(3):245–296
- [133] Park C, Lee S (2000) Free end effects on the near wake flow structure behind a finite circular cylinder. *Journal of Wind Engineering & Industrial Aerodynamics* 88(2-3):231–246
- [134] Perrin R, Braza M, Cid E, Cazin S, Barthet A, Sevrain A, Mockett C, Thiele F (2007) Obtaining phase averaged turbulence properties in the near wake of a circular cylinder at high Reynolds number using POD. *Experiments in Fluids* 43(2):341–355
- [135] Perrin R, Braza M, Cid E, Cazin S, Chassaing P, Mockett C, Reimann T, Thiele F (2008) Coherent and turbulent process analysis in the flow past a circular cylinder at high Reynolds number. *Journal of Fluids and Structures* 24(8):1313–1325
- [136] Polsky S, Imber R, Czerwicz R, Ghee T (2007) A Computational and Experimental Determination of the Air Flow Around the Landing Deck of a US Navy Destroyer (DDG): Part II. In: 37 th AIAA Fluid Dynamics Conference and Exhibit
- [137] Poornachandra S, Sasikala B (2010) Digital signal analysis. Third edition. Tata Mc Graw Hill



- [138] Prevezer T, Holding J, Gaylard A, Palin R (2002) Bluff body asymmetric flow phenomenon- Real effect or solver artefact? *Wind and Structures* 5(2):359–368
- [139] Raupach M, Antonia R, Rajagopalan S (1991) Rough-wall Turbulent Boundary Layers. *Applied Mechanics Review* 44(1):25
- [140] Rebuffet P (1966) *Aérodynamique expérimentale*, vol Tome 1
- [141] Reddy K, Toffoletto R, Jones K (2000) Numerical simulation of ship airwake. *Computers and Fluids* 29(4):451–465
- [142] Rhoades M (1990) A Study of the Airwake Aerodynamics Over the Flight Deck of an AOR Model Ship. Master's thesis, Naval postgraduate school Monterey
- [143] Richards PJ, Hoxey RP (2002) Unsteady flow on the sides of a 6m cube. *Journal of Wind Engineering and Industrial Aerodynamics* 90:1955–1866
- [144] Richards PJ, Hoxey RP (2006) Flow reattachment on the roof of a 6m cube. *Journal of Wind Engineering and Industrial Aerodynamics* 94:77–79
- [145] Richards PJ, Hoxey RP (2008) Wind loads on the roof of a 6m cube. *Journal of Wind Engineering and Industrial Aerodynamics* 96:984–993
- [146] Richards PJ, Hoxey RP, Short LJ (2001) Wind pressure on a 6m cube. *Journal of Wind Engineering and Industrial Aerodynamics* 89:1553–1564
- [147] Richards PJ, Hoxey RP, Connell B, Lander DP (2007) Wind-tunnel modelling of the Silsoe Cube. *Journal of Wind Engineering and Industrial Aerodynamics* 95:1384–1399
- [148] Roper D, Owen I, Padfield G (2005) CFD Investigation of the Helicopter-Ship Dynamic Interface. In: *American Helicopter Society 61<sup>st</sup> Annual Forum*, American Helicopter Society International, Inc, Grapevine, TX, vol 61, pp 1985–2002
- [149] Roper D, Owen I, Padfield G, Hodge S (2006) Integrating CFD and piloted simulation to quantify ship-helicopter operating limits. *Aeronautical Journal* 110(1109):419–428
- [150] Rowe SJ, Hawson D (2008) Validation of the offshore helideck turbulence criterion. In: *Maritime Operations of Rotorcraft*
- [151] Ruiz T, Sicot C, Brizzi LE, Borée J, Gervais Y (2010) Pressure/velocity coupling induced by a near wall wake. *Experiments in Fluids* 49(1):147–165
- [152] Sagaut P (2006) *Large eddy simulation for incompressible flows: an introduction*. Springer Verlag

- [153] Saunders G (1975) Dynamics of helicopter flight. Wiley, New-York
- [154] Schewe G (1985) Investigation of the aerodynamic forces on Bluff bodies at high Reynolds numbers. Technical translation ESA-TT-914, European Space Agency
- [155] Schewe G (2001) Reynolds-number effects in flow around more-or-less bluff bodies. *Journal of Wind Engineering and Industrial Aerodynamics* 89:1267
- [156] Schlichting H, Gersten K (2000) Boundary-layer theory, 8th edn. Springer Verlag
- [157] Sedov L (1993) Similarity and dimensional methods in mechanics. CRC press, Inc.
- [158] Shi L, Liu Y, Wan J (2009) Influence of wall proximity on characteristics of wake behind a square cylinder: PIV measurements and POD analysis. *Experimental Thermal and Fluid Science*
- [159] Shi L, Liu Y, Wan J (2010) TR-PIV measurement of separated and reattaching turbulent flow over a surface-mounted square cylinder. *Journal of mechanical science and technology* 24(1):421–428
- [160] Sirovich L (1987) Turbulence and the dynamics of coherent structures. I-Coherent structures. II-Symmetries and transformations. III-Dynamics and scaling. *Quarterly of applied mathematics* 45:561–571
- [161] Smith E (2009) Ship helicopter gust response alleviation using avctive trailing edge flaps. In: AHS
- [162] Smith E, Keller J, Kang H (1998) Recent developments in the analytical investigation of shipboard rotorcraft engage and disengage operations. In: Fluid dynamics problems of vehicles operating near or in the air-sea surface, Research and Technology Organization, vol RTO Meeting proceedings, pp 1–1
- [163] Sousa J (2002) Turbulent flow around a surface-mounted obstacle using 2D-3C DPIV. *Experiments in Fluids* 33(6):854–862
- [164] Spalart P, Allmaras S (1994) A one equation turbulence model for aerodynamic flows. *Recherche aérospatiale* pp 5–5
- [165] Spalart P, Rumsey C (2007) Effective Inflow Conditions for Turbulence Models in Aerodynamic Calculations. *AIAA Journal* 45(10):2544
- [166] Spazzini P, Iuso G, Onorato M, Zurlo N, Di Cicca G (2001) Unsteady behavior of back-facing step flow. *Experiments in Fluids* 30(5):551–561

- [167] Stanislas M, Carlier J, Foucaut J, Dupont P (1999) Double spatial correlations, a new experimental insight into wall turbulence. *Comptes Rendus de l'Académie des Sciences-Series IIB-Mechanics-Physics-Astronomy* 327(1):55–61
- [168] Steele-Perkins AP, Johnston RP, Barton P (1992) Royal naval helicopter ditching experience. In: *Agard conference proceedings 532, Cesme, Turkey*, pp 36.1–36.6
- [169] Syms G (2004) Numerical Simulation of Frigate Airwakes. *International Journal of Computational Fluid Dynamics* 18(2):199–207
- [170] Syms G (2008) Simulation of simplified-frigate airwakes using a Lattice-Boltzmann method. *Journal of Wind Engineering and Industrial Aerodynamics* 96(6):1197–1206
- [171] Tai T (2001) Airwake Simulation of Modified TTCP/SFS Ship. In: *RTO Applied Vehicle Technology Panel (AVT) Symposium, Leon, Norway*
- [172] Taillemite J, Courcoux P, Bonidal A, Giry P (1993) Les accidents d'hélicoptère dans la Marine nationale de 1980 à 1991. «Le survol maritime est-il plus dangereux que le survol terrestre». *Médecine aéronautique et spatiale* 32(127):150–156
- [173] Tattersall P, Albone C, Soliman M, Allen C (1998) Prediction of Ship Air Wakes over Flight Decks using CFD. In: *AVT Symposium on fluid dynamics problems of vehicles operating near or in the air-sea interface, Research and Technology Organization, RTO MP-15, Amsterdam, The Netherlands*
- [174] Taylor J, Glauser M (2004) Towards practical flow sensing and control via POD and LSE based low-dimensional tools. *Journal of Fluids Engineering* 126:337
- [175] Tinney C, Ukeiley L (2009) A study of a 3-D double backward-facing step. *Experiments in Fluids* 47(3):427–438
- [176] Tinney C, Ukeiley L, Glauser M (2008) Low-dimensional characteristics of a transonic jet. Part 2. Estimate and far-field prediction. *Journal of Fluid Mechanics* 615:53–92
- [177] Türk M, Emeis S (2007) Wind- und Turbulenzmessungen an der Offshore-Messplattform FINO1. *Meteorologentagung Dach*
- [178] Turner G, Clark W, Cox I, Finlay B, Duncan J (2006) Project SAIF-Assessment of Ship Helicopter Operating Limits Using the Merlin Helicopter Simulator. In: *Annual Forum Proceedings, American Helicopter Society, Inc., vol 62, p 226*

- [179] Van Gool P (1997) Rotorcraft responses to atmospheric turbulence. PhD thesis, Delft University of Technology
- [180] Vickery B (1967) Load Fluctuations on Bluff Shapes in Turbulent Flow. Engineering Science Research Report BLWT-4-67, University of Western Ontario, London, Ontario, Canada
- [181] Vickery B (2006) Fluctuating lift and drag on a long cylinder of square cross-section in a smooth and in a turbulent stream. *Journal of Fluid Mechanics* 25(03):481–494
- [182] Wakefield N, Newman S, Wilson P (1998) CFD predictions of the influence of external airflow on helicopter operations when operating from ship flight decks. In: RTO AVT Symposium on fluid dynamics problems of vehicles operating near or in the air-sea interface, Research and Technology Organization, RTO MP-15, Amsterdam, The Netherlands, pp 2.1–2.10
- [183] Wakefield N, Newman S, Wilson P (2002) Helicopter flight around a ship's superstructure. *Proceedings of the Institution of Mechanical Engineers, Part G: Journal of Aerospace Engineering* 216(1):13–28
- [184] Wang H, Zhou Y (2009) The finite-length square cylinder near wake. *Journal of Fluid Mechanics* 638:453–490
- [185] Wang ZY, Plate EJ, Rau M, Keiser R (1996) Scale effects in wind tunnel modelling. *Journal of Wind Engineering and Industrial Aerodynamics* 61:113–130
- [186] West G, Apelt C (1982) The effects of tunnel blockage and aspect ratio on the mean flow past a circular cylinder with Reynolds numbers between 104 and 105. *Journal of Fluid Mechanics* 114:361–377
- [187] Whitbread R, Coleman S (2000) Research on offshore helideck environmental issues. Tech. Rep. CAA PAPER 99004, Civil Aviation Authority, London
- [188] Whitehouse G, Brown R, London U (2003) Helicopter Rotor Response to Wake Encounters in Ground Effect. In: Annual forum proceedings, American Helicopter Society, Inc., vol 59, pp 1802–1817
- [189] Wilkinson C, Zan S, Gilbert N, Funk J (1998) Modelling and simulation of ship air wakes for helicopter operations- a collaborative venture. In: RTO AVT symposium on fluid dynamics problems of vehicles operating near or in the air-sea interface, Research and Technology Organization, RTO MP-15, Amsterdam, The Netherlands

- [190] Wilkinson C, Roscoe M, Van der Vliet G (2001) Determining fidelity standards for the shipboard launch and recovery task. In: AIAA Modeling and Simulation Technologies Conference Proceedings, Montreal, Canada, Paper AIAA 2001-4062
- [191] Willmer M (1966) The Motion of Helicopter Blades at Low Rotor Speeds in High Winds. Tech. Rep. C.P. No. 852, Ministry of aviation, aeronautical research council
- [192] Wolochuk M, Plesniak M, Braun J (1996) The effects of turbulence and unsteadiness on vortex shedding from sharp-edged bluff bodies. *Journal of Fluids Engineering* 118:18
- [193] Woo H, Peterka J, Cermak J (1977) Wind-tunnel measurements in the wakes of structures. Tech. Rep. CR-2806, NASA
- [194] Yakhot A, Anor T, Liu H, Nikitin N (2006) Direct numerical simulation of turbulent flow around a wall-mounted cube: spatio-temporal evolution of large-scale vortices. *Journal of Fluid Mechanics* 566:1–9
- [195] Yakhot A, Liu H, Nikitin N (2006) Turbulent flow around a wall-mounted cube: A direct numerical simulation. *International Journal of Heat and Fluid Flow* 27(6):994–1009
- [196] Yu D, Kareem A (1998) Parametric study of flow around rectangular prisms using LES. *Journal of Wind Engineering and Industrial Aerodynamics* 77:653–662
- [197] Zan S (2001) Surface flow topology for a simple frigate shape. *Canadian Aeronautical Journal* 47(1):33–43
- [198] Zan S (2003) Technical comment on 'computational-fluid-dynamics based advanced ship-airwake database for helicopter flight simulation'. *Journal of Aircraft* 40(5):1007



This study is concerned about the safety of helicopter launch and recovery on frigates. Therefore, it consists in investigating the airwake of a simplified frigate, modeled by a 3D backward facing double step in order to have a better understanding of such 3D unsteady flows. The mean and fluctuating velocity fields have been analyzed mainly experimentally through PIV, hot-wire anemometry, oil-flow visualizations ... This has enabled to observe 3D structures, confirmed by a numerical computation. In particular, the results show a mean flow asymmetry. A sensitivity study around the zero degree drift angle has shown that the flow is bi-stable for this geometry. This bi-stability has been observed in several wind-tunnels for a wide variety of upstream geometric conditions. The understanding of this phenomenon is required for future control of such complex flows.

Cette étude s'inscrit dans le domaine de la sécurisation de l'appontage des hélicoptères sur les frégates. Il s'agit ici d'analyser le sillage aérodynamique d'une frégate générique modélisée par une double marche descendante dans le but de mieux comprendre ce type d'écoulement tridimensionnel instationnaire. Les champs de vitesse moyen et fluctuant ont été analysés essentiellement par voie expérimentale (PIV, fil chaud, visualisation pariétale...) et ont permis de valider la présence de structures tridimensionnelles mises en évidence grâce à une simulation numérique. Les résultats montrent en particulier la présence d'une asymétrie de l'écoulement moyen. Une étude fine autour de l'angle de dérapage nul a permis de confirmer le caractère bi-stable de l'écoulement autour de cette géométrie. Cette bi-stabilité a été observée dans différentes installations et pour un large éventail de conditions géométriques amont de la maquette. La compréhension de ce phénomène est déterminante avant toute tentative visant à mettre en oeuvre le contrôle de ce type d'écoulement complexe.